Diss. ETH No. 15226

Loss Mechanisms in Labyrinth Seals of Shrouded Axial Turbines

A dissertation submitted to the

SWISS FEDERAL INSTITUTE OF TECHNOLOGY ZURICH
(ETH Zürich)

for the degree of

Doctor of Technical Sciences

presented by

Axel PFAU
Dipl.-Ing., Universität Karlsruhe (TH)
born September 6, 1970
citizen of the
Federal Republic of Germany

accepted on the recommendation of

Prof. Dr. R.S. Abhari, examiner
Prof. Dr. L. Kleiser, co-examiner

Zurich 2003

ACKNOWLEDGMENTS

ABSTRACT

The interaction flows associated to open cavities in shrouded, high pressure turbines were experimentally investigated in this dissertation. For this purpose a two-stage, shrouded, axial turbine was built and commissioned. The measurement campaign focused on the rotor tip labyrinth seal, comprising two seal gaps, 0.3% and 0.8% blade height. The labyrinth seal consists of an open inlet cavity, closed labyrinth cavities and an open exit cavity. The size of those cavities is small in comparison to the main flow channel height (15% of blade height). Therefore, a new probe measurement technology of minimum blockage effect was developed. The new virtual four sensor, fast response aerodynamic probe (FRAP) resolves the deterministic, unsteady flow field up to 25kHz in terms of flow angles, velocity and total and static pressure.

The inlet cavity to the labyrinth seal is subject to strong in and out flows, which involve up to four times the leakage mass with a superimposed unsteady fluctuation of $\pm70\%$ of the leakage mass flow. The in and out flow happens in specific flow regions set up by the downstream flow field of the stator. This results in unsteady fluctuations on the downstream rotor inlet flow field. A control volume analysis revealed the forces which act on the fluid close to the interaction zone. The radial equilibrium of forces is applied to the inflow streamline, explaining the inviscid exchange mechanism. Due to the sucking of the leakage the flow loses circumferential and axial momentum across the interaction zone, which results in a negative incidence at the rotor blade tip. A flow model is derived which predicts negative incidence angles of -9° for gap widths of the order of 1.5% blade height. The cavity flow is dominated by two toroidal vortices, which swirl around the annulus at a high tangential velocity of 82% blade tip speed. Both vortices are stretched in space and time, due to the fluctuating velocity gradients setup by the moving pressure fields.

A small portion of losses was found to be caused by the inlet cavity flow itself, which are mainly due to wall friction effects (2.7% of stage loss). Additional losses may be induced within the rotor blade row due to the negative incidence in combination with fluctuating flow angles and velocities at the rotor tip inlet. This region is of importance to the secondary flow formation within the rotor passage. The inlet boundary conditions to the rotor tip region found in this configuration is discussed in detail.

The exit cavity flow comprises three flow features, which interact among each other: the cavity fluid flow being a toroidal vortex, the leakage jet and the main flow. The cavity flow is mainly driven by the jet due to viscous shear. The tangential velocity of the cavity flow was found to depend on the strength of the

jet. Most part of this viscous interaction happens from the last seal till mid axial cavity position. Downstream of this location the leakage jet starts interacting with the main flow while it re-enters into the main annulus. The leakage fluid radially migrates into the rotor wake. Furthermore, the leakage jet is redistributed according to the trailing edge pressure field.

The highest losses found in this investigation were the windage effect within the closed cavities and the mixing effects downstream of the rotor, 33% respectively 10% of the stage loss. A two-step mixing calculation was applied in order to quantify the downstream mixing losses. Some potential of reducing these downstream mixing losses was found in the way the leakage jet is fed back into the main flow. From this finding a non-axisymmetric last gap shape is proposed, whose task it is to reconfigure the leakage jet before it interacts with the main flow. The resulting beneficial effect is of the order of 0.1% efficiency.

KURZFASSUNG

In dieser Dissertation wurden die Interaktionsströmungen, wie sie in axialen Hochdruckturbinen mit Deckbändern in den Ein- und Austrittskavitäten der Labyrinthdichtungen auftreten, experimentell untersucht. Zu diesem Zweck wurde eine zweistufige Versuchsturbine gebaut und in Betrieb genommen. Die Messkampagne konzentrierte sich auf die Rotorspitzendichtung, wobei zwei verschiedene Spaltweiten, 0.3% und 0.8% der Schaufelhöhe, untersucht wurden. Eine Labyrinthdichtung besteht aus einer offenen Eintrittskavität, einigen geschlossenen Kavitäten und einer offenen Austrittskavität. Die Kavitäten sind mit je einer Drosselstelle (Spalt) miteinander verbunden. Die Abmasse dieser Kavitäten sind im Verhältnis zum Hauptströmungskanal relativ klein (15% der Kanalhöhe). Um in diesen Kavitäten messen zu können, wurde eine neue Sondenmesstechnik entwickelt, die sich durch minimierter Versperrung auszeichnet. Diese neue virtuelle Vier-Sensor-Sonde misst das deterministische, instationäre Strömungsfeld bis zu Frequenzen von 25kHz. Dabei liefert die Sonde Strömungswinkel, Strömungsgeschwindigkeit sowie Total- und statischen Druck.

Die Interaktionsströmung in der Eintrittskavität besteht aus Ein- und Ausströmungen, die bis zum Vierfachen des Leckagemassenstromes umfassen und mit ±70% des Leckagemassenstromes fluktuieren. Die Ein- und Ausströmungen befinden sich innerhalb genau lokalisierbarer Bereiche der Statorabströmung und erzeugen instationäre Fluktuationen im Rotoreintritt. Mit Hilfe der Kontrollvolumenmethode wurden die Fluidkräfte analysiert, die in der Interaktionszone wirken. Das Kräftegleichgewicht in radialer Richtung wurde angewendet und erklärt den reibungsfreien Impulsaustausch. Die Absaugung der Leckage erzeugt eine negative Inzidenz der Rotorzuströmung im Spitzenbereich dadurch, dass sowohl axialer als auch tangentialer Impuls der Interaktionszone entzogen wird. Ein in dieser Arbeit entwickeltes Strömungsmodell sagt eine negative Inzidenz von -9° für Spaltweiten von 1.5% der Schaufelhöhe voraus. Die Kavitätenströmung besteht aus zwei Toruswirbeln mit entgegen gesetztem Drehsinn, die mit einer Geschwindigkeit von 82% der Rotorgeschwindigkeit umlaufen. Die Wirbel werden durch Geschwindigkeitsgradienten in Raum und Zeit gedehnt und gestreckt.

Die Eintrittskavität an sich erzeugt einen relativ kleinen Verlustanteil von 2.7% der Stufenverluste auf Grund des Wandreibungseffekts. Durch die Interaktionsströmung können zusätzlich Verluste im Rotor induziert werden, da die negativen Inzidenzen zusammen mit den fluktuierenden Effekten die Sekundärströmungsentwicklung nachhaltig beeinflussen. Die Eintrittsströmung im Spitzenbereich des Rotors wird eingehend diskutiert.

Die Strömung in der Austrittskavität ist durch drei Phänomene bestimmt, die miteinander interagieren: die Kavitäten-, die Hauptströmung und der Leckage-strahl. Die Kavitätenströmung wird hauptsächlich vom Leckagejet über Reib-kräfte angetrieben. Die Umfangsgeschwindigkeit in der Kavität hängt von der Stärke des Strahls ab. Der grösste Teil dieser Interaktion findet zwischen der letzten Dichtungsdrossel und der Mitte der Kavität in axialer Richtung statt. Weiter stromab kommt die Leckage mit der Hauptströmung in Berührung, während der Leckstrom in den Hauptkanal zurückkehrt. Der Leckagestrom wandert radial in die Nachlaufdelle des Rotors und wird dabei vom Druckfeld der Rotorhinterkante umverteilt.

Die grössten Verluste wurden sowohl in der Reibleistung des Labyrinths als auch in der Mischung des Leckagestrahls gefunden. Ersterer betrug 33% der Stufenverluste, letzterer etwa 10%. Mit einer zweistufigen Mischungsrechnung wurden die Verluste in der Rotorabströmung berechnet. Daraus entwickelte sich die Möglichkeit, die Verluste durch gezieltes Ausblasen des Leckage-stroms zu reduzieren. Dazu müsste dem Leckagestrom durch eine gewellte Dichtungsspaltform eine asymmetrische Verteilung aufgeprägt werden. Der Wirkungsgradgewinn durch diese Massnahmen bewegt sich in der Grössenord-nung von 0.1%.

VI

TABLE OF CONTENTS

1 INTRODUCTION

The principal idea of turbomachines is the continuous power conversion between thermodynamic energy of a fluid and rotational power of a shaft. Turbines extract energy from the fluid and compressors use the mechanical power on the shaft to lift the working fluid to a higher level of energy. In the case of a turbine, the fluid is expanded in a stationary row of blades (stator) resulting in a highly swirling flow. The generated rotational momentum is transmitted onto the rotating shaft via tangential forces acting on a rotating row of blades (rotor). Both blade rows together define a stage and generate mechanical power on a rotating shaft. Therefore, a turbomachine, compressor or turbine, always consists of alternating stationary and rotating rows of blades. Rotating and stationary parts inherently need a gap in between, which allows the relative movement. Since these gaps introduce leakages into the system, which bypass the working section, the performance of the machine is reduced. This dissertation deals with these primary leakage flow paths as found in shrouded high pressure turbines. A detailed introduction to the problem is given in the following sections.

Turbomachines are designed to be part of a continuous process of energy conversion. Since the invention and realisation of the first turbomachines at the end of the 19$^{\text{th}}$ century, two fields of application were particularly successful: the generation of electric power based on a steam or gas cycle and the generation of thrust for aeroplane application using solely a gas turbine cycle. In all fields of application the competitiveness of a turbine is a melange of several factors: efficiency, life time, power density, direct operation cost, manufacturing costs, emissions. While in the beginning of the turbomachinery the development of more efficient engines had highest priority, [71] shows that nowadays the cost of manufacturing, operating, and maintaining those machines decides on the success of a new type of turbine. This is specially true for gas turbines and flight engines. In the case of large steam turbines used for power generation, the efficiency still is the important marker.

From a thermodynamic point of view an obvious target is to reduce the leakage, which is inherently introduced to the turbine between the stationary and rotating parts. Either the blades are built free standing or are equipped with a labyrinth seal on top of the blade end. Fig. 1.-1 shows two examples of shrouded high pressure steam turbine stages. The low pressure stages are free ending. In both cases of blade tip design a minimum tip clearance to the casing or the hub is the goal. The labyrinth seal consists of a series of flow resistances in form of sealing knives (see Fig. 1.1.1-1). The knives are positioned perpendicular to a ring called shroud, which covers the blades. Therefore, blade passages of

shrouded turbines are confined on four sides of the passage including the hub and tip end wall. The labyrinth seal is advantageous, since less leakage mass flow at the same seal gap passes in comparison to a free standing blade. This is because a high number of flow restricting knives increases the sealing effect.

Fig. 1.-1   High and mid pressure steam turbines with shrouded blades

From a mechanical and heat transfer point of view shrouds on rotating rows impose considerable difficulties. The higher mass at the blade tip induces additional mechanical stresses due to the increased centrifugal forces. In gas turbines shrouds have to be cooled, since hot gases and windage effects in the labyrinth lead to high surface temperatures ([68], [70]). In addition, the manufacturing of shrouded blades is more elaborate and therefore usually more expensive.

These technically and economically limiting factors restrict the application of shrouds to blades of low and medium aspect ratios as they are found in high and intermediate pressure turbines. Low pressure turbines with aspect ratios greater than 5:1 are not supplied with shrouds. Supplying a high pressure turbine stage with labyrinth seals introduces open cavities at the casing and hub end walls. The leakage mass flow is sucked into the inlet cavity, passes through the labyrinth seal, which consists of several closed cavities, and enters into the main flow path again through the exit cavity. The flow within the open cavities is driven by the main flow and the leakage jet.

Flow interactions of the main flow with the open cavities, particularly if a leakage jet is present, determine the inlet flow conditions to the end wall region of a downstream blade row. This is essential for the secondary flow formation within the downstream blade row. In addition, the flow processes associated to the flow interactions contribute to the loss generation within the turbine stage. For steam turbines these open cavities are particularly large since the design must allow for the axial thrust variation and the thermal expansion of the rotor during warming up and down cycles.

1.1 LITERATURE SURVEY

1.1.1 Labyrinth seals

Labyrinth seals have been subject of research from the early beginnings of turbomachinery. As an inherent need of turbomachines, gaps must be present between stationary and rotating parts to allow the relative movement. Those gaps open bypass ways which reduce the amount of mass within the working section of the turbine or compressor. Introducing labyrinth seals into these gaps helps to reduce the leakage mass flow, thus increasing the efficiency. In Fig. 1.1.1-1 some examples of labyrinth geometries are depicted. The labyrinth seal arrangement at the blade tip consists of an inlet cavity, a series of closed cavities and an exit cavity. The size of the cavities can be relatively large in comparison to the blade size and channel height. This is in order to allow for the axial displacement of the rotor due to thermal growth or axial thrust variations.

Major effort in research was undertaken to reduce the leakage mass flow due to improved seal design. An example of an early contribution to this is [13], who investigated look through as well as stepped labyrinth seals with one or several sealing fins. Comparable publications with the aim of improving the leaking characteristic of the seals are [56],[72], [74] and [37]. These publications also give empirical discharge coefficients for various labyrinth seal geometries and applications. A compendium of the theory on labyrinth seals is given by [60] and a review on this subject is given in [54].
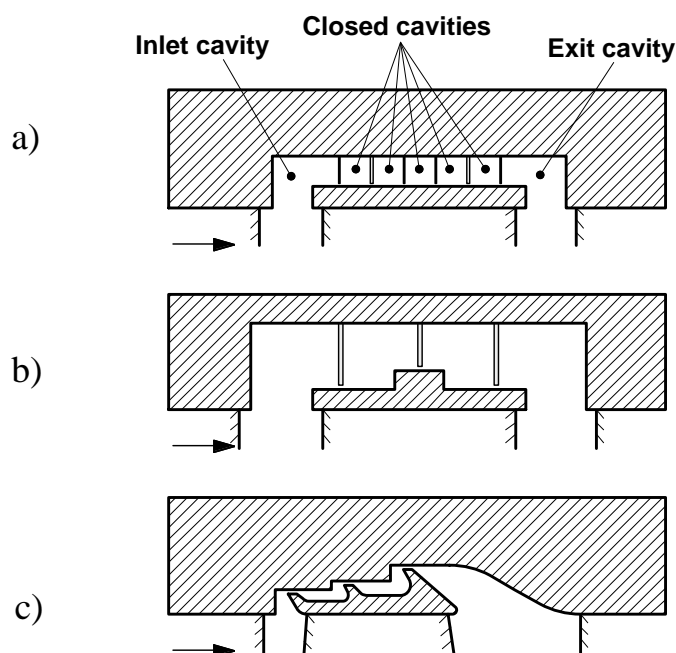
Fig. 1.1.1-1   Examples of labyrinth seal configurations: a) look through, b) stepped labyrinth, c) gas turbine

The throughflow of an ideal labyrinth seal calculates to

$$\dot{m}_{id} = A p_{in} \sqrt{\frac{2}{R T_{in}}} \sqrt{\frac{\kappa}{\kappa - 1} \left(\left(\frac{p_{out}}{p_{in}} \right)^{2/\kappa} - \left(\frac{p_{out}}{p_{in}} \right)^{(\kappa + 1)/\kappa} \right)} \qquad (1.1)$$

assuming ideal nozzle flow of the same area and pressure ratio. Equation (1.1) is based on the equation of de Saint Venant and Wantzell. The gap area is denoted with A. In the literature ([60], [43], [72]) a discharge coefficient is used defined as

$$C_D = \frac{\dot{m}_{leak}}{\dot{m}_{id}}, \qquad (1.2)$$

which describes the real behaviour in terms of through flow. Empirical ([67]) and numerical ([43]) approaches are used to determine C_D. The discharge coefficient depends mainly on the pressure ratio, the numbers of seals, and the labyrinth seal design. For large numbers of seals n, the leakage mass flow is inversely proportional to the square root of n. The accurate prediction of the leakage mass flow is essential for the prediction of the turbine performance. From an aerodynamic point of view the goal is to have smaller gaps and seal designs with higher flow resistances.

From a heat transfer point of view the aerodynamic design rule may not be appropriate. The prediction of heat transfer coefficients and surface temperatures are crucial for the life time of gas turbine blades. Therefore, a temperature rise due to wall friction at the rotating shroud is an issue for the labyrinth seal design in gas turbines. This so-called windage effect was addressed by [33], which states that the windage is strongly affected by the leakage mass flow. The windage heating also depends on the surface areas. The same level of windage is present for labyrinth seals of the same surfaces area (but different design), same nominal radii at the same flow level.

From a rotor dynamic point of view, labyrinth seals are a potential source of unsteady, whirling pressure forces. These pressure forces are caused either by eccentric rotor shafts [38] or flow instabilities within the cavities [39].

1.1.2   Turbine flow field

Secondary flows

The modern design target for competitive turbines is driven from economical considerations: Use less stages and less blades per stage for the same demand

of power at the same or a higher efficiency. In order to achieve lower counts of stages and blades the blade loading has to increase. Particularly in low aspect ratio passages this results in enhanced secondary flows, which might cover up to 30% of the passage area. In recent decades of blade development, several three-dimensional design features, e.g. leaned blades, end wall contouring [18], leading edge bulb [42] and dove tails [12] were introduced to control and reduce the secondary flows.

Secondary flows can be defined as components of the flow motion which deviate from the design intent and therefore are not parallel to the mean streamlines. Vortices, which evolve in the blade passage due to the turning of an incoming vorticity sheet as present in a boundary layer, create velocity components perpendicular to their mean flow direction. In the exit of a blade row, this results in a local deviation of the flow angle to higher and lower values. Secondary flows are not welcome since they store secondary kinetic energy, which reduces the lift of the blade. The resulting non-uniform exit flow angle changes the work output and may cause additional losses in downstream blade rows. In addition, secondary flows in themselves create loss of working potential [17], [30].

Steady models on the secondary flow field in turbine blade rows are derived from cascade experiments, where the flow field within and downstream of a single blade row is investigated. Langston [30] and Sieverding [51] give an overview of flow models derived in recent decades of research. Basic elements of the secondary flow field are the passage vortex, the horse-shoe vortex and the corner vortex. The basic precondition for the formation of secondary flows is the end wall boundary layer, as depicted in Fig. 1.1.2-1 ([49]). The boundary layer can be described either in terms of a velocity profile or as a layer of tangential vorticity. Both descriptions help to understand the formation of secondary flow. Due to the cross passage pressure gradient streamlines close to the wall have a much smaller turning radius than the main flow within the passage. This motion sets up a rotating flow motion. The tangential vorticity vector of the incoming boundary layer is turned within the passage, which results in a stream-wise vorticity component. Both mechanisms create the passage vortex. The passage vortex is pushed toward higher span by approaching the suction side surface. The inlet boundary layer fluid is moving with the passage vortex and finally is gathered in a loss core on the suction side of the blade wake. Downstream of the cross passage movement of the passage vortex a new thin end wall boundary is formed.

The horse-shoe vortex forms in the end wall leading edge corner, where the boundary layer separates at a saddle point. The suction side leg of the horse-shoe vortex wraps around the passage vortex. The pressure side leg of the

horse-shoe vortex merges into the passage vortex, since both vortices have the same sense of rotation.

Wang et al. [66] give an even more complex picture of the steady vortex system within a blade passage (Fig. 1.1.2-2). Additional to the main vortices, described with Fig. 1.1.2-1, a corner vortex and a leading edge corner vortex are also detected.
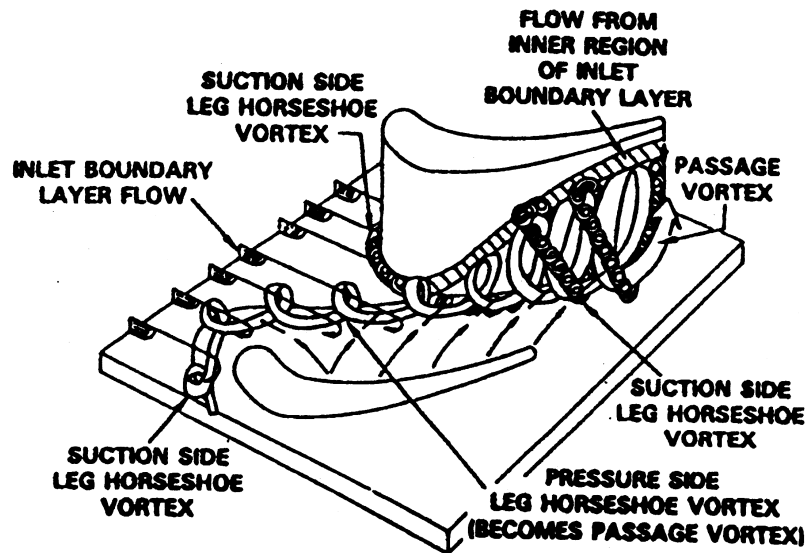
Fig. 1.1.2-1   Vortex development in blade passage: Sharma et al. [49]
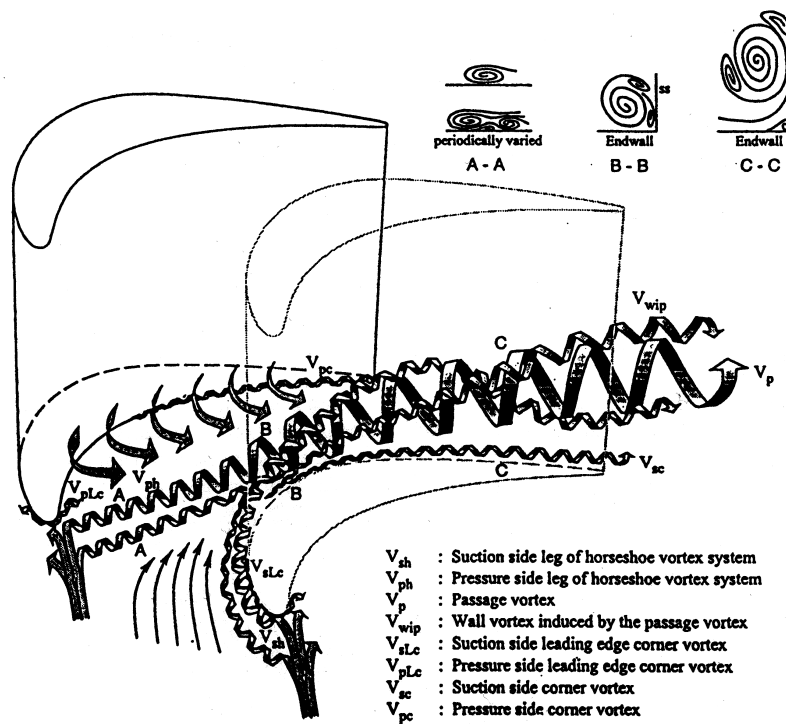
Fig. 1.1.2-2   Secondary flow development: Wang et al. [66]

The actual secondary flow pattern and the associated losses of a blade passage depend on several parameters: blade loading and loading distribution, aspect ratio, pitch to chord ratio, incidence, the three-dimensional blade shape, and the inlet boundary layer.

In all of these above mentioned secondary flow models the incoming boundary layer plays a central role. In clean cascade experiments, the boundary layer is axisymmetric and can be adjusted to the shape of interest, e.g. boundary layer thickness, shape factors, turbulence level of main flow. In a shrouded turbine however the formation of a boundary layer in the sense of a long undisturbed endwall is not possible. The presence of inlet and exit cavities (Fig. 1.1.1-1) are expected to change the inlet condition to a downstream blade row in the steady and unsteady flow regime, and thus the formation of the secondary flow field. This specific topic is rarely considered in open literature and will be discussed in a later section (1.1.3).

Unsteady flow

The flow field within turbines is unsteady due to the movement of the rotor relative to the stator and due to turbulence. The unsteadiness can be divided into two main groups:

1) random unsteadiness associated to turbulence and stochastic processes.

2) periodic unsteadiness that occurs at the blade passing frequency or rotational frequency and the higher harmonics.

The degree of periodic unsteadiness in a flow field can be characterised, using the reduced frequency

$$f_{red} = \frac{fx}{v} = \frac{\text{Convection Time}}{\text{Disturbance Time}},\qquad(1.3)$$

where x denotes a characteristic length of the geometry, e.g. axial blade chord, f the frequency of incoming disturbances, e.g. wakes, and v the convective velocity. For values of $f_{red} \gg 1$ unsteady effects dominate the flow. Values around 1 indicate that quasi-steady and unsteady characteristics are mutually present. As the reduced frequency only expresses the ratio of convection time scale versus disturbance time scale a quantitative expression of the importance of unsteady effects is not given.

Several kinds of periodic unsteady interactions are present in a turbine, which will be discussed in the following sections: Wake-to-blade interaction and clocking, potential field interaction and vortex interaction. The unsteady interactions caused by open cavities are discussed in 1.1.3.

Wake-blade row interactions

Wakes of an upstream blade row release periodic disturbances onto the blade passage of the following blade row. The wakes are chopped and an avenue of wake pieces is generated as [5] describes. Convecting through the blade passage the wake segment is bowed in the first part of the passage due to the higher velocity of the middle passage flow, sheared near the suction surface and stretched near the pressure surface as discussed in [24]. The net result of this process is that a big portion of the wake fluid is gathered on the suction side of the passage with a tail stretching back to the rotor trailing edge as can be seen in Fig. 1.1.2-3.
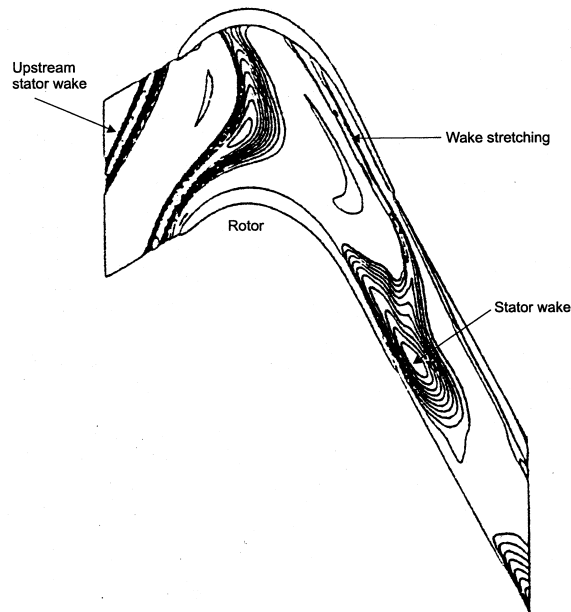
Fig. 1.1.2-3   Stator wake development in a downstream rotor passage [24]

Wakes are detectable in the flow field many blade rows downstream of their origin. The relative position of those wakes to downstream blade rows of the same frame of reference is affecting the efficiency. Thus an interaction effect happens from stator to stator as well as rotor to rotor blades in how the stator rows or rotor rows are positioned relative to each other. This so-called clocking effect was investigated by [25]. The authors report of a ±0.5% change of efficiency depending on the clocking position, i.e. the relative stator-to-stator position.

When a wake is chopped and a piece is convecting through the rotor passage, the wake is influencing the boundary layers on the blade surfaces. The wake can be described as a negative jet moving low kinetic energy fluid from the pressure side to the suction side [32]. The boundary layer on both the pressure and suction side of the passage are periodically disturbed by this wake remnants. However, the boundary layer on the suction side is much more sensitive

to disturbances due to its tendency to separate. The periodic disturbances of the wake jets can be beneficial [47], if the Reynolds number is relatively low as in low pressure turbines. Then the separation on the suction side of a highly loaded blade is suppressed. As the wake moves along the suction surface it induces bypass transition of the boundary layer. The boundary layer downstream of the point of transition is less sensitive to separation, because it contains a so-called calmed region of thinner and more stable boundary layer [48]. Therefore, the blade is able to perform a higher turning at the same efficiency.

Potential field interaction

In subsonic flow the potential pressure field of leading and trailing edges is acting both upstream and downstream of the blade proportional to

$$p \sim \exp\left(-2\pi\sqrt{1 - \mathrm{Ma}^2}\frac{x}{L}\right) \tag{1.4}$$

where x is the distance to the blade and L is the blade pitch [34]. Equation (1.4) describes the potential field effect in the case of a two-dimensional cascade moving with blade Mach-number M=U/a in stationary air. From (1.4) it can be seen that the pressure decay is higher in low Mach-number flows and decays exponentially with the distance x. Note that the decay scales with the blade pitch and not the blade chord. This is important if different blade loadings (pitch-chord ratios) are being considered. In the three-dimensional, unsteady flow environment of a turbine, the propagation of pressure waves becomes a three-dimensional problem, since the pressure waves are propagating in all directions at the speed of sound. In addition, the convective speed is superimposed on the pressure field propagation such that the downstream decay is attenuated. In the extreme case of choking flow no downstream pressure information reaches the location of sonic condition.

The potential field interaction may cause noise and blade vibrations, especially when the axial inter-blade gap is reduced. Potential field interactions are also responsible for strong pulsations of the coolant flow within the holes of film cooled flight engine stages, as investigated by Abhari [1]. As a result of the unsteady fluctuations the film cooling effectiveness on the pressure side of the rotor blade is substantially reduced.

In terms of aerodynamic effects, potential field interactions will cause fluctuating streamlines and vortices due to the relative movement of the convective flow field to spatial and temporal gradients of the static pressure field. The motion of the static pressure field in space and time is inviscid. However, non-linear effects on viscous flow features like boundary layers due to acceleration and deceleration or unsteady vortex tilting and stretching may cause additional loss-

es.

In the turbine under investigation the flow is subsonic with an axial through-flow Mach-number M_x=0.12. The blade tip Mach-number is M_{Tip}=0.33 and the blade row axial gap is 33% of blade pitch. Therefore, the pressure field at mid axial gap position is a superposition of upstream and downstream acting pressure fields, where one of them is moving relative to the other. At this location, each blade row contributes 50% of their initial pressure amplitude (1.4).

Vortex interactions

The secondary flow field downstream of a blade row contains a system of vortices as discussed in the above section. Harrison [20] has shown that in low aspect ratio machines, the secondary flows in the form of streamwise vortices are significant across the blade covering up to 30% of the blade span. This number can be even higher for lower aspect ratios. The vortices are convected downstream towards the next blade row where they interact with blade passage flow.

Due to the relative movement of blade rows vortices are cut by the downstream blade row. In this vortex-blade interaction a vortex breakdown may occur as reported for the first time by Binder [4]. The interaction processes comprise vortex filling and cutting. Together with the strong deformation of the vortex cross-sectional area as the vortex enters into the downstream blade row, a vortex breakdown is triggered. The vortex-rotor interaction can cause atypical flow angle distributions as experimentally verified in Hobson and Johnson [23] and Sharma et al. [50]. The spanwise distribution of the flow angle in the exit of a second stator inverts in comparison to the classical secondary flow behaviour of overturning at endwall regions and underturning in mid span regions. This effect was attributed to the vortex interaction happening within the stator passage. Chaluvadi et al. [7], [8] experimentally and numerically investigated the vortex transport in downstream blade rows. It was found that the stator passage vortex develops two counter-rotating legs of the vortex on the pressure and suction side of the downstream rotor passage. The authors derived a kinematic model which describes the vortex transport assuming the incoming vortex to be a concentrated vortex filament.

1.1.3   Shrouded turbine blade rows

An early publication on flow interactions in shrouded turbines is Denton and Johnson [10]. The flow patterns around the shroud of a single-stage turbine rotor equipped with a single sealing fin was found to be complex and difficult to measure. The leakage jet exiting the single seal has a considerable tangential velocity due to the initial tangential momentum induced by the stator on the one

hand and due to the windage effects of the rotating shroud onto the jet on the other hand.

It was not until recent years that the subject of steady and unsteady flow field associated to labyrinth seals and open cavities was addressed more frequently. Taylor et al. [57] investigated different shroud configurations combining sealing fins with fences. No statement is given about the design intent of the fences. However, from the picture given it can be concluded that the task of the fences is to align the leakage flow to the relative exit flow angle of the rotor. The authors identified strong periodic unsteadiness in the tip region. The driving mechanism was named to be an unsteady pressure field interaction between the stator and the rotor. Peters et al. [35] examined the effect of gap size on the steady interaction between the leakage flow and the secondary flow field of a subsequent stator in a 1.5-stage, shrouded axial turbine. The authors report about the negative incidence of the leakage flow to the downstream stator. The stator passage is intensified with increasing gap width. Hunter and Manwaring [26] concentrated on the second stator labyrinth seal of a 2-stage, large scale axial turbine. The authors reported about two extra vortices found downstream of the second stator blade row. Their origin was identified to be the leakage flow of the first stator labyrinth. A primary source of loss was found to be associated with the mixing of circumferential momentum components at the cavity exit. In an experimental investigation performed in a stationary, annular cascade the present author [36] discovered that the leakage sheet exiting the last seal gap breaks up into one distinct jet per blade pitch. The cause of the splitting process was found to be high kinetic energy fluid originating from the pressure side corner of the blade passage entering the cavity. Two additional driving mechanisms were identified: the pitch-periodic static pressure field and the passage vortex.

Wallis et al. [65] attempted to make use of the kinetic energy of the labyrinth leakage jet in turning devices placed on top of the rotor shroud. In doing so within a four-stage shrouded axial turbine the efficiency dropped dramatically. From additional CFD calculations strong unsteady interactions in the open cavities were identified. The following blade rows were found to receive the tip flow at a negative incidence. Anker and Mayer [3] numerically investigated the leakage interaction with the main flow and found that the tip leakage flow is not uniform in the pitch-wise direction. Schlienger et al. [46] changed the geometry of the labyrinth exit cavities and compared the effects on the main flow as well as on the efficiency.

1.1.4   Loss generation and quantification

The thermodynamic measure of loss generation is the increase of entropy according to the second law of thermodynamics. For a perfect gas the entropy change of a fluid particle is defined as

$$\Delta s \;=\; c_p \ln \frac{T}{T_{ref}} - R \ln \frac{p}{p_{ref}} .$$ (1.5)

In turbomachinery various loss coefficients are used in order to quantify the entropy increase, which are discussed in detail in Denton [11]. The pressure loss coefficients defined as

$$Y \;=\; \frac{p^o_{in} - p^o_{out}}{p^o_{out} - p_{out}}$$ (1.6)

describes very well the entropy increase in a stationary blade row, where the total temperature stays constant. More useful for entire turbine or compressor stages is an entropy loss coefficient which can be defined as

$$\zeta \;=\; \frac{T\Delta s}{h^o_{out} - h_{out}} .$$ (1.7)

Several mechanisms present in turbomachinery create entropy, namely: viscous effects in boundary layers, mixing processes in free shear layers, heat transfer across finite temperature differences, and non equilibrium processes such as shock waves.

Of particular interest to this investigation is the mixing process in free shear layers and jets. As shown in Fig. 1.1.4-1 several regions of mixing in a labyrinth seal arrangement can be addressed: The leakage jet shortly downstream of the last gap mixes with the cavity flow. Re-entering into the main flow path, the partially diffused leakage jet starts mixing with the main flow. The mixing process further continues within the downstream blade passage. Although the leakage jet will mix with the entire main mass flow, most of the entropy generation will have happened by the time the jet has mixed with about 5 times its own flow rate of the main flow. This mixing will occur within a few diameters of the jet (see [11]) and therefore will affect mainly the region in close vicinity to the end wall.
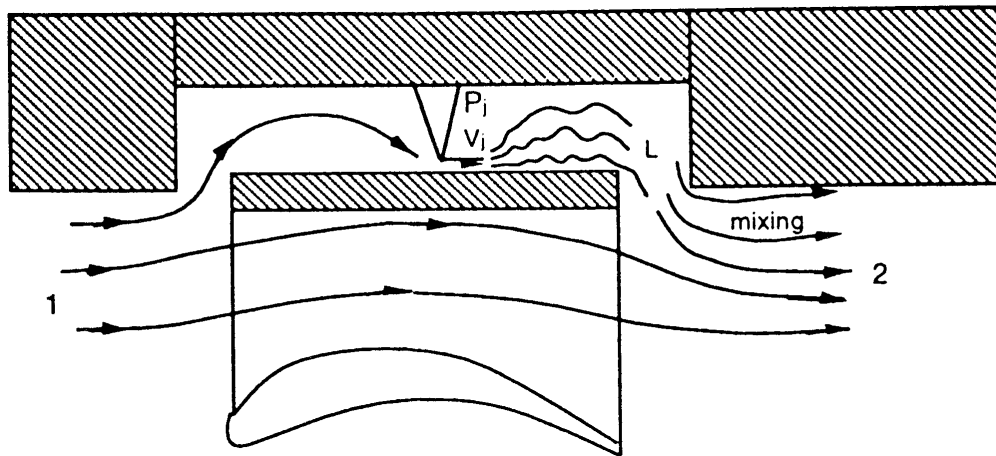
Fig. 1.1.4-1   Flow over a shrouded rotor tip seal [11]

For the simplified situation given in Fig. 1.1.4-1 Denton [11] derives a mixing model of the leakage jet. The author performs the calculations in the relative frame of reference and assumes that the relative stagnation enthalpy of the main (m) and leakage (l) flow is the same. The fluid is also assumed to be incompressible. From this approach Denton obtains

$$T\Delta s = \frac{\dot{m}_l}{\dot{m}_m}\left[v_{\Theta m}^2\left(1 - \frac{v_{\Theta l}}{v_{\Theta m}}\right) + v_{zm}^2\left(1 - \frac{v_{zl}}{v_{zm}}\right)\right], \qquad (1.8)$$

where the circumferential and axial velocity components (v_Θ, v_z) of the main flow are denoted with m and the ones of the leakage with l. From this equation it can be concluded that the mixing losses associated to the labyrinth leakage are proportional to the leakage fraction and therefore to the tip clearance. It is also observed that the losses increase with a larger mismatch of both velocity components. In the blade relative coordinate system the tangential velocity component is roughly three times higher than the axial velocity component. Therefore, the same rate of adjusting the leakage jet momentum to the main flow momentum (v_l/v_m) is generating more entropy in the circumferential direction than in the axial direction.

1.2 MOTIVATION AND CONTRIBUTION

As it can be seen from 1.1.3, the published work on the subject of leakage interaction in shrouded turbines is focused mainly on the interaction happening in the main annulus and the downstream blade passage. However, since the origins of these interactions are the open cavities of labyrinth seals, the contribution of this dissertation is on the associated steady and unsteady flows. The unsteady fluctuations may create large-amplitude deviations to the time-averaged structure of the cavity flow. Thus, the actual cavity flow may be quite different from the steady model proposed by Pfau et al. [36]. In addition, increasing the seal gap, e.g. through wear during the life time of a turbine, has significant influence on the flow field due to sucking more leakage mass flow into the inlet cavity and due to a stronger jet within the exit cavity which mixes out in a downstream blade row. Therefore, a gap variation is of importance for the subject of cavity interaction flows.

This dissertation deals with the flow field related to labyrinth seals in shrouded turbines and the associated loss mechanisms in the open cavity flow and the main flow. The detailed questions to answer are as follows:

1) Clarify the steady and unsteady flow interactions associated to open cavities.

2) Describe and quantify loss production mechanisms caused by labyrinth seals in shrouded turbines.

3) Develop theoretical models to describe the flow effects in an analytical way.

4) Translate the knowledge into design recommendations and modifications accounting for changed end wall inlet conditions to the blade rows. Assess the potential of loss reduction by applying these means.

In order to attack those goals a 2-stage axial research turbine was developed and brought into operation. The test rig is a subsonic, continuously running turbine with 400kW maximum power and a suction peak Mach number in the stator rows of 0.4. The blade aspect ratio is 1.8 and the blade-shroud design is representative for a high pressure steam turbine. Additionally, the appropriate measurement technology was developed. A measurement campaign comprising operation point and gap widths variation was performed.

1.3 THESIS OUTLINE

A literature review has been given in chapter 1.1. The two elements, main flow in high pressure turbines and labyrinth seal flow, are discussed separately. In a third section previous work carried out by other researchers on the leakage and open cavity flow interaction is reviewed.

Chapter 2 presents the 2-stage, axial research turbine "LISA" and the applied instrumentation, data acquisition and measurement technology. An error analysis of the measurement chains and the global parameters, e.g. the mass flow and the efficiency, is given. Furthermore, the measurement campaign and the resulting experimental data sets are discussed.

In order to measure the three-dimensional, unsteady flow within open cavities a special measurement technology was developed. The virtual four sensor fast response aerodynamic probe (FRAP) is described in detail in chapter 3.

Chapter 4 gives an overview of the turbine performance and the main flow field of the measurement stage. The general boundary conditions of the cavity flow interaction are described. The efficiency of the turbine is discussed and the stage loss production is quantified.

The closed cavities of the labyrinth seal are the subject of chapter 5. The labyrinth seal characteristics are discussed. The leakage mass flow is estimated from empirical correlations and compared to the experimental results.

Chapter 6 is dedicated to the inlet cavity of the rotor labyrinth seal. A time resolved volume data set was measured for one configuration. The drivers of the flow interaction are identified and described. An experimentally based flow model is presented, which predicts the change of incidence angle to the rotor tip region due the change of labyrinth clearance. The chapter concludes with descriptive flow models of the flow interactions.

Chapter 7 deals with the leakage jet interaction within and downstream of the exit cavity. The influence of the rotor-stator interaction on the mixing of the leakage fluid is found in the experimental results. A new design strategy for shrouds attempting to optimize the leakage to main flow mixing losses is presented.

Chapter 8 concludes the dissertation with a summary of the identified loss mechanisms and their quantification and proposes future work.

2 EXPERIMENTAL FACILITY AND METHODS

True experimental conditions in the sense of a true unsteady, aero-thermodynamic environment can only be provided by a steam or a gas turbine itself. As it was pointed out in chapter 1, shrouds are used in high or mid pressure turbines of both steam and gas turbines. The thermodynamic conditions are characterized by high temperatures and high pressures ranging from 500°C/150bars for steam turbines to 1800°C/20bars for gas turbines. Flow velocities are high subsonic or transonic and blade passing frequencies may range up to 6kHz. In addition, chemically reactive substances may be present. The accessibility to the flow in true machines is limited, because of small scales within the flow path and mechanical limits of the casing.

Experimental investigations under these circumstances are very expensive and often impossible to do. As such, the experiments need to be simplified in one or the other way. Today two types of experimental simplification are applied, which provide boundary conditions close to the true unsteady flow in turbine stages.

Short duration facilities reach correct flow conditions in terms of non-dimensional numbers and power output during some milliseconds to a few seconds ([62], [52]). The requirements for measurement and control technology is high due to the transient nature of the experiment. In terms of flow similarity, the results gained from this type of experiment, can be directly applied to the true flow since the non-dimensional numbers are the same. The cost reduction for this experiment stems from the fact that the produced high power has to be absorbed during a short period only. A mechanical energy storage system, for instance a fly wheel, in combination with an aerodynamic brake, or an eddy current brake is sufficient.

The other way to perform cost-saving experiments in an unsteady flow environment is to continuously absorb a reduced level of power. This approach demands a reduction in speed, temperature and pressure ratio of the turbine stage characteristics, wherefore this type of experiments are called low-speed facilities. In these model turbines, true aero-thermodynamic conditions are not reached. This is balanced by the fact that a continuously running test rig allows higher temporal and spatial resolution within the flow field of interest and is easier to control. In addition accuracy of relative and absolute efficiency measurements is higher, since the measurement of mass flow, torque and rotational speed in a steady-state facility is more accurate.

2.1 THE RESEARCH FACILITY "LISA"

The model turbine used in this investigation is of the low-speed, continuously running type. In order to study unsteady effects on the leakage interaction the turbine is equipped with two stages, where the first one is considered to be a generator of unsteadiness and flow history and the second one to be the object of interest, the measurement stage. The name "LISA" stands for *L*eakage *I*nteraction in *S*hrouded *A*xial turbines.

2.1.1 Infrastructure and Safety Systems

The infrastructure of the test rig consists of a quasi-closed air loop with atmospheric condition at the turbine exit, occupying three floors (see Fig. 2.1.1-1). A radial compressor of 750kW power drives the air loop with a pressure ratio of up to 1.5 and a volume flow rate of up to 12.5m³/s. The water-cooled heat exchanger is part of the control feed-back loop which controls the inlet temperature of the turbine. Downstream of the cooler, a filter, a bend and a flow conditioning inlet stretch of 800mm diameter are following. The latter is equipped with honeycombs and a flow straightener. The turbine is mounted vertically and is on the main floor. The turbine outlet is connected to a calibrated Venturi nozzle which is integrated into the back flow pipe. All piping downstream of the turbine is of 700mm diameter, which results in flow velocities lower than 5m/s and therefore in low pressure losses in the piping.

The power, which is produced by the turbine, is transmitted via a torque meter and a vertical hollow shaft to an angular gear box, which performs a gear reduction of two to one. The horizontal shaft of the gear box connects to a DC generator of 400kW maximum power at a maximum speed 1500rpm. The generator and the gear box are mounted on a framework, which forms the third floor. An electrical power converter feeds the current back into the power line.

Several safety systems of aerodynamic, mechanical and electronic nature are part of the installation and play together in the case of an emergency stop. In all emergency cases the aerodynamic power supply of the turbine must be cut off as fast as possible in order to prevent an uncontrolled acceleration of the turbine. This is done with two fast acting, spring loaded valves which connect the compressor outlet to the inlet via a bypass and close the cooler inlet. The remaining energy stored in the volume given by the cooler, the filter and the inlet stretch lasts one to two seconds to further feed the turbine. In parallel the compressor and the generator fields are switched off. The turbine spins down unbraked.

In case of an over-torque, e.g. caused by a mechanical blockage of any rotating part, two safety couplings between generator, gear box and turbine decouple

the power train and trigger an emergency stop. Thus, the mechanical damage is limited to the failing component. The torque meter, which is part of the power train, is also able to trip an emergency stop if a numerical limit for speed or torque is reached.
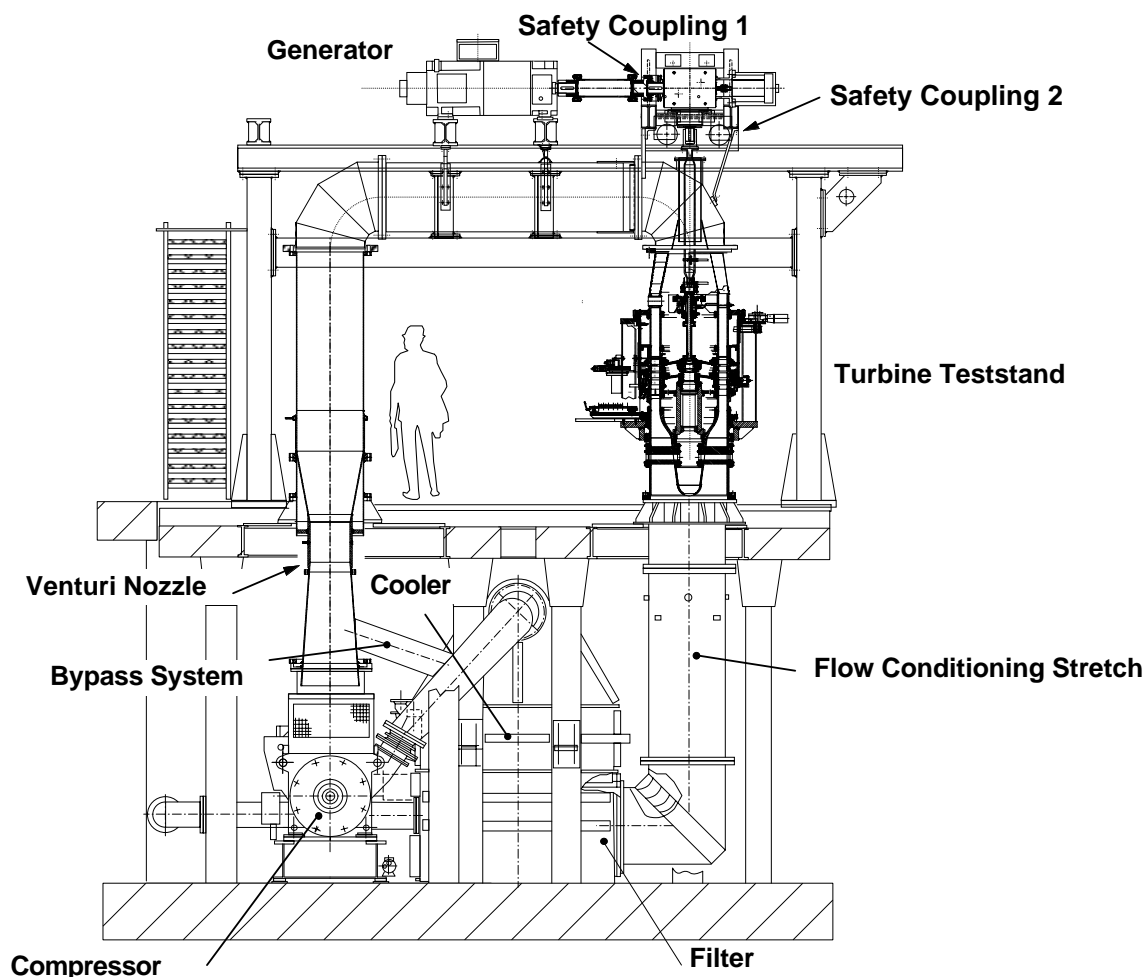
Fig. 2.1.1-1   Infrastructure and overview of the research facility "LISA"

A power line failure may induce high current peaks in the generator, which in turn may result in a torque peak. To prevent a torque peak, which has to be absorbed by the frame work, a coil of 7.5mH is introduced into the armature circuit. The coil acts as a damper in fast transients, because the current is sustained shortly.

Emergency stops are triggered by one single master relay, which is part of a hard wired relay system. All system components are represented by single subrelay surveying permanently the condition of all relevant system components and parameters: Compressor, speed, torque and vibrations of the turbine and the gear box, gear box oil supply, generator and safety couplings. Each relay is connected to the master relay as a condition.

2.1.2   The 2-stage axial turbine

The design of the 2-stage axial turbine is depicted in Fig. 2.1.2-1. Some characteristics of the turbine and features of the design are discussed in the following sections. A summary of relevant parameters is given in Tab. 2.1.2-2.
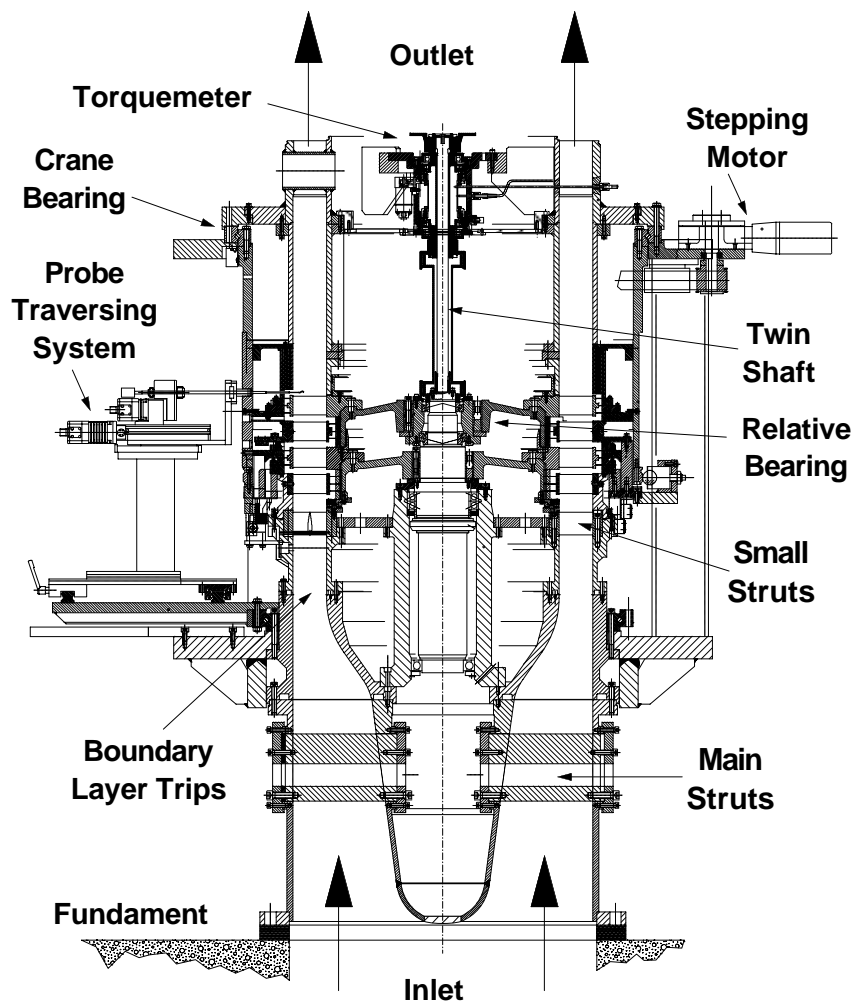
Fig. 2.1.2-1   Cross sectional area of the 2-stage research turbine

Compressor power	750kW	Torque meter max.	780Nm
Pressure ratio	1.5	Turbine max. speed	3000rpm
Mass flow range	8.5 to 12kg/s	Turbine inlet temperature	35 to 45°C
Generator max. power	400kW	Turbine exit pressure	ambient
Generator max. speed	1500rpm	Tip diameter	800mm
Gear box ratio	2:1	Blade height	90mm

Tab. 2.1.2-2   Global parameters of the test rig

Rotor design and bearing

The concentric twin shaft arrangement of a hollow and a full shaft, as it is depicted in Fig. 2.1.2-1, allows to separately measure the torque of the second stage. To do so the torque of the first stage is bypassing the torque meter via the inner full shaft. The torque of the second stage is connected to the torque meter through the outer hollow shaft. After the torque meter the first and the second stage are mechanically connected, which results in the same blade speed for both rotor blade rows. A bearing introduced between both power trains allows for relative positioning of the rotor discs. Therefore the twin shaft arrangement allows to clock the rotors relative to each other.

As a consequence of the twin shaft design the bearing of the turbine rotor needs special care. The rotor bearing consists of a fixed upper roller bearing and a loose lower roller bearing both of high precision quality. Between both rotor discs a relative bearing is necessary to allow small changes of the circumferential positions relative to each other. Due to the different torsional stiffness of both shafts, the relative angular phase shift of the rotor positions under running conditions have to be taken into account while mounting the rotor discs.

The rotor bearings are integrated into the inlet nozzle, which contracts the area from a full circle to the annulus. The nozzle is supported by three main struts at the lower part and six smaller struts on the level of the upper rotor bearings. The first take the weight, the thrust and the radial forces into the casing and the fundament of the turbine. The latter provides additional stiffness to the upper rotor bearing, thus taking the radial forces and avoiding bending vibrations of the bearing casings.

The rotor blades are made as bladed discs with integrated shrouds at the blade tip. The geometry is spark eroded out of high quality aluminium. With this manufacturing procedure an accuracy of ±0.05mm for blade profile and passage throat is reached. In addition, mechanical failure risks due to screwed on or shrunk on shrouds are completely avoided. Due to the high precision in manufacturing a balancing of the rotor discs and blade rows is normally not necessary.

Casing and Stator Blade Rows

The casing rings, which form the end wall contour of the turbine, are made out of forged steel rings, which are nickel-plated after manufacturing. The manufacturing tolerances of these rings are ±0.1mm. The roundness and the centricity to the rotor axis is checked during the mounting procedure to within ±0.05mm. The rings are pinned together, which ensures the reproducibility of their positions. Special attention is paid on the seal clearance gap. The sealing

fins are laser cut out of 0.5mm thick sheet metal. The roundness of the sealing inner diameter is adjusted to within ±0.05mm by filing away the manufacturing tolerances and checking with a high precision gauge.

The casing rings are bolted into an outer casing shell, which can be turned circumferentially by a stepping motor. The rings are pivoted on a crane bearing of 1.1m diameter and the range of circumferential movement is ±2 pitches. Any instrumentation embedded or fixed to these rings can be moved circumferentially relative to the stator blades. Therefore, both stator blade rows have to be fixed to the fundament via two so-called crown rings.

The stator blade rows are also manufactured as bladed discs, for reasons of mechanical precision. It is possible to continuously position the first inlet guide vane relative to the second one, which allows the investigation of stator-stator clocking effects.

Probe traversing system

The test rig is equipped with a 3-axis, fully automated probe traversing system, which is adjustable in the axial direction. One stepping motor controls a longitudinal guideway of 400mm length on which the second stepping motor is-mounted. Both stepping motors enable radial movements and the turning of probes around their centre line. Together with the third stepping motor for the circumferential positioning of the casing, area traverses relative to the stator can be performed. The probe is immersed into the flow field through drilled holes in the casing. The resolution of the flow field is defined by the positioning of those probe holes. Due to the nature of probe mounting through a hole and the fact that the probe is moving with the casing rings in circumferential direction, the sealing task of the probe against the casing is easily done with an o-ring.

The accuracy of probe position is given by the mounting procedure of the probe into the traversing system and the repeatability of the stepping motors. In radial direction the probe is mounted to within ±0.1mm relative to the outer casing diameter. The yaw angle position is found with a spirit-level to within ±0.05°. The circumferential position is given by an encoder to ±0.01 mm. The stepping motors give a repeatability in position in radial direction of ±0.01mm and in yaw angle position of ±0.01°. These values are theoretical system accuracies. Experience showed that long term achievable repeatability was ±0.05mm in circumferential position, ±0.05mm in radial position and ±0.05° in yaw angle.

Mounting procedure of the turbine

The vertical arrangement of the turbine is advantageous for mounting and disassembly. The radial positions of casing and rotor rings during mounting are not affected by gravity, thus the acquired accuracy in roundness and seal gap width can be set and checked with high precision gauges. In order to get crane access to the casing rings and the rotor discs the gear box, which is mounted together with the outlet bend onto a chariot, has to be shifted horizontally. The chariot can be lifted onto wheels for this purpose. While running the turbine the chariot is bolted and pinned to the framework as shown in Fig. 2.1.1-1.

Flow path

The main flow path is formed by a constant annulus with an outer diameter of 800mm. The blade height is 90mm and the axial chord around 50mm. The aspect ratio of the blades is of the order of 1.8 depending on the chosen blading. The annular nozzle to the inlet of the turbine performs an area contraction of 0.4. It is carried by two rows of struts: the three main struts and the upper row of six smaller struts. Latter struts are not equally distributed, but having 54° angular space between each other. The resulting larger distance of 90° is positioned such that the wakes of the smaller struts do not pass the probe measurement area within the stages.

Downstream of the annular nozzle contraction two boundary layer trips are installed at the hub and the tip. They are located more than five axial blade chords upstream of the leading edge of the first guide vane. This measure ensures turbulent inlet boundary layers. Downstream of the second rotor an exit flow stretch of constant annulus and a length of more than 11 blade chords guarantees circumferentially constant exit conditions for the last stage. At the end of this exit stretch the channel is open to ambient.

An undesirable effect of the rotor design are secondary leakages at the hub to the inner plenum of the turbine, which is connected to atmospheric pressure. The driving pressure difference is setup by the pressure of the working fluid (see Fig. 2.1.2-3). Axial look-through labyrinth seals are applied to the second and third leakage mass flow. The first leakage mass flow is reduced by a radial labyrinth seal. Pressure distributions within the turbine will cause a back flow from the inner plenum into the turbine flow at the location of the third secondary leakage. Furthermore, these secondary leakages depend on the type of blading and the operation point. The secondary leakages sum up to around 0.5% of the main mass flow. Further details will be discussed in 2.2.3.
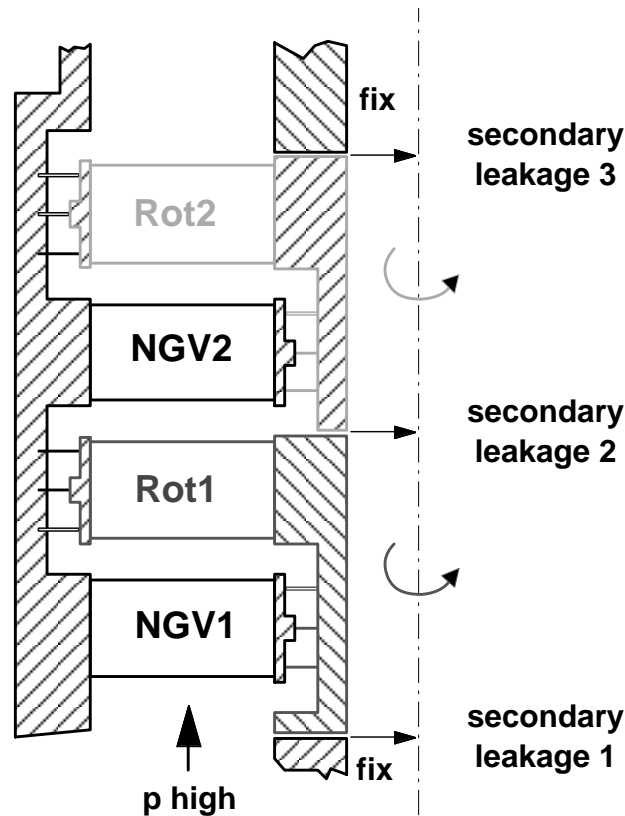
Fig. 2.1.2-3   Secondary leakages affecting the flow

2.2 DATA ACQUISITION

2.2.1   Fixed instrumentation and control

The air loop

The temperature within the air loop is measured with Pt100 resistant thermometers with a range of 0 to 60°C. They provide a 4 to 20mA signal proportional to the temperature. The transducers are fed with a constant voltage source of 24VDC. At the inlet to the turbine four resistant thermometers are installed measuring the actual inlet temperature. Downstream of the turbine and the following bend four resistant thermometers supply the exit temperature. At the exit of the cooler a resistance thermometer provides the feedback for the control loop of the turbine inlet temperature. The control loop consists of a PID controller having a fuzzy logic self tuning function and a water valve as actuator controlling the cooling water.

The mass flow measurement is done with a calibrated Venturi nozzle. The calculation of the mass flow requires the absolute pressure, the temperature and

the humidity of the flow at the exit of the Venturi nozzle as well as the pressure drop across the nozzle contraction. Therefore, an additional four resistant thermometers and a humidity sensor are placed at the Venturi exit. The pressure drop is measured using a calibrated Rosemount differential pressure transducer of 4kPa full scale. Both the humidity gauge and the Rosemount transducer deliver a 4 to 20mA signal. The absolute pressure level is measured with a Scanivalve Hyscan system, which is described in more detail later in this chapter.

The calibration of the Venturi nozzle was done by Delft Hydraulics on a certified calibration rig for flow meters. Thereby, the throughflow coefficient of the nozzle is determined as a function of the Reynolds-number (see chapter 2.2.3 and Tab. 2.6-2). Since the inlet flow to the nozzle is distorted by two upstream bends and therefore is not conform to the DIN standards of measuring mass flows ([61]) the entire back flow piping including the bends and the nozzle had to be calibrated.

All signals of 4 to 20mA standard are led onto high precision resistances of 100Ω. The resulting voltage signals with a range of 0.4 to 2V are measured with a NB-MIO-16L A/D-board implemented in a Macintosh computer (8600 PowerPC, 60 MHz). The communication to the measurement junction happens via a SCXI bus. The signal is amplified by the factor 5 before it is digitized at a 16 bit resolution.

The power train

Part of the power transmission train is the torque-meter. The angular deflection of the hollow shaft within the torque-meter is proportional to the transmitted torque. This hollow shaft is equipped with toothed discs at the top and bottom. The phase shift of the teeth between the top and bottom disc is proportional to the torque and measured with inductive distance gauges. A data acquisition box process the data to rotational speed and torque, which is accessible via a RS232 interface.

Acceleration and displacement along the power train are measured and monitored at several locations with a Schenck Vibrocontrol 4000 system of 18 channels. The system measures vibrating velocity in a frequency range of 1Hz to 10kHz and transforms it to further quantities, like vibrating displacement and acceleration. The two main rotor bearings are surveyed with two accelerometers each, where the two transducers are positioned with 90° relative to each other. The gear box bearings of the fast and slow spinning shaft as well as the generator are supplied with additional accelerometers. The spinning rotor discs are monitored in their radial and axial movements with inductive displacement sensors. The location of measurements are on the shroud of the rotors for the

radial direction and on the disc for the axial direction.

The safety related temperatures of the rotating parts are measured with resistance thermometers. These temperatures are the rotor main bearings, the gear box bearings, the oil temperature at the inlet to the gear box and the temperature of the cooling air flow of the generator. The latter two are controlled to 35°C for the oil and 30°C for the generator with the help of a PID controller and a motor driven water valve.

The turbine

The turbine is equipped with numerous pressure taps from the inlet over the two stages to the outlet. In order to efficiently measure many channels in parallel a Scanivalve Hyscan System is used. The Hyscan system consists of a 486 PC, a SPC 3000 pressure calibrator, 116 differential pressure transducers on 7 ZOC16 modules and two absolute pressure transducers. The PC provides a GPIB interface for data exchange. On commands over the GPIB port the implemented software performs sensor calibrations, controls the system settings and scans the pressure channels.

The differential sensors have a full scale of 35kPa, which does not cover the pressure rise of the compressor against ambient. Therefore, the back sides of the sensors are connected to the a pressure tap between both stages. One of the absolute pressure transducers is connected to this pressure level, which allows to shift the differential transducers to higher absolute pressure levels. Therefore, one pressure measurement always consists of one absolute pressure reading and one differential sensor reading.

The first 48 differential channels are connected to a channel hub close to the measurement section. 38 channels are dedicated to measure operational pressures, like the inlet total pressure. 10 channels are reserved to be used with pneumatic five-hole probes. The other 64 channels are divided in two groups of 48 and 16 channels, each group being connected to its proper pneumatic connector. This gives high flexibility in measuring wall pressures, since different groups of wall pressure taps can be connected to the pressure scanner. Since the turbine casing can be positioned circumferentially, highly resolved wall pressure measurements with a reduced number of pressure taps are possible. The wall pressure taps are designed as insets of 4mm outer diameter having a drilled hole of 0.3 mm diameter. These insets are glued into the casing rings.

For unsteady wall pressure measurements Kulite differential pressure sensors XCS-062D of 35kPa pressure range are used. These sensors are temperature compensated and have a diameter of 1.6mm. Their sensitivity is 125mV F.S. and the frequency response is linear up to 300kHz.

At the inlet measurement plane six thermocouples are mounted into the small struts. The thermocouple voltages are measured with a NB-MIO-16L A/D-board. Since the Seebeck-effect is of the order of 5mV per 100°C, the signal needs to be amplified by the factor of 1000 before measuring. The amplification happens after several meters of cable, which makes the signal susceptible for electrical noise. One source of noise acting on the thermocouples was found to be the stepping motors of the traversing system.

2.2.2   DAQ system and monitoring

The time averaged data acquisition, logging and displaying of operating point and the control of the probe positioning unit is performed by a Macintosh computer (8600 PowerPC, 60 MHz). The software used is Labview 3.1. This master computer controls the data acquisition for operation point display and probe traversing, including the stepping motors and the measurement device. The sub systems of the master computer are depicted in Fig. 2.2.2-1.

In monitoring mode the labview program performs a loop of measuring, displaying and saving the operation point of the turbine. This measurements consist of torque, speed, all temperatures, humidity and relevant pressures, like the total pressure at inlet and the static pressure. In addition the mass flows through the Venturi nozzle and through the standard nozzle of the secondary leakage system are calculated. The mass flow calculation is in agreement with [61]. Depending on the Reynolds-number the correct throughflow coefficient is chosen from the calibration. Humidity effects on the density are accounted for.

If the user starts a probe traversing the monitoring loop is halted. The traversing sub routine performs a measurement of the operation conditions before and after each probe traversing task. The operation conditions are stored into the result file. The stepping motors are controlled with a text file of three columns, for each stepping motor one. Each line corresponds to a measurement position of the probe tip and triggers a measurement. The measurement device can be either a pneumatic probe, a FRAP probe, Kulite sensors or steady wall pressure tappings. Depending on the user's choice different sub routines perform the measurements.

If unsteady pressures, either of a FRAP probe or of Kulites, are measured the FRAP-PC is connected to the LISA-Mac via a RS232 interface. The FRAP-PC is equipped with a fast sampling, 4 channel A/D-board of 200kHz parallel sampling rate. The FRAP-PC in addition controls the Probe Pressure Unit (PPU), which sets the correct reference pressure to the back side of the FRAP or Kulite sensor and performs sensor calibrations before and after each traversing task.

A Pentium 4 PC monitors and logs vibration data as well as speed and torque

delivered from the Torque meter. Labview 6 is used to perform the tasks on the PC which comprise all measurements related to the safe operation of the test rig. The vibrations are measured and saved to the hard disc. The levels are displayed as time and FFT diagrams.
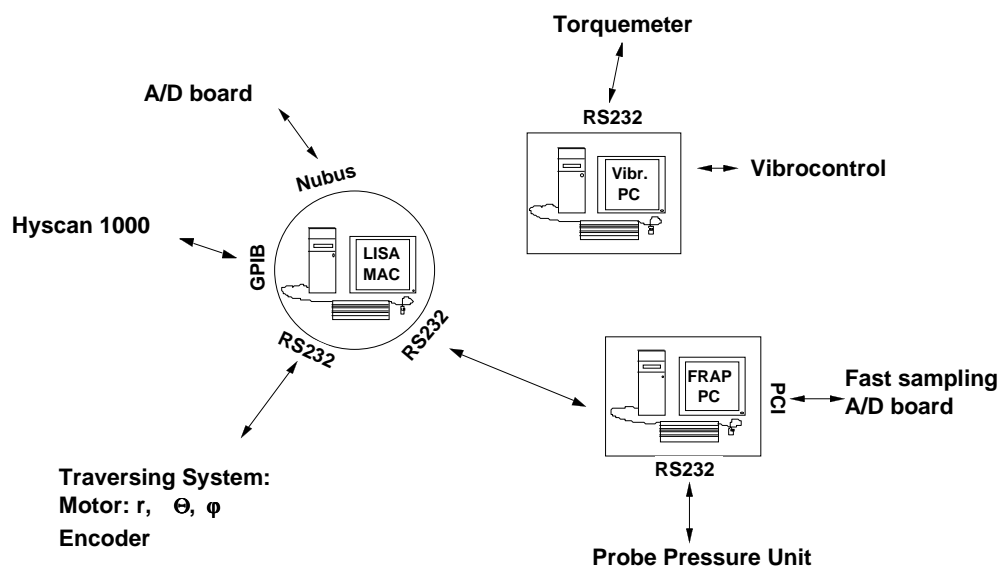
Fig. 2.2.2-1   Data acquisition net work

2.2.3   Operation of the test rig

For running the test rig under defined conditions, the operating point must be measured and controlled. In general the operating point of a turbine is defined by the pressure ratio, the temperature ratio, which both together result in an enthalpy drop and the rotational speed. Since this turbine is a low speed test rig, where fluid flow can be considered to be incompressible, it is more convenient to define the operating point as pressure difference from inlet total pressure to exit static pressure rather than as pressure ratio. This pressure drop across the two stages is constantly measured, logged and monitored. By changing the inlet guide vane position of the compressor the pressure drop can be changed. The pressure drop is of the order of 32kPa for the configurations under investigation and is maintained to within ±100Pa over one day of running. The absolute pressure level in the test rig depends on the atmospheric pressure, the density and therefore the actual mass flow as well as the power changes at constant pressure drop. Further details about the chosen operation points will be discussed in chapter 4.

 The setting value for the inlet temperature control loop was 40°C. The accuracy of control was within ±0.3°C over one day of running time. The exit temperature depends on the load characteristic of the turbine stages and their

efficiency and settles at around 20°C for this investigations. The inlet temperature must be high enough in order to prevent water condensation of the humid air at the exit. Critical exit temperatures are around 15°C and lower.

The rotational speed is kept constant to within ±1rpm by the controller of the generator. The torque depends on the enthalpy drop and the stage mass flow. The latter is a function of the atmospheric pressure, as the turbine is open to the ambient. Therefore, torque and speed as well as the actual mass flow are constantly measured and saved to the hard disc.

As discussed in 2.1.2 the rotor design introduces secondary leakages from the main flow annulus to the turbine inner plenum. In order to preserve mass continuity for the measurement stage during operation, the pressure level within the plenum must be lowered such that no mass flow occurs across the third secondary labyrinth. Additionally, the leakage mass flow must be known in order to calculate the true main mass flow. Therefore, a secondary leakage system consisting of a side channel pump and a standard mass flow nozzle was set up. This system is connected to the inner plenum. The side channel pump sucks additional leakage mass flow out of the turbine through the standard nozzle, thus lowering the pressure level in the plenum. During operation of the test rig a pressure drop across the third secondary labyrinth was set to zero within a range of ±20Pa, which was considered to induce a negligible mass flow across this labyrinth. The mass flow being sucked out by the pump under this condition is the sum of the leakage mass flows of the first and second secondary labyrinth. This sum of mass flows is measured with the standard nozzle and the mass flow measurement gained from the Venturi nozzle is corrected with this value. The typical leakage of the secondary labyrinths is given in Fig. 2.2.3-1.
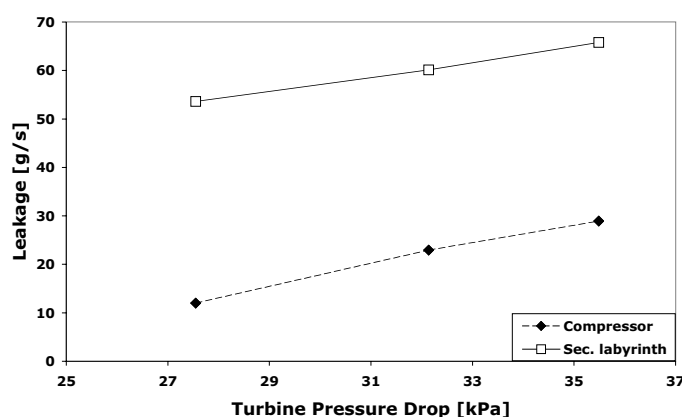
Fig. 2.2.3-1   Secondary leakage map: Compressor, secondary labyrinths

Another location of secondary leakages is the compressor labyrinth seal, which seals the impeller hub from the compressor outlet to the ambient. This leakage

depends on the pressure rise within the compressor for a specific operation point. The leakage was mapped in measuring the leakage exit velocity at the leakage outlet with a wind speed gauge. An estimate of the outlet temperature of 50°C and of the static pressure of ambient are shown in Fig. 2.2.3-1. The leakage mass flow is separately accounted for in the efficiency calculation.

2.3 PROBE MEASUREMENT TECHNOLOGY

2.3.1 Pneumatic five-hole probes

The design of all 5-hole-probes in use is based on the manufacturing technology developed by Treiber [59]. Five tubes are hot soldered together with a centre tube and four tubes equally spaced around the centre. This package of tubes is then bent into the desired shape. The probe tip is finished by cutting the tubes in aligned position to the centre of the shaft and then machining a cut pyramid on the tip. After this procedure the centre hole shows a surface perpendicular to the expected flow. The four side holes open onto 45°-inclined surfaces. The calibration coefficients are then given by

$$K_\varphi = \frac{p_2 - p_3}{p_1 - p_m} \, ; \; K_\gamma = \frac{p_4 - p_5}{p_1 - p_m} \, ; \; K_t = \frac{p_{tot} - p_1}{p_1 - p_m} \, ; \; K_s = \frac{p_1 - p_{stat}}{p_1 - p_m} \, , \qquad (2.1)$$

where $p_m = (p_2 + p_3 + p_4 + p_5)/4$.

Two types of five-hole probes were developed, an L-probe designed for efficiency probe traversing close to the rotor exits and a hook-shaped probe with a minimised outer envelop diameter of 8mm. The latter is advantageous, because it is easily mounted through a positioning hole of 10mm diameter, as they are implemented into the turbine casing. In addition the traversing of the probe has a lower risk of mechanical damage within the labyrinth cavities. The pneumatic probes are presented in Fig. 2.3.1-1.

The probe calibrations were performed in a free jet calibration facility, which allows ranges of ±180° in yaw and ±36° in pitch angle and Mach numbers up to 0.9. This facility is described in detail by Kupferschmied [28]. The calibration of the five-hole probes cover an over all range of angles of ±30° in both directions. Since the flow in the turbine is sub sonic and does not exceed a Mach number of 0.35 a calibration at a single Mach number is sufficient. The L-five-hole probes which are mainly used to traverse the rotor exit flow field were calibrated at M=0.15. All other probe calibrations were done at Mach 0.3.

Throughout this investigation the measurement results gained with the five-hole probes are considered to represent the time averaged flow. The probes are used in an unsteady flow environment containing wakes and secondary flow

structures. The fluctuating velocity components may contribute to an increased reading of the stagnation pressure in each of the holes. An estimation of this is given in [63]: at a high level of turbulence (Tu=20%) an error of 2% occurs for the total pressure, which can be attributed to the way how the probe averages the flow, the so-called pneumatic averaging. However, it is the author's belief that the turbulence level and the deterministic pressure and flow fluctuations contribute a much lower error. This is supported by the fact that the integrated five-hole probe results match to within 1% to the mass flow measurements performed with the calibrated Venturi nozzle.
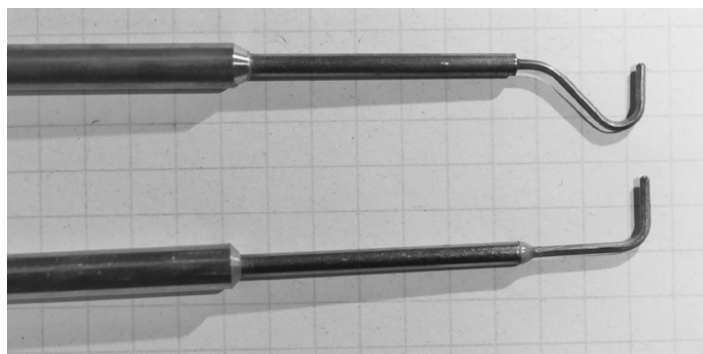
Fig. 2.3.1-1   Developed five-hole probes: head diameter 0.9mm

2.3.2   FRAP probes

The unsteady main flow of the turbine is measured with a virtual three sensor FRAP probe as it is described in [28]. The cylindrical probe head has a diameter of 1.8mm. Due to the measurement concept the measured flow quantities are yaw angle, total pressure and static pressure, resulting in a 2D flow vector phase-lock averaged to a specific blade trigger. The frequency band width of the probe is 80kHz and the calibration range covers $\pm 30°$ in yaw angle at M=0.3. Additionally, the probe provides steady temperature measurements similar to a resistance thermometer. The total or static temperature can be evaluated using a recovery factor given in [28]. The probe is shown in Fig. 2.3.2-1.
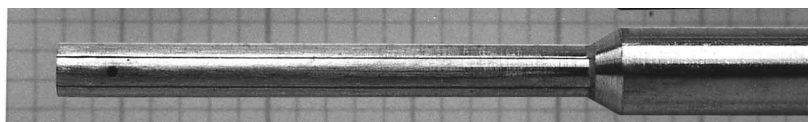
Fig. 2.3.2-1   Single sensor FRAP probe: head diameter 1.8mm

For measuring within the labyrinth cavities a new virtual four sensor FRAP probe was developed and brought into operation, having a head diameter of 0.84mm and frequency response of 25kHz. The probe's capability of measur-

ing three-dimensional, unsteady flow is extensively discussed in chapter 3. Both types of probes, the single sensor FRAP and the virtual four sensor FRAP, use the same type of sensor. The data reduction starting from the raw sensor voltage data to the flow quantities, is in principal the same for both types of probes. Therefore, the reader is referred to chapter 3 for detailed information about the FRAP measurement technology.

2.4 TEST CASES AND MEASUREMENT CAMPAIGN

2.4.1 Flow path design

The stage arrangement with shrouds and labyrinth seals is depicted in Fig. 2.4.1-1. The blade count for all rows is 42 and the rotational speed in all experiments 2700rpm. The blade height is 90mm and the axial chord is 50mm resulting in a constant aspect ratio of 1.8. The thin dashed lines downstream of rotor 1 and 2 indicate the positions, which come closest to repeating stage positions.

A cylindrical coordinate system, r, θ, z is used to describe the geometry. The directions of the axis are indicated in Fig. 2.4.1-1. The circumferential coordinate θ is positive in rotational direction ω. The radial coordinate r is made non-dimensional (R) with the blade height. The hub radius is denoted with R=0 (see Fig. 2.4.1-1). The circumferential position is made non-dimensional (Θ) using one blade pitch. For displaying purposes, the circumferential direction θ is inverted and made non-dimensional with one blade pitch (Θ). Thus, the view in all diagrams is upstream into negative axial direction. For the axial location a local coordinate Z is introduced, which is made non-dimensional with a local axial length, e.g. the axial gap width of the cavity. The yaw angle is counted positive into rotational direction from the turbine axis. Positive pitch angles result in positive radial velocity components facing from hub to tip.

The labyrinth design, as depicted in Fig. 2.4.1-1, shows large cavities and large axial gaps. This is due to the fact that steam turbine rotors are prone to large thermal growth in axial direction. The three-step labyrinth design with knife edge seals is advantageous to steam turbine design, since it is rather simple and cost effective. The knife edges allow the rotor shroud to rub without major damage. The rotors are designed to run into the specified seal clearance. The three steps reduce the leakage of the labyrinth seal in comparison to a look through arrangement, nevertheless allowing for axial displacement of the rotor blade rows.
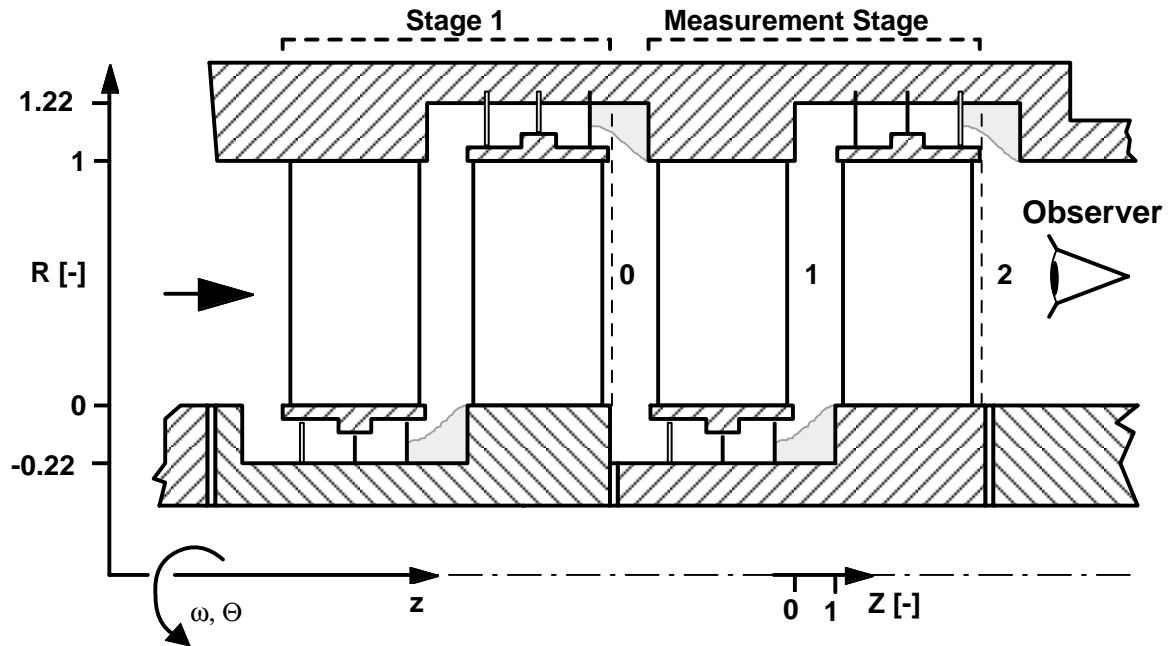
Fig. 2.4.1-1   Cross section of the two stages; Coordinate system

The stage geometry is representative of a mid pressure steam turbine stage of medium loading and through-flow. The design was done by Alstom Power. The design velocity triangles at mid span position of both stages are given in Tab. 2.4.1-2. The flow coefficient ϕ and the load coefficient λ are made non-dimensional with the corresponding design values of the second stage. The flow into the first stage of the turbine is axial. The Reynolds number based on axial chord and throughflow is of the order of $Re=1.3 \times 10^5$ in all blade rows. Both stages have a reaction of 53% calculated from the velocity triangles. The first stage is slightly higher loaded than the second creating a spanwise non-uniform inlet swirl to the second stator with a larger swirl angle at the hub. The stator blades are leaned by 10° and the rotor blades are twisted having a constant exit metal angle. Owing for the constant annulus the throughflow coefficient increases with the decrease of density. The flow is accessible with probes 2.9 axial chords upstream of the first stage and at several axial positions each at inlet to (0), in the mid position of (1) and at the exit of (2) the measurement stage.

	α_1	β_2	ϕ	λ
Stage 1	72.4°	-72.0°	0.88	1.07
Stage 2	69.7°	-69.6°	1	1

Tab. 2.4.1-2   Design velocity triangles at mid span

2.4.2   Geometric and operating point variations

The test matrix describing the measured configurations and operating points is given in Tab. 2.4.2-1, which also indicates the degree of experimental effort applied to the test case. The datum configuration for this investigation is marked with a frame. In the datum test case, twelve axial measurement planes (MP) were measured with pneumatic five-hole probes and eight measurement planes with FRAP probes. The turbine was running at design throughflow conditions (DP).

The datum labyrinth seal gaps were designed for 0.3% of the blade height. The gap widths measured while stationary are listed in the Appendix. Running at design speed the rotor discs grow equally about 0.1mm resulting in effectively reduced gaps. Note the unequal gap widths encountered in a labyrinth for the datum case due to manufacturing tolerances. The smallest gap of the first rotor labyrinth seal is found to be the third fin. Here the effective gap clearance under operation condition is 0.15mm. The smallest gap in the second rotor labyrinth seal is the second fin, having an effective clearance of 0.18mm. The average effective gap for the first rotor seal is 0.20mm and that of the second rotor labyrinth 0.24mm. At the hub an average effective clearance of 0.34mm was measured.

The datum seal gap is small in comparison to real application. Therefore, a larger seal gap of 1% was chosen as geometry variation. The average effective clearances were measured to 0.75mm at the tip and 0.84mm at the hub. The small gap case allows to investigate the pure cavity to main flow interaction in inlet and exit cavities. In the big gap case an realistic interaction of the leakage flow with the main flow is present and can be compared to the pure cavity interaction flow of the small gap case.

For the smaller gap width an additional geometric variation in the exit cavity of all labyrinth seals was performed by introducing special inserts. The inserts are depicted in light grey in Fig. 2.4.1-1. The design was done by Alstom Power with the intent to guide the leakage jet in a more smooth way into the next blade row, thus reducing the mixing of the leakage jet within the exit cavity. Schlienger et al. (2002) investigated this comparison under the view of secondary vortex interactions in the main flow path.

The operation point variations were chosen to be around ±8% in throughflow coefficient resulting in a load variation of ±15%. This load and mass flow variation covers a range of turbine power demand of the order of ±20% around the design point. Since steam turbines as power generating devices are mostly running in base or mid load corresponding to the daily power demand, the variations of operation point in a real machine running in mid load are expected to

Geometry Seal gap [%h]	OP1 $\phi_{DP} - 8\%$	DP ϕ_{DP}	OP2 $\phi_{DP} + 8\%$
TC1 Tip: 0.96% Hub: 1.15%	5MP pneu. 3MP FRAP	5MP pneu. 3MP FRAP	5MP pneu. 3MP FRAP
TC03 Tip: 0.24% Hub: 0.33%	2MP pneu. 3MP FRAP	12MP pneu. 8MP FRAP	2MP pneu. 3MP FRAP
TC03_I as TC03 with inserts	-	2MP pneu. 3MP FRAP	-

Tab. 2.4.2-1   Test matrix of the measured geometric configurations and operating points

be smaller than the here applied ±20% power variation. For the gap width variation all three operation points were measured. The test case with the cavity inserts was investigated at design conditions only. In addition to the given number of probe measurement planes (Tab. 2.4.2-1) the measurement campaigns for each configuration also comprise steady and unsteady wall pressure measurements across the tip casing.

2.5 DETERMINATION OF EFFICIENCY

The total-to-total efficiency of the second stage is evaluated according to Equ. (2.2). The total-to-static efficiency is calculated by replacing p_{out}^{o} with p_{out} in

$$\eta_{oo} = \frac{\omega T_q}{\dot{m}_{stage} c_p T_{in} \left[1 - \left(\dfrac{p_{out}^{o}}{p_{in}^{o}} \right)^{\frac{\kappa - 1}{\kappa}} \right]}. \tag{2.2}$$

The ratio of total pressures is built with mass-averaged values representing the inlet and exit total energy of the measurement stage. The mass-averaged total pressure at inlet and exit requires the fully resolved flow area including the leakage jet. five-hole L-probes as presented in Fig. 2.3.1-1 were used to measure the flow shortly downstream of rotor one and two as discussed in 2.4.1. The applied grid resolution of 23x40 points per plane is performed during one day of data acquisition resulting in two days of measurements for one operation

point. Therefore, the operation point varies slightly between one day and the other due to changes in the atmospheric pressure and the repeatability of the operating conditions, i.e. the pressure drop over both stages. Assuming an atmospheric pressure change of ±0.5kPa and a pressure drop variation of ±40Pa, the total enthalpy drop across both stages varies by 0.5% and less than 0.1%, respectively. These variations are considered to be small and the turbine can be assumed to run at constant efficiency.

To evaluate the efficiency, the measured speed, torque and mass flow are taken at one of the operation setting, e.g. the setting present while traversing the stage inlet plane. Changes in atmospheric pressure have to be accounted for the pressure ratio, only. The absolute pressure levels of p_{in}^o and p_{out}^o are adjusted by using a representative turbine pressure drop and a reference atmospheric pressure of 96kPa to back calculate from the non dimensional pressures C_p to absolute pressures.

The rotational speed ω is set by the generator controller within ±1rpm and measured with the torque meter. A constant value of $\omega=2\pi45$Hz is used in Equ. (2.2). The specific heat of air is $c_p=1007$J/kg/K and the corresponding isentropic exponent $\kappa=1.4$.

The torque measurements T_q are averaged over the period of probe traversing. The windage of the second stage comprises wall friction of the rotating disc and the hollow shaft, only. No rotating bearings contribute to the windage loss. The windage is considered to be independent of the operation point for this investigation, since rotational speed did not vary. The windage loss was determined in a separate experiment using unbladed discs. The unbladed discs were accelerated to different speeds between 400 and 1400rpm. The extrapolation of the resulting torque meter measurements to 2700rpm was performed using a least error fitted, parabolic equation. This resulted in a windage loss of 3.5Nm at operation speed, which has to be added to the measured torque.

The inlet temperature T_{in} into second stage is not measured directly but estimated using the measured inlet and exit temperature of the turbine. With the velocity triangles (Tab. 2.4.1-2) the total enthalpy drop of each stage is available. The first stage causes 51.7% of the over all power output.

The stage mass flow $\dot{m}_{stage}$ is calculated from the Venturi nozzle measurements of the main mass flow by subtracting the compressor leakage according to Fig. 2.2.3-1 and the measurement of the secondary leakage mass flow as described in 2.2.3. The mass flows through the Venturi and the standard nozzle are measured once before and after each probe traversing task. The average is taken as input to (2.2).

2.6 ERROR ANALYSIS

This section gives an error analysis of the experimental set up including the mass flow and efficiency measurement. The accuracy of all measurement devices described in the above sections is listed in Tab. 2.6-1.

Measurement Device	Parameter	Full scale	Deviation	$\delta x/x$ [%]
Resistance Thermometer	T	0...60°C	0.3°C	0.1
Thermocouples	T	0...400°C	1°C	0.3
Relative Humidity Sensor	H	0...100%	1%	1
Rosemount	$\Delta p_{\text{Venturi}}$	0...4kPa	8Pa	0.2
Scanivalve ZOC	Δp	0...35kPa	20Pa	0.065
Scanivalve abs. Pressure	p_{atm}, p_{ref}	1.07, 1.35bar	20Pa	0.02
Torque meter	T_{TQM}	780Nm	1	0.13
Torque meter	n	2700rpm	1rpm	0.04

Tab. 2.6-1   Accuracy of measurement devices

The error propagation of the systematic error of a result

$$R = X_1^a X_2^b X_3^c ... \tag{2.3}$$

is evaluated according to [27] as

$$\frac{\delta R}{R} = \left\{ \left(a\frac{\delta X_1}{X_1} \right)^2 + \left(b\frac{\delta X_2}{X_2} \right)^2 + \left(c\frac{\delta X_3}{X_3} \right)^2 ... \right\}^{0.5}. \tag{2.4}$$

The mass flow is measured according to the norm [61] using a calibrated Venturi nozzle and the throughflow equation

$$\dot{m} = \frac{\pi}{4} \frac{C\varepsilon}{\sqrt{1 - \beta^4}} \sqrt{2\Delta p\rho}. \tag{2.5}$$

The Venturi nozzle has an inlet diameter of D=700.58mm and a contraction diameter of d=419.94mm according to its calibration sheet. The ratio of inlet and contraction diameter is denoted with β=d/D. The discharge coefficient C is Reynolds number dependent. The mass flow of the turbine ranges from 8 to 12kg/s, which corresponds to a range of Reynolds numbers of Re_D=0.83 to 1.24×10^6 in the Venturi nozzle. For this range the discharge coefficient C is listed in Tab. 2.6-2.

Re_D [10^6]	0.7688	0.9164	1.058	1.207	1.347
C [-]	0.9934	0.9940	0.9946	0.9947	0.9950

Tab. 2.6-2   Calibrated throughflow coefficient of the Venturi nozzle

The expansibility factor ε is close to 1, since the flow is incompressible. In agreement with [61] the uncertainty of the mass flow is calculated with

$$\frac{\partial \dot{m}}{\dot{m}} = \left\{\left(\frac{\partial C}{C}\right)^2 + \left(\frac{\partial \varepsilon}{\varepsilon}\right)^2 + 4E^4\left(\beta^8\left(\frac{\partial D}{D}\right)^2 + \left(\frac{\partial d}{d}\right)^2\right) + \left(\frac{\partial \Delta p}{2\Delta p}\right)^2 + \left(\frac{\partial \rho}{2\rho}\right)^2\right\}^{1/2} \quad (2.6)$$

where the relative uncertainty of the density is evaluated with

$$\frac{\partial \rho}{\rho} = \left\{\left(\frac{\partial p}{p}\right)^2 + \left(\frac{\partial T}{T}\right)^2\right\}^{1/2} \text{ (a) and } E = \frac{1}{\sqrt{1 - \beta^4}} \text{ (b).} \quad (2.7)$$

The relative uncertainty of the mass flow measured with the Venturi nozzle becomes 0.26% with the values given in Fig. 2.6-3.

Parameter	C	e	D	d	ρ
$\delta x/x$ [%]	0.16	0.01	0.001	0.002	0.121

Fig. 2.6-3   Relative uncertainties contributing to the mass flow error

In a similar manner the relative accuracy of the efficiency measurement is evaluated. The relative accuracy of torque and mass flow has to account for the secondary effects, e.g. windage torque and secondary mass leakages, with

$$\frac{\partial T_q}{T_q} = \frac{\partial T_{TQM}}{T_{TQM}} + \frac{\partial T_{wind}}{T_{TQM}} \text{ (a) and}$$

$$\frac{\partial \dot{m}_{stage}}{\dot{m}_{stage}} = \frac{\partial \dot{m}}{\dot{m}} + \frac{\partial \dot{m}_{secLeak}}{\dot{m}} + \frac{\partial \dot{m}_{compr}}{\dot{m}} \text{ (b)} \quad (2.8)$$

The pressure term in (2.2) can be linearized for the purpose of error estimation.

$$\frac{\kappa - 1}{\kappa}\frac{\Delta p^o}{p_{in}^o} \text{ with } \Delta p^o = p_{in}^o - p_{out}^o. \quad (2.9)$$

The resulting equation to estimate the error of efficiency measurement becomes

$$\frac{\partial \eta}{\eta} = \left\{ \left(\frac{\partial T_q}{T_q} \right)^2 + \left(\frac{\partial \omega}{\omega} \right)^2 + \left(\frac{\partial \dot{m}_{stage}}{\dot{m}_{stage}} \right)^2 + \left(\frac{\partial T_{in}}{T_{in}} \right)^2 + \left(\frac{\partial \Delta p^o}{\Delta p^o} \right)^2 + \left(\frac{\partial p^o}{p^o} \right)^2 \right\}^{1/2} , \quad (2.10)$$

where κ is constant. The uncertainty of the stage efficiency becomes 0.61% with the values given in Tab. 2.6-4. The largest contributor to the uncertainty of efficiency in this facility are the torque meter, the mass flow and temperature measurement. The accuracy of efficiency differences is around 0.3%.

Parameter	T_q	ω	$\dot{m}_{stage}$	T_{in}	Δp^o	p^o
$\delta x/x$ [%]	0.37	0.04	0.33	0.3	0.13	0.13

Tab. 2.6-4   Relative uncertainties contributing to efficiency error

The accuracy of steady and unsteady flow measurements via five-hole probes and FRAP probes are given in Tab. 2.6-5. The uncertainties given for the five-hole probes were evaluated by Treiber (2002) and do not change here, since the measurement chain is the same. The error estimation of the unsteady flow measurements with FRAP probes is discussed in detail in chapter 3. Tab. 2.6-5 also gives the angular calibration range of the probes.

Type of probe	Calibration Range	Parameter	Deviation	$\delta x/x$ [%]
5 Hole Hook	$\varphi \pm 10°$, $\gamma \pm 30°$	φ	0.2°	
5 Hole L-shape	$\varphi \pm 30°$, $\gamma \pm 10°$	γ	0.2°	
		p_{tot}	60Pa	0.06
		p_{stat}	130Pa	0.13
FRAP V4SS	$\varphi \pm 30°$, $\gamma +21\text{-}30°$	φ	0.35°	
FRAP 2D	$\varphi \pm 30°$, $\gamma \pm 0°$	γ	0.7°	
		p_{tot}	120Pa	0.12
		p_{stat}	85Pa	0.085
		T_{tot}	0.4°C	0.14

Tab. 2.6-5   Accuracy of probe measurements: pneumatic five-hole probes and FRAP probes

3 MEASURING 3D UNSTEADY FLOW

Measuring three-dimensional unsteady flow as it is present in a turbine is a challenge. Several measurement techniques are available today, which resolve the velocity field in space and time. One of the earliest unsteady measurement technologies is the hot wire. Today, 3D probe heads of a 2x2x2mm measurement volume are available. Optical methods are well established, like 3D laser-Doppler anemometry, giving the three-dimensional flow vector in a single point ([55]). A more recent development is the 3D particle image velocimetry, which allows to resolve the velocity field in a sheet of light.

Another established unsteady measurement technology is the fast response probe based on piezo-resistive miniature silicon sensors measuring differential pressures at the tip of a probe head. This approach has the advantage to resolve the total and static pressure of the flow field in addition to the velocity field. Three review papers on the efforts of developing these probes have been published recently: Ainsworth et al. [2], Sieverding et al. [53] and Kupferschmied et al. [29]. These papers together give a broad conspectus of the current state of the art. In order to exploit the full frequency band width of the sensors and to reduce influences of Reynolds-number effects Ainsworth et al. [2] work with flush mounted sensors in a kiel-probe head geometry. A new probe concept to avoid wake-induced unsteady perturbation on the pressure signals was developed and brought into operation by Brouckaert [6].

Only few cylindrical probes with 3D capability have been developed. The earliest is the true four sensor probe of Epstein [14] shortly later followed by Gossweiler [16]. Schlienger et al. [45] demonstrated that pitch angle information can be gained out of five measurements with a single sensor probe of specific elliptical or spherical head design. Using commercial sensors, this is a cost-effective way to measure the unsteady total pressure.

These approaches of probe design resulted in relatively big probe diameters. However, measuring in small-scale flows as within the open cavities of labyrinth seals requires lowest blockage in addition to the capability of measuring three-dimensional flow. Therefore, it was a requirement for the subject of this dissertation to develop a new, low-blockage fast-response aerodynamic probe.

3.1 THE VIRTUAL FOUR SENSOR PROBE

3.1.1 Aerodynamic measurement concept

The measurement concept is based on the idea of emulating a true four-sensor probe with two single-sensor probes. Figure (3.1.1-1) explains the way both probes work together in tandem. Probe 1 is turned into three positions similar to a virtual three sensor probe. Position 1 is the centre position which is close to the total pressure of the flow. Due to the cylindrical surface of the head p2 and p3 give yaw angle sensitivity. To derive the pitch angle a forth measurement is necessary. In a second set up, probe 2 is positioned into exactly the same radial and angular position as probe 1 in position 1. The pressure on the inclined surface p4 compared with the pressure in position 1 gives pitch angle sensitivity.
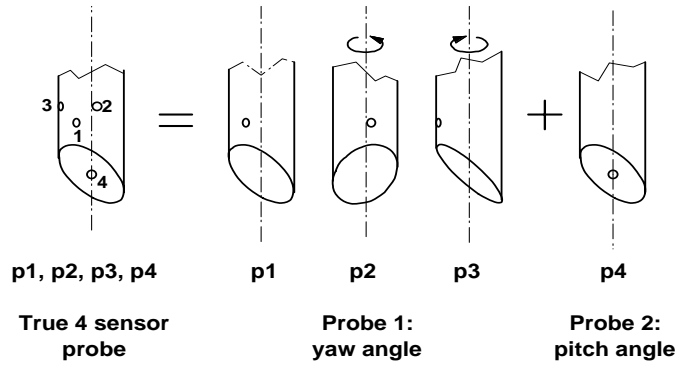
Fig. 3.1.1-1   Measurement concept of a virtual 4 sensor probe.

All four pressure signals are brought together in a set of calibration coefficients representing a dimensionless yaw (K_φ) and pitch angle (K_γ) and total (K_t) and static pressure (K_s) (see eq.1). The signals must be phase locked to each other by an independent blade or rotor trigger signal. Consequently, the phase locked data sets have to be averaged to gain the deterministic portion of the true unsteady flow. The stochastic portion of the unsteady signal is lost during the averaging procedure.

$$K_\varphi \ = \ \frac{p_2 - p_3}{p_1 - p_m} ; K_\gamma \ = \ \frac{p_1 - p_4}{p_1 - p_m} ; K_t \ = \ \frac{p_{tot} - p_1}{p_1 - p_m} ; K_s \ = \ \frac{p_1 - p_{stat}}{p_1 - p_m} , (3.1)$$

where $p_m \ = \ (p_2 + p_3)/2$.

By using polynomial calibration models of the dependencies $\varphi(K_\varphi, K_\gamma)$ and $\gamma(K_\varphi, K_\gamma)$ the flow angles can directly be derived out of the pressure signals. In a second step total and static pressure are calculated using polynomial calibration models of the form $K_t(\varphi, \gamma)$ and $K_s(\varphi, \gamma)$.

3.1.2 Probe head optimization and design

To do the optimization of the head design a pneumatic probe with exchangeable head of 4mm diameter was built. Several head geometries were designed with view on the manufacturing process and tested within the free jet calibration facility of the laboratory. All probe head parts are wire eroded which only allows the creation of prismatic surfaces.

Out of this process an optimal design was deduced featuring a cylindrical surface whose centre axis is perpendicular to the probe axis. The design is depicted in Figure (3.1.2-1). The diameter of the curvature was chosen to be 2.4 times the head diameter. The cylinder cuts the head such that it merges tangentially on the front side of the probe. The hole of the first probe, giving the yaw angle sensitivity, is placed at a distance of 1.1 mm to the tip. The second probe has a hole inclined under 45°, which gives pitch angle sensitivity. The hole to shaft diameter ratio is 0.3.

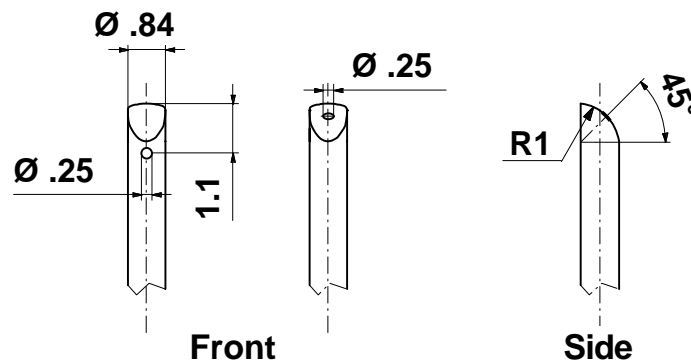*Fig. 3.1.2-1   Final probe head design*
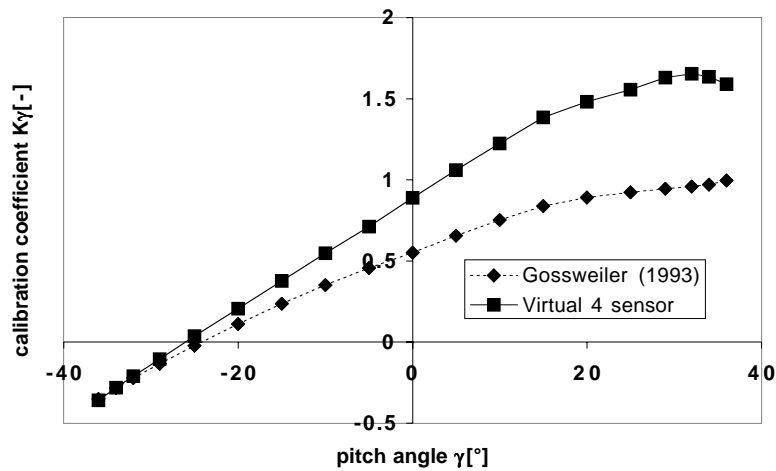
Fig. 3.1.2-2   Comparison of calibration coefficient K_γ: Gossweiler ([16]) and virtual 4 sensor probe, $\varphi=0°$

In Figure (3.1.2-2) the pitch sensitive calibration coefficient at 0° yaw angle is presented. At positive pitch angles around 25° the curve flattens and passes a maximum. The pitch angle sensitivity was found to be in average 50% higher than in the case of Gossweiler's geometry ([16]).

3.1.3 Manufacturing

The manufacturing technology is based on consequent miniaturization of the probe head components and the sensor packaging. The technology was first developed and applied by [28] in order to realise a Pitot-probe. The sensor has the dimensions of 1.6x0.6x0.4mm. The probe head consists of three parts, which are wire eroded. The wire has a diameter of 0.05mm, which defines the smallest possible structure. The base part integrates the reference pressure channel and the side walls, which align and protect the sensor. The sensor is glued into it using a soft silicon adhesive. Different thermal expansion coefficient of the base metal and the sensor material are compensated within the silicon layer such that thermal stresses are not induced into the sensor.

To complete the probe heads outer shape two parts, a long and a short cover, are glued onto the base part. The short cover is made in two different versions: one with a hole on the stem cylinder the other having no hole. The size of these parts are at 0.84x0.6x0.3mm. In order to achieve pitch angle sensitivity a hole is introduced into the pitch angle sensitive surface.

A reference pressure tube and wires are connected to the probe head. Both, tube and wires, lay within a shaft of 2.5mm, which connects to the main shaft of 6mm outer diameter. At the end of the shaft a small box containing the amplifier completes the probe.

Altogether, an estimated 40 different mechanical and micro-mechanical steps of several hours each are necessary to build one probe. Each step is followed by a hardening time of at least 6 hours. This sums up to 500 hours of elapsed time per probe. The finished pair of probes is presented in Figure (3.1.3-1).
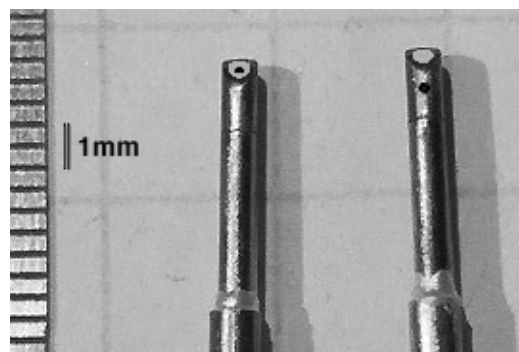
Fig. 3.1.3-1   a) Pitch sensitive probe, b) Yaw angle sensitive probe

3.2 PROBE SUBSYSTEMS AND CALIBRATION

3.2.1 Sensors

A schematic of the pressure sensor is given in Fig. 3.2.1-1. The pressure sensors working principal is the Wheatstone-bridge. The bridge is diffused into a silicon diaphragm, which deforms with the applied pressure difference. The circuit is fed by a constant current source of I_e=1mA. The excitation voltage U_e and the signal voltage U are amplified by the factor of 100 and measured. Thereby, the excitation voltage is a measure for the membrane temperature and the signal voltage is proportional to the differential pressure across the membrane. The sensors, which were build into the probes, have a sensitivity of 8.1mV/mbar for probe 1 and 7.8mV/mbar for probe 2 after amplification.
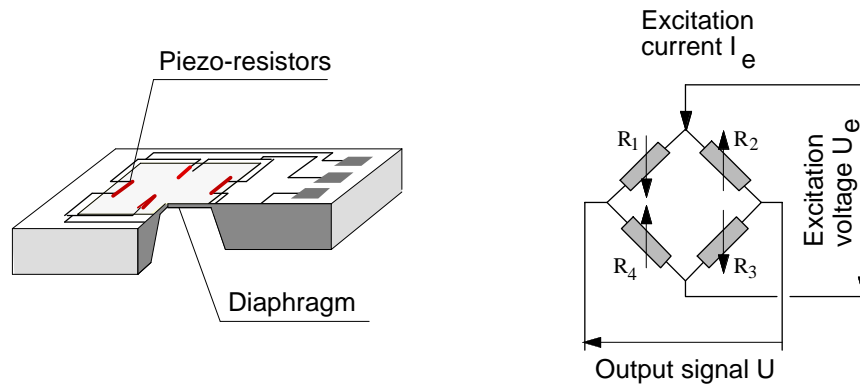
Fig. 3.2.1-1   Piezo-resistive pressure sensor

Each sensor needs to be calibrated individually. The calibration procedures described in [28] were applied in this case. To derive a sensor calibration model the probe head is exposed to a constant-temperature air stream of low velocity (5m/s) within a calibration oven. The temperature steps chosen for this calibration were 15, 25, 35, and 45°C. Each temperature plateau was held for at least 4 hours to ensure temperature equilibrium. During each temperature step pressure cycles of 6 different levels were applied to the reference pressure tube. The pressure range covered by this calibration was 2 to 45kPa. The amplified signal of the sensor is measured and stored automatically.

The gathered data is used to get the relationship of voltages to pressure $p(U,U_e)$ and temperature $T(U,U_e)$. This is performed via a two-dimensional polynomial interpolation of 2nd order in both directions.

It has been previously known that the type of sensors used here are affected by a time-depending offset drift of the signal U while the excitation voltage U_e stays relatively constant with time. The drift affects the offset of the sensor but

not its sensitivity. To account for the effect of drift the offset of the sensor must be known during measurements with the probes. Therefore, an adjustment procedure is applied to the probes before and after each measurement task. The probes must be brought into an environment where the pressure at the probe tip is known. This can be achieved by pulling the probe out of the flow regime into a settling chamber where the fluid is at a rest and the static pressure can be measured. Then two pressure levels are applied to the reference pressure tube and U and U_e are measured. The resulting two adjustment coefficients affect the offset and the gain of the sensor model ([40]).

An additional undesirable behaviour of the piezo-resistive sensor is the effect of self-heating. If the air around the probe head is at a complete rest the heat produced in the sensor is not convected away. This leads to a higher sensor membrane temperature and therefore also to a higher temperature reading of the probe (U_e). Investigating this effect it was found that a velocity step from 5m/s to 0m/s and back to 5m/s resulted in a temperature change in both step directions of 2°C. This implies that good quantitative steady temperature measurements are difficult to achieve.

Concentrating on accurate pressure measurement, the sensor adjustment and evaluation procedures were optimized and tested against a first order accurate pressure measurement device. The accuracy of pressure evaluation was found to be ±20Pa for both probes covering the pressure range of application 0...30kPa, which equals to 0.07% FS. This result was also found to be true across velocity step of 5 to 0m/s and back where all velocity conditions were kept constant for one hour.

3.2.2   Steady aerodynamics

The steady aerodynamic behaviour of the probe determines the calibration range in yaw and pitch angle. It is evaluated by measuring in a well defined steady flow environment. The free jet probe calibration facility used for the calibration allows a yaw angle variation of ±180° and pitch angle variation of ±36°.

In Figure (3.2.2-1) the non-dimensional pressure readings C_p of both probes for varying yaw angle at a constant pitch angle of 0° are depicted. The data are extracted from the aerodynamic calibration data, which in view of the application comprises two Mach numbers, 0.15 and 0.3. For the yaw angle sensitive probe 1 C_p becomes 0 at a turning angle of ±45°. These positions were chosen to measure positions 2 and 3 in the measurement concept (see also Fig.(3.1.1-1)).
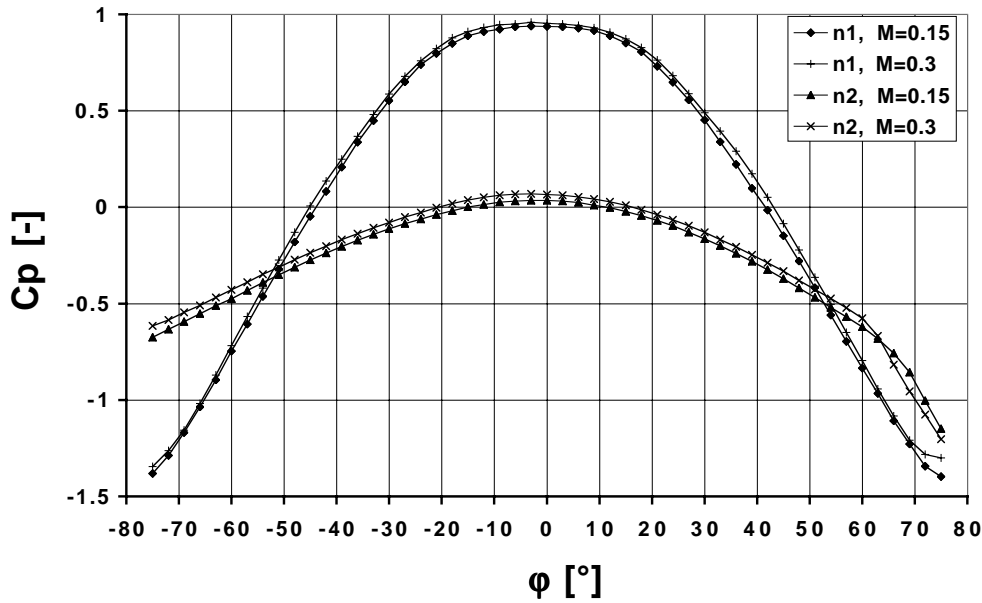
*Fig. 3.2.2-1   Pressure reading of both probes at 0° pitch angle and two Mach
                numbers, M=0.15, 0.3*

Changes in pressure distribution due to Mach number variations are small. The
Reynolds-number based on the head diameter is Re_d=2400 at the lower and
Re_d=4800 at the higher Mach number. This is well within the subcritical range
of 10^3 to 10^5 where the drag coefficient of the probe head stays constant. There-
fore, any viscosity effects on the probe head can be omitted for a range above
a Mach number of 0.06.

The set of calibration data was taken on an equidistantly spaced grid covering
±30° in yaw and pitch angle. The chosen mesh width of 3° resulting in 21x21
points. The data was non-dimensionalized to correct for the change in atmos-
pheric pressure. Since positions 2 and 3 are shifted by 45° and -45° respective-
ly, the absolute range of probe yaw angle positions to calculate C_{p2} and C_{p3} are
15°....75° and -75°...-15°. In Fig.(3.2.2-2) the pressure distribution of position
4 is shown. It can be seen that pitch angle sensitivity is decoupled from yaw an-
gle position. Like in Figure (3.1.2-2) the non-dimensional pressure flattens for
pitch angles around 24°.

With equation (3.1) all calibration coefficients are defined. According to the C_p
definition (4.1), Cp_{tot} and Cp_{stat} have values of 1 and 0, respectively. To get
the mathematical representation of the calibration the coefficients are interpo-
lated by using 2 dimensional polynomials of 6th order for the flow angles and
4th order for total and static pressure coefficients. The polynomial coefficients
are found by using the least square method. The resulting functions are
$\varphi(K_\varphi, K_\gamma)$, $\gamma(K_\varphi, K_\gamma)$ and $K_t(\varphi, \gamma)$, $K_s(\varphi, \gamma)$.
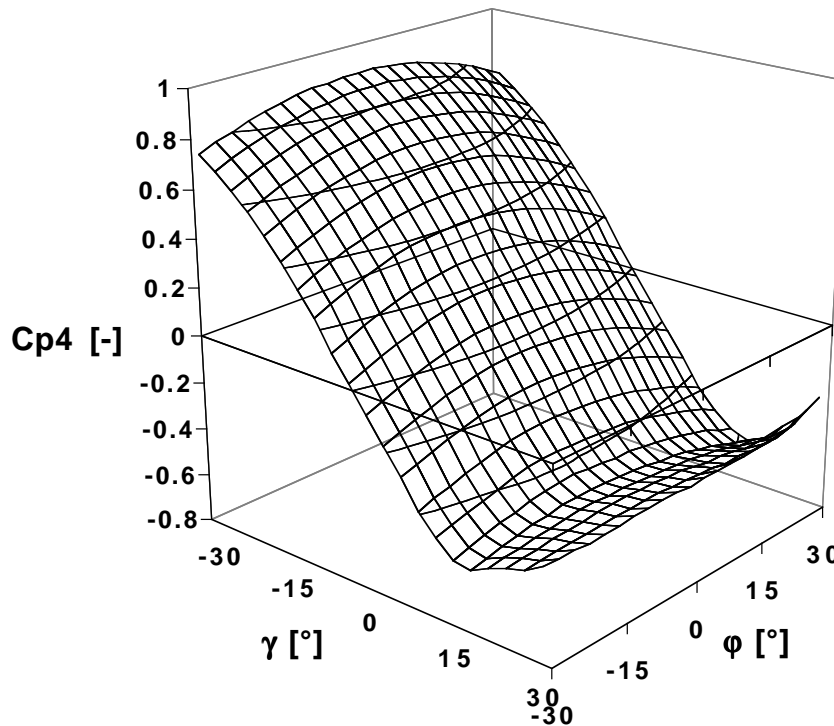
Fig. 3.2.2-2   Non-dimensional pressure C_{p4}, M=0.3

In order to get a working aerodynamic model, the calibration range had to be limited in positive pitch angle direction to 21°. For values higher than 21° the results of the angle evaluation would be ambiguous due to the flattening of the C_{p4} distribution, see Figure (3.2.2-2). Therefore, the calibration limits can be given to ±30° in yaw and -30° to 21° in pitch angle. In Figure 7 the calibration surfaces are shown. The lines of constant φ and γ in Figure 7a and b are normal to each other, which shows the desired decoupling of both calibration coefficients K_φ and K_γ. Only in the corners of the calibration range orthogonality gets distorted. That is also the region where the highest residual in the polynomial interpolation occur. The yaw and pitch angle sensitivity defined as $(\partial K_\varphi)/(\partial \varphi)$ and $(\partial K_\gamma)/(\partial \gamma)$ at φ=0° and γ=0° are 0.09 and 0.032, respectively. For K_t values around 0 are expected. In the extremes of the calibration range K_t becomes as high as 1.8. In most parts K_s shows values around 1.

In order to account for blockage effects within the free jet a static pressure correction was applied to the K_s surface. A cylindrical probe causes a static pressure increase in the measurement plane due to a widening of the jet. Wyler [73] gives a static pressure correction for cylindrical probes in free jets

$$\frac{\Delta p}{p_{tot} - p_{stat}} = -\frac{2(1.15 + 0.75(M - 0.2))}{\pi(1 - M^2)}\frac{d}{D}.$$

(3.2)
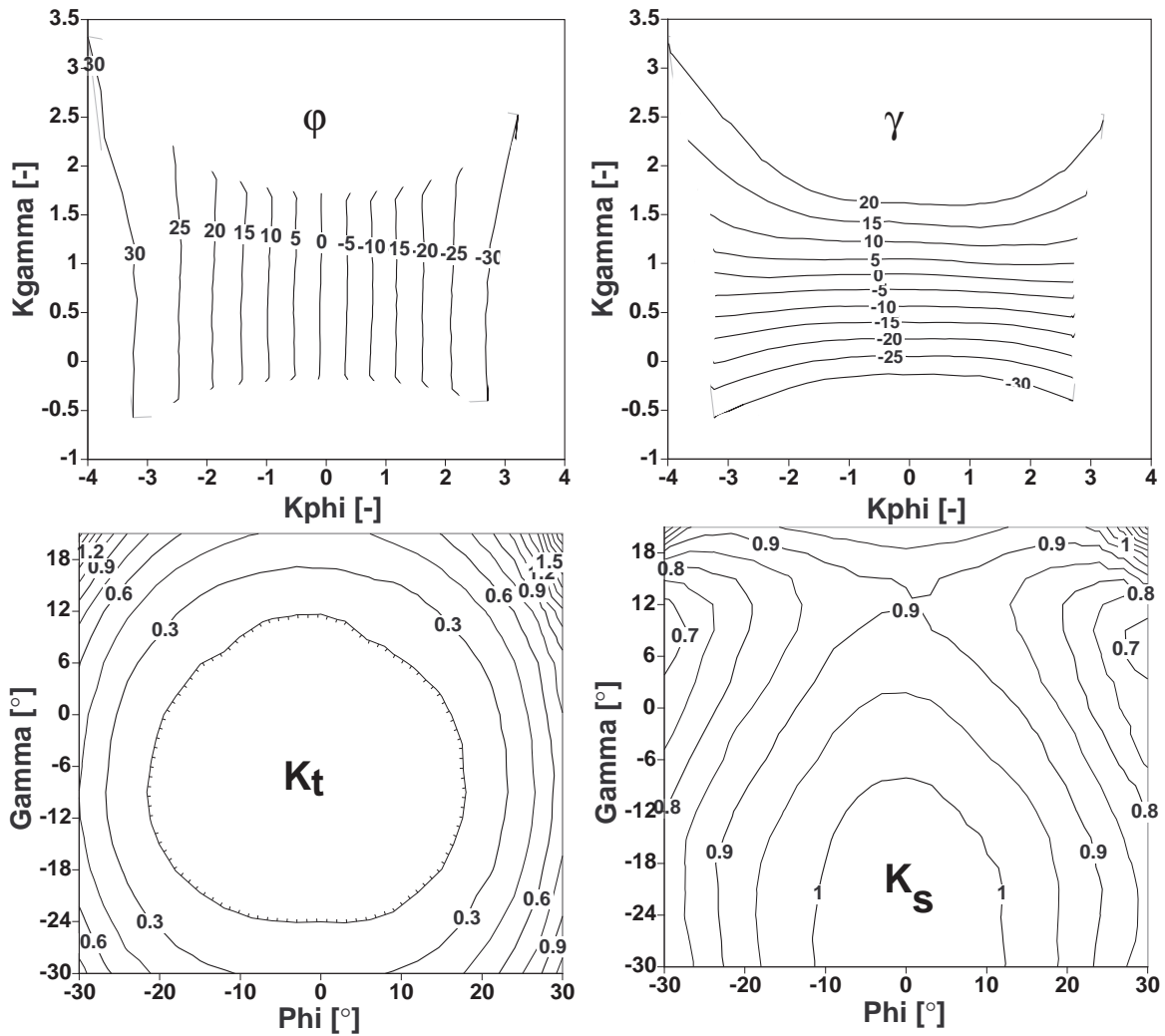
Fig. 3.2.2-3   Aerodynamic calibration surfaces: φ, γ, K_t, K_s

The ratio of diameters d/D assumes a probe shape of constant diameter within the jet. This is not the case for this probe since the diameter increases in steps from 0.84 mm to 2.5 mm from the centre of the jet to its outer radius. Therefore, an equivalent diameter of the probe shaft was used, such that the wetted area within the jet stays constant. For this probe the equivalent diameter is 2mm. At a Mach number of 0.3 the correction becomes 100Pa.

Equation (2) is only valid if the probe shaft is perpendicular to the flow. For the virtual four sensor probe a pitch angle depending correction is necessary. This was achieved in using Wyler's correction for the zero pitch angle case as the maximum correction. Pitching the probe leads to less blockage area and therefore a smaller correction has to be applied. In order to get the reduction the wetted area within the measurement plane was calculated and set into ratio to the full area. With that the values of K_s were corrected for pitch angles -6 to 9°. For pitch angles out side this range the correction values became negligible. The

correction for positive pitch angles is higher because the recirculation zone behind a body also contributes to the blockage effect.

3.2.3   Frequency response

Two different aerodynamic effects influence the frequency response of a FRAP probe. The pneumatic cavity between the pressure tab and the sensor membrane is one source of influence. Associated with the characteristic length of the cavity is an acoustical resonance. It causes higher amplitudes and shifted phase of the signal in a frequency range around the eigen-frequency. The other stems from the fact that probes are intrusive to the flow, resulting in a distortion of the flow field at the location of measurement. The von-Karman vortex street downstream of a cylindrical body can also affect the measurements at the probe tip due to fluctuating flow vectors. In addition to these aerodynamic effect, mechanical vibrations of the probe shaft might also alter the frequency response of the probe. The mechanical eigen-frequency of the sensor membrane is very high (around 500kHz [16]) and therefore plays no role in this type of application.

Pneumatic eigen-frequency

An estimate of the eigen-frequency of both pneumatic cavities was obtained in the free jet. The turbulent total pressure fluctuations within the core of the jet were sufficient to acoustically excite the cavity. The free jet was running at a Mach number of 0.3. In order to have the same kind of excitation for both probes, both probes were positioned such that the holes were facing the flow. Then the data were Fourier-analysed. The result of these measurements is given in Fig.(3.2.3-1).

In the right part of the diagram the eigen-frequencies of both pneumatic cavities are present: 44kHz for probe 1 and 34kHz for probe 2. Both values are close to the eigen-frequency of the miniature Pitot-probe described by Kupferschmied (1998), which is 46kHz. The larger cavity of probe 2 due to the internal design is reflected in the lower eigen-frequency.

Mechanical vibrations

The FFTs of both probes given in Fig.(3.2.3-1) also reveal mechanical vibrations of the both shafts due to aerodynamically induced forced response. For probe 1 and 2 two sharp peaks occur having frequencies of 5.7kHz and 9.7kHz. At around 700Hz several frequencies are excited but with a smaller amplitude than the two peaks. The eigen-frequencies were estimated using the equation of a simple mass-spring-system

$$f = \frac{1}{2\pi}\sqrt{\frac{c}{m}},$$ (3.3)

where c denotes the spring constant and m the mass.

The partial shafts were modelled as beams with a uniform load due to their drag. The two peaks could be identified being the eigen-frequencies of the probe head itself and the second shaft, which is also visible in Fig. (3.1.3-1). The intermediate shaft of 2.5mm diameter gives an eigen-frequency of around 700Hz.
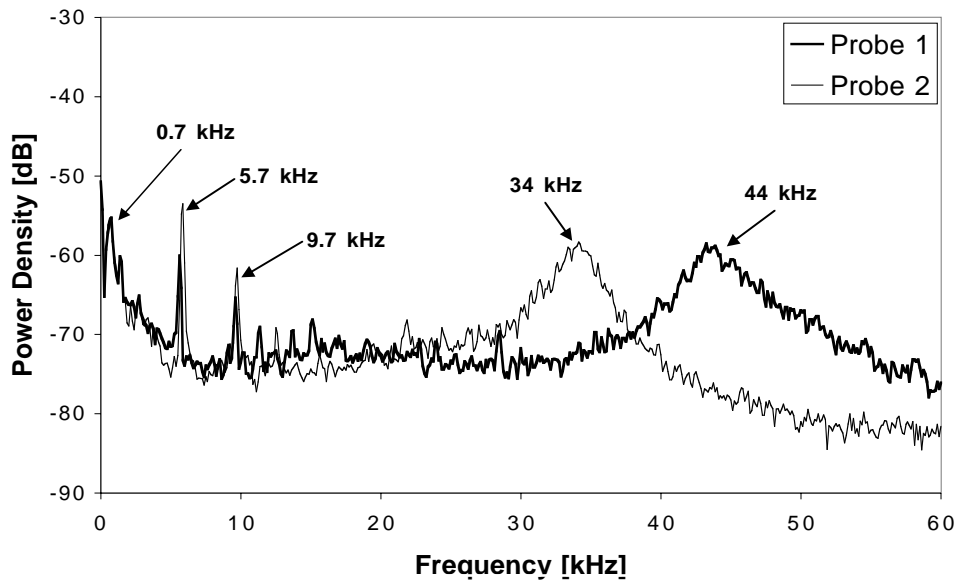

Fig. 3.2.3-1   FFT analysis of Probe 1 and 2: free jet core
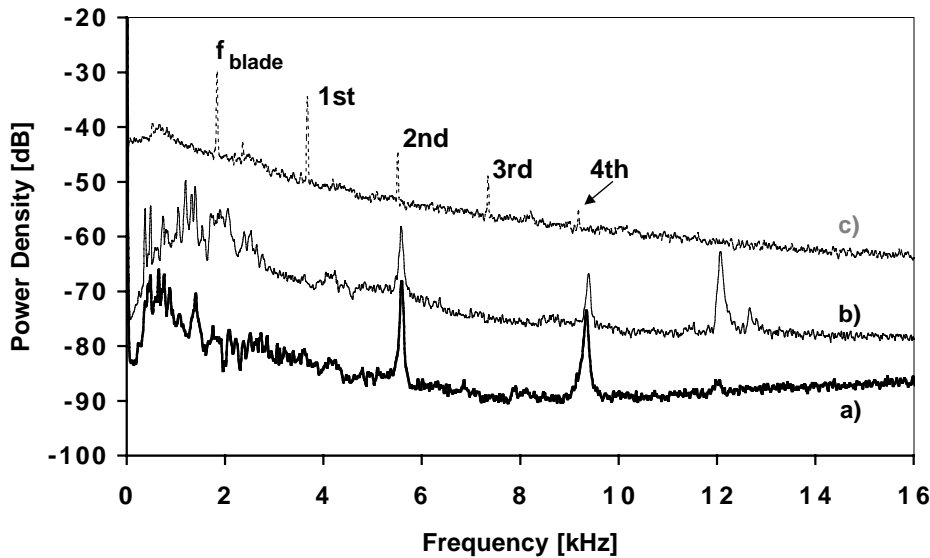
Fig. 3.2.3-2   FFT analysis of probe 1: a) Free jet core, b) Free jet turbulent edge, c) LISA stator exit at mid span

Using the probe within the turbine test rig those mechanical vibrations were not detected as can be seen in Figure (3.2.3-2). It compares the FFT of three different signals of probe 1. One was taken in the turbine test rig. The probe was mounted downstream of the second stator with the tip at mid span position. The Mach number is comparable high to the free jet test cases. The blade passing and the higher harmonics up to the fourth order are present. No further significant frequencies are found.

Both FFTs taken in the free jet show different levels of power density of the signal. While the probe tip is situated in the jet core a low noise level of around -85dB is present. The measurement chain without flow acting on the probe tip has a constant noise level of -105dB. The mechanical eigen-frequencies have a maximum peak of -68dB and -73dB respectively. The noise level gets comparable to the level present in the test rig if the probe tip is positioned into the turbulent mixing layer of the free jet edge. No frequencies associated to mechanical vibration are detected. The vibration induced pressure amplitudes get smaller than the local turbulent dynamic head variations. This is an important finding, which suggests that mechanical vibrations of this probe get swallowed in high turbulent flows and therefore play no role in the measured signal.

For the present application a correction of the pressure signal of the probes based on a transfer function is not considered necessary. The highest frequency present in the test rig, 10kHz, is well away from the first rise in amplitude at 30kHz. For frequencies lower than 25kHz no change in amplitude and phase is expected.

Dynamic effects

Dynamic interactions of the probe body with the fluctuating flow are difficult to quantify and to correct. The reduced frequency as given in Equation (3.4) is a non-dimensional measure for the probe's response to excitation frequencies:

$$k = \frac{fd}{v} \tag{3.4}$$

For this application two characteristic flow regimes have to be investigated. Downstream of the rotor flow velocities range up to 35m/s, downstream of the stator velocities are higher up to 120m/s. With a blade passing frequency of 1890Hz the reduced frequency of the probe becomes 0.045 and 0.013 for the two characteristic velocities. Gizzi [15] suggested a limit of k>0.1, above which corrections on dynamic probe measurements become necessary. Both flow regimes are well below the critical reduced frequency due to the miniature dimensions of the probe head.

The miniature size of the probe is also beneficial to the characteristics of the von-Karman vortex street. The shedding frequency is given by the Strouhal-number. For the range of Reynolds-number it becomes 0.2. The two flow regimes within the test rig have an accompanying shedding frequency of 8.3kHz for the lower and 28.5kHz for the higher velocity. Realistically, a coupling of the shedding frequency of the probe to a frequency present in the flow signal is only possible downstream of a rotor. Here the lowest coupling frequency would be the 4th harmonic to the blade passing frequency. Therefore, it is reasonable to neglect vortex shedding effects, too.

3.3 ERROR ANALYSIS

The error calculation was implemented directly into the evaluation program whose structure follows Fig. 3.3-1. It is based on the error propagation equation (3.5) and follows the scheme of Treiber et al. [59]

$$\Delta F = \pm \sqrt{\left(\frac{\partial F}{\partial x} \cdot \Delta x\right)^2 + \left(\frac{\partial F}{\partial y} \cdot \Delta y\right)^2 + \ldots} \ \text{ with F=f(x,y,...).} \tag{3.5}$$

Starting point of the error calculation was the differential pressure measured with the sensors. The process of evaluating the sensor voltages, including the offset and gain correction coefficients J1 and J2, was found to be accurate to within ±20Pa against a first order accurate pressure measurement device.

A list of resulting uncertainties is given in Table (3.3-2). Two characteristic cases, the flow downstream of a rotor (M=0.1) and the flow downstream of a stator (M=0.35) were investigated. A higher dynamic head is of course beneficial to the absolute accuracy of the flow angles, as the calibration coefficients are inversely proportional to the dynamic head. The total pressure is less accurate than the static pressure since the residuals of the polynomial model are higher and contribute to the error. One possibility to achieve a lower error would be to partition the calibration surface in additional areas. With that, the polynomial approximation would get closer to the points of calibration values.

Looking at the relative accuracy of the local dynamic head downstream of the stator the errors of total and static pressure add up to 3.5% of dynamic head. Downstream of the rotor this becomes 12% of dynamic head. At even lower Mach numbers the measurement accuracy becomes less. Experience shows that the lowest velocity at which the probe is still giving reasonable data in that sense is M=0.06.
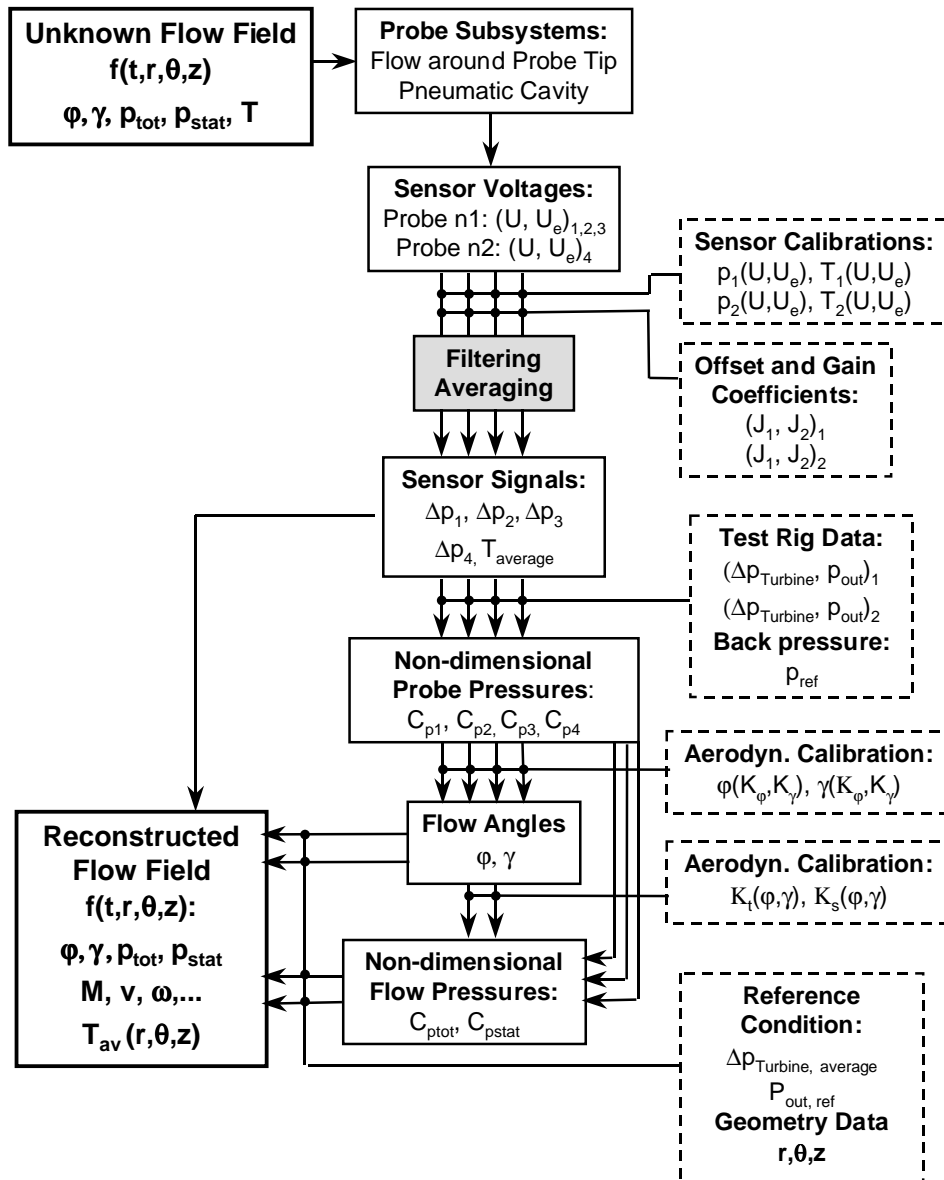
Fig. 3.3-1   Signal paths from flow to measurement results

Parameters	Rotor Exit	Stator Exit
φ	$\pm 1°$	$\pm 0.35°$
γ	$\pm 2°$	$\pm 0.7°$
C_{ptot}	± 0.0025	± 0.0033
C_{pstat}	± 0.0012	± 0.0022
p_{tot}	$\pm 80 Pa$	$\pm 120 Pa$
p_{stat}	$\pm 60 Pa$	$\pm 85 Pa$

Tab. 3.3-2   Typical error band widths of flow parameters

3.4 EXPERIENCE AND IMPROVEMENTS

This section gives a short list of possible improvements and proposals for the further development of the virtual four sensor probe and the FRAP measurement technology in general.

1) Calibrate the virtual four sensor for steady total temperature measurements.

2) Change the polynomial interpolation functions into $\varphi(K_\varphi, K_\gamma)$, $\gamma(K_\varphi, K_\gamma)$, $K_t(K_\varphi, K_\gamma)$, $K_s(K_\varphi, K_\gamma)$.
Thus, the propagation of the flow angle error to the total and static pressure evaluation is avoided.

3) Include the Mach number into the data reduction routines in order to account for density effects. This is important for measurement campaigns in flows of M>0.5.

4) Calibrate the probes at different turbulence levels and include the turbulence into the data evaluation procedure. The boundary layers around the probe tip are sensitive to the turbulence and affect the static pressure readings of the probe. Thus, the static pressure measurement can be improved.

5) Both holes of the pitch and yaw sensitive probes are at different radial positions defining the dimension of the measurement volume in radial direction. Thus, a strong radial pressure gradient may induce a pitch angle which is not representative for the local streamline. Correcting the measurements for strong total and static pressure gradients in radial direction would enhance pitch angle and total and static pressure measurements.

4   PERFORMANCE OF THE TURBINE

4.1   OPERATION MAP AND EFFICIENCY

4.1.1   Operation points

The pressure drop across the turbine is measured with one inlet Pitot-tube and one pressure tab at the hub of the turbine exit. The turbine pressure drop is used to non-dimensionalise all pressures occurring within the system according to

$$C_p = \frac{p - p_{exit}}{p_{in}^o - p_{exit}} .$$ (4.1)

The operation point of the turbine is set to a specific pressure drop. For reasons of accurately repeating the operation points this specific pressure drop was chosen at the beginning of the measurement campaign and set at each of the following measurement days. The pressure drop was repeatable to within ± 20Pa. The three operation points chosen for this configuration and the corresponding mass flows are given in Tab. 4.1.1-1. The through flow coefficient is calculated at mid span position of the rotor exit flow field, using the circumferentially mass averaged axial velocity component. The loading coefficient is given at the mid span position. The flow coefficient as well as the loading is made non-dimensional with the corresponding values of the design point.

Operation point	OP1	DP	OP3
Pressure drop Δp_T [kPa]	27.55	32.14	35.49
Mass flow [kg/s]	8.82	9.64	10.22
Flow coefficient ϕ_2	0.883	1	1.028
Loading λ_2	0.865	1	1.077

Tab. 4.1.1-1   Operation points: Pressure drop, mass flow, flow coefficient, loading coefficient

Since the atmospheric pressure determines the pressure level and the density of the turbine flow, mass flow variations at constant pressure drop occur. These variations will reach $\pm 1.5\%$ at extreme weather conditions, e.g. a thunder storm in comparison to an average atmospheric pressure.

4.1.2 Efficiency

The efficiency measurements were performed as described in 2.5. The resulting isentropic total-to-static efficiency map is given in Fig. 4.1.2-1.

The results show that the efficiency drops with opening the seal clearance. The average efficiency drop is dη/dg=-2.5%/%, where g denotes the seal clearance in percentage of blade height. The 0.3% gap case with inserts, which is equipped with inserts in the exit cavities, shows a 0.3% lower efficiency than the corresponding case without inserts.
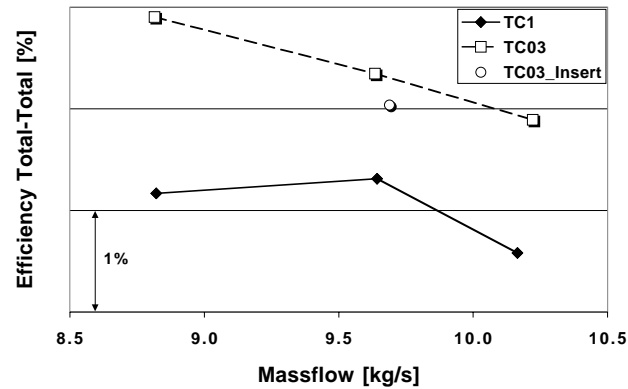
Fig. 4.1.2-1   Efficiency map of all tested steam turbine configurations

With the given results of efficiency and total pressure ratio the overall generated specific entropy of the second stage can be evaluated using the entropy relation

$$\Delta s \ = \ c_p \ln \frac{\overline{T_{o0}}}{T_{o2}} - R \ln \frac{\overline{p_{o0}}}{p_{o2}}. \tag{4.2}$$

The indices refer to the stagnation values of temperature and pressure at the inlet and exit of the stage. As the total temperature is not measured directly, the temperature ratio can be given with the help of

$$\frac{\overline{T_{o0}}}{\overline{T_{o2}}} \ = \ 1 - \eta_{oo}\left(1 - \left(\frac{\overline{p_{o0}}}{\overline{p_{o2}}}\right)^{\frac{\kappa-1}{\kappa}}\right), \tag{4.3}$$

where η_{oo} denotes the total-to-total efficiency.

The resulting generated specific entropy Δs as well as the associated entropy generation rate S' is presented in Tab. 4.1.2-2. The efficiency of the first stage was assumed to be 0.5% lower than the second stage. This assumption is based

on the fact that the first stage has a higher loading than the second stage in addition to the absence of an inlet swirl.Taking the average stage temperature the dissipated power of each stage calculates to

$$P_{diss} = S' \cdot \overline{T}_{stage}.$$ (4.4)

	0.3% gap			1% gap		
	Δs [J/kg/K]	S' [W/K]	P_{diss} [kW]	Δs [J/kg/K]	S' [W/K]	P_{diss} [kW]
Stage 1	3.95	38.08	11.72	4.37	41.92	12.91
Stage 2	3.63	34.96	10.41	3.99	38.52	11.47

Tab. 4.1.2-2   Entropy generation in both stages at DP

4.2 INLET CONDITIONS

The inlet boundary layers were measured using a 5 hole L-probe of 0.9mm head diameter. The inlet measurement plane was positioned 2.9 axial chords upstream of the first stator blade row. Boundary layer trips were placed 2.5 axial chords upstream of the inlet measurement plane. The measurements were conducted at all three operation point. The results of the probe traverses are given in Fig. 4.2-1. The yaw angle and pressure distributions for the off-design points have not been plotted, since the results fall onto each other. The casing boundary layer is thicker than the one at the hub due to the shorter effective length at the hub. The static pressure is constant across the annulus, which indicates that radial redistribution of stream lines is not happening. The absence of a static pressure gradient also confirms that no swirl is present as the yaw angle distribution shows.
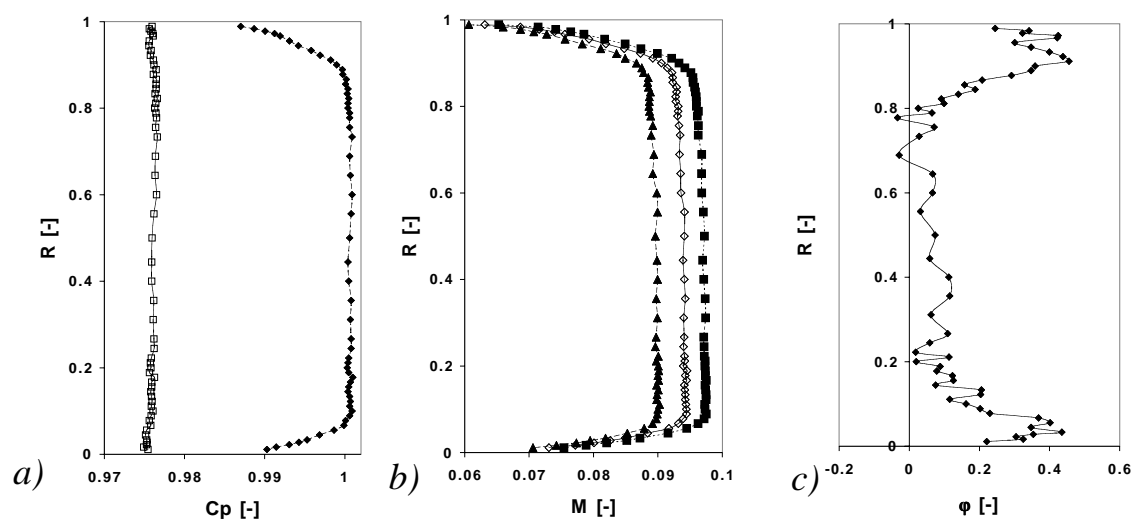
Fig. 4.2-1   Inlet boundary layer: a) Non-dimensional total and static pressure at DP, b) Mach number OP1, DP, OP3, c) yaw angle DP

From the velocity profile the boundary layer characteristics are derived and given in Tab. 4.2-2. The definitions of displacement thickness δ_1, momentum thickness δ_2, and energy thickness δ_3 are taken from Schlichting [44]. The form factors are defined as $H_{12} = \delta_1/\delta_2$ and $H_{32} = \delta_3/\delta_2$. The boundary layer thickness is δ_H=0.077 at the hub and δ_T=0.122 at the tip. All characteristic thicknesses show higher values at the tip boundary layer in comparison to the hub. In the case of a flat plate flow, the form factor H_{12} has values of 1.28 for fully turbulent and 2.59 for laminar boundary layer ([69]). The high value of H_{12} at the hub indicates a more laminar boundary layer, whereas at the tip it is more turbulent

Six thermocouples incorporated into the small struts measure the inlet temperature condition. The temperature variation around the circumference is less

	δ_1 [-]	δ_2 [-]	δ_3 [-]	H_{12} [-]	H_{32} [-]
Tip	0.019	0.011	0.020	1.74	1.82
Hub	0.012	0.005	0.010	2.22	1.85

Tab. 4.2-2   *Boundary layer characteristics at design point*

than ±0.5°C and controlled to 41°C within ±0.3°C over one day of operating time. A constant difference of 1°C occurs between the setting value for the control loop and the measured value at the inlet to the turbine.

4.3 BLADE PROFILE PRESSURES

In this section the blade profile pressure measured on the stator blade are presented. The operation point variation discussed in Tab. 2.4.2-1 results in a change of blade loading as presented in Fig. 4.3-1. The suction peak of this profile is found at 70% axial chord. The blade profile pressures reflect the increase of mass flow with a larger envelop area, which is equivalent to the net tangential blade force. Due to the change of throughflow at constant rotational speed the incidence angle at the stator leading edge changes. The stagnation point on the leading edge shifts to the pressure side of the blade.

Fig. 4.3-1   *Stator blade profile pressures, R=0.5: DP, OP1, OP2*

4.4 MAIN FLOW

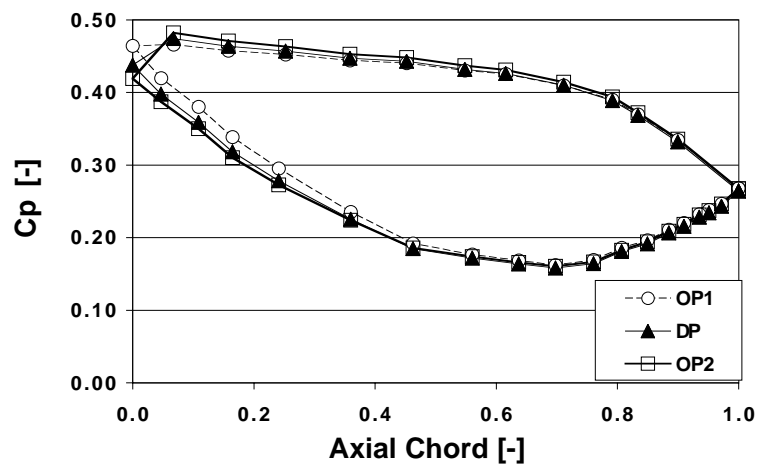In this section the main flow characteristics across the measurement stage of the datum configuration is discussed. Unless stated other wise, these results were gained with a pneumatic five hole probe.

4.4.1   Pitch-wise mass averaged results

The pitch-wise mass averaged distribution of the total pressure, the static pressure, and the yaw angle at the inlet, mid, and exit plane of the measurement stage is given in Fig. 4.4.1-1. The measurements were taken at mid axial gap position. Downstream of the first stage most parts of the outer span show a uniform distribution of total pressure at a level of $C_p=0.477$. Some variations around R=0.8 are present, where the remnants of the chopped stator tip loss core and the rotor tip passage vortex are expected. The static pressure is constant at Cp=0.443 in this region. The swirl changes from tip to R=0.25 from -6° to -30°. Close to the hub a secondary flow structure is present having a strong over and under turning behaviour in the flow angle. The minimum in static pressure indicates a rotor hub vortex. The local minimum of the total pressure is slightly shifted to the hub in comparison to the minimum of the static pressure.

Downstream of the stator, the flow swirls at an angle of 70°. The swirl induces a radial gradient of the static pressure. Close to the hub the swirl reduces by 2° for R smaller than 0.3. The over turning under turning in this region is less pronounced than downstream of the first rotor. A slight local minimum in total pressure at R=0.11 indicates a reduced total pressure loss core. End wall fluid gets sucked into the stator hub inlet cavity reducing the boundary layer thickness at the inlet to the stator hub endwall. At the tip a total pressure loss core is present at R=0.78. A steep radial total pressure gradient, indicating a shear layer, separates the main flow and the cavity flow. The tip passage vortex can be found in the underturning/ overturning characteristic of the yaw angle distribution between R=0.83 and 0.93. Closer to the cavity the flow of lower total pressure turns into tangential direction.

The exit of the second rotor shows in principal similar distributions in yaw angle and static pressure to the exit of the first rotor. The over and underturning effect at the hub is comparably smaller and the exit swirl reduced by 10°. The local minimum in static pressure at the hub is also reduced. The total pressure in contrast to the exit of the first rotor exhibits a different distribution due to multi-stage effects and labyrinth seal leakage. A region of increased total pressure between R=0.61 and 0.96 can be assigned to the first rotor tip leakage flow being sucked into the stator loss core. Close to the hub the total pressure profile is much less pronounced in comparison to the exit of the first rotor.
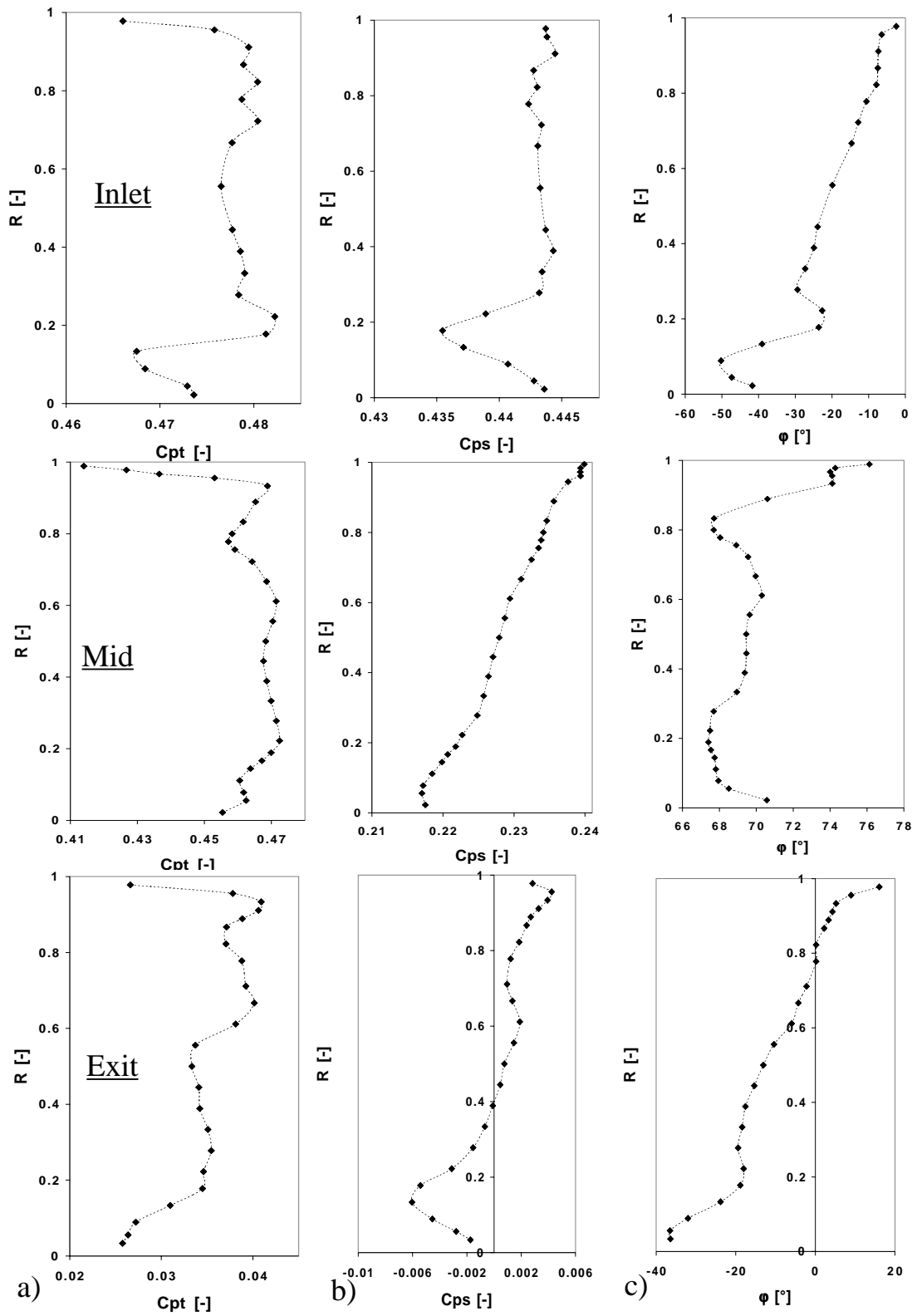
Fig. 4.4.1-1   Pitch-wise mass averaged data at inlet, mid, and exit plane of the measurement stage: a) total pressure, b) static pressure, c) yaw angle

4.4.2   Pressure Field

The total and static pressure fields across the second stage are presented in more detail in Fig. 4.4.2-1. Downstream of the first rotor the potential field of the following stator leading edge influences the flow field. An increased static pressure is observed in front of the leading edge at Θ=-0.2. As the blade is leaned so the contours are. At the same tangential location the stagnating effect of the leading edge on the upstream flow causes an increase of total pressure. Therefore, a reduced velocity is present at this location.

Three effects in superposition shape the three-dimensional static pressure field at the mid-stage position: the trailing edge represented by two dotted lines, the blade lean, and the swirl-induced radial static pressure gradient. Downstream of the trailing edge the static pressure is increased. Considering the total pressure contours, the wake of the stator blade convected by $\Delta\Theta$=-0.3 to Θ=0.2 owing to the strong swirl. The distinct loss core near the tip is situated at Θ=0.1 and R=0.78. Closer to the inlet cavity of the rotor tip labyrinth a strong total pressure gradient in a circumferentially wavy form is present. At the hub the loss core is much less pronounced and is detected at R=0.13 and Θ=0.2. The main flow, exiting the blade passage, exhibits some non uniformity in total pressure due to the history of the upstream stage.

In the exit of the second rotor, total and static pressure are not uniform. Since no stationary blade row follows these effects are of kinematic type and caused by the steady inflow condition to the rotor blade row. The remnants of the chopped stator wake and the loss core are traced as regions of lower total pressure at Θ=0.1 and R=0.33 and R=0.88 respectively. Two regions of lower static pressure, one at the hub and one at the tip, are observed. The region close to the hub has the same radial position as the over and under turning effect found in Fig. 4.4.1-1c R=0.14, which suggests the presence of a hub vortex.
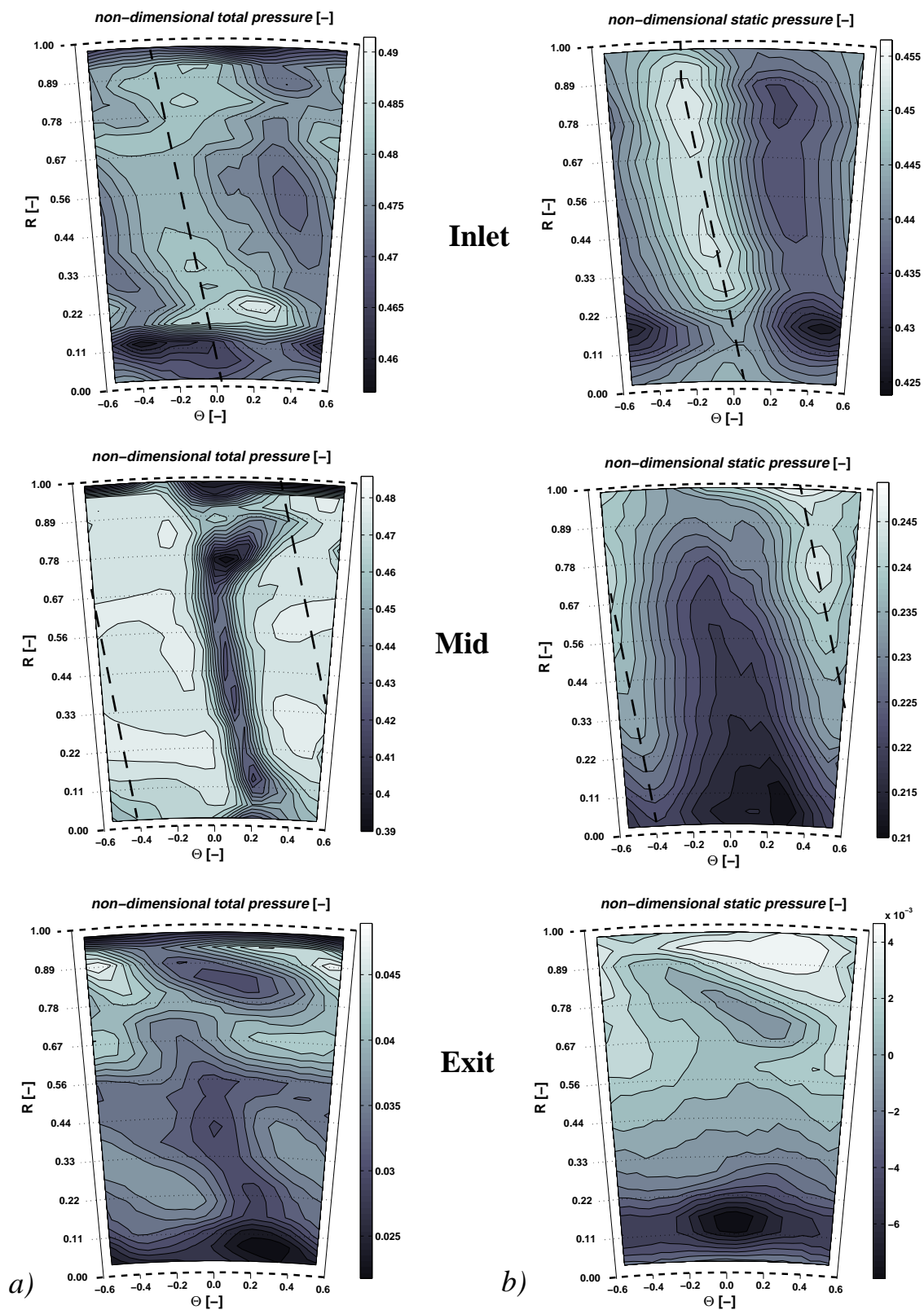
Fig. 4.4.2-1   Pressure field at inlet, mid and exit measurement plane: a) total
                pressure C_{po}, b) static pressure C_p

4.4.3   Flow angles

In Fig. 4.4.3-1 the steady flow angles are presented, including the secondary flow vectors within the pitch angle diagrams. The secondary flow vector is defined as the difference between the local velocity vector and the circumferentially averaged flow vector at the corresponding radial position. The potential field of the stator leading edge is causing the streamlines of the rotor exit flow to divide in front of the stator leading edge (see dashed line in Fig. 4.4.3-1a). The yaw angle results in s-shaped iso-lines over the span due to this dividing effect. The secondary flow vectors also reveal the dividing effect of the leading edge. Close to the tip end wall, the leading edge pushes flow into the exit cavity of the rotor labyrinth. In the mid passage position at $\Theta=0.3$ and $R=1$ cavity flow is sucked into the stator passage. At the hub the leading edge also causes inflow into the hub cavity. Similar to the tip region fluid is sucked out of the hub cavity at mid passage position ($R=0$, $\Theta=-0.4$).

The stator exit flow field is dominated by the passage vortex at the tip end wall, which is depicted with an arrow. Inflow to the tip cavity is observed at $\Theta=-0.3$. The loss core is pushed radially inward as the high pitch angle region and the secondary flow vectors infer. The secondary flow field at the hub is less pronounced, since the hub boundary layer at the inlet to the stator is sucked into the labyrinth seal. Therefore, the hub passage vortex is much weaker than the passage vortex at the tip. Some upward moving flow on the suction side of the wake is present.

The turbine exit flow field is horizontally stratified concerning the yaw angle. The stator flow field is not mixed out at this measurement stage. Secondary flow vectors and the pitch angle distribution reveal vortical structures in absolute frame of reference. A strong feature of positive pitch angles up to $6°$ is present in the position $R=0.5$, $\Theta=-0.4$.

Fig. 4.4.3-1   Flow angles at inlet, mid and exit measurement plane: a) yaw angle φ, b) pitch angle γ

4.4.4   Temperature

The total temperature measurements were performed with a virtual 3-sensor FRAP probe as shown in Fig. 2.3.2-1. From Fig. 4.4.4-1, which presents pitch wise averaged profiles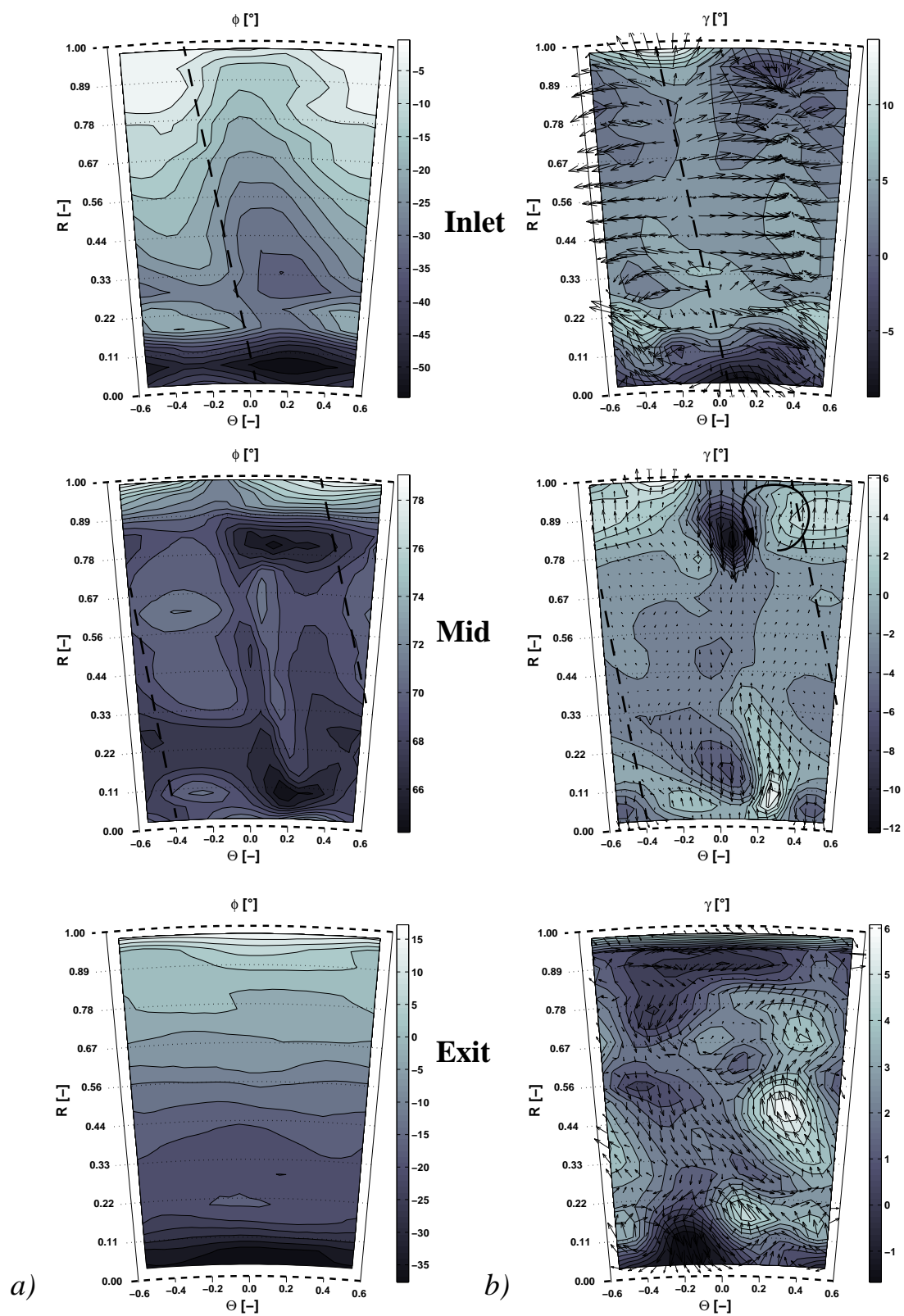 as well as the area distributions, it is evident that the total temperature profiles have a span wise variation of up to $\pm 1°C$. Starting with the inlet to the second guide vane, a local maximum of total temperature at the hub (R=0.18) is present, which corresponds to the hub secondary flow of the rotor. At the tip a temperature gradient toward higher temperatures in the exit cavity of the rotor tip labyrinth seal is apparent. As the corresponding area plot shows, there is no circumferential variation at the inlet measurement plane. The rotor movement leads to a pitch wise averaging of the rotor exit temperature field. Comparing the stator inlet to the exit profile the local maximum at the hub is diffused at the exit measurement plane. At the tip a local maximum of 27.1°C at R=0.9 and Θ=0.3 is present. Close to this position the total pressure loss core is situated (R=0.79, Θ=0.25), which shows 27.6°C. The wake is observed to have a total temperature of 26.4°C. Temperature differences of around 0.4°C are present within the main flow. At the tip a strong radial temperature gradient at R=0.95 and Θ=0.35 is present, perhaps due to heat transfer to the outer casing.

Downstream of second rotor blade row (Fig. 4.4.4-1c) the temperature differences cover a range of 2.3 °C. Similar to the temperature field at the exit of the first rotor, a stripe of higher temperature appears close to the hub at R=0.15. However, a high temperature region is apparent in the middle of the flow, at R=0.7 and Θ=0.1. This region of higher temperature is interpreted as the remnant of the high total temperature spot at the inlet to the rotor tip region (see Fig. 4.4.4-1b). A radial temperature gradient toward the exit cavity of the rotor labyrinth seal indicates a higher temperature of the leakage flow. In contrast to the main flow fluid, the leakage fluid has done no work and total temperature remains somewhat unchanged across the labyrinth. The leakage mass flow, having a higher total temperature, causes an uneven temperature distribution in the main flow due to the migration of the fluid to the mid channel direction. This effect is inherent to labyrinth seals and will be stronger at the tip than at the hub.
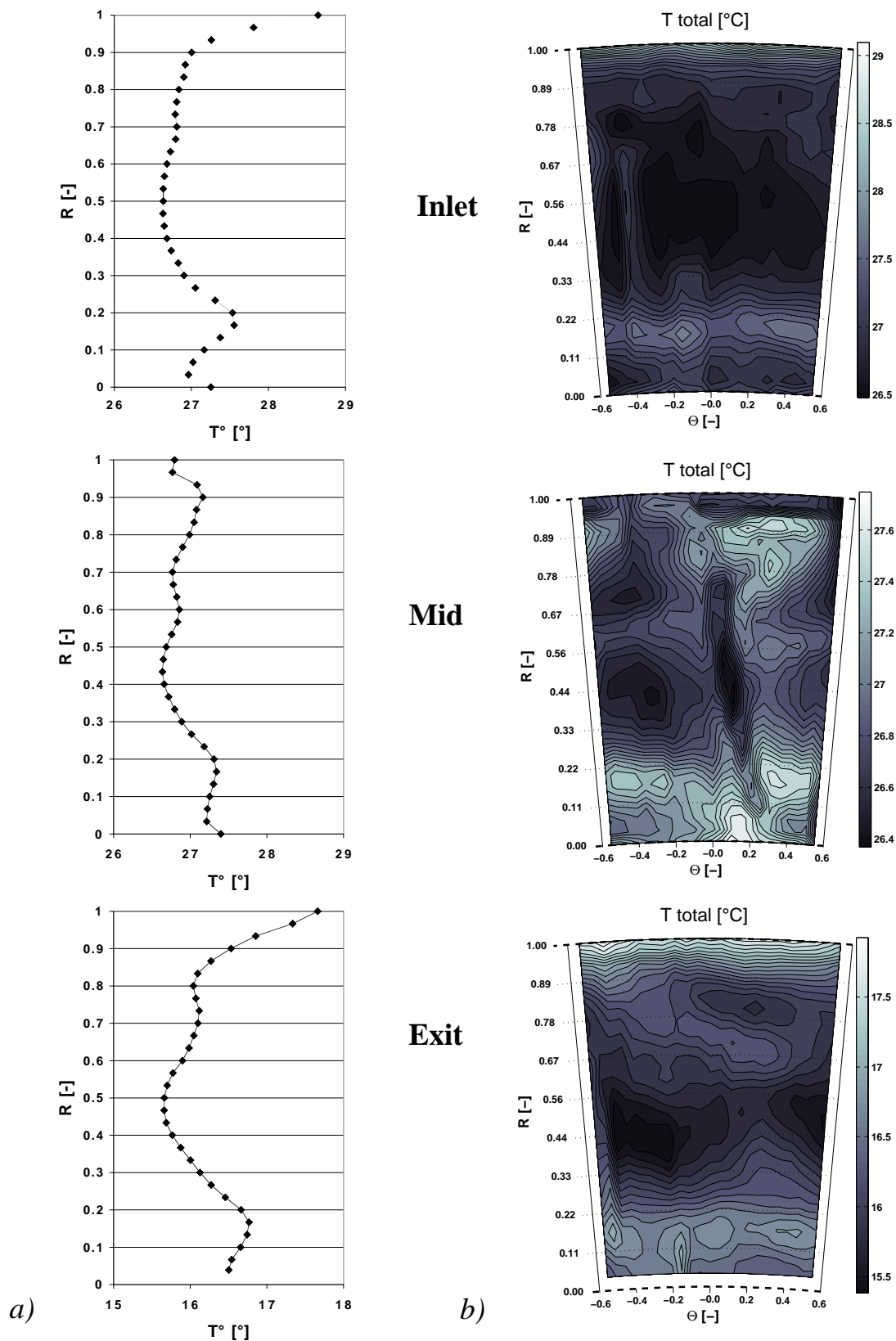
Fig. 4.4.4-1   Total temperature field T°: a) pitch wise averaged, b) area plot

5 LABYRINTH SEAL PERFORMANCE

5.1 EXPERIMENTAL RESULTS

5.1.1 Wall pressure measurements

Pneumatic wall pressure taps

A pressure signal can be described as

$$p(t) = \bar{p} + \hat{p}\sin(\omega t), \tag{5.1}$$

which is composed of an average pressure level $\bar{p}$ and a fluctuating part of the amplitude $\hat{p}$ and the frequency ω. The wall pressure measurements presented in this paragraph were performed at design operation point. In Fig. 5.1.1-1 the pitch-wise averaged wall pressures across the labyrinth casing wall of the second rotor are presented for both gap widths. The dashed lines indicate the positions of the sealing fins. The axial locations of the pressure taps are depicted in the sketch and made non-dimensional with width of the labyrinth groove.
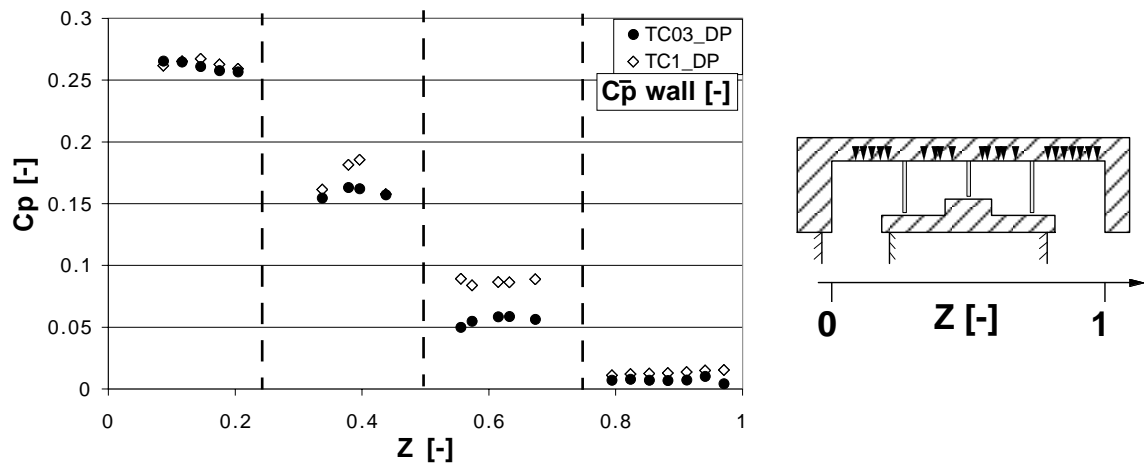
Fig. 5.1.1-1   Pitch-wise averaged wall pressures, second rotor labyrinth, $C_{\bar{p}}$

The over all pressure drop is the same for both gap widths. The gap width variation has a major impact on the pressure levels of the second closed cavity. In the 0.3% gap case, the effective gap in the middle position of the labyrinth is 26% smaller than the average gap width of all three seals and the gap at the third fin is 23% larger than the average. For the 1% gap case these tolerances in seal clearance are not greater than 2%. Consequently, constant pressure steps of $C_{pw}=0.08$ are observed for the 1% gap case, whereas the pressure drop across the third fin in the 0.3% gap case is significantly lower than both other pressure

differences.

The results found in the first closed cavity show two points of higher pressure in the middle of the cavity (Z=0.4). This position coincides with the shoulder of the step in the shroud geometry. The leakage jet entering the first closed cavity gets deflected in the corner of the forward facing step and hits the casing at the points of higher pressure. The difference in leakage mass flow and momentum flux due to the gap width variation results in a wall pressure difference. Smaller differences of static wall pressures are also identified in the inlet and exit cavity indicating changes in the flow field.

Unsteady wall pressure measurements

The results gained with the Kulite sensors are presented as FFT diagrams in Fig. 5.1.1-2. The diagrams show the signal-to-noise ratio for both gaps. The noise level is determined as an average of the logarithmic amplitudes in a frequency band from 1kHz to 3kHz. No measurements of the unsteady pressure within the second cavity of the 0.3% gap case are available. The peak of the blade passing frequency is present in all diagrams. The inlet cavity encounters frequencies up to the third harmonic of the blade passing frequency. In contrast, the closed cavities exhibit reduced pressure fluctuations of the blade passing frequency, only. The wall pressure signal of the exit cavity is composed of two frequencies, the blade passing and the third harmonic. An interesting finding is that the amplitudes found in the open cavities of the 1% gap case are lower than in the 0.3% gap case. This is especially true for the exit cavity.

As for the inlet and exit cavity, these pressure amplitudes $C_{\hat{p}}$ are of the order of ± 110Pa at the blade passing frequency. The pressure amplitudes are damped to ± 25Pa within the first and ± 15Pa within the second closed cavity as presented in Fig. 5.1.1-3. Although these results indicate an unsteady leakage mass flow the pressure fluctuations are considered to be negligible if compared to the dynamic head of a leakage jet of 1500Pa. Thus, it can be concluded that unsteady information of the upstream inlet cavity is not transmitted across the labyrinth seals. The inlet jet to the labyrinth as well as the exit jet within the last seal gap are mainly driven by the steady and unsteady flow conditions set up in the open cavities. Reducing the numbers of fins would generate an increased carry over of unsteady and steady flow effects from the inlet to the exit cavity.
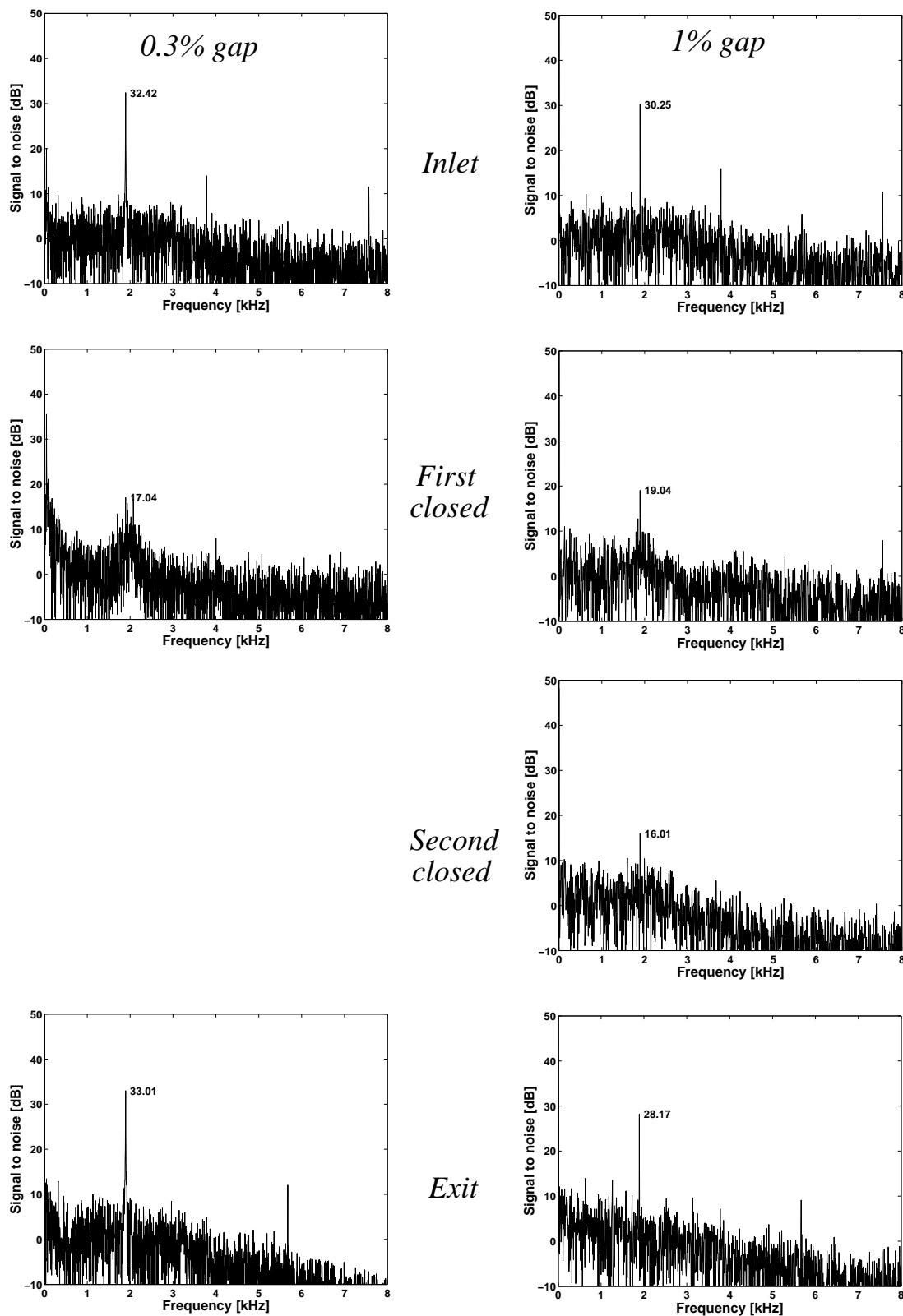
Fig. 5.1.1-2   Unsteady wall pressure p̂ of labyrinth cavities at DP: FFT
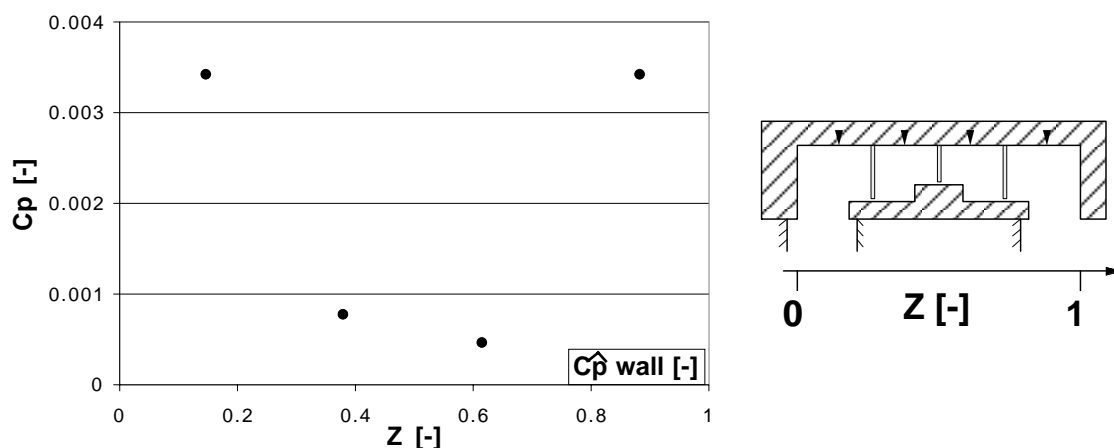
Fig. 5.1.1-3   Wall pressure amplitudes, second rotor labyrinth, 1% gap, $C_{\hat{p}}$

5.1.2   Exiting leakage jet

Using an L-shaped five hole probe it was possible to traverse the leakage jet close to the shroud trailing edge. The position of the jet traversing is sketched in Fig. 5.1.2-1. This diagram presents the pitch-wise mass averaged results at design operation point. The two vertical arrows indicate the effective gap width in the non-dimensional radial coordinate used in the diagrams. The outer radius of the shroud is on R=1.056. The radial extent of the traversing is limited to ΔR=0.02. Flow angles at higher R increase such that the L-probe calibration of ±30° in conjunction with the limited turning angle of the probe of 30° cannot capture the flow.

The flow angle is of the order of 50° in all cases. The 1% gap case causes a 5° lower yaw angle in comparison to the 0.3% gap case. Both jets exiting the first and second rotor labyrinth with TC1 have a local minimum at R=1.06 for the flow angle. The leakage jet experiences a contraction within the vena contracta to an area of approximately 0.6 times of the mechanical clearance (Trutnovsky [60]). Downstream of this point the jet gets thicker, due to viscous momentum exchange at the edge of the jet and the maximum velocity reduces. Schlichting [44] defines a wall jet by its maximum speed v_{jet} and its thickness ΔR_{jet}. The jet thickness is given as the location within the velocity profile, where the average of the maximum speed and the neighbouring flow velocity is reached. A generic wall jet is depicted in Fig. 5.1.2-2. The jet thickness ΔR_{jet} can also be interpreted as the dividing streamline of the jet and the neighbouring flow field. The average Mach number within the exit cavities of rotor 1 and 2 is 0.09 (see chapter 7). The maximum velocity is M=0.17 for the TC1 case and second rotor exit, which results in a jet thickness of ΔR_{jet}=0.011. At the exit of the first rotor the maximum velocity is M=0.19 and the jet thickness is ΔR_{jet}=0.01.
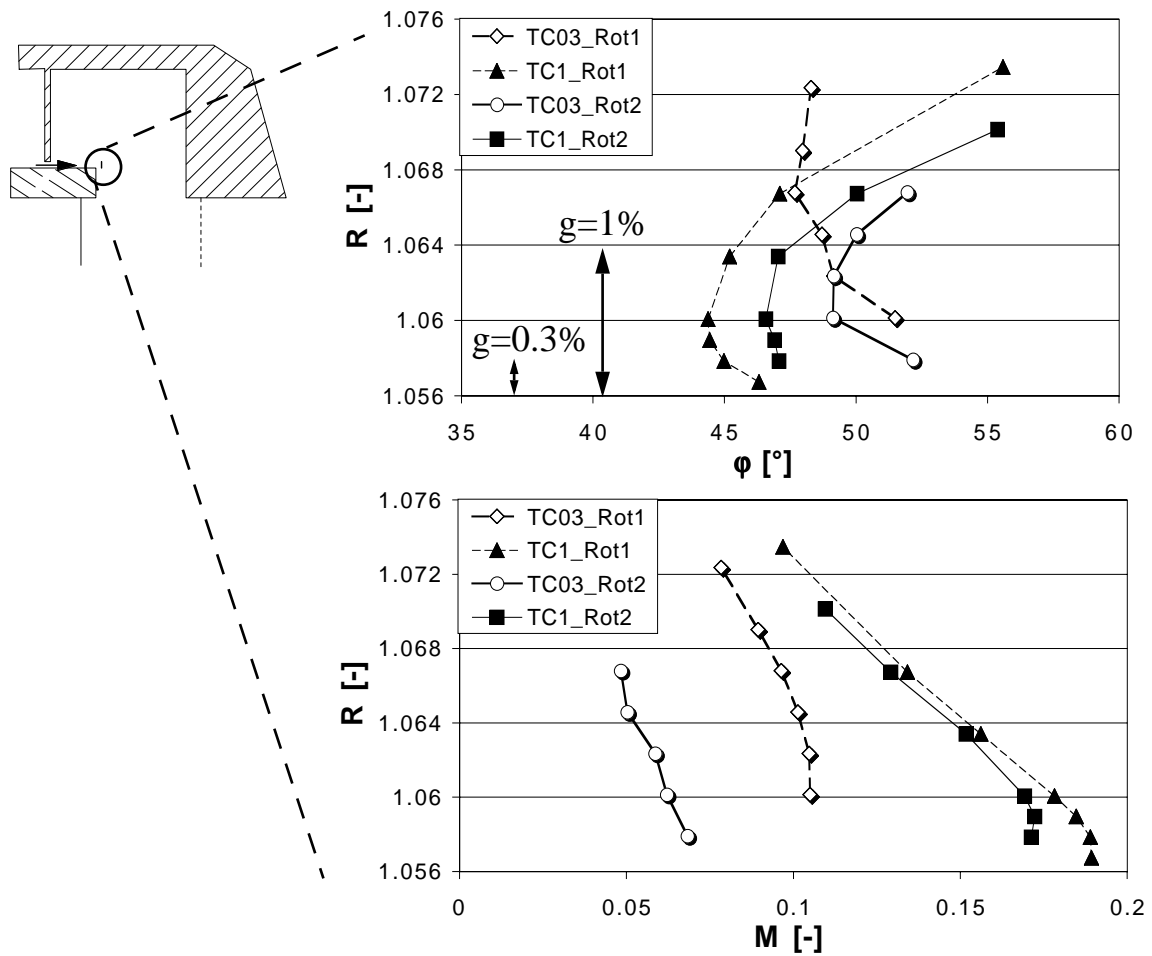
Fig. 5.1.2-1   The leakage jet: rotor 1 and 2 labyrinth, 1% and 0.3% gap at DP
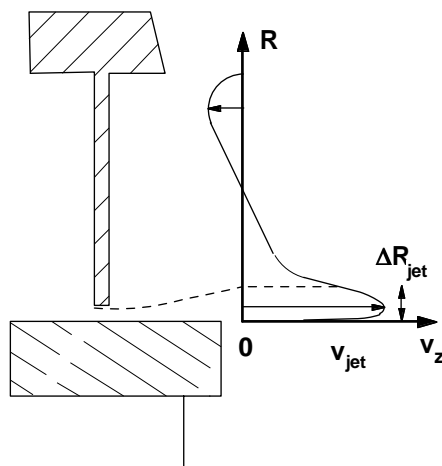
Fig. 5.1.2-2   Leakage jet: description as wall jet

The datum case (0.3% gap) is characterised with very small gap widths. As given in 2.4.2 the gaps vary significantly within each of the two rotor tip labyrinths. Although the average gap of the first rotor labyrinth is smaller than the one of the second, the corresponding leakage flow is much higher with M=0.11 in comparison to M=0.07. Due to the relatively large exit gap and the smaller pressure drop across the last fin the second leakage jet starts with a much lower velocity and momentum. Thus, it is diffused faster than the first rotor leakage jet. The first rotor leakage jet has a higher velocity and momentum than the second leakage jet, since the last seal gap of the first rotor labyrinth is the smallest. Consequently, the jet persists longer against diffusion and causes the higher Mach number at the location of measurement. The average Mach numbers of the bulk fluid flow are 0.03 in the second rotor exit cavity and 0.045 in the first rotor exit cavity. A jet thickness can not be given, because the average velocity is out side the measured area. The flow angles show no clear effect and interpretable distribution. One reason is the ratio of probe size to flow feature being around 50%, which is not an optimum for this investigation.

5.2 LEAKAGE CHARACTERISTICS

5.2.1 Leakage mass flow

This section is dedicated to the evaluation of the leakage mass flow passing through the different configurations. The approaches applied are the ideal labyrinth calculation according to Egli [13], the application of an empirical correlation given by Traupel [58], and the integration of five hole probe results, taken within the exit cavity.

Labyrinth calculation

Single gap calculation (ideal labyrinth)

The theoretical throughflow of an ideal labyrinth seal can be calculated according to Egli [13] using the conditions p_i and ρ_i upstream of the sealing contraction in

$$\dot{m}_{leak,th} = A\alpha\Psi_{th}\sqrt{\rho_i p_i}. \tag{5.2}$$

The gap area is denoted with A, α is the area contraction in the vena contracta and Ψ_{th} the expansion number

$$\Psi_{th} = \sqrt{\frac{2\kappa}{\kappa-1}\left(\left(\frac{p_{i+1}}{p_i}\right)^{2/\kappa} - \left(\frac{p_{i+1}}{p_i}\right)^{(\kappa+1)/\kappa}\right)}. \tag{5.3}$$

The calculation assumes perfect dissipation of kinetic energy into heat within the cavity as well as zero initial velocity upstream of the gap. The driving pressure ratio over the gap is given by the local static pressure. In cavities with high swirling flow, e.g. the inlet cavity of the rotor labyrinth, the static pressure at the casing wall is higher than in the flow field due to the positive radial static pressure gradient. Therefore, building the pressure ratio with wall pressure measurements will probably lead to an over estimation of the leakage flow.

In Tab. 5.2.1-1 the leakage mass flow and the axial jet velocity expressed as Mach number is calculated for each individual sealing fin using the circumferentially averaged wall pressures as found in Fig. 5.1.1-1. The gap area A is calculated with the measured gaps given in the Appendix and α=0.6. Note that measurement results for the inlet and first closed cavity of the first rotor labyrinth are not available.

		rotor1	rotor2		
		fin 3	fin 1	fin 2	fin 3
0.3% gap	m_{leak} [g/s]	24	32	25	27
	M_{jet} [-]	0.233	0.199	0.216	0.150
1% gap	m_{leak} [g/s]	103	86	85	86
	M_{jet} [-]	0.196	0.182	0.174	0.187

Tab. 5.2.1-1   Theoretical ideal labyrinth, α=0.6, DP

A consistent picture of the leakage jets results from this approach. The datum case has very low leakages of 0.3% of the main mass flow in both rotor labyrinths. The large gaps produce 0.9% leakage mass flow. The first rotor labyrinth has a slightly higher throughflow. Note that the jet velocities in gap 3 differs by as much as 20% from the average jet velocity in the 0.3% gap case. This is due to the fact that the gap areas vary strongly within each labyrinth. As given in the Appendix the gap 3 of rotor1 has the smallest value.

Empirical correlation

An additional way of calculating the leakage mass flow is to use an empirical correlation as given by Traupel [58]. Here the leakage mass flow calculates with

$$\dot{m}_{leak,emp} = A\varepsilon\sqrt{p\rho} \tag{5.4}$$

where the discharge characteristic ε of a specific labyrinth geometry, i.e. a stepped configuration in this case, is evaluated empirically. Thus, ε also incor-

porates the jet contraction α and the numbers of seals. The discharge coefficient was determined to be $\varepsilon=0.167$ taking the pressure ratio across the entire labyrinth. The gap area A was taken as the average of the three gaps. Then the leakage mass flow of the second rotor labyrinth is estimated to be at 1.18% (114g/s) of main mass flow for the 1% gap case and 0.38% (37g/s) for the 0.3% gap case. These results have the same order of magnitude as calculated with (5.2), but the empirical correlation gives roughly 30% higher values than the theory of the ideal labyrinth. Assuming this 30% off set to be systematic, an empirical leakage mass flow for the first rotor labyrinth and the large gap of 1.37% (134g/s) can be given using the result of Tab. 5.2.1-1. In the 0.3% gap case this results in 31g/s. A list of the resulting leakage mass flows is presented in Tab. 5.2.1-2

	rotor1	rotor2
0.3% gap	31	37
1% gap	134	114

Tab. 5.2.1-2   Empirical correlation (Traupel [58]): m $_{leak}$ [g/s]

Jet integration

Performing an integration of the data given in Fig. 5.1.2-1 the leakage mass flow can be derived directly. The integration was performed from the shroud outer radius to the jet thickness found in 5.1.2. The results are summarised in Tab. 5.2.1-3. At the exit of rotor 2, the jet integration is in good agreement with the calculated mass flows. The calculation according to Egli [13] gives a 20 to 40% lower mass flow for both gaps. The estimation after Traupel [58] is giving comparable numbers to the probe traversing. The exit of rotor 1 shows much higher values for both gaps. This results seems to be unrealistic in light of the fact that the average gap width of the first rotor labyrinth is smaller than for the second rotor of both gap cases. In addition the steady wall pressure measurements leading to Tab. 5.2.1-1 do not indicate an increase of mass flow due to a higher pressure drop across the first rotor.

	rotor1	rotor2
0.3% gap	82	48
1% gap	156	108

Tab. 5.2.1-3   Integration of leakage mass flow: m $_{leak}$ [g/s]

The presence of a downstream stator leading edge can significantly alter the driving mechanisms of the cavity flow (see chapter 7). The effect may be a

higher rotational speed of the vortical flow in comparison to the rotor 2 exit cavity as depicted in Fig. 5.2.1-4. In fact, additional five hole probe measurements support this picture. The higher rotational speed in turn would lead to a higher velocity of the neighbouring flow field of the jet. The jet thickness would then be expected to be thinner, since velocity differences are smaller and therefore less diffusion would act on the jet from the gap up to the jet traversing plane. An explanation of this result could be that the leakage jet is less thick at the location of measurement as estimated in 5.1.2.
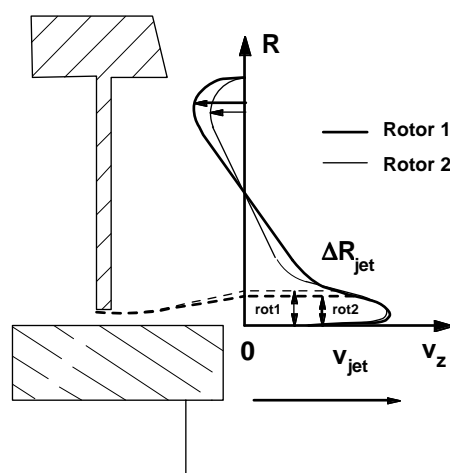
Fig. 5.2.1-4   Changed leakage jet thickness due to the presence of a downstream stator

Summary

Providing a quantification of the leakage mass flow is difficult to achieve. The three approaches presented in the previous paragraphs give agreeing results in the exit cavity of the second rotor labyrinth. In the 1% gap case the results vary by ±15%, in the datum case this reaches ±27%. The exit cavity of the first rotor labyrinth shows a less consistent picture. The jet integration delivers values up to a factor three higher than the analytical single-jet calculation. The jet integration is sensitive to the limits of integration and therefore to the ability of locating the dividing streamline of jet and neighbouring flow. A high degree of resolution in measurements as well as understanding the flow field is required in order to determine the integration limits correctly.

In order to determine the most trustworthy numbers for the leakage mass flow a list of pros and cons of the different approaches is given in Tab. 5.2.1-5. An important fact is that the empirical correlation gives similar results to the probe integration within the inlet cavity as discussed in chapter 6. Considering all

	+	-
Egli	consistent in itself	ideal flow
Traupel	good agreement with probe integration in chapter 6	applicability of empirical correlation
Jet integration	direct measurement	grid resolution probe size to flow feature integration limits

Tab. 5.2.1-5   Comparison of the approaches to determine the leakage flow

three approaches, the empirical correlation has less overall uncertainty than the others. Therefore, the leakage mass flow is referred to Tab. 5.2.1-2, throughout this document.

Additional uncertainties of the leakage mass flow quantification are the gap width, the static pressure field in the cavities, and the true discharging behaviour of this labyrinth arrangement. An accurate way of measuring the running seal clearance as well as the jet velocity would be necessary to provide a more accurate leakage mass flow measurement.

5.2.2   Tangential momentum transport

A missing parameter for the characterisation of the leakage jet is the associated aerodynamic torque, since it is part of the momentum conservation in tangential direction and therefore a measure of lost power. The values in Tab. 5.2.2-1 are derived out of the jet integration by taking the axial mass flow times the tangential velocity and the radius. The results are positive since the exit swirl of the leakage jet is in rotational direction. The leakage mass flow passes the labyrinth, where wall friction on the stationary parts reduce the tangential momentum and the moving rotor shroud induces momentum. The latter effect is also known as windage effect, which in general causes an increase of the temperature (Millward [33]). Therefore, the results in Tab. 5.2.2-1 express a balance between both wall friction effects within the labyrinth. In the 0.3% gap case the exit jet of the second rotor labyrinth conveys 85W of kinematic power into the exit cavity.

Taking the results of the torque balance of the inlet cavity given in Tab. 6.2.3-2, a loss of aerodynamic power can be calculated. A volume data set, which allows this integration, is only available for the datum configuration. Between the two integration surfaces a negative torque of -0.3Nm is exerted on the fluid. This is equivalent to a power loss of 85W or about 0.8% of the over all stage

	rotor1	rotor2
0.3% gap	0.88	0.30
1% gap	2.56	1.72

Tab. 5.2.2-1   Integration of torque: T_{leak} [Nm]

losses. Looking at the 1% gap case the torque transport through the first seal gap can be estimated using Fig. 6.2.5-3, where the tangential velocity in the first gap is 71% of the rotor speed. This results in a loss of torque across the labyrinth for the 1% gap case of -2.7Nm, which is equivalent to 6.6% of the stage losses.

The change of angular momentum from the first to the last seal gap as quantified in the previous section incorporates the windage effect within the closed cavities. The windage of the shroud surface is an additional loss, which has to be quantified. In [31] a method is presented to estimate the windage effect within a labyrinth seal. It is based on the torque balance for a closed labyrinth cavity

$$T_R - T_C = \dot{m}_{leak} r \cdot \Delta v_\Theta \tag{5.5}$$

and the wall friction correlations given in (6.10) to (6.14). T_R and T_C denote the angular momentum being exerted by the rotor and casing wall, respectively. In an iteration on the velocity ratio in (6.12) and (6.13) the torque balance in (5.5) is found. The analysis of the windage effect was performed assuming the same velocity ratio of cavity core flow to rotational speed for both closed cavities. As a boundary condition to this calculation the exit jet was taken from Tab. 5.2.2-1 and the inlet jet at the first seal was taken from Tab. 6.2.3-2. The results are summarised in Tab. 5.2.2-2. The resulting velocity ratio is around 0.5 and the windage losses range around 600W. Thus, the windage contributes around 6% of the stage losses.

	$\dfrac{v_{\Theta, cav}}{u}$	P_{win} [W]
0.3% gap	0.582	536
1% gap	0.470	764

Tab. 5.2.2-2   Windage losses

6 THE INLET CAVITY

6.1 EXPERIMENTAL RESULTS

The flow field in the inlet cavity was measured with steady and unsteady measurement technology. The flow field in the larger gap case was resolved only in mid gap position as the numbers in Tab. 2.4.2-1 indicate. In contrast, the 0.3% gap case was resolved in 6 axial positions with steady 5-hole probes and 5 axial positions with the virtual four sensor fast response probe. The axial locations and radial extension of the traversing is shown in Fig. 6.1.0-1. Therefore, a spatially and temporally highly resolved volume data set is available for the 0.3% gap case. The data will be discussed starting with circumferentially averaged wall pressure and mass averaged steady flow data measured in the absolute system. Then the time averaged unsteady data is presented within the relative frame. Finally the fully unsteady flow field is discussed. Wherever possible a comparison of the two gap cases is given.

a) 5 Hole Probe	b) Virtual 4 Sensor Probe
(Z=0.17, 0.28, 0.41, 0.5, 0.67, 0.83)	(Z=0.28, 0.41, 0.5, 0.67, 0.83)
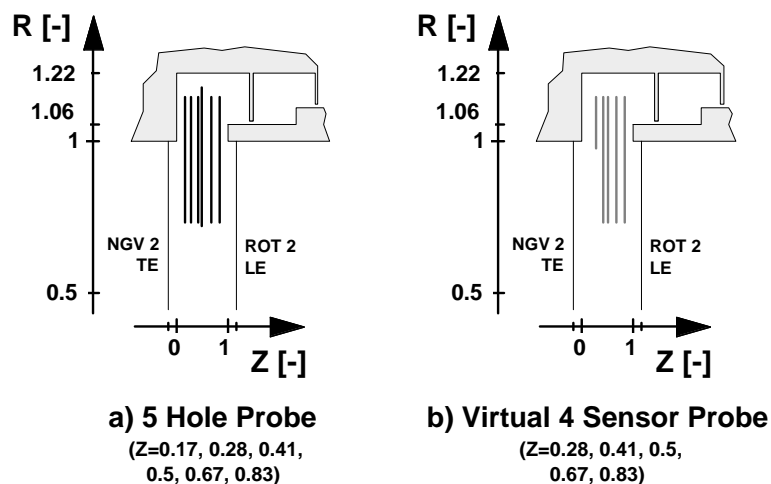
Fig. 6.1.0-1   Measurement positions within the inlet cavity for 0.3% gap case

6.1.1 Absolute Frame of Reference

Pitch-wise averaged data

Wall pressure

The wall pressure measurements shown in Fig. 6.1.1-1 reveal a maximum for the 1% gap case at a local axial position of Z=0.83. The cavity flow is affected by closing the gap such that the high pressure region is shifted upstream to lower Z. A local maximum could not be identified for the datum case, since addi-

tional upstream pressure taps were missing. In contrast to the findings in the exit cavity (Fig. 7.1.1-1), a foot print of the shroud leading edge position at Z=1 can not be identified in these measurements.
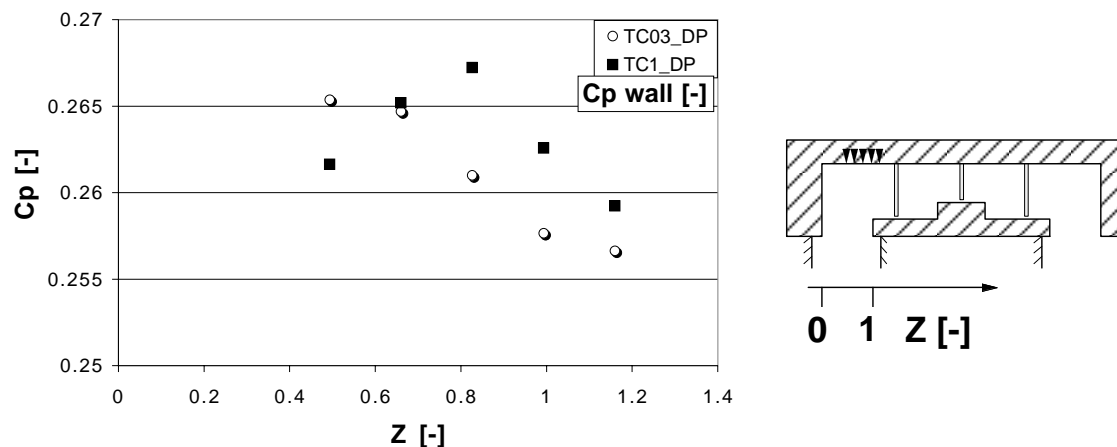
Fig. 6.1.1-1   Circumferentially averaged wall pressure measurements: Inlet cavity to second rotor tip labyrinth

Cavity and main flow

Figure 6.1.1-2 presents the pitch wise averaged data for the 0.3% and the 1% gap case. Firstly, the results of the 0.3% gap case are discussed at the first, middle, and last axial positions (Z=0.17, 0.5, and 0.83) referring to the left column of Fig. 6.1.1-2. Then the comparison of the 1% gap to the 0.3% gap case at Z=0.5 is described using the right column of Fig. 6.1.1-2. The error band is given for each quantity.

The non-dimensional total pressure in Fig.6.1.1-2a shows a strong radial gradient between R=0.93 and 0.99. It decays with increasing Z. At Z=0.17, a total pressure wake at R=1 and a jet at R=0.97 are present. The wake jet character gets mixed out at the next axial position. The cavity flow shows a lower total pressure than the main flow. Close to the rotor inlet at Z=0.83 the total pressure profile has a more uniform distribution at radii lower than 0.93. Note the kink in the profile at R=1.08 and the associated higher level of total pressure at around R=1.03. The effect stems from the rotating shroud leading edge entraining kinetic energy into the fluid via shear. Comparing the 0.3% to the 1% gap case, two regions show different characteristics. The loss core of the second stator passage flow is shifted from R=0.78 to 0.72. Close to the cavity the maximum total pressure increases by $\Delta C_{po}=0.01$. Within the cavity, the 0.3% gap case shows a local maximum at R=1.16, which is not present with the 1% gap.

The static pressure distribution in Fig.6.1.1-2b is showing a radial pressure gradient. It is in radial equilibrium with the centrifugal forces to keep the fluid in a swirling motion. Coming from lower span the gradient increases in the vicin-

ity of R=1. Here the first and last axial position Z=0.17 and 0.83 show a local maximum in contrast to the mid cavity position. All axial positions encounter a local minimum of static pressure around R=1.06. A strong radial pressure gradient connects the local minimum to the cavity floor wall. Note that the wall pressures of Z=0.5 and 0.83 at R=1.22 are seen by the pitch wise averaged wall pressure tap measurements. The obvious difference of the static pressure profile associated to the 1% gap case to that of the 0.3% gap case is a local high pressure at R=0.9. In addition, the local minimum within the cavity formerly found at R=1.06 is not present. The radial pressure gradient within the cavity is less steep in the 1% gap case, especially around R=1.13.

The axial velocity component, made non-dimensional with the blade tip speed, is given in Fig. 6.1.1-2c. The over and under turning effect of the flow due to the stator passage vortex are seen in the velocity profile. The local maximum at R=0.8 is caused by under turning. The over turning leads to a kink in the axial velocity profile at R=0.93. Zero through flow is found around R=1.06. The back flow component within the cavity reaches values up to 10% of the blade tip speed. The position of the local minima shift radially downwards with increasing Z. Comparing this region of back flow of both gap cases, a significant difference is found. Instead of a local strong back flow found at R=1.16, the axial velocity profile linearly approaches the cavity wall in the 1% gap case. This linear profile does not indicate the presence of a second toroidal vortex close to the sealing fin as the 0.3% gap velocity profile does. The vorticity field will be discussed in a later section.

The radial velocity in Fig.6.1.1-2d indicates a vortical flow within the cavity having negative components at Z=0.17 and positive components at Z=0.83. Note that the absolute value at Z=0.83 is about 0.07 higher than at Z=0.17. The sense of rotation is counter clock wise resulting in positive vorticity, see also Fig.6.1.1-6. The centre of the vortex is characterized by a local minimum in static pressure. The local minimum in Fig.6.1.1-2b at R=1.06 suggests the existence of a vortex core. From the comparison of the 1% and 0.3% gap case no differences in shape but in absolute values can be reported. The 1% gap case exhibits higher positive values in a region between 90% and 106% blade height than the 0.3% gap case. This indicates an increased radial mass flow into the cavity caused by the bigger leakage mass flow. Close to the cavity wall the trend inverts: the 0.3% gap case is characterised with higher positive values than the 1% gap case. Both toroidal vortices are cut at different axial positions relative to their centre. The strong back flow of Fig. 6.1.1-2c is moving closer to the cavity wall. Another observation can be made with the help of the static pressure profile. The local maximum found at R=0.89 for the 1% gap case corresponds to that point in the radial velocity profile, where the v_r=0 is passed.

In Figure 6.1.1-2e the over and under turning behaviour results in a local maximum and minimum of tangential velocity at R=0.8 and R=0.93, respectively. At Z=0.17 a shear layer with a strong gradient in tangential velocity connects the over turning region to a wake of low tangential momentum. It has a velocity deficit of 0.08 compared to the swirling velocity of the cavity flow and 0.2 compared to the region of over turning at R=0.93. Moving downstream to Z=0.5 the wake is filled up as tangential momentum is transferred from the main flow and the cavity flow into the wake. Close to the shroud leading edge at Z=0.83 the wake is filled up and has gained additional momentum. There are two sources of tangential momentum entrainment in this flow region: the rotating shroud and the higher swirl component of the main flow. The shroud outer diameter at R=1.06 coincides with the kink in the tangential velocity profile. Finally comparing the 0.3% and 1% gap cases reveals small differences close to the cavity wall and stronger ones in the main flow due to the different under and over turning characteristic of both cases.

Pressure and Velocity field

The total and static pressure distributions at mid cavity position is displayed in Fig.6.1.1-3 for both gap cases. The cavity floor is depicted with a thick line. The tip radius and the trailing edge position of the stator are indicated with dashed lines. Firstly, Fig. 6.1.1-3a is discussed before the comparison to the 1% gap case is drawn.

Both distributions show similar features as described in Pfau et al. [36]. The cavity flow has a lower level of total pressure than the main flow. The main flow exhibits the secondary flow structure of a blade passage showing a loss core at R=0.76. On the pressure side of the stator wake the high total pressure gradient reaches the tip radius R=1. Here the thin boundary layer created on the passage tip end wall meets the cavity flow. Above the loss core, i.e. on the suction side of the blade wake, a low total pressure region has formed at R=0.97 showing the same order of magnitude as the loss core. This region is part of a wake in tangential momentum, as described in Fig.6.1.1-2e. It originates from the backward facing surface of the cavity at a radial position slightly higher than 1. The arrows illustrate the radial movement in to and out of the cavity, which will be further discussed later in this section.

The static pressure field in Fig.6.1.1-3 is circumferential non uniform due to the stator trailing edge. Close to the position of the trailing edge around Θ=0.35 a high static pressure is induced. At Θ=-0.1 the distance to the suction side surface is larger and therefore the static pressure is lower. This circumferential distribution propagates into the cavity volume and varies over one pitch by $\pm$0.003 at R=1.07. Comparing total and static pressure distribution, the blade wake has
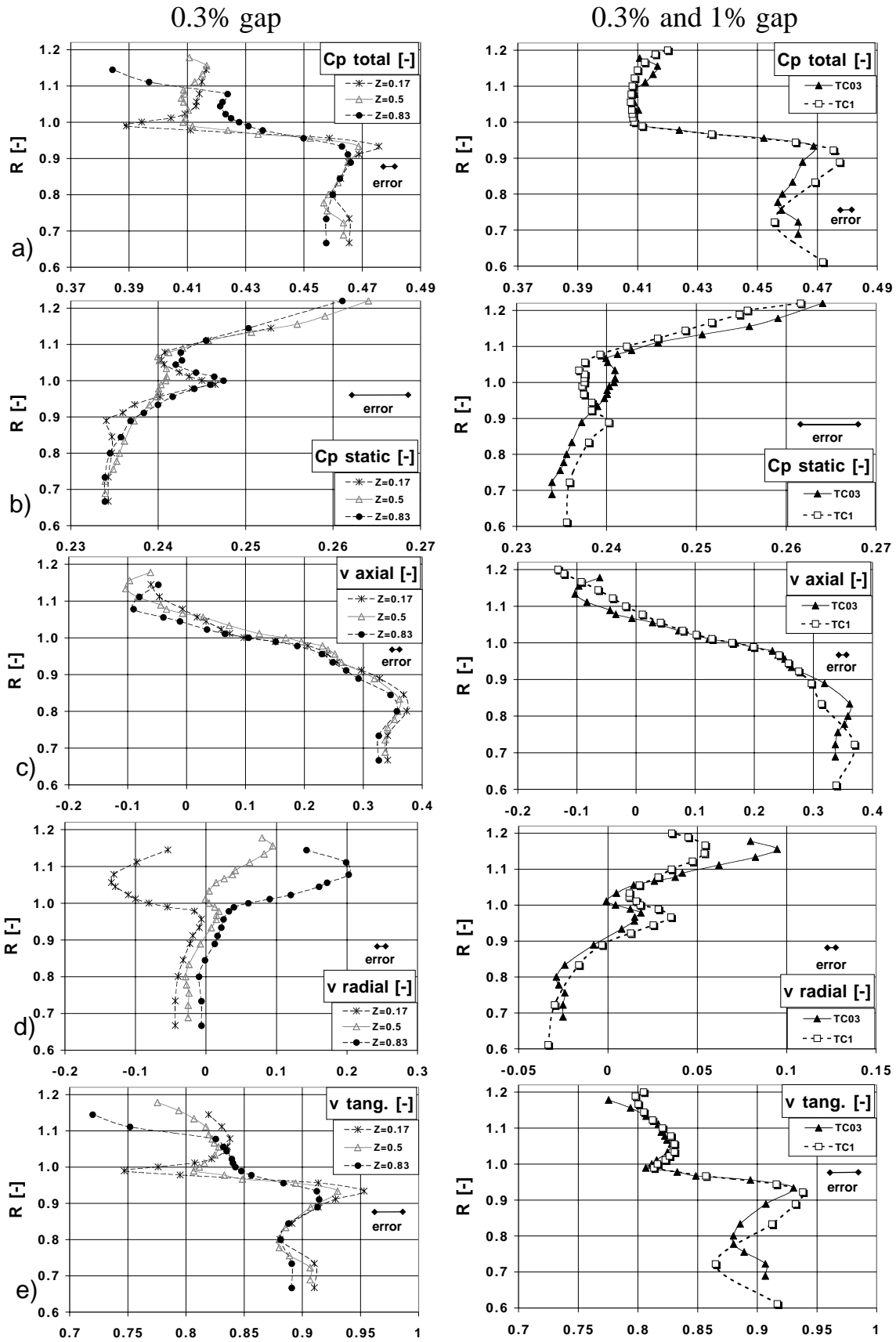
Fig. 6.1.1-2   Pitch-wise averaged results: a) C_{po}, b) C_p, c) V_z, d) V_r, e) V_θ

convected $\Delta\Theta$=-0.4 from the trailing edge position. The local minimum in static pressure at R=1.06 coincides with streaks of lower total pressure. The inflow region marked with an arrow encounters a low local static pressure. High kinetic energy fluid is pushed into the cavity.

Comparing now the 0.3% and 1% gap case, some differences are pointed out. The loss core moves to R=0.72 as measured in Fig. 6.1.1-2a and has a different shape in the upper right corner. Shape and size of the outflow region above the wake changes to a narrow band, whose centre line lies closer to the tip radius than the one in the 0.3% gap case. The three-dimensional character of the static pressure field is preserved. However, the contours of the low pressure region are altered due to an increase of static pressure at R=0.89 as reported in Fig. 6.1.1-2b.

The radial velocity distributions given in Fig. 6.1.1-4 verify the arrows discussed in the previous section. A direct comparison of the radial velocity component is given in the middle diagram showing the pitch wise profile at R=1. In both gap cases, high positive radial velocities can be localised in a spot in the pressure side corner of the wake (R=0.98, Θ=-0.3). Parts of the streamlines passing through this area of the main flow will enter the cavity. The low kinetic energy fluid within the loss core and the wake migrates radially inward. At the same circumferential position of the wake the fluid crosses R=1 with negative radial velocity. The comparison of both cases in the area distribution do not show big differences in contours as it was expected from Fig. 6.1.1-2d. However, in Fig. 6.1.1-4b a constant shift in radial velocity between the two cases is observed. The sucking of the leakage mass flow induces a higher radial velocity at this location. It can be inferred from these plots that the kinematic driving mechanisms for the 0.3% and the 1% gap case are in principal the same and are set up by the stator exit flow field. The sucking of the labyrinth seal affects the radial inflow in a pitch-wise symmetric way.

The flow in and out of the cavity is shown in greater detail in Fig.6.1.1-5 with a contour plot of radial velocity for the 0.3% gap case. The view is in the positive radial direction. The thick line at Θ=0.35 indicates the position of the stator trailing edge at R=1. At Z=0 and 1 thick lines mark the axial position of the inlet corner and the shroud leading edge. Positive and negative radial velocities can be observed parallel to a line of zero radial velocity indicated with a dashed line. Close to the upstream corner radial velocities are negative, since the toroidal vortex pushes fluid into the main flow. On the downstream side of the axial gap fluid particles move into the cavity. In addition, the centrifugal forces induced by the rotating shroud leading edge surface contribute to the inflow.
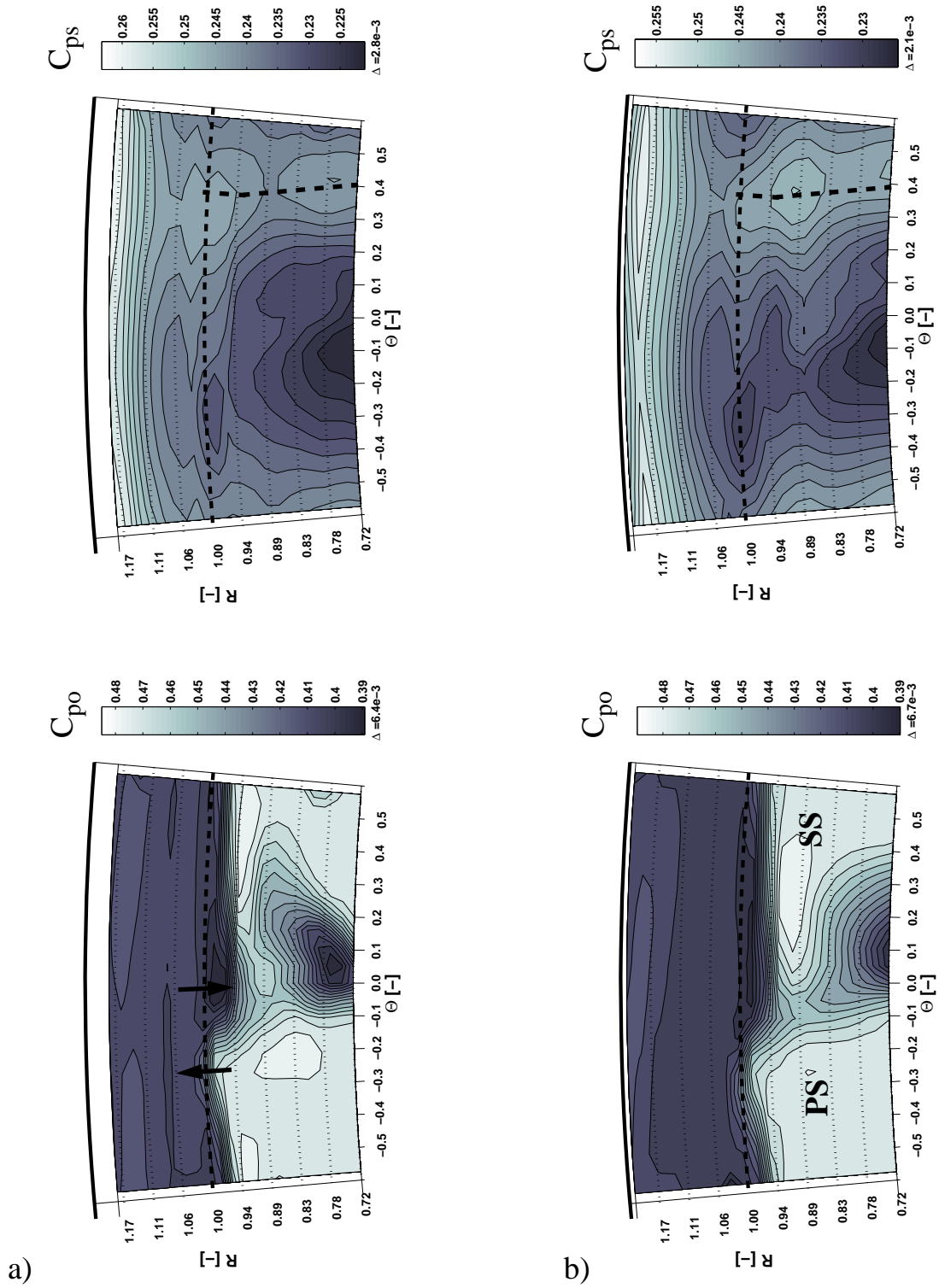
Fig. 6.1.1-3   Total pressure C_{po}, Static pressure C_p, Z=0.5:
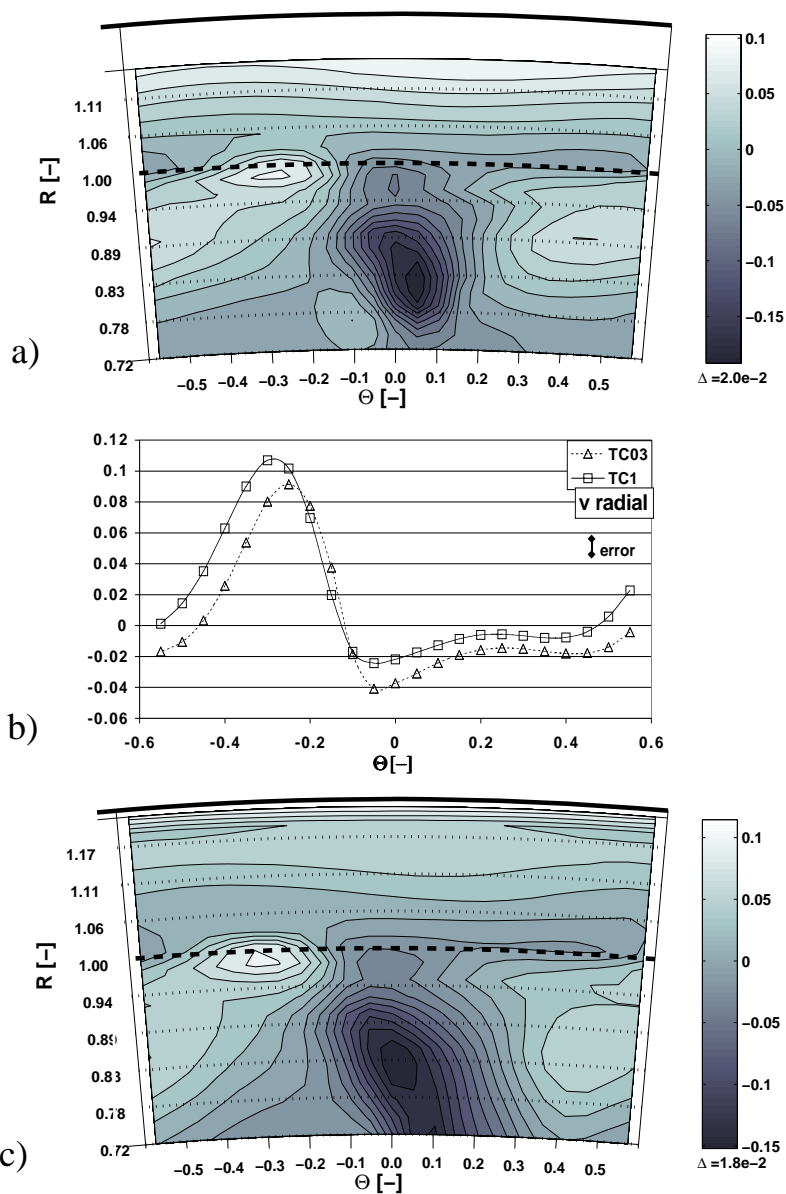a) 0.3% gap, b) 1% gap

*Fig. 6.1.1-4   Radial velocity component V_r, Z=0.5: a) 0.3% gap, b) compari-
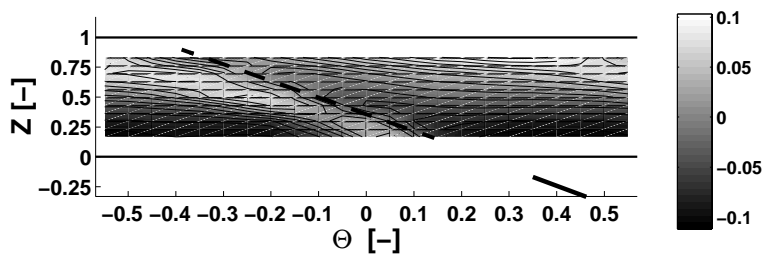son of 0.3% and 1% gap at R=1, c) 1% gap*

Fig. 6.1.1-5   Radial velocity V_r, R=1, 0.3% gap

Vorticity field

The flow in the cavity is three-dimensional with a high level of unsteadiness in pressure and velocity. Representing the flow structure in terms of vorticity in this case permits a better physical insight into the entrainment and loss generation using only a single parameter. The vorticity is defined as the curl of the velocity field [69]:

$$\omega = \Delta \times v. \tag{6.1}$$

The vorticity components in cylindrical coordinates are

$$\text{in r:} \ \omega_r = \frac{1}{r}\frac{\partial v_z}{\partial \theta} - \frac{\partial v_\theta}{\partial z}, \tag{6.2}$$

$$\text{in } \theta\text{:} \ \omega_\theta = \frac{\partial v_r}{\partial z} - \frac{\partial v_z}{\partial r}, \tag{6.3}$$

$$\text{in z:} \ \omega_z = \frac{1}{r}\frac{\partial r v_\theta}{\partial r} - \frac{1}{r}\frac{\partial v_r}{\partial \theta}. \tag{6.4}$$

The calculation of the vorticity field was directly calculated by taking the partial derivatives of the velocity field within the measurement volume and applying (6.2) to (6.4), as described in [41]. In this document, the vorticity is made non-dimensional by using solid body rotation and taking a reference angular speed calculated with the blade passing frequency according to

$$\Omega = \frac{\omega}{2 \cdot 2\pi f_{blade}}. \tag{6.5}$$

Figure 6.1.1-6 presents the non-dimensional circumferential and axial vorticity components of a circumferential position of $\Theta=0.25$. High positive tangential vorticity dominates the measurement volume inside the cavity. Maximum values occur in a region at $Z=0.4$ and $R=1.07$ as well as in the vicinity of the shroud leading edge. Close to the corner, formed by the sealing fin and cavity floor, the sign of vorticity changes. This suggests the presence of a second counter rotating vortex with the centre approximately at $Z=1$ and $R=1.15$ as the circular arrow indicates.

The axial vorticity component shows an alternating pattern of high positive, high negative and back to high positive values at the $Z=0.17$ as R increases. The axial vorticity as given in (6.4) is a measure of tangential shear, if radial shear is comparably small. The region of high and low axial vorticity at $R=1$ and $R=0.96$ are confining the centre of the tangential momentum wake, which was found in Fig.6.1.1-2e. The higher axial vorticity at $R=0.9$ as well as the lower

at R=0.96 is induced by the overturning profile also found in Fig.6.1.1-2e at R=0.94. As the gradients in tangential velocity decrease with Z, the axial vorticity also decreases. Note that some negative axial vorticity is induced from the rotating shroud leading edge.

A combined view of axial and tangential vorticity reveals the centre of the toroidal vortex. The condition for the centre of a toroidal vortex is zero vorticity in radial and axial direction, which is fulfilled in the local maximum of tangential vorticity at R=1.073 and Z=0.41. Closer to the shroud the tangential vorticity stays positive. However the axial vorticity becomes negative. These two conditions can be explained with a skewed boundary layer induced by the tangential shear and the radial pumping effect of the rotating shroud and rotor leading edge. An important finding is that the centre of the toroidal vortex is found to be at a slightly higher span than it was determined with circumferential averaged data in Fig.6.1.1-2b. This indicates a pitch wise variation of the vortex centre.
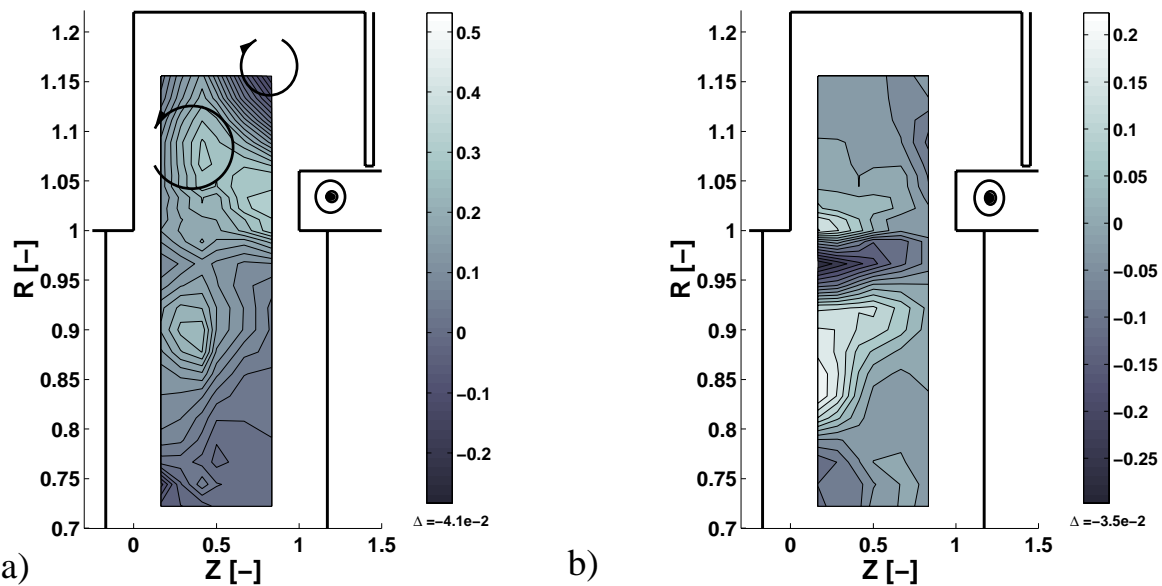
Fig. 6.1.1-6   Vorticity components at $\Theta=0.25$: a) Ω_θ, b) Ω_z

In Fig. 6.1.1-7, the tangential vorticity component at different circumferential positions is presented. Taking $\Theta=0.25$ in Fig.6.1.1-6a as a starting point, the diagrams Fig. 6.1.1-7a through c follow the convective direction of the toroidal vortex at $\Theta=-0.05$, -0.35, and -0.5. In position $\Theta=-0.05$ the main flow shows a high negative tangential vorticity. It is generated by the change of negative radial migration present in the blade wake with increasing Z. The high positive tangential vorticity at R=1 and Z=0.17 indicates the point on the pressure side of the stator wake where the inflow to the cavity starts. Comparing with Fig.6.1.1-5, it seems that at $\Theta=-0.35$, the region of high tangential vorticity is detached from the cavity corner and has moved into the mid axial gap position.

This movement is continued in the next circumferential position while the magnitude of vorticity diminishes. At the end of the periodic cycle the region of higher vorticity merges with the flow region close to the shroud as can be observed in Fig.6.1.1-6a. It is through this process that vorticity is entrained into the toroidal vortex.
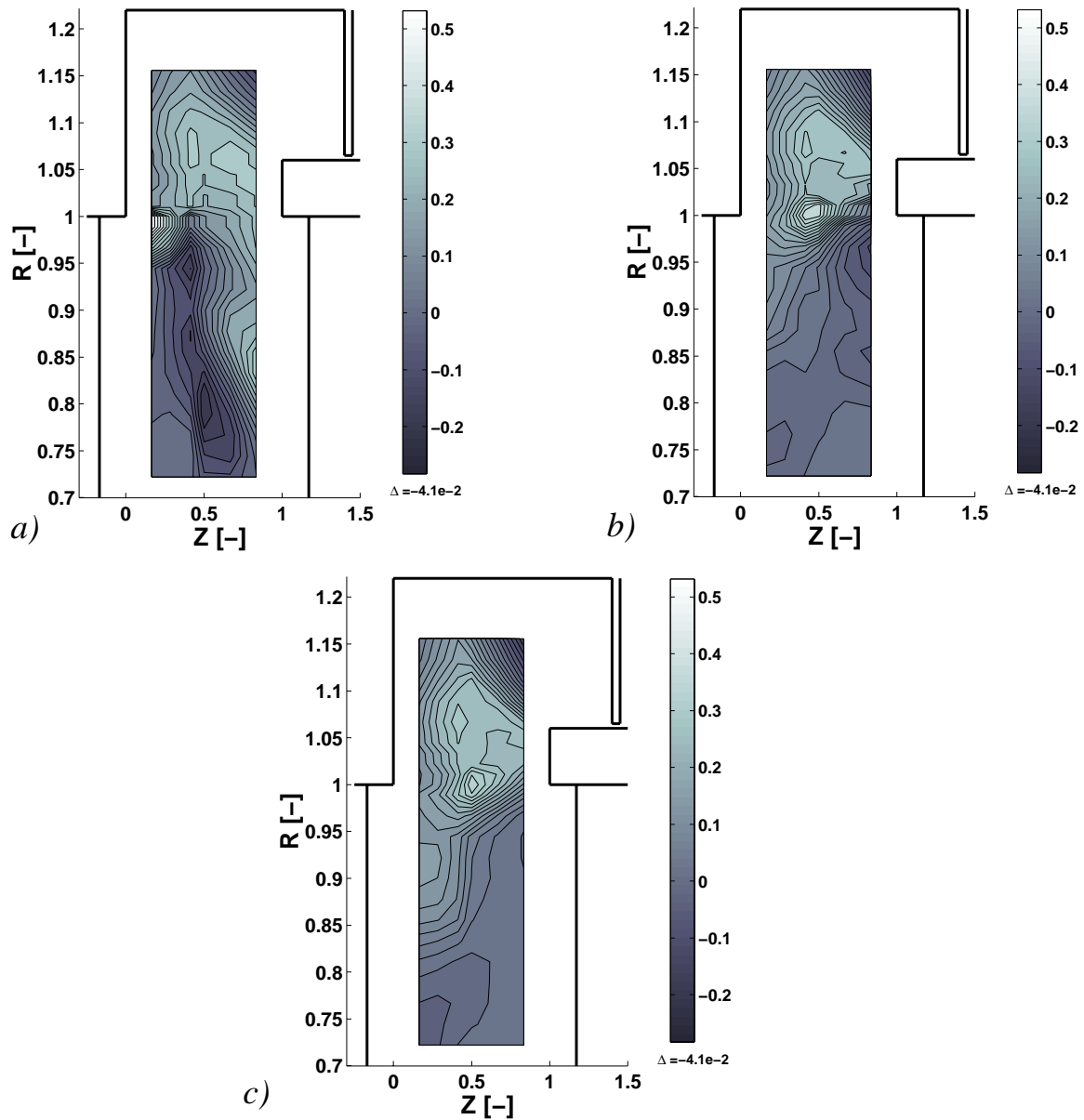
Fig. 6.1.1-7   Circumferential vorticity component Ω_θ: a) $\Theta=-0.05$,
                b) $\Theta=-0.35$, c) $\Theta=-0.5$,

The radial position and the angular speed defined at the centre of the toroidal vortex are presented in Fig. 6.1.1-8. As the cavity flow swirls in negative Θ direction, the vortex undergoes stretching and tilting in the absolute frame. The cause of the spinning up and down of the vortex can be found in the static pres-

sure field given in Fig.6.1.1-3b. Within the cavity at Θ=0.4 a local maximum of static pressure is observed, and vorticity of the toroidal vortex is low. The fluid within the vortex accelerates due to a favourable tangential static pressure gradient. At Θ=-0.1 the vortex reaches a low pressure field and vorticity is high. While passing one stator pitch the vortex is pushed outward to R=1.08 and then moves back to the lower radius R=1.07. The maximum absolute difference in radial position is 1.4mm which is 7% of the cavity height. The resolution of the measurement grid in axial direction is not sufficient to detect an axial displacement of the vortex. Therefore, the axial position is given to Z=0.41 as discussed in Fig.6.1.1-6.
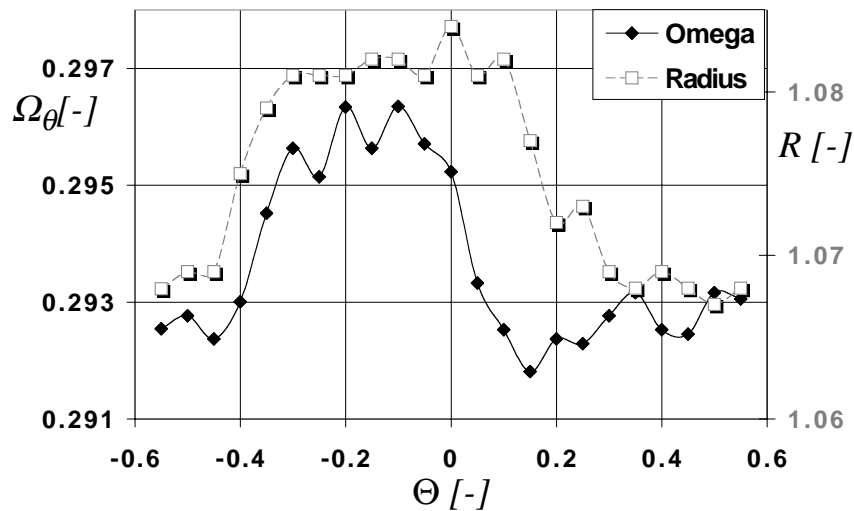
Fig. 6.1.1-8   Vorticity and radial position of the toroidal vortex:
            0.3% gap, Z=0.41

6.1.2   Relative Frame of Reference

In this section the measurement results of the virtual four sensor probe are presented in the relative frame of reference. Figure 6.1.2-1 shows the time averaged relative total pressure. The tip radius is indicated with a thick dashed line. The leading edge position of the rotor is given by the vertical dashed line at Θ_{rel}=0. The view is upstream and the arrow indicates the sense of rotation of the coordinate system.

Within the cavity the relative total pressure shows a wavy structure but has a lower variation than in the main flow region. At the cavity floor, the relative total pressure is higher than upstream of the shroud leading edge.

The incoming flow field to the rotor passage is dominated by a high relative total pressure region at Θ_{rel}=0. The pressure contours are a result of two superimposed effects of the rotor blade on the upstream flow field. One is the leading

edge potential field being responsible for an increase in static pressure. The other is found in the through flow distribution which is set up in a rotor passage due to the turning of the flow. The highest velocity is present on the suction side of an airfoil, where the local axial through-flow velocity reaches a maximum. The upstream effect of this interaction causes a higher relative dynamic head on the suction side of the leading edge. Figure 6.1.2-1 confirms this observation, where a region of higher relative total pressure at $\Theta_{rel}=-0.15$ and R=0.81 is present.
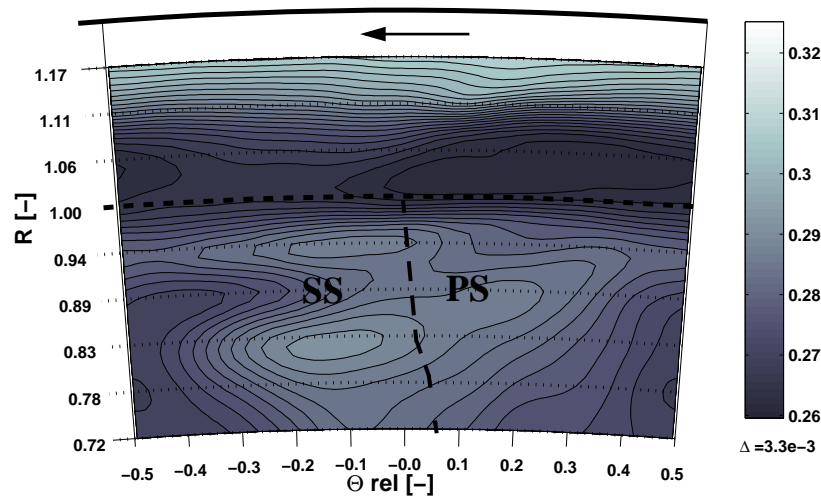
Fig. 6.1.2-1   Time averaged relative total pressure C_{porel}
rotor relative, Z=0.5

The relative circumferential velocity distribution at Z=0.5 is given in Fig.6.1.2-2. The cavity flow is swirling at a lower tangential velocity than the rotational speed of the rotor. Close to the cavity floor the values are high negative. The centre of the cavity vortex at R=1.07 is accelerated and decelerated according to the static pressure field.The cavity vortex fluid moves into positive Θ_{rel} direction. The fluid is accelerated out of the high static pressure region across the leading edge position until it reaches the maximum relative velocity at $\Theta_{rel}=0.4$. The static pressure there is therefore low. Close to the rotor leading edge the static pressure field induced by its potential field is clearly evident. Figure 6.1.2-3 shows a high static pressure upstream of the rotor leading edge. This pressure field propagates into the cavity. In the main flow region a low pressure faces the rotor passage.
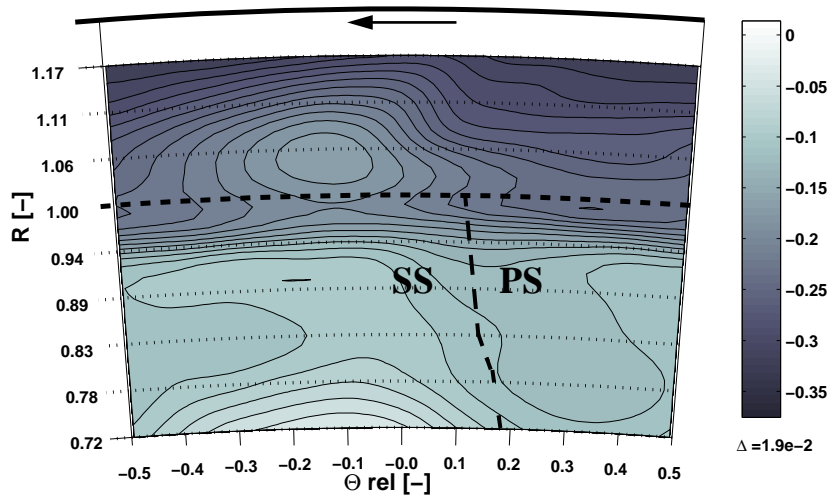
Fig. 6.1.2-2   *Time averaged relative tangential velocity $V_{\theta rel}$*
                   rotor relative, Z=0.5
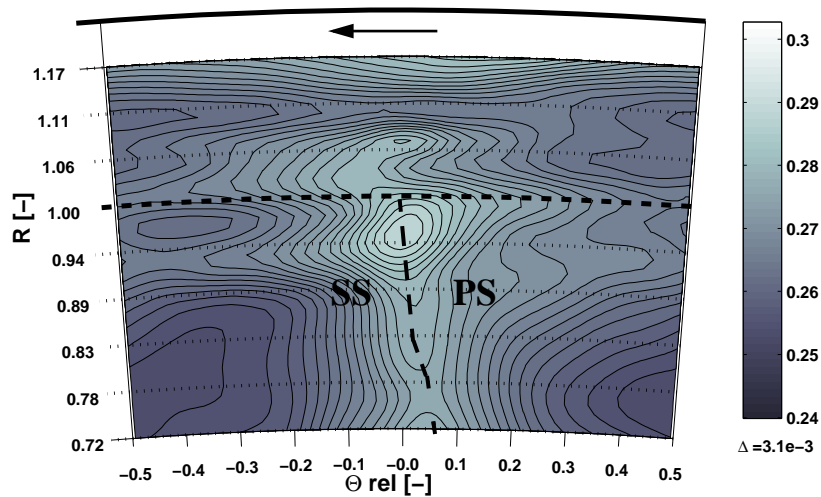
Fig. 6.1.2-3   *Time averaged static pressure C_p*
                   rotor relative, Z=0.83

The upstream effect the leading edge and passage potential field causes the distribution of the radial velocity as presented in Fig.6.1.2-4 and Fig. 6.1.2-5. The contours of zero radial velocity are highlighted with white lines. In the time average the tip end wall of the rotor passage (R=1) exceeds positive and negative radial flow over the entire pitch. Surprisingly, the largest positive radial velocity is not found at $\Theta_{rel}=0$ directly above the leading edge, but shifted to the pressure side of the passage. Looking at the relative tangential velocity (Fig.6.1.2-2), one can observe values of around -0.2 in the relevant area. From the azimuthal cut (Fig. 6.1.2-5) it is evident that the radial velocity distribution across

the cavity is set up by the upstream effect of the rotor passage. On the pressure side the fluid is pushed into the cavity and on the suction it is sucked out. The amplitude of circumferential variation is decaying from the rotor leading edge to the stator trailing edge, which confirms that it is upstream potential effect. The time averaged radial velocity components in Fig.6.1.2-4 and Fig. 6.1.2-5 had to be adjusted to the results found in Fig. 6.1.1-2d, since the differences were to high, Δv_r=0.04.
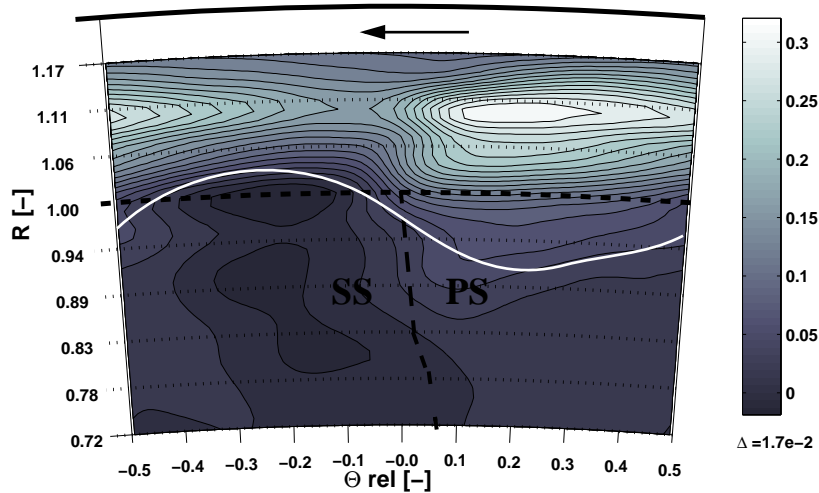
Fig. 6.1.2-4   Time averaged radial velocity V_r
                rotor relative, Z=0.83
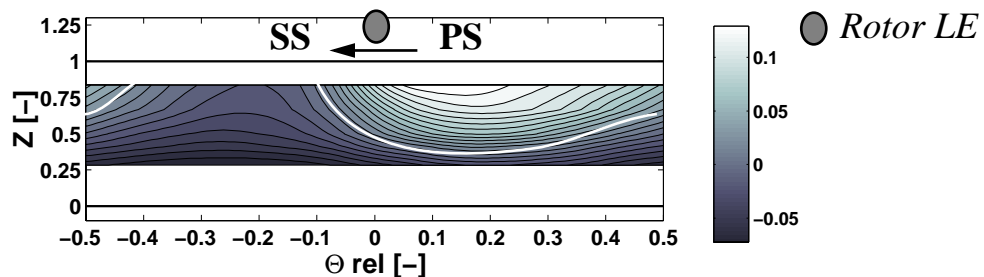
Fig. 6.1.2-5   Time averaged radial velocity V_r, rotor relative, R=1

The rotor inlet flow field close to the tip end-wall is altered considerably as the previous sections showed. Considering the stream wise vorticity field in Fig. 6.1.2-6, they reveal additional details. Note that the scale of the diagram ranges from 0 to -0.3. The dashed line represents the contour line of zero radial velocity. Within the cavity a region of positive Ω_{stream} is present, which belongs to the second toroidal vortex close to the sealing fin and is displayed without grey shades. The values within the main flow region are negative in most parts. Just above the rotor leading edge at R=1.04 a spot of high negative Ω_{stream} is observed. The arrows indicate the fluid motion relative to the rotor blade. The results suggest that the rotor passage receives a sheet of negative stream-wise

vorticity between the tip radius and R=0.94. This vorticity sheet is caused by a skewed velocity profile. The skewness origins from the cavity outflow which happens under a negative incidence angle relative to the main flow direction and the blade leading edge. The sheet of vorticity is modulated by the rotor leading edge and has the same sign as the rotor tip passage vortex. Considering the radial velocities it becomes obvious that a streak of negative Ω_{stream} is entering the blade passage on the suction side, which will downstream become part of the rotor passage vortex.
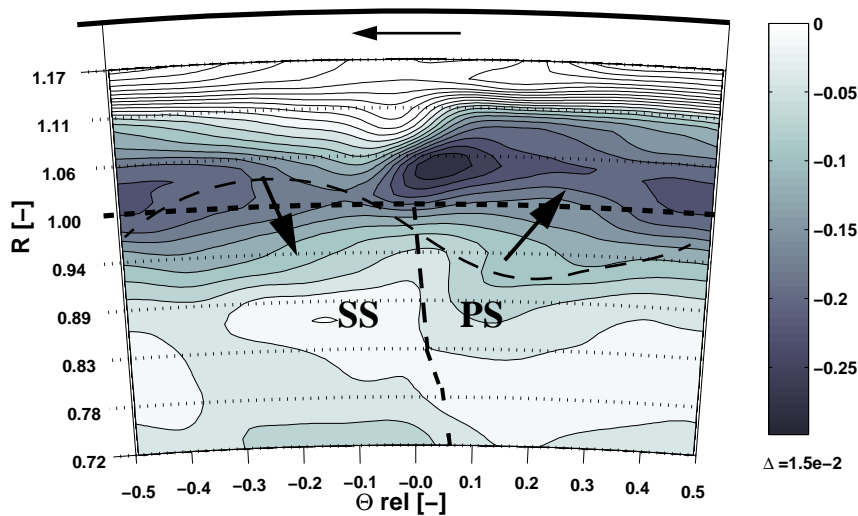
Fig. 6.1.2-6   Stream-wise vorticity Ω_{stream}, rotor relative, time-averaged, Z=0.83

6.1.3   Unsteady flow field

The unsteady flow field is discussed with the help of Fig.6.1.3-1 and Fig.6.1.3-2, which show the non-dimensional total pressure and the non-dimensional tangential vorticity component for the 0.3% gap case. One period of rotor blade passing is resolved with four time frames. The data are given in the absolute frame of reference. The thick dashed lines indicate the blade tip radius as well as the leading edge position of the rotor. For clarity the latter is shown as a straight line.

The total pressure sequence starts with the rotor leading edge aligned with the stator wake. Comparing figures 6.1.1-3a and 6.1.3-1a the loss core has an increased value due to the potential effect. Following the time sequence the loss core region undergoes large changes in position, size and magnitude of pressure. If the open rotor passage is facing the loss core, as in t/T=0.5, the loss core covers a large area and values are low due to the accelerating lower static pressure.

Directing the attention to the cavity flow, regions of high and low total pressure are apparent. They move with rotor blade velocity. The high pressure region is $\Delta\Theta=0.15$ ahead of the rotor leading edge position. Note that it is more round shaped and covers 30% of pitch, whereas the low pressure region is more narrowly shaped and covers 70% of pitch. The low pressure region also coincides with the region of high negative relative tangential velocity in Fig.6.1.2-2.

The wavy shear layer has changed the form in comparison to the time averaged picture. At $\Theta=0$ in the initial time step the shear layer reaches to as low radii as R=0.94. The S-shape with the centre at $\Theta=-0.1$ is more pronounced. At t/T=0.25 it reaches to R=0.91 but has a minimum total pressure at R=0.96 and $\Theta=0$. The outflow area, as it was determined in Fig.6.1.1-3, undergoes unsteady periodic variations. The changes to the position of inflow ($\Theta=-0.25$, R=0.98) however are less affected by the rotor interactions

The time sequence of the non dimensional circumferential vorticity component as given in Fig.6.1.3-2 shows the unsteady vortex evolution within the cavity as well as the secondary flow field of the stator exit flow. At the first time step high positive values at $\Theta=0.1$ and R=0.89 indicate the position of the passage vortex. The region of high negative values at $\Theta=-0.05$ and R=0.8 coincides with the tangential total pressure gradient in Fig.6.1.3-1. Radial migration within the wake and the loss core can have this effect on vorticity. The loss core region faces the rotor leading edge. As the rotor moves in time, both regions change their size and value. At t/T=0.5, the covered area is large and the measured vorticity values are lower than at the beginning of the sequence. Thus, the rotor passage is facing the loss core region.

The centre of the toroidal vortex is found at radii around 1.1. This is located higher than the position determined with the five hole probe measurements in Fig. 6.1.1-8. Regions of high and low vorticity alternate in a similar manner as the total pressure in Fig.6.1.3-1. The high vorticity coincide with low total pressure regions. Looking at the first time step t/T=0 the pitch-wise variation of vorticity at R=1.1 ranges from 0.1 to 0.4. The maximum time averaged value found in Fig.6.1.1-6 was 0.3. The vortex changes rotational speed in both space and time. The amplitude of the unsteady vorticity fluctuation is larger than the time averaged, pitch wise variations measured with the five hole probe in Fig. 6.1.1-8. The sign of vorticity does not change in time. Furthermore, the unsteady mechanism of vorticity entrainment into the toroidal vortex can be discussed. The inflow region at R=1 and $\Theta=-0.35$ encounters a local positive maximum of tangential vorticity (Fig.6.1.1-3a). While the region of high vorticity within the cavity passes this position, both areas merge together (t/T=0.74). Due to higher gradients vorticity is also transferred into the low vorticity regions of the toroidal vortex at this point (t/T=0.25).
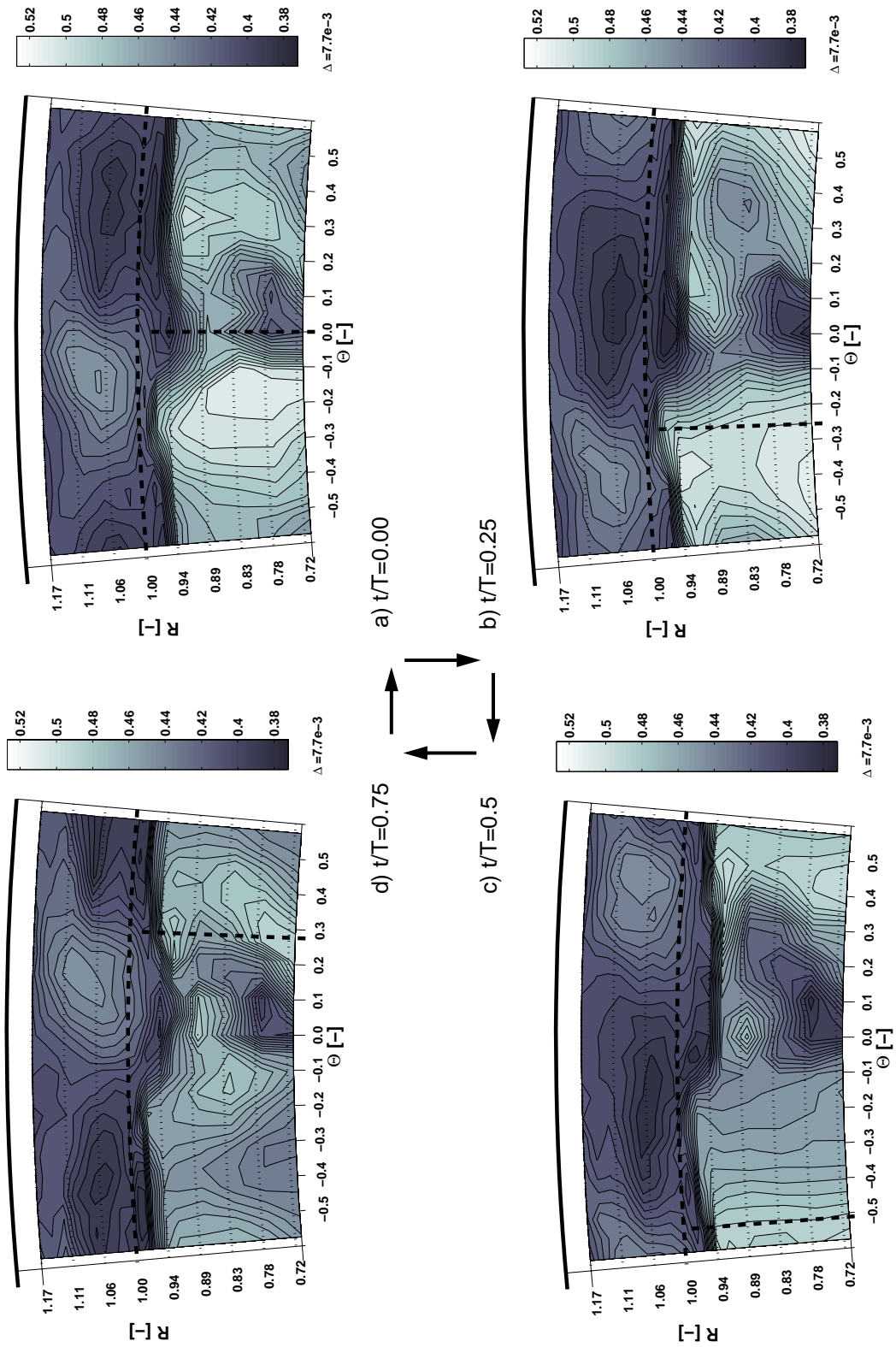
Fig. 6.1.3-1   Time sequence of total pressure C_{po}, Z=0.5, 0.3% gap
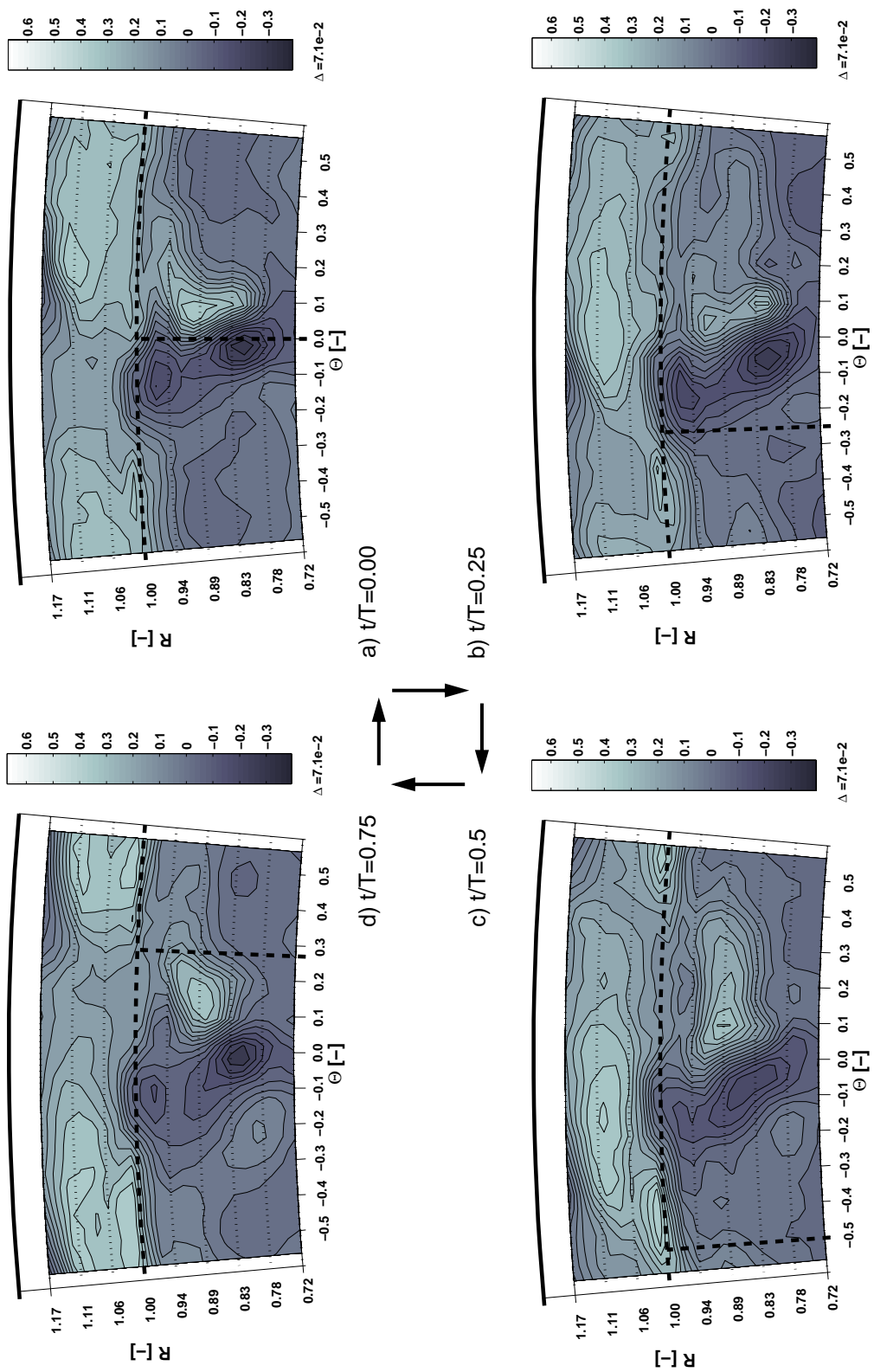
Fig. 6.1.3-2   *Time sequence of tangential vorticity Ω_θ, Z=0.5, 0.3% gap*

6.2 MASS AND MOMENTUM EXCHANGE

The inlet cavity was resolved in a volume of measurement points as shown in Fig. 6.1.0-1, using the five hole probe and the virtual four sensor probe. The volume data set was further processed using a numerical control volume analysis tool. The tool uses linear interpolation within the measurement grid. Each time step is evaluated in a quasi-steady way. Non-slip conditions at the stationary and rotating walls are applied. The region between the nearest measurement point to the point on the wall is linearly interpolated. The outer boundaries of the control volume covered by the measurement results and the integration tool are depicted in Fig. 6.2.0-1. The integration can be performed on surfaces of constant radii, constant axial or circumferential position. In addition, the integration tool allows to individually switch on and off single measurement points within the volume, which allows to track flow features and the associated flow quantities.
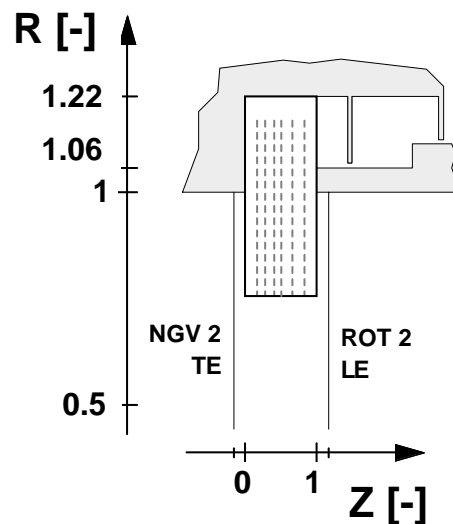
Fig. 6.2.0-1   Boundaries of the control volume

6.2.1   Time averaged (absolute frame)

The mass and momentum exchange due to the interaction flow of the main flow with the open inlet cavity is investigated using the control volume as given in Fig. 6.2.1-1 and the integration tool described above. In circumferential direction pitch-periodic condition was assumed. The boundary conditions on the inlet and exit axial plane Z=0 and Z=1 were set to the measurement values of the closest measurement plane. The wall corner points at Z=0 and Z=1 were set to zero velocity, full-filling the non-slip condition. The outer surface at R=1 represents the interface between main and cavity flow. The inner surface was chosen to R=0.91. At this radial location the area integration of constant radius

delivers a net radial mass flow of approximately 0. For R>0.91 this integration becomes positive, for R<0.91 negative. Therefore, R=0.91 is interpreted as a dividing surface: Below R=0.91 the negative radial migration of the main flow dominates, above R=0.91 the flow field is affected by sucking mass into the cavity.
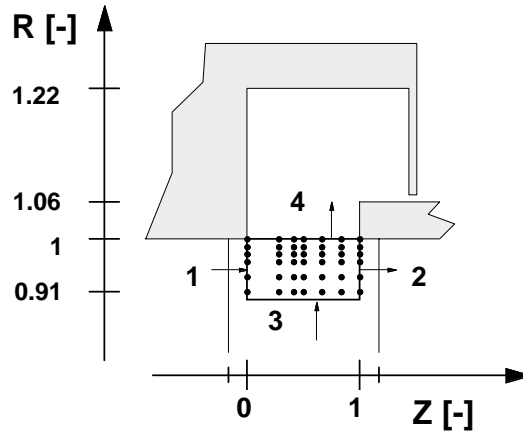
Fig. 6.2.1-1   Control volume for mass and momentum integration

The results of the integration are given in Tab. 6.2.1-2 representing the full annulus. Fluxes out of the control volume are counted positive and external forces on the control volume are calculated. In tangential direction the momentum flux is expressed as torque.

Considering first the sum of mass flows and fluxes in the last row of Tab. 6.2.1-2, continuity is preserved within 11g/s. The sum of the momentum fluxes is positive in radial and negative in axial direction. Sucking mass flow into the cavity reduces the axial momentum in the end wall region, since some of the incoming axial momentum is transformed into radial momentum. In tangential direction the sum is close to 0, since no external forces act in this direction. The components of the external force acting on the control volume are depicted in Fig. 6.2.1-3.

Surface i	$\dot{m}_i$ [g/s]	F_{ir} [N]	T_i [Nm]	F_{iz} [N]
1 (in)	606	0.5	-24.2	-17.1
2 (out)	-562	1.8	22.3	14.2
3 (in)	2	0.4	-0.2	-0.2
4 (out)	-35	0.4	1.8	0.6
sum	11	3.1	-0.3	-2.4

Tab. 6.2.1-2   Control volume integration according to Fig. 6.2.1-1: mass flow and momentum fluxes on the full annulus
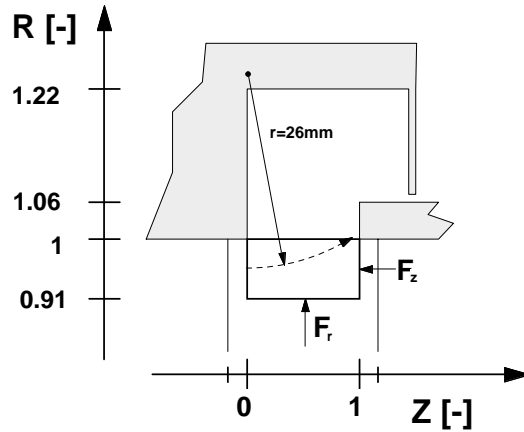
Fig. 6.2.1-3   External forces on control volume F_r, F_z; radius of average streamline curvature

6% of the main mass flow passes through the control volume. The assumption $\dot{m}_3 = 0$ is met to a good level. The net mass flow at surface 4 compares well to the leakage mass flow evaluated in chapter 5.2.1. Associated to the inflow into the cavity at surface 4 is the transport of a torque of 1.8Nm.

The local radial pressure gradient across this control volume is not sufficient to keep the flow on a constant radius. Streamlines from the stator pressure side corner enter the cavity. This effect arises from the presence of a sudden area increase due to the cavity and from the sucking of the leakage mass flow. The radial equilibrium of forces acting on a circular motion is

$$v_z \frac{\partial v_z}{\partial z} \sin\gamma + \frac{v_z^2}{r_z} \cos\gamma - \frac{v_\Theta^2}{r} = -\frac{1}{\rho}\frac{\partial p}{\partial r} + \frac{F_r}{\rho V}, \tag{6.6}$$

where r_z denotes the radius of the streamline in the meridian plane. The first term describes the radial acceleration along the streamline. The second term is the radial component of the centripetal acceleration due to the meridian curvature. The third term on the left hand side represents the centripetal acceleration directed radially inward due to the main swirling flow. These three terms are balanced by the radial pressure gradient and the radial external force. In this case, (6.6) can be simplified with the help of the experimentally based assumption that the pitch angle of the initial streamlines in surface 1 of Fig. 6.2.1-1 is zero which leads to

$$\frac{v_z^2}{r_z} - \frac{v_\Theta^2}{r} = -\frac{1}{\rho}\frac{\partial p}{\partial r} + \frac{F_r}{\rho V_{CV}}. \tag{6.7}$$

The unknown in this equation is r_z. All other terms can be derived out of the measurement volume. The second term on the left hand side is evaluated in taking the arithmetic average of all values within the control volume according to

$$\frac{v_\Theta^2}{r} = \overline{\frac{v_{\Theta ijk}^2}{r_{ijk}}}. \tag{6.8}$$

A representative radial pressure gradient is found in taking the pressure difference of each opposing pair of grid points, which lay on the surfaces 3 and 4. These local pressure differences are arithmetically averaged. The external radial force is taken from Tab. 6.2.1-2. An average v_z on the surface 1 can be given to 0.19 of shroud rim speed. From this approach a representative streamline with an average meridian radius of r_z=26mm is calculated. The streamline is included in Fig. 6.2.1-3 as dotted circular arc starting at mid radial height of surface 1 with an experimentally based pitch angle γ=0. The inflow of surface 1 connects well to the area around Z=0.8 of surface 4, where most of the inflow to the cavity happens (see also Fig. 6.1.1-5).

The axial component of the external force F_z is the result of a static pressure increase across the cavity. To verify this finding a pressure force integration was performed taking the measured static pressure at surfaces 1 and 2. The force calculated with the pressure difference becomes -2.6N, which compares well to the control volume integration. Across the cavity opening a positive axial pressure gradient is observed. The same procedure applied to the main flow region (R<0.92) results in a negative axial pressure gradient as expected.

Additional insight could be gained by observing the quantities associated to the in and outflows across surface 4, which are summarised in Tab. 6.2.1-4. As much as four times of the leakage mass flow enters the cavity and transports up to 5Nm of torque, 0.9N of radial momentum flux and 1.5N of axial momentum flux. The outflow of roughly three times the leakage mass flow conveys less momentum in all three components. However, the major contribution to the radial and axial momentum balance of the control volume are found in the surfaces 1 and 2.

Surface i	$\dot{m}_i$ [g/s]	F_{ir} [N]	T_i [Nm]	F_{iz} [N]
4 (in, v_r>0)	127	0.9	5.1	1.5
4 (out, v_r<0)	-92	-0.5	-3.3	-0.9
sum	35	0.4	1.8	0.6

Tab. 6.2.1-4   Mass and momentum fluxes across surface 4, absolute frame

The fluid particles, which pass the inflow area of surface 4 can be tracked upstream to the exit of the stator at Z=0. The same can be done with the outflow area, which can be connected to the inlet of the rotor at Z=1 (surface 2). The first (Z=0) is a flow area covering Θ=0 to Θ=-0.15 and R=0.92 to 1, where all radial velocity components are positive. The outflow area at Z=1 covers Θ=-0.15 to Θ=-0.35 and R=0.93 to 1 with the corresponding radial velocities being negative. The integrations of these specific areas are given in Tab. 6.2.1-5.

Surface i	$\dot{m}_i$ [g/s]	F_{ir} [N]	T_i [Nm]	F_{iz} [N]
1 ($v_r>0$)	125	0.7	5.2	4.1
2 ($v_r<0$)	-93	-0.4	-3.5	-2.2

Tab. 6.2.1-5   Mass and momentum fluxes: Inflow area surface 1, outflow area surface 2 in Fig. 6.2.1-3

The mass flows fit to the in and outflows found in surface 4 (Tab. 6.2.1-4). The torque difference between the surfaces 1 and 2 is caused by the difference between the in flow and the outflow regions of surface 1 and 2, only. From these results it can be concluded that streamlines of a rather small area on the pressure side corner of the stator enter the cavity, partially pass through the labyrinth and partially move back into the main flow.

6.2.2   Time averaged (relative frame)

The associated fluxes to the in and outflow generated by the rotor pressure field are discussed in this section. To do so, the surface integration of surface 4 in Fig. 6.2.1-1 was performed in the relative frame of reference. The radial velocity distribution of this surface is presented in Fig. 6.1.2-5. In comparison to Fig. 6.1.1-5, the results are restricted to four axial positions, which reduces the area covered by experimental results. The same boundary conditions as described in 6.2 were applied to the integration procedure. The integration results are shown in Tab. 6.2.2-1. The mass flow integration compares well to the results in Tab. 6.2.1-4, because the radial velocity components were adjusted to the five hole probe results as discussed in 6.1.2. The radial component of momentum fluxes is larger than in the stator relative flow field. The axial component of the momentum fluxes compares well to the results in the absolute frame of reference. The important result here is that the rotor in time average extracts torque from the cavity, since the sum of in and outflows is negative.

Surface i	$\dot{m}_i$ [g/s]	F_{ir} [N]	T_i [Nm]	F_{iz} [N]
4 (in, $v_r>0$)	148	1.6	1.1	1.4
4 (out, $v_r<0$)	-110	-0.6	-1.3	-0.9
sum	38	1.0	-0.2	0.5

Tab. 6.2.2-1   Mass and momentum fluxes across surface 4, rotor relative

6.2.3   Torque balance

Coming back to the torque being transported into and out of the cavity, the question is how much of this torque is lost within the cavity due to friction and how much passes the first seal of the labyrinth. For this reason the tangential momentum balance of the control volume given in Fig. 6.2.3-1 is investigated more closely at this point.
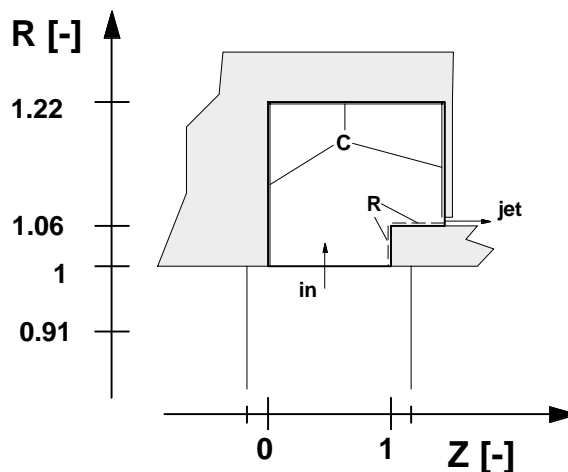
Fig. 6.2.3-1   Control volume for loss estimation

The torque balance can be written as

$$T_{in} + T_C + T_R = T_{jet}, \tag{6.9}$$

where the indices C and R denote the torque contribution generated by wall friction at the casing and rotor walls, respectively. This analytical ansatz of a torque balance follows a scheme presented in [19] and [31], which discuss the windage generation in labyrinth seals in terms of heat production and torque. The contribution T_{in} can be split into two parts, one generated by the sum of in and outflows of the stator (Tab. 6.2.1-4) and the other by the rotor interactions (Tab. 6.2.2-1). The exit condition of the leakage jet T_{jet} within the first gap is not known so far.

The angular momentum exerted by the walls onto the cavity fluid is a function

of the wall shear τ

$$T_{C,R} = \tau_{C,R} \cdot rA, \tag{6.10}$$

which can be expressed in terms of a reference dynamic head using the blade speed u as

$$\tau_{C,R} = c_{C,R} \cdot \frac{1}{2}\rho u^2. \tag{6.11}$$

The wall friction coefficients $c_{C,R}$ have to be evaluated empirically. The corresponding correlations are given in [19],

$$c_C = 0.063\left(\frac{v_{\Theta,cav}}{u}\right)^{1.87} Re_R^{-0.2} \tag{6.12}$$

$$c_R = 0.042\left(1 - \frac{v_{\Theta,cav}}{u}\right)^{1.35} Re_R^{-0.2} \tag{6.13}$$

with the Reynolds-number modified as

$$Re_R = \frac{\omega r_o (r_o - r_i)}{v}. \tag{6.14}$$

Note that the torque exchange with the cavity flow depends on the ratio of the swirl velocity of the cavity fluid and the rotational speed of the shroud. Applying (6.10) through (6.14) to the inlet cavity, where the velocity ratio was experimentally evaluated to 0.82, the torque exchanges are found: T_C=-1Nm and T_R=0.04Nm. The rotor shroud surface in Fig. 6.2.3-1 contributes much less angular momentum to the cavity flow than the casing walls, since the wetted surface is smaller as well as the relative velocity between the cavity fluid and the shroud.

Given the loss of torque due to wall friction and the torque transmitted across the interface the missing tangential velocity component of the leakage jet can be estimated as

$$v_{\Theta,jet} = \frac{(T_{in} + T_C + T_R)}{\dot{m}_l \cdot r_{jet}}. \tag{6.15}$$

Applying the leakage mass flow found in Tab. 5.2.1-2 and the results found in the previous sections, (6.15) results in an averaged tangential velocity of the leakage jet of 35% of shroud rim speed. Concerning the losses within the inlet cavity itself it can be concluded that they are of the order of 1Nm, which is equivalent to 2.7% stage losses.

$T_{in, stator}$ [Nm]	$T_{in, rotor}$ [Nm]	T_C [Nm]	T_R [Nm]	T_{jet} [Nm]
1.8	-0.24	-1.0	0.04	0.6

Tab. 6.2.3-2   Torque balance of the inlet cavity, Control volume Fig. 6.2.3-1

6.2.4   Unsteady fluxes

The same surface integration procedure as described in 6.2 is applied to the unsteady data set of surface 4. The integration is performed at each time step. The blade passing period is resolved with 106 samples. The results for radial mass flow, forces and torque are presented in Fig. 6.2.4-2. It is convenient for the discussion of the results to have the relative position of rotor and stator in mind. Therefore, two relative positions are depicted in the right part of Fig. 6.2.4-2, representing the positions of maximum (t/T=0.05) and minimum (t/T=0.55) mass flow into the cavity.

The lines of torque and mass flow lie on top of each other with minor differences of shape. Therefore, both parameters can be displayed in one diagram with two different ordinate axis. As torque and mass flow are coupled, both reach the minimum (t/T=0.55) and maximum (t/T=0.05) at the same instant of time. At the minimum net inflow, the amount of in and out fluxes (v_r>0, v_r<0) are at a minimum, too. The maximum net inflow goes along with the maximum amounts of involved fluxes. The amplitudes of the fluctuations around the time averaged values (Tab. 6.2.1-4) are given in Tab. 6.2.4-1.

Surface 4	$\dot{m}_i$ [g/s]	F_{ir} [N]	T_i [Nm]	F_{iz} [N]
in	±25	±0.45	±0.98	±0.2
out	±15	±0.13	±0.62	±0.2
sum	±16	±0.33	±0.63	±0.1

Tab. 6.2.4-1   Mass and momentum fluxes: Amplitudes

The radial component of the momentum flux reaches its minimum 15% of the blade period earlier than the mass flow and the torque. As can be derived from (6.7) the meridian curvature of the streamlines is inversely proportional to the radial external force acting on a control volume. Thus, a minimum in radial external force results in a larger radius of curvature. This in turn indicates that less streamlines are bent into the cavity. The time shift t/T=15% could be explained with inertia effects of the streamlines to change their curvature. The net axial component of the external force acting on this surface is constant in time, since the negative and positive parts fluctuate symmetrically.
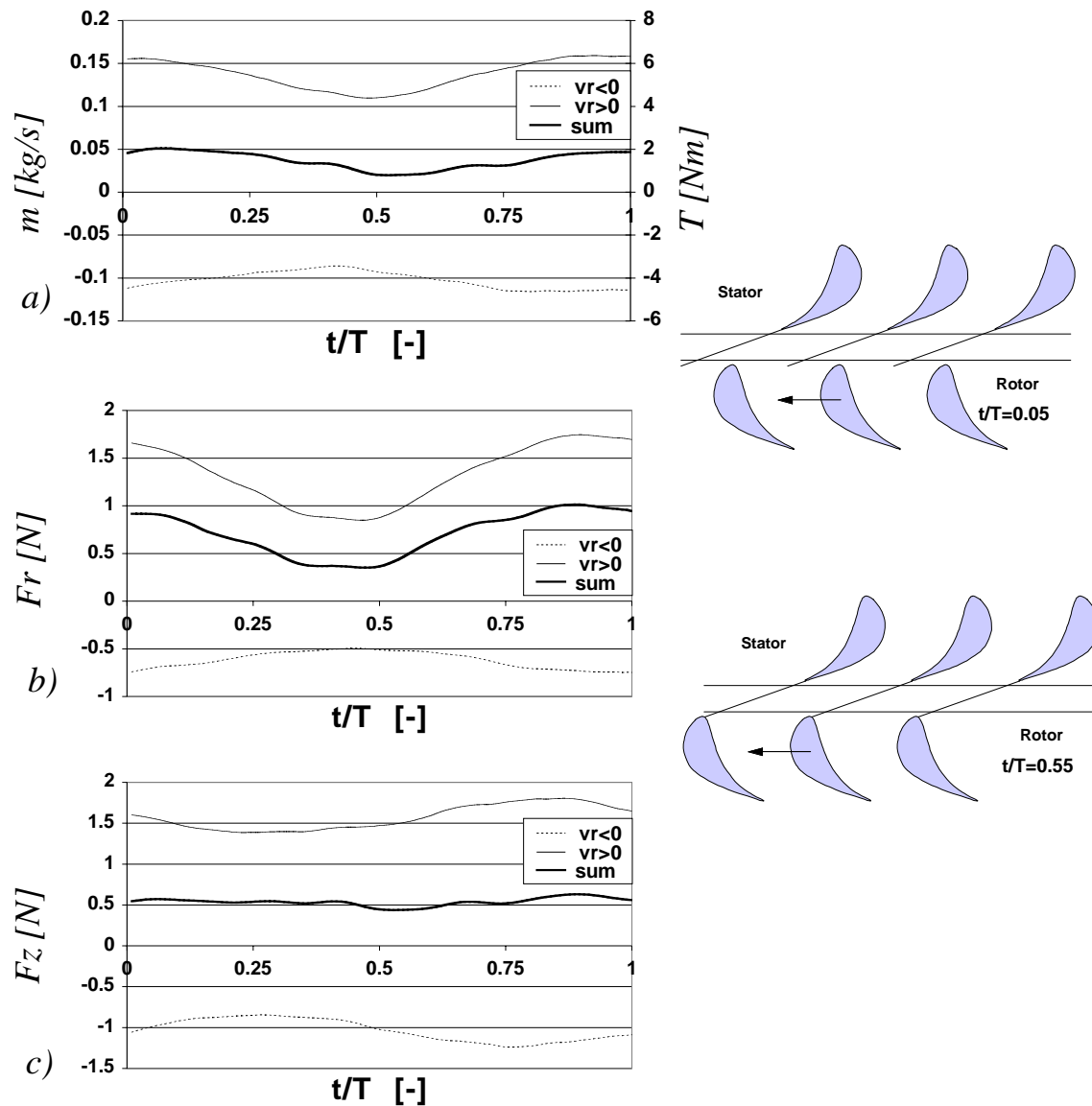
*Fig. 6.2.4-2   Unsteady fluxes across surface 4: a) mass flow, torque
                 b) radial momentum flux, c) axial momentum flux*

The fluctuations in mass flow, torque and momentum fluxes stem from the in-
teraction of the stator flow field and the rotor upstream effects. At t/T=0.05 the
mass and torque transport is at a maximum, since the inflow area of surface 4
on the pressure side of the stator wake coincides with the upstream effect of the
passage pressure side, e.g. shown in Fig. 6.1.2-4. The upstream sucking effect
on the suction side of the rotor passage enhances the outflow of the cavity. Vice
versa the upstream effect of the rotor passage diminishes the stator triggered in
and outflows at t/T=0.55.

6.2.5   Steady flow model

A steady 1D flow model is developed in this section, which describes the change of flow field due to the presence of an inlet cavity with the help of the control volume depicted in Fig. 6.2.5-1. The parameter to vary is the seal gap width g. The model is based on the measurement results of the 0.3% gap.

The flow is assumed to be steady and incompressible. Applying the mass conservation in axial direction and the momentum conservation in tangential direction allowing for the exchange of torque with the confining walls

$$v_{z2} = \frac{v_{z1}A_1 - v_{zjet}A_{jet}}{A_2} \text{ and} \tag{6.16}$$

$$v_{\Theta 2} = v_{\Theta 1}\frac{(v_z rA)_1}{(v_z rA)_2} - v_{\Theta jet}\frac{(v_z rA)_{jet}}{(v_z rA)_2} + \frac{T_C + T_R}{(\rho v_z rA)_2} \tag{6.17}$$

the velocity components of a representative inlet velocity triangle to the rotor tip region are derived (surface 2). Across the surface 3 in Fig. 6.2.5-1 the net fluxes of mass and momentum are neglected. The exit flow field of the stator tip region is available from measurements and a mass averaged velocity triangle is used based on the data given in Fig. 6.1.1-1. This results in the velocity components v_{z1} and $v_{\Theta 1}$. The leakage jet is modelled using the empirical correlation for the leakage mass flow given with (5.4). The circumferential component of the jet was found in 6.2.3.
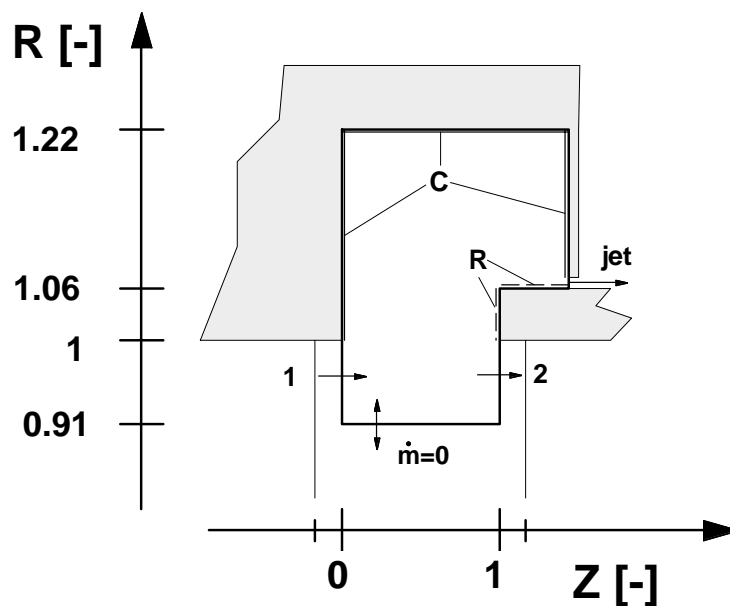
Fig. 6.2.5-1   Control volume for steady flow modelling

Since the exit flow field at surface 2 is known at one gap width the model can be verified in this point. For this purpose, the experimentally gained inlet and exit velocity triangles plus the velocity triangle derived from the model are given in Tab. 6.2.5-2. The relative angle into the rotor tip region (surface 2) is -25.7°, which is around 8° lower than at lower radii (surface 2, R=0.91 to 0.73). In addition the relative velocity is 27% lower than compared to lower span flow (R=0.91 to 0.73). For this 0.3% gap configuration the relative flow angle changes by -1.7° across the inlet cavity. The values found with the model compare well to the experimental results.

Surface i	α [°]	v [-]	β [°]	w [-]
1 exp. data	74.9	0.925	-24.0	0.264
2 exp. data	75.7	0.919	-25.7	0.252
2 model	75.6	0.918	-25.9	0.253
Δ_{21}	0.8	-0.006	-1.7	-0.012

Tab. 6.2.5-2   Comparison of velocity triangles of flow model and experimental results, 0.3% gap: surface 1 and 2

The change of incidence to the rotor can be calculated in dependency of the gap width. The underlaying assumptions are:

a) The variation of the gap width does not change the exit flow field of the stator at Z=0. The boundary conditions in surface 1 do not change.

b) The pressure ratio across the labyrinth is not affected by the gap variation but set up by the operation point of the turbine. The axial velocity component of the leakage jet is not affected by the gap variation

c) The torque exchange with the rotational and stationary walls T_C and T_R is assumed to be independent of the gap variation. The velocity ratio of cavity core flow and the rotor speed stays constant. This assumption is justified with the help of Fig. 6.1.1-2e.

In order to satisfy the boundary condition $\dot{m}_3 = 0$ while changing the gap width, the exit surface 2 is calculated as

$$A_2 = A_1 - \Delta A_{jet} \tag{6.18}$$

where the change of leakage area due to the gap variation is subtracted

$$\Delta A_{jet} = A_{jet} - A_{jet, 0.3\%}. \tag{6.19}$$

The tangential velocity component of the leakage jet can not be assumed to be

independent of the gap width. The tangential velocity component of the jet is calculated using the approach in 6.2.3. From Fig. 6.1.1-4 it is known that the gap width variation acts on the radial velocity component at the interface, reflecting the change of leakage mass flow with an linear increase of the radial velocity component. Here, it is assumed that the gap width variation acts homogeneously across the interface. With this assumption, the integration of the torque fluxes across the interface was redone for several offsets in radial velocity. It was found that the torque fluxes across the interface in Fig. 6.2.3-1 changed linearly with leakage mass flow for both, the rotor relative and stator relative, time averaged flow field. Therefore, the angular momentum fluxes were calculated, applying assumption b) (v_{zjet}=const.) given in the previous section:

$$T_{in,\ stator} = 1.8 \frac{A_{jet}}{A_{jet,\ 0.3\%}}, \tag{6.20}$$

$$T_{in,\ rotor} = -0.2 \frac{A_{jet}}{A_{jet,\ 0.3\%}}, \tag{6.21}$$

(see Tab. 6.2.1-4 and Tab. 6.2.2-1). Thus, equation (6.15) becomes part of the flow model.

The change of relative angle versus the change of gap width is plotted in Fig. 6.2.5-3, which can also be looked at as the change of incidence angle to the rotor. In addition, the diagram contains the circumferential velocity component of the leakage jet, as it is predicted with (6.15). Close to zero clearance the model approaches a singularity and the tangential velocity approaches infinity. For gaps larger than 1% the tangential velocity approaches the value of the swirl velocity of the cavity (82% of rotor speed). The trend of the angle variation is nearly linear within the plotted range. For the 1% gap case, the model predicts a change in relative angle of -5° against the stator exit flow field. With this steady 1D-model a tool is at hand to predict time-averaged incidence angles to the rotor inlet flow field caused by the sucking of the labyrinth seal.
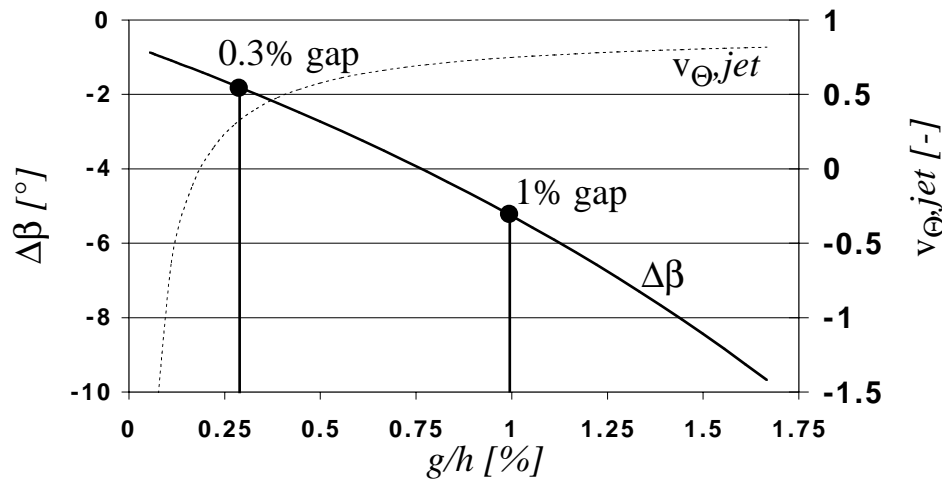
Fig. 6.2.5-3   Change of relative flow angle with effective gap width g

6.3 MODEL FLOW DESCRIPTIONS

6.3.1   System of toroidal vortices

As the experimental results show, at least two toroidal vortices are present within the inlet cavity. Both vortices swirl at a tangential velocity of 82% of the shroud rim speed around the annulus. This tangential velocity is influenced little by the gap width and depends on the operation point, i.e. the swirl of the main flow. The tangential velocity of the vortex fluid expresses the momentum balance of the inlet cavity. The change of operation point had little influence on the rotational speed of the toroidal vortex. The centre position and strength of both vortices depend on the gap width, which is schematically displayed in Fig. 6.3.1-1. The small triangles at the cavity bottom indicate the location of the high pressure region found with the wall pressure measurements. These points are interpreted as stagnation points of the in flow passing between and driving the two toroidal vortices. This flow consists of the inflow streamlines originating from the pressure side corner of the wake as well as of the boundary layer fluid being pushed into the cavity by the potential field of the rotor. Streamlines, representing the circumferentially averaged flow, are introduced in both cases. If the seal gap is opened a bigger portion of fluid flow transporting positive axial momentum is sucked into the labyrinth. Consequently, less axial momentum needs to be redirected into radial and upstream (negative) axial momentum. The second, downstream vortex gets smaller and weaker. The toroidal vortex within the interaction zone moves into the cavity and slightly downstream, since the diameter increases and the vorticity drops. This movement of the vortex centre is indicated with a open and filled circle.

0.3% gap   1% gap

a)   *b)*
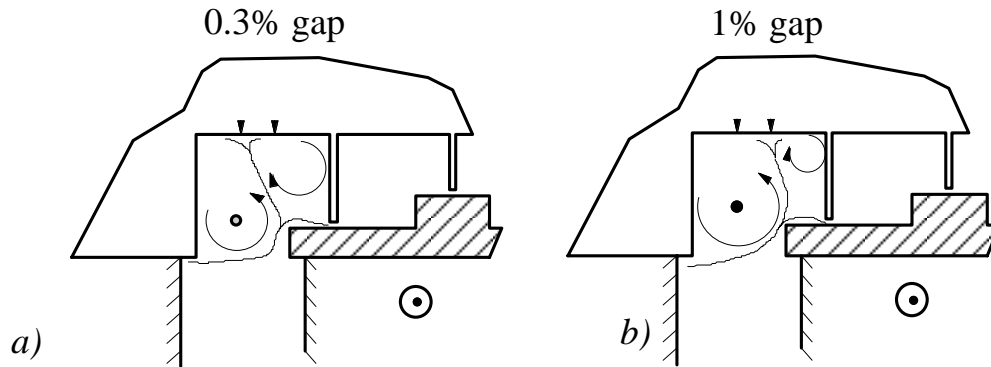
Fig. 6.3.1-1   Proposed schematic of the vortex system within the inlet cavity

6.3.2   Vortex relative frame of reference

In order to better understand the effects on the fluid movements a flow relative system is helpful. A vortex relative coordinate system is proposed as described in Fig.6.3.2-1. It rotates at the average tangential velocity of the toroidal vortex. By moving with the vortex in the swirling direction rotor and stator events pass at two different relative velocities. At design point the velocities are split into 17% of blade passing frequency for the rotor relative and 82% for the stator relative frequency according to the tangential velocity in the cavity.

Absolute System   Vortex

U rotor

U vortex

Vortex Relative System   Vortex relative

U rel rotor

U rel stator

U rotor
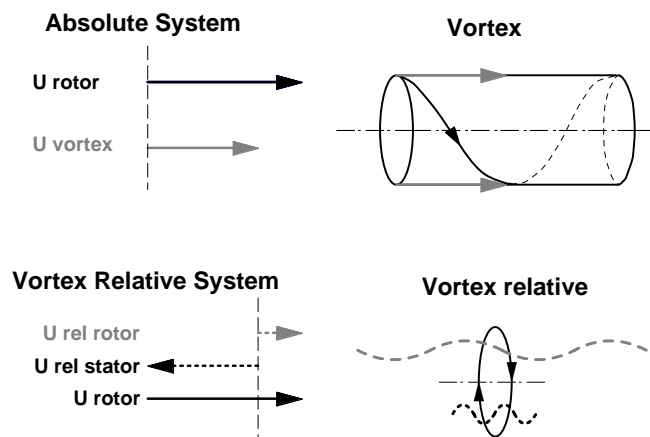
Fig. 6.3.2-1   Vortex relative system

6.3.3   Interaction zone and driving mechanisms

The flow field of the inlet cavity and the interaction zone is dominated by a three-dimensional, unsteady static pressure field. Five independent sources of pressure fields are present:

1) Stator pressure field

2) Rotor pressure field

3) Upstream effect of the rotor passage (suction and pressure side)

4) Cavity recess (step in and out)

5) Swirling flow (radial pressure gradient)

The periodic unsteadiness stems from the relative movement of the rotor pressure field. Due to the interference of the stator and rotor pressure field, the kinematic flow parameters, e.g. flow angles, velocity components, mass flows, experience high and low amplitudes, which depend on space and time.

The kinematic boundary condition to the flow area is set up by the stator exit flow containing wakes, boundary layers and secondary flow structures. This results in specific areas of inflow and outflow for the cavity flow. Close to the exit of the flow area the kinematic effects are shaped by the radial pumping effect of the rotor leading edge alternating with the open rotor passage.

The cavity flow is dominated by two toroidal vortices. The vortices move at an average tangential velocity of 82% of the blade tip speed. The reason for this level of velocity is found in the angular momentum balance of the involved fluxes and friction forces. The stator flow field adds momentum to and the rotor interaction subtracts momentum from the cavity flow. The centre vortex close to the interaction zone undergoes stretching and tilting in space and time caused by different drivers of the cavity flow. They are summarized in Tab.6.3.3-1.

	Stator	Rotor
Tangential Momentum	In flow	Non-slip condition
		Potential field
Tangential Vorticity	In flow	Radial pumping
	Axial velocity shear profile	
Stretching	Potential field	Potential fIeld

Tab. 6.3.3-1   Identified drivers of the cavity flow

A sketch of the flow drivers is given in Fig.6.3.3-2. The inflow and outflow regions are boundary conditions set by the exit flow field of the stator. The high potential fluid originating from the stator pressure side corner has enough kinetic energy to penetrate into the cavity. Radial equilibrium is not maintained in this area and the fluid follows a tangential direction, feeding tangential momentum to the cavity fluid. Partially, the incoming fluid is sucked directly into

the labyrinth gap, partially it is deviated upstream close to the cavity floor, thus contributing to the rotational movement of the toroidal vortex. The area covered by the in flow region is 5.7 times larger than the average gap area.

The outflow contains cavity fluid of low total pressure, low tangential momentum and negative incidence to the rotor tip profile section. This fluid affects the rotor passage flow field in an adverse way by doing less work on the rotor blades. The area covered by the outflow region is 5 times larger than the average gap area of the labyrinth.
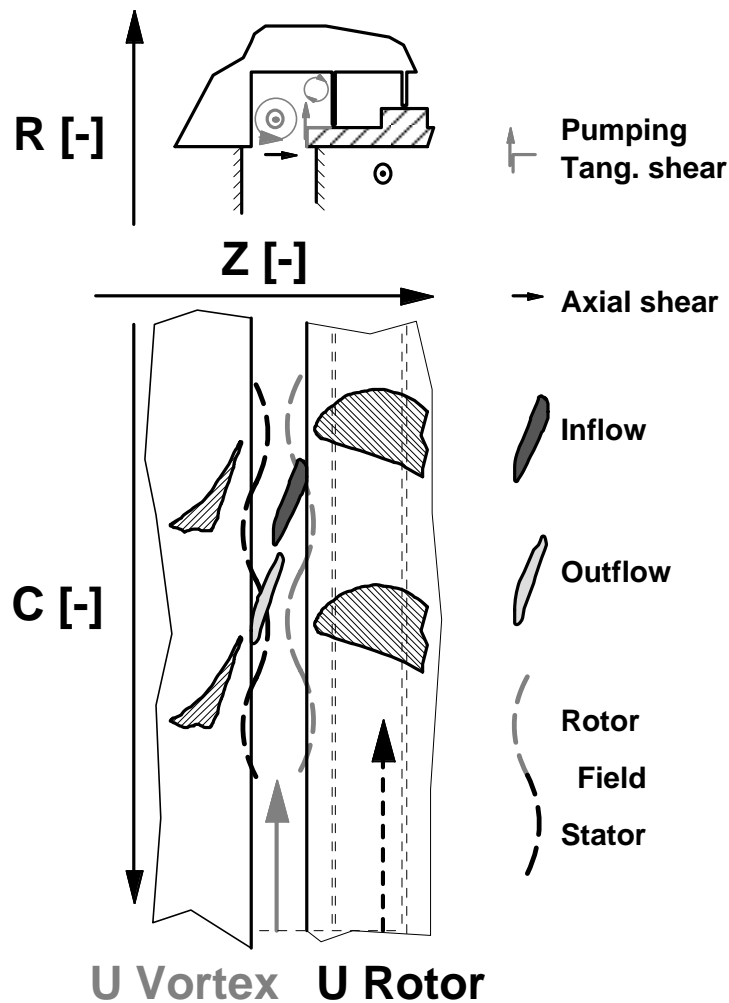

Fig. 6.3.3-2   Flow model: Side and above view

6.4 DESIGN CONSIDERATIONS

The loss generated within the inlet cavity itself is of the order of 2.7% of the stage losses. This relatively low number does not promise large improvements for the cavity flow itself. However, looking at the integrated system of the open cavity and the upstream and downstream blade rows, some potential of improvement lies in the adoption of the flow understanding to the design procedures.

Today's turbine design process is based on meridian cut (S2) and blade-to-blade (S1) calculations. Quasi-three-dimensional and three-dimensional design tools have been introduced to the design cycle in the recent decade with increased numerical power [22]. These tools often use mixing plane approaches between the blade rows, which suppresses the exchange of unsteady information from one blade row to the next. True three-dimensional unsteady calculations are still not applicable to the daily design routine due to its time consuming efforts. In future, the design process might be based on three-dimensional, unsteady calculations fully modelling multistage and small scale effects.

Concerning the inlet cavity, two sources of flow non-uniformity in the end wall region were identified:

1) The exit flow field of the stator including one distinct inflow jet and one distinct outflow region per blade pitch. The inflow jet is set up in the pressure side corner of the passage. The outflow happens on the suction side of the stator wake.

2) The upstream effect of the rotor passage. On the suction side of the rotor passage, cavity fluid is sucked into the passage. On the pressure side of the passage in conjunction with the stagnating effect of the leading edge fluid particles are pushed into the cavity.

The in and outflows set up by the stator are degrading the performance in two ways: Firstly, the incorporated exchange mass flows induce additional losses via enhanced friction and mixing in the cavity (2.7% stage loss). Secondly, the evolving unsteady effects on the rotor passage and its secondary flow development are generating additional loss there. From that point of view the design consideration given by Dawes in [9] concerning the shroud flow re-entry is applicable: minimise the non-uniformity, minimise the associated losses.

On the other hand, beneficial multistage effects might be initiated in the non-uniform cavity flow. These effects evolve from multistage interactions, e.g. vortex interaction or wake interaction. The design for multistage effects is difficult, since their isolation and quantification is complex in view of the strong

interdependency of all parameters. For the stator induced non-uniformities it is the author's believe that they are degrading the rotor passage flow due to the unsteady perturbation of the secondary flow development more than they might contribute to a positive multistage effect. For the rotor induced non-uniformity this might not be true, since they happen in the rotor relative frame of reference and might be used to generate a desirable secondary flow field in the rotor passage, which in turn would contribute to a beneficial multistage effect, e.g. vortex interaction in a downstream blade row.

From these considerations first some design modifications are presented, which have the aim to reduce the stator induced non-uniformities. Then a design idea is presented, which is meant to act on the secondary flow development of the rotor by controlling the inlet end wall flow.

In Fig. 6.4-1 a meridian cut of the inlet cavity is drawn. The lip on the stator side of the cavity is designed to reduce the circumferential wake as found in Fig. 6.1.1-2 and to turn the toroidal vortex into axial direction. The static pressure gradients originating from the trailing edge and acting on the interaction zone are reduced due to the potential field decay. The axial distance between this lip and the shroud leading edge was kept constant. The roundness of the shroud leading edge would reduce the effective cross sectional area by the protrusion of the outer part of the shroud modification. Thus the amount of penetrating flow would be reduced, which in turn would reduce the tangential velocity of the cavity fluid contributing to the torque balance. This is beneficial for the wall friction losses as described in [31] as well as for the mixing losses. Making the cavity corners round at the casing, would reduce the wetted area and therefore the wall friction in circumferential direction.
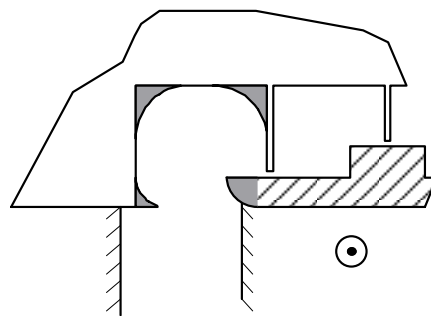
Fig. 6.4-1   Design changes of the cavity: reduce stator non-uniformities

Non-axisymmetric endwall contouring in the stator passage is a promising tool to reduce secondary losses as reported in [21]. This approach has the potential to reduce the inflow and outflow due to the end wall curvature. Applied to the inlet cavity would mean that the end wall on the pressure side would have to be convex. The induced static pressure drop would provide the fluid in the pres-

sure side corner with additional kinetic energy. Thus the fluid particles tend less to penetrate the cavity.

The same target can be followed with an additional approach. Introducing a local lean to the stator trailing edge causes a local load increase as depicted in Fig. 6.4-2. The pressure side corner fluid then would experience an additional radial force due to the imposed local static pressure gradient. A larger radius of streamline curvature is resulting from this, see (6.7).
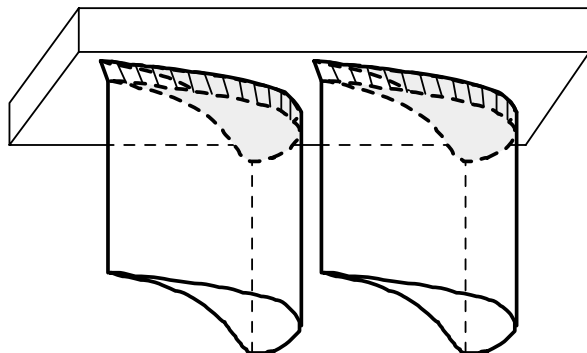
Fig. 6.4-2   Design changes: stator passage

With the shroud leading edge design the secondary flow formation within the rotor passage can be influenced. In Fig. 6.4-3 two leading edge modifications are proposed. The first, Fig. 6.4-3a, is designed to reduce the interaction flow across the cavity-to-main flow interface. One expected effect would be that the radial velocity distribution as presented in Fig. 6.1.2-5 is more homogenous and the peak radial velocities are reduced. The working principal is depicted in Fig. 6.4-4. On the pressure side of the rotor passage the shroud leading edge is positioned at a higher radius than on the suction side. The effect of this is that streamlines of a lower curvature are entering on the pressure side. Less fluid is pushed into the cavity at this point. On the suction side the cavity fluid has to reach lower radii in order to being sucked into the rotor passage. In terms of streamline curvature, more fluid is pushed into the cavity at the suction side than on the pressure side.

The second modification Fig. 6.4-3b is designed to do the opposite of the above described modification, i.e. it is the goal to enhance the interaction flow such that the inlet stream wise vorticity distribution as found in Fig. 6.1.2-6 would show a higher value at the suction side to the rotor tip inlet. Consequently, the rotor passage vortex would increase its strength and change position. At first glance, this might be not a beneficial effect. But considering a designer's need to increase the rotor tip passage vortex in order to compensate incoming or downstream vorticity of the opposite sign (vortex interaction), this might be the correct approach.
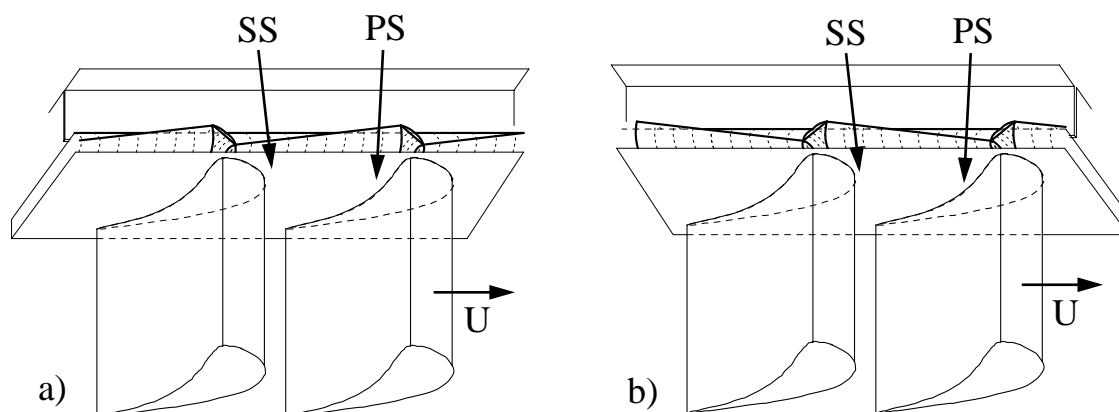
Fig. 6.4-3   *Shroud leading edge modification: a) reducing upstream inter-*
                  action, b) enhancing upstream interaction
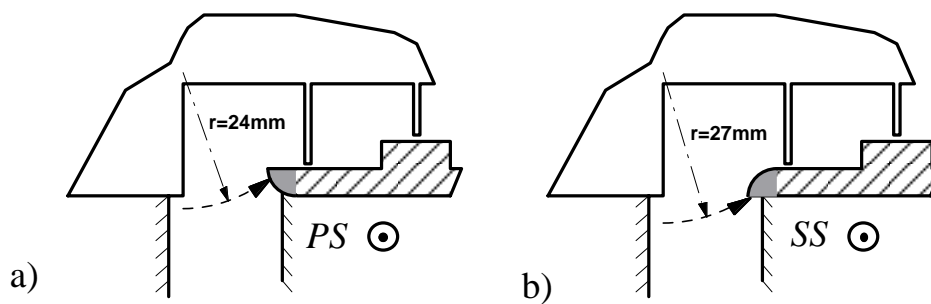
Fig. 6.4-4   *Shroud leading edge modification: Leading edge position ad-*
                  justed to streamline curvature, a) pressure side, b) suction side

7   THE EXIT CAVITY

7.1   EXPERIMENTAL RESULTS

7.1.1   Steady pitch-wise averaged results

In order to set up the boundary conditions of the exit cavity flow field some wall pressure measurements are presented first. Within the interaction zone of labyrinth exit cavities the main flow and the leakage flow meet each other. These interactions depend on the characteristics both streams have adopted until the intersection point. Therefore, the initial condition of the main flow at the corresponding end wall region is discussed briefly, before the downstream evolution of the flow field is presented. The initial leakage jet conditions are described in detail in chapter 5.1.2.

Wall pressure

The circumferentially averaged casing wall pressures within the exit cavities and downstream of the second rotor are presented in Fig. 7.1.1-1 for the datum case and the 1% gap case. The axial coordinate is made non-dimensional with the axial cavity gap width, such that Z=1 denotes the downstream end of the cavity and Z=0 the shroud trailing edge. The gray dashed lines mark the positions of the five hole probe traverses presented later in this chapter.

The casing pressure of the exit cavity of rotor 1 shows maximum values close to the cavity corners. At Z=0, the shroud trailing edge position, a local minimum is present. The average difference between the two gap cases is ΔCpw=0.009. The wall pressure of the second rotor exit cavity shows a different pattern for the two gap cases. The datum case is characterised with a mostly constant pressure, which exhibits some variation close to the downstream corner. The pressure for the 1% gap case is in average ΔCpw=0.006 higher than in the datum case. In addition it exhibits an axial gradient which in this case indicates an acceleration of the fluid in upstream direction. Downstream of the cavity lip a recirculation zone with subsequent attachment line at Z=1.5 is detected. The change of leakage mass flow does not alter the location of attachment within the axial resolution of this experiment. Further downstream the wall pressure stays constant.
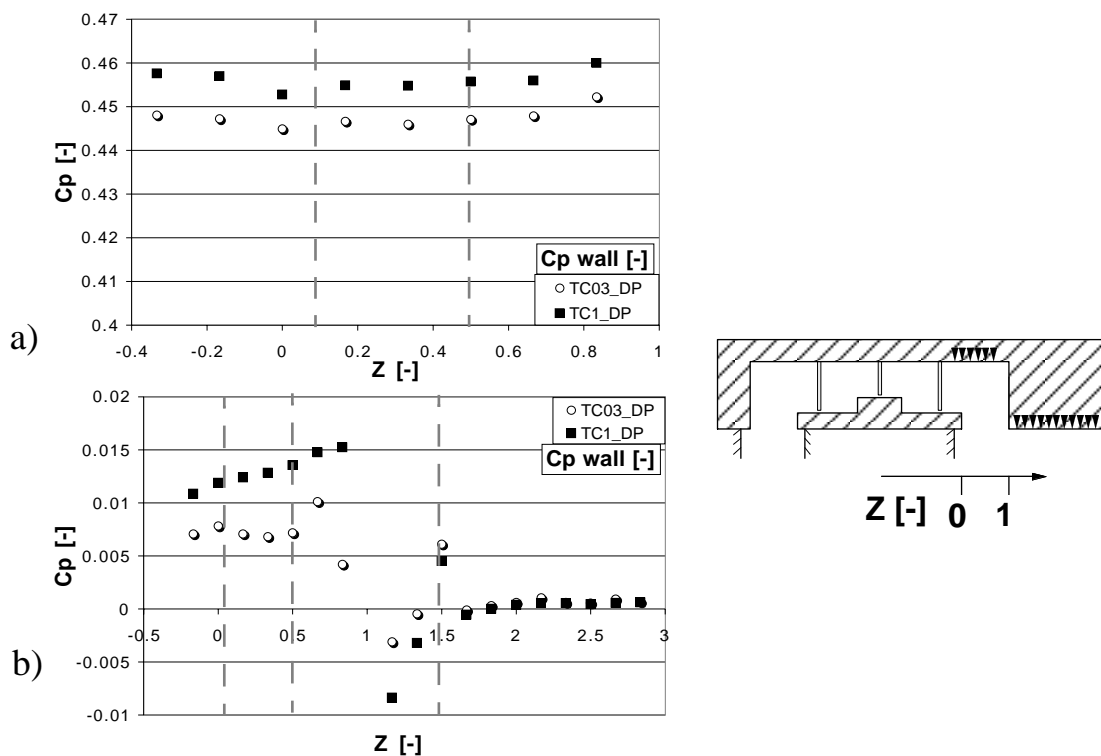
Fig. 7.1.1-1 *Pitch-averaged wall pressure in exit cavities: a) rotor 1, b) rotor 2 and downstream of cavity*

Main flow at rotor exit

The measurement results presented in this section were taken with an L-shaped five hole probe, allowing to traverse the probe tip close to the rotor trailing edge. The flow velocities are made dimensionless with the local rotational speed of the rotor. The boundary layer of the first rotor exit flow field can be observed in the total pressure as well as in the axial velocity component of Fig. 7.1.1-2. The same parameters (p^o and v_z) in the exit of the second rotor show changed profiles with a maximum around R=0.93 and a minimum around R=0.8, which indicates the presence of additional secondary flow features. The static pressure in the exit of the first rotor is a straight line. Whereas downstream of the second rotor C_p shows a positive radial pressure gradient from R=0.75 to R=0.95.

The radial gradient in tangential velocity component confirms the load distribution of the stages having a higher load at the hub. Close to the tip radius a local minimum in tangential velocity is registered with a slight increase in the last two points. The same region of the radial velocity profile shows a sudden increase toward the tip. The flow within R=0.95 and R=1 is affected and deflected by the corner of the shroud trailing edge similar to a backward facing step. This effect is consistently observed in both rotor exit flow fields.

exit rotor 1   exit rotor 2

a)   *b)*
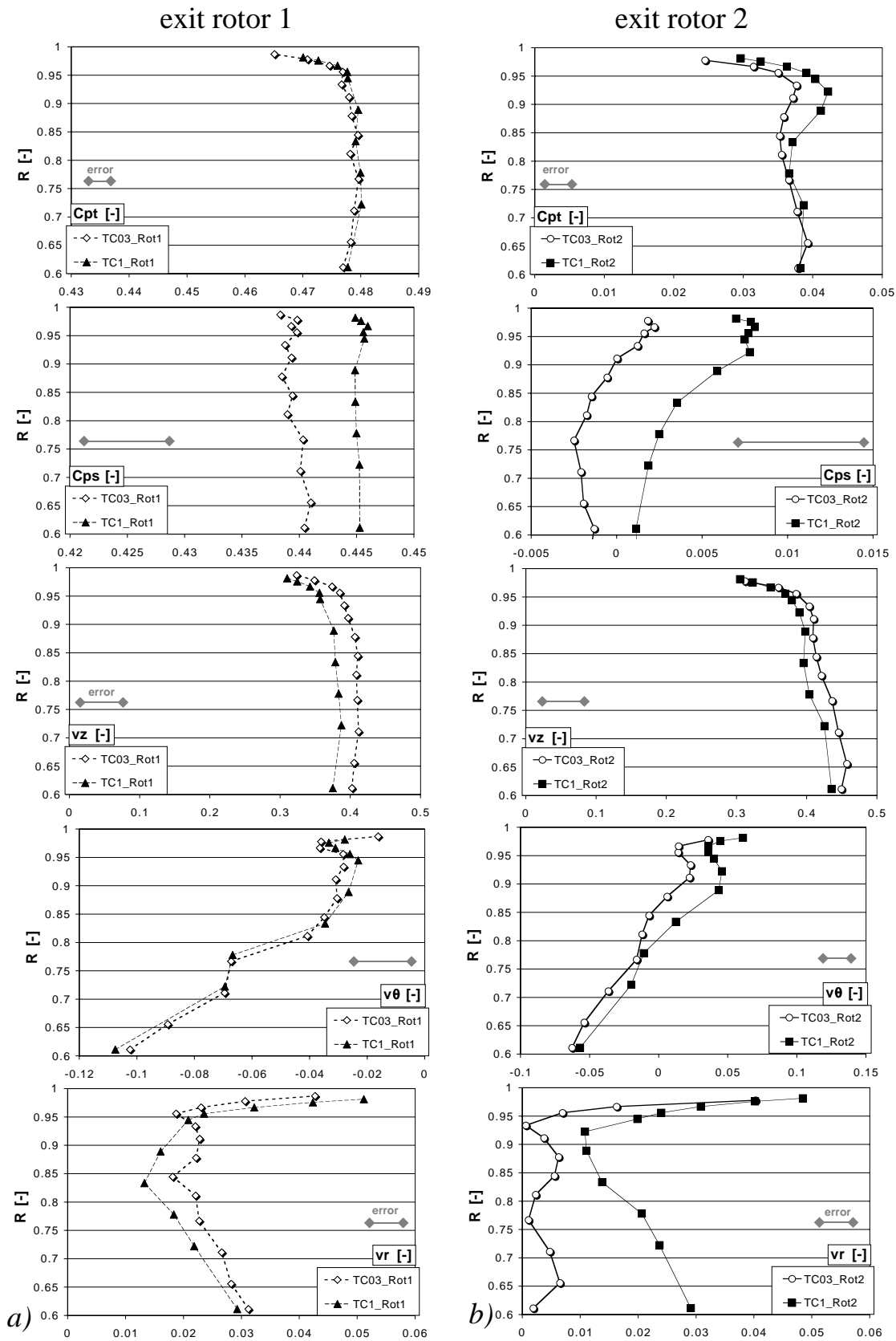
*Fig. 7.1.1-2   Pitch-wise averaged data of rotor exit flow field, Z=0.1: a) first
stage, b) second stage*

Mid gap flow field

The results discussed in this section are pitch-wise mass averaged data taken with a five hole probe. In Fig. 7.1.1-3 the results of the 0.3% gap case (TC03) are compared with the 1% gap case (TC1). The left column presents the first rotor exit flow field in the mid blade gap axial position. The right column is dedicated to the second rotor exit flow field at the same downstream position of the rotor trailing edge. Comparing first and second rotor exit flow field in addition, allows to discuss the upstream influence of the potential field of a subsequent stator. The error bands are given for each quantity as a gray band. The error band of the velocity components are particularly sensitive to the flow angle. Therefore, several error bands are given for the axial and circumferential velocity components, which apply to the neighboring range of radii. The error bands of total and static pressure and of the radial velocity component apply to the entire diagram.

Opening the gap increases the total pressure within the cavity (R>1.1) in Fig. 7.1.1-3a1 and a2. The big clearance induces distinct jet profiles for radii ranging from R=1 to R=1.1 downstream of both rotors. At R=1 a total pressure wake is present separating the main flow field from the jet flow. The main flow field downstream of rotor1 is not affected by the clearance variation. However, at the exit of rotor2 it is. The 1% gap case shows a locally increased total pressure in the end wall region. A stronger secondary flow field exits the second rotor, which is caused by the rotor 1 labyrinth flow. Only a very weak jet is present for the datum case at the exit of rotor 2. The measurements within the exit cavity of rotor1 for the 0.3% gap turned out to be very difficult due to the stagnating character of the fluid in combination with the upstream effect of the stator potential field. The latter induces strong circumferential yaw and pitch angle variations such that the probe calibration was not covering the flow angle range.

The static pressure profiles presented in Fig. 7.1.1-3b show the same trend in the exit of rotor 1 and 2, when the seal gap is increased. The static pressure within the cavity is increased as well as the radial static pressure gradient in the end wall region (R=0.9). The effective pressure drop across the labyrinth is decreased about 1% by opening the gap, accounting for the pressure drop within the inlet cavity due to stronger sucking. Note that the last points at R=1.22 are circumferentially averaged wall pressure measurements taken at the same axial location as the five hole probe traverse. The difference within the second rotor exit cavity is small, whereas for the first rotor exit cavity the difference is just within the error band of the five hole probe measurements. For the radial pressure gradient within the cavity two trends are observed. The rotor 2 exit flow field shows increasing static pressure with increasing R (R>1). In the exit cav-

ity of rotor 1 this gradient (R>1) changes the sign leading to lower static pressures close to the cavity floor.

The most obvious difference in the axial velocity profiles (Fig. 7.1.1-3c) is found in the jet region, where the bigger gap induces a local maximum. With the 0.3% gap the axial velocity profile is similar to that of a simple driven cavity, which comprises back flow close to the cavity floor and a velocity gradient from the cavity to the main flow driving the cavity by viscous shear. The characteristic flow feature in such a cavity is a toroidal vortex. Opening the gap adds a driver to the cavity. The velocity profile encounters a wake at the same position (R=1) as the total pressure distribution. In the exit of rotor 2 both axial velocity profiles fall onto each other around R=1.1, but the profile of the 1% gap case slightly out passes the other close to the cavity floor with v_z=-0.1 versus v_z=-0.07. The toroidal vortex is spinning slightly faster in the 1% gap case. Comparing now the second rotor to the first rotor exit (1% gap) the maximum velocity close to the cavity floor is v_z=-0.12, ΔR=0.04 further away from the cavity floor. This indicates a higher rotational speed of the vortical flow in the first rotor exit cavity due to the higher leakage mass flow and a changed interaction behaviour due to the presence of the leading edge potential field of the stator.

The total pressure increase in the cavities due to the opening of the gap is found again in the tangential velocity level in Fig. 7.1.1-3d. The leakage jet drives the tangential movement of the toroidal vortex and the cavity flow. The velocity gradient across the interaction zone is continuous and no wake-like structure is present. The higher, positive tangential velocity of the jet leads to negative incidence at the following stator blade row.

Finally, the radial velocity component is discussed (Fig. 7.1.1-3e). The jet core, defined as the point of maximum total pressure and axial velocity (R=1.04), is found to have zero radial velocity in the 1% gap case. Fluid at lower radii (1<R<1.04) is moving out of the cavity. The stream lines of the upper half of the jet are moving into the cavity at this axial position. In circumferential average the jet separates the main flow from the cavity flow, i.e. the toroidal vortex. The closed gap flow field shows no negative radial velocity components at this axial location and no separating effect of the leakage jet can be reported. However, a spike of higher positive radial velocity just below the tip radius indicates some inflow to the cavity from the main flow region.
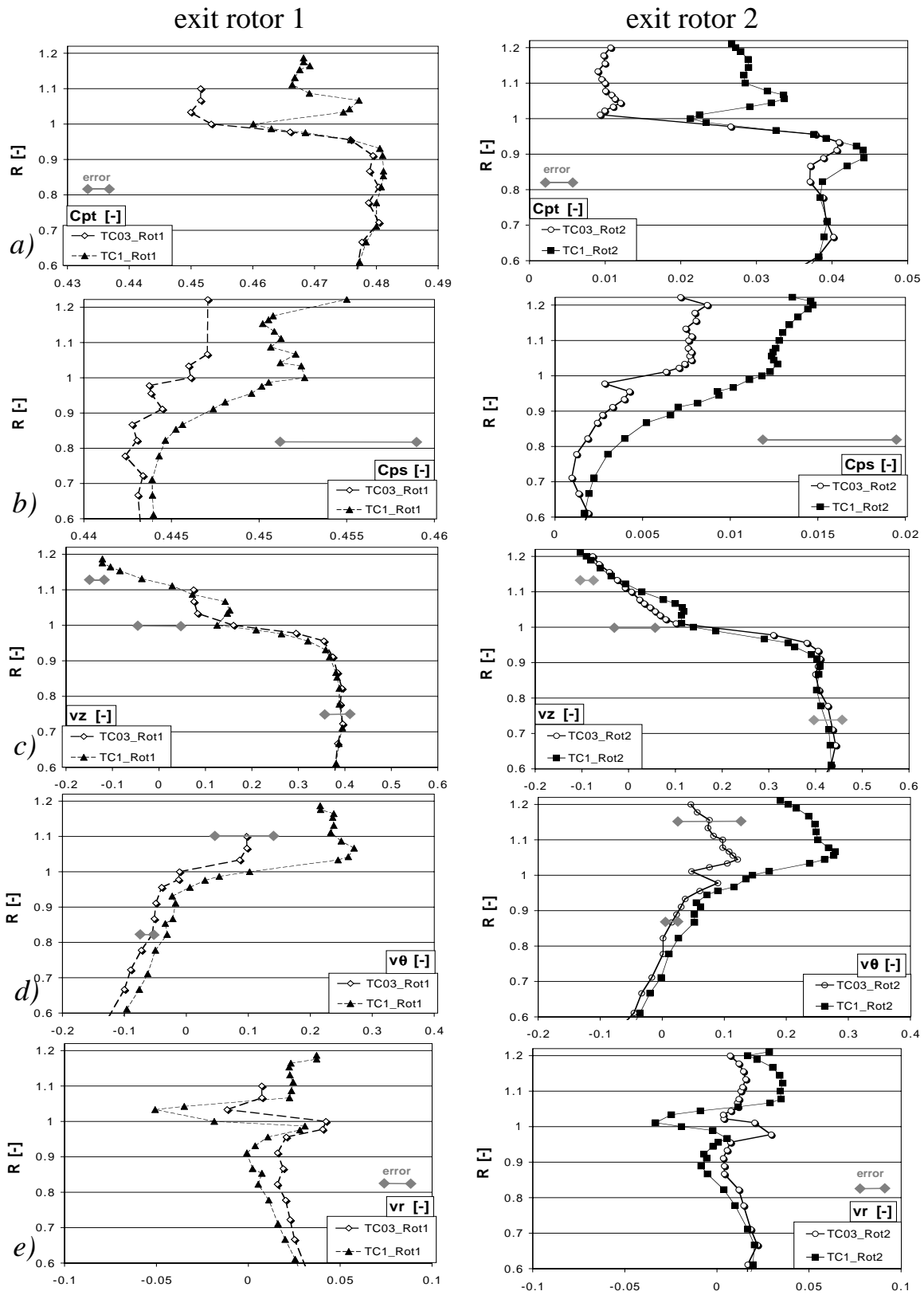
Fig. 7.1.1-3   Pitch-wise averaged data of rotor exit flow field, Z=0.5
a) C_{po}, b) C_p, c) V_z, d) V_Θ, e) V_r

Downstream of the exit cavity

The flow field downstream of the second rotor exit cavity was measured at a location of Z=1.5, which is at a distance of 50% axial cavity gap width downstream of the cavity exit lip. This position coincides with the attachment line found in 7.1.1-1. The general secondary flow distribution in both gap cases persist across the cavity. This is found in comparing the total pressure distribution in 7.1.1-4 at Z=1.5 with 7.1.1-2, which was taken at Z=0.1. However, the local maximum is pushed from R=0.92 to R=0.88 in the 1% gap case. The leakage mass flow re-entering into the main flow pushes the main flow away from the casing wall. This effect should be smaller in the datum case, since less leakage mass flow is involved. The measurement results indeed indicate a smaller radial shift from R=0.93 to R=0.92. The same effect of redistributing the end wall flow field is found in the profile of the axial velocity component. The static pressure distribution shows a local minimum with both gap widths at R=0.96. The circumferential velocity component is increased near the casing wall due to the opening of the gap. The incidence to the following blade row at the end wall region depends on the leakage jet characteristic. At the location of an attachment line the streamlines point to the wall in the surrounding flow field, which is observed in the radial velocity distribution. For radii higher than R=0.95 the radial velocity profiles of both gap cases differ slightly. The remnants of the leakage jet may be allocated at R=0.98. A definite allocation is not possible since the layer thickness of the corresponding leakage mass flow covers less than $\Delta R=0.01$.

Velocity triangles

From the velocity profiles given in the above sections, the circumferentially mass averaged velocity triangles are deduced for the main flow and the labyrinth leakage jet. The second rotor exit flow is first discussed. Then the first rotor downstream flow field is compared against the second rotor.

Second Rotor Exit Cavity

The velocity triangles as well as the corresponding radial and axial locations within the second rotor exit cavity are presented in Fig. 7.1.1-6. Let us consider first the main flow velocity triangles. The changes of the main flow vectors from station to station are small. The numerical values are given in Tab. 7.1.1-5. Concerning the axial velocity component, the datum case exhibits a drop and an increase over the three stations of measurement ending with a 2.6% higher velocity. In the case of the 1% gap the axial velocity increases in all stations until a 4.6% higher value at the last station. The tangential velocity components experience a similar development for both gap cases. Over the three axial sta-

tions the values first increase by 1% and then drop again by around 1% of reference velocity.
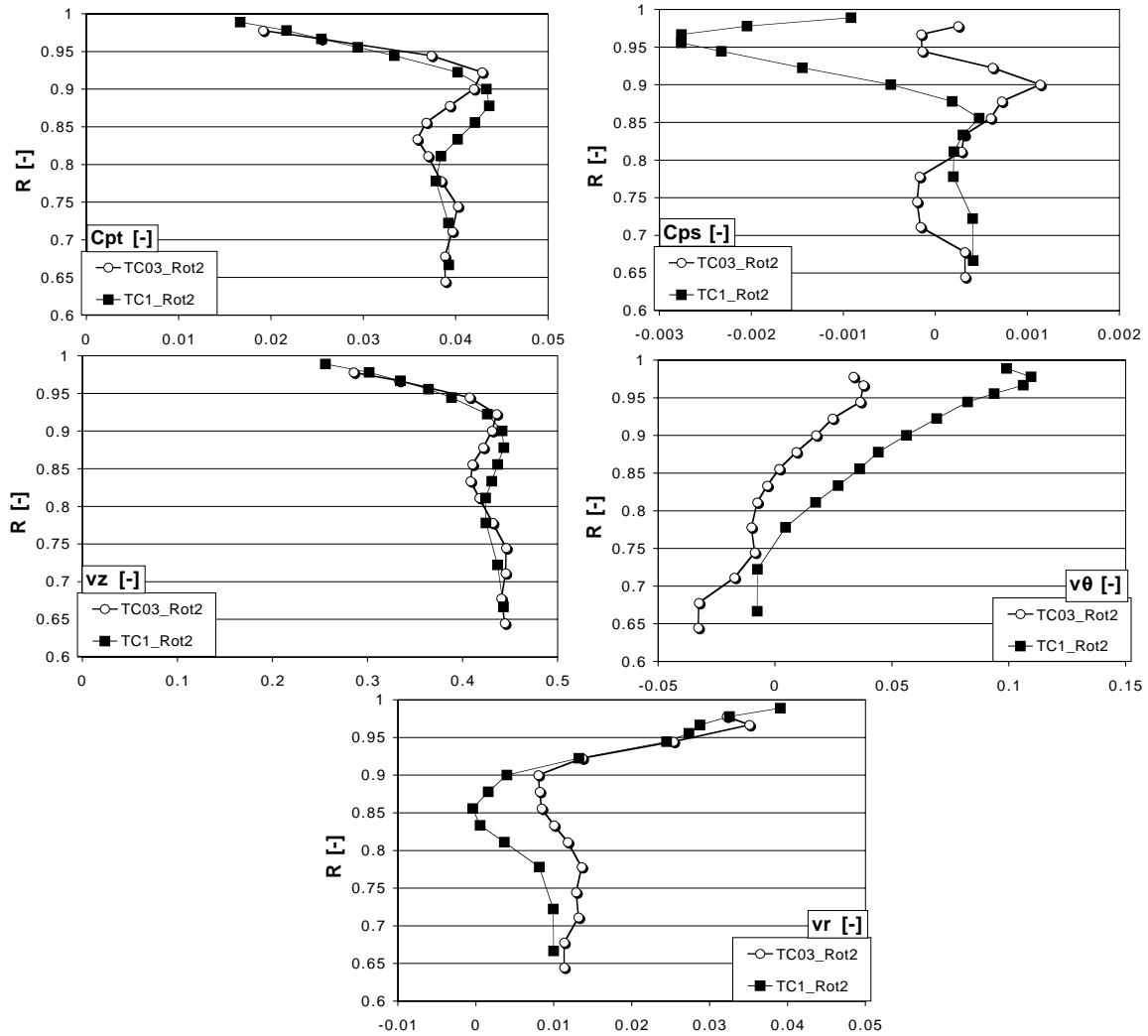
Fig. 7.1.1-4   Exit cavities Z=1.5: pitch-wise mass averaged results, DP, 0.3% gap, 1% gap

	0.3% gap		1% gap	
Z	V_z	V_Θ	V_z	V_Θ
0.1	41.0	2.2	39.8	4.3
0.5	40.5	3.7	40.9	5.2
1.5	43.6	2.5	44.4	4.4

Tab. 7.1.1-5   Components of main flow velocity triangles, second rotor exit,% of local rotor speed

Consider now the leakage jet vectors. An obvious finding is the under-turning of the jet in the absolute frame of reference leading to a miss match in flow direction with the main flow vectors. The leakage jet loses kinetic energy from Z=0.1 to Z=0.5, which reduces to 58% for the datum case and to 66% for the 1% gap case from the initial value. In both gap cases the axial component of velocity diminishes stronger than the tangential component resulting in a steeper flow angle at Z=0.5. Concerning the relative frame of reference, the behaviour of both jets shows a qualitative difference. The weak jet's initial over-turning at Z=0.1 is enhanced at Z=0.5. On the contrary, the stronger jet enters the exit cavity with an under-turning characteristic which is changed into an over-turning at Z=0.5. The leakage jet faces the exit step of the cavity, which causes two effects: the axial velocity component of the jet reduces while it is deflected into tangential and radial direction. The radial deflection to lower radii of the leakage jet starts at an earlier axial position for the datum case jet than for the stronger jet.

Convecting from Z=0.5 to Z=1.5 the leakage jets leave the exit cavity, pass the exit lip and enters back into the main flow. The penetration depth depends on the radial momentum, which the jet has at the point of re-entry. From the radial positions depicted in Fig. 7.1.1-6 it can be concluded that the stronger jet penetrates deeper into the main flow field than the datum case jet. At Z=1.5 the stronger jet exhibits a negative incidence of 12° and the weak jet causes an incidence angle of 3° in comparison to the main flow. At the leading edge position of a fictitious blade row, at Z=1.17, the incidence angle might be even higher in addition to be expected at a lower radius than at Z=1.5 due to the presence of the recirculation zone downstream of the exit corner.

First Rotor Exit Cavity

Downstream of the first rotor, the velocity triangles are deduced in two axial measurement planes, i.e. expressed in the local axial coordinate at Z=0.1 and Z=0.5. The main flow velocity triangles show slightly negative flow angles in the absolute frame, which confirms that the first stage is working at a higher load than the second stage. The initial velocity triangles of the leakage jet exhibit higher axial velocity components as downstream of the second stage. A reason for this fact could be the higher pressure ratio across the first rotor. Similar to downstream of the second rotor, the jet loses rapidly axial momentum from station Z=0.1 to Z=0.5. The downstream development of the jet will be strongly affected by the leading edge of the subsequent stator. Due to the stagnating effect this is expected to also change the development of the pitch-wise velocity triangles in comparison to the second rotor.
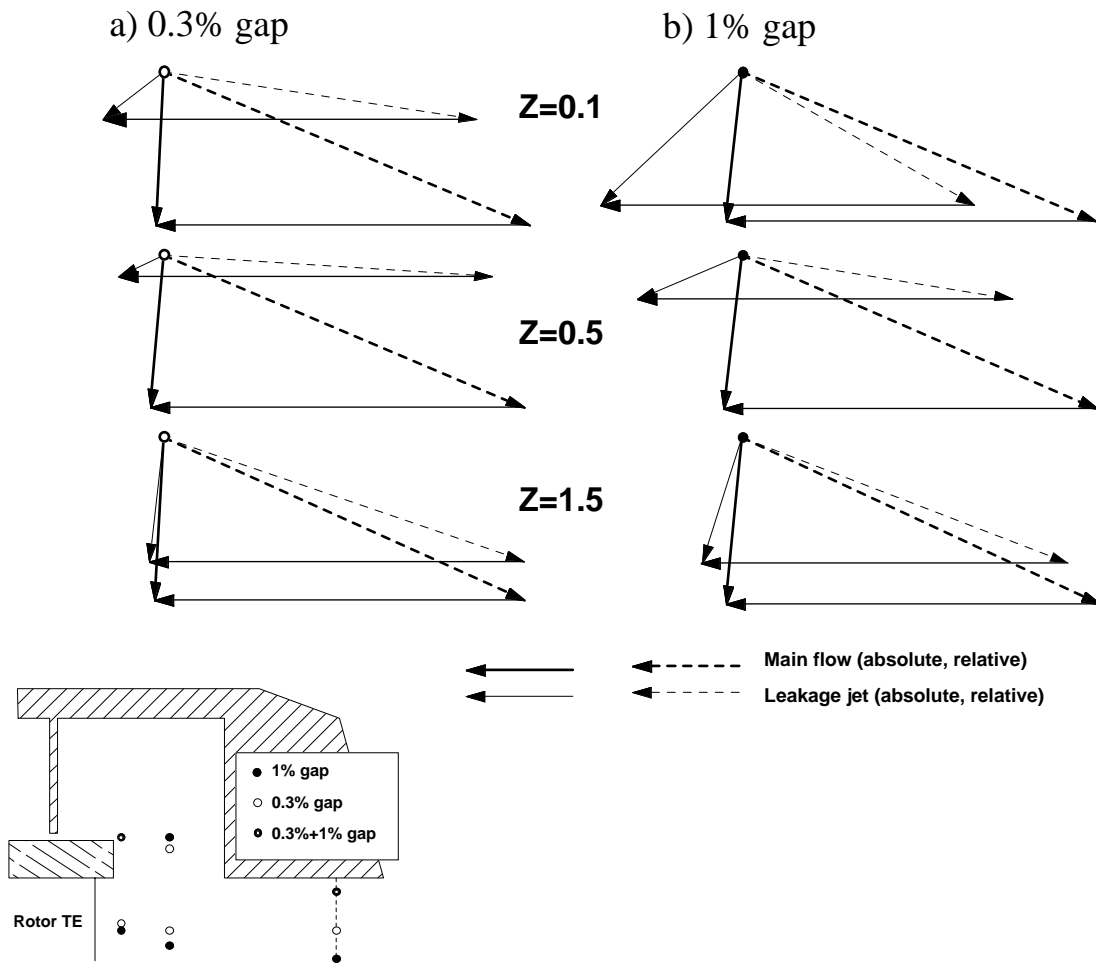
Fig. 7.1.1-6   Evolution of main flow and leakage jet velocity triangles down-stream of the second rotor labyrinth: a) 0.3% gap, b) 1% gap
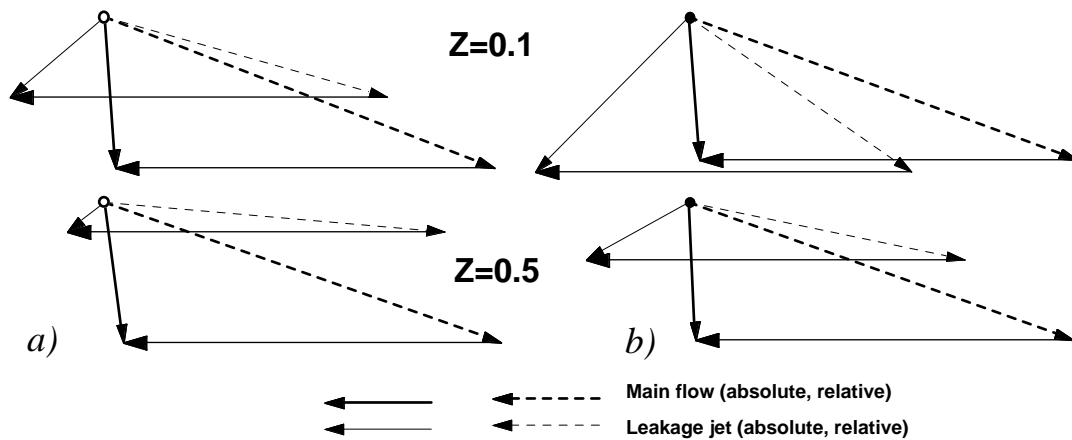
Fig. 7.1.1-7   Evolution of main flow and leakage jet velocity triangles down-stream of the first rotor: a) 0.3% gap, b) 1% gap

7.1.2   Potential field influence on exit cavity flow

The exit cavity flow field is influenced by the presence of a downstream blade row. The upstream potential effect of the blade leading edge and blade passage induces three-dimensionality into the flow field. Fig. 7.1.2-1 shows the deviation against the mean value for both, yaw and pitch angle, measured at the leakage jet position of Z=0.1. In the exit cavity of rotor 2 the flow field shows no circumferential variation. The leakage jet in the exit cavity of the first rotor labyrinth however gets distorted. On the pressure side of the passage the fluid is pushed into the cavity and the yaw angle is shifted toward higher values. On the suction side the opposite effect is observed as the arrows in Fig. 7.1.2-1 indicate. Consequently, the outflow of the cavity will happen more on the suction side of the downstream blade row than on the pressure side.
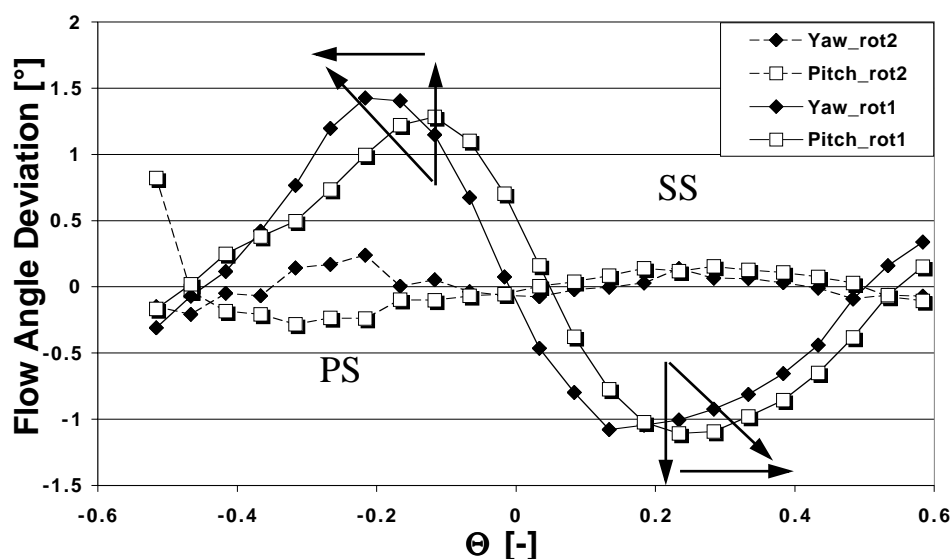
Fig. 7.1.2-1   *Potential field influence of stator leading edge on leakage jet:*
                flow angle deviation against mean, Z=0.1, 1% gap

The previously described effect is persistently observed one measurement plane downstream at Z=0.5. At this location the influence of the potential field is discussed in more detail using Fig. 7.1.2-2. It presents the static pressure field within the exit cavity of the first rotor labyrinth as well as the M-number combined with secondary flow vectors for the 1% gap case. The dashed vertical line indicates the stator leading edge. A high pressure region is observed upstream of the stator leading edge as expected. The M-number is reduced in this region due to the decelerating pressure field. The streamlines in the vicinity of the leading edge stagnation line are deviated to the right and to the left as the secondary flow vectors reveal. The static pressure field extents into the cavity, where the flow is not only deviated to the right and left but also into and out of

the cavity. The secondary flow vectors indicate a major in flow region at $R=1.05$ and $\Theta=-0.25$ (see white circle). The major out flow is observed at $R=0.75$ and $\Theta=0.1$ (see white circle). Considering the blade passage rather than the blade leading edge, the in and out flow distribution is induced due to the lower through flow velocity on the pressure side in comparison to the higher through flow on the suction side. Thinking of the stagnation line as a dividing line a deviation of the stagnation line from the blade leading edge around the tip radius is proposed. The double arrow indicates the superposition of the leading edge stagnation and the upstream effect of the passage pressure and suction side.

a)

b)
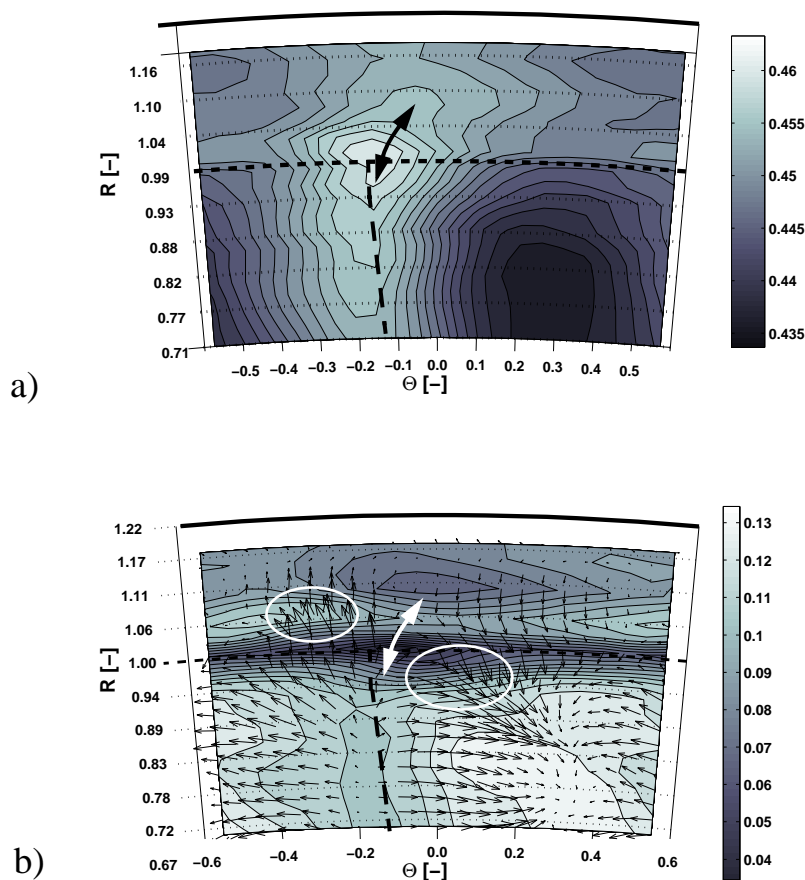
Fig. 7.1.2-2   *three-dimensional flow field, Z=0.5, 1% gap:*
                 a) C_p, b) M and secondary flow vectors

7.1.3   Unsteady results

The unsteady measurements taken in the downstream flow field of the first and second rotor are presented in Fig. 7.1.3-1 and Fig. 7.1.3-3, respectively. The measurement plane is at mid blade gap position (Z=0.5). The unsteady data sets

are post-processed to the time-average of the relative M-number and the static pressure within the rotor relative frame of reference. The arrows indicate the sense of rotation of the relative coordinate system. The discussions of the results within this section happen in the relative frame, if not stated otherwise.

At this point it is worthwhile to recall the radial positions of the leakage jets found with the pitch-wise, mass averaged five hole probe measurements (chapter 7.1.1). The stronger leakage jet for 1% gap case is found at R=1.06 within both exit cavities. In the case of the 0.3% gap the weaker leakage jet could be detected within the second exit cavity at R=1.044, whereas a distinct jet position within the first rotor exit cavity was not found.

First Rotor Exit

First consider the static pressure field measured in the first rotor exit for the datum case. The pressure distribution reveals the trailing edge position of the rotor blade at Θ_{rel}=-0.25, where a high static pressure is induced. The circumferential pressure variation from high to low pressure at Θ_{rel}=0.3 in the main flow region is also seen in the cavity. The pressure in the cavity is of the same magnitude of order as within the main flow region. Comparing these results to the 1% gap case two differences are observed: Firstly, a stripe of higher static pressure at the radial position of the leakage jet (R=1.06) is found. The low pressure region within the leakage jet is found at Θ_{rel}=0.38, which is shifted into positive Θ direction. Secondly, the level of static pressure within the cavity is higher, which is in compliance with Fig. 7.1.1-3.

The M_{rel}-number distribution of the 0.3% gap case is discussed first. The distribution shows the rotor wake at Θ_{rel}=0.1 and an incorporated region of reduced M_{rel} at R=0.87. The wake is convected into tangential direction by $\Delta\Theta_{rel}$=0.35 from the location of the trailing edge. On the pressure side of the wake a higher M_{rel} is detected than on the suction side. Assuming a constant relative total pressure this is induced by the static pressure field. Closer to the tip radius the wake becomes wider. Within the cavity a lower M_{rel}-level is found, which is in agreement to the velocity triangles Fig. 7.1.1-7.

Comparing the two gap cases a different behaviour within the cavity is found: For the 1% gap case the lowest M_{rel}=0.24 is found in a region having its centre at Θ_{rel}=0.2 and R=1.05. A local minimum, but at a higher level M_{rel}=0.29, is also present in the flow field of the 0.3% gap case. However, it is found in R=1.05 and Θ_{rel}=-0.35, which is shifted to the suction side of the wake in comparison to the 1% gap case. Both regions of lower M_{rel} are connected to a circumferential band of lower velocity, which corresponds to the radial leakage jet position. The circumferential static pressure distribution in principal
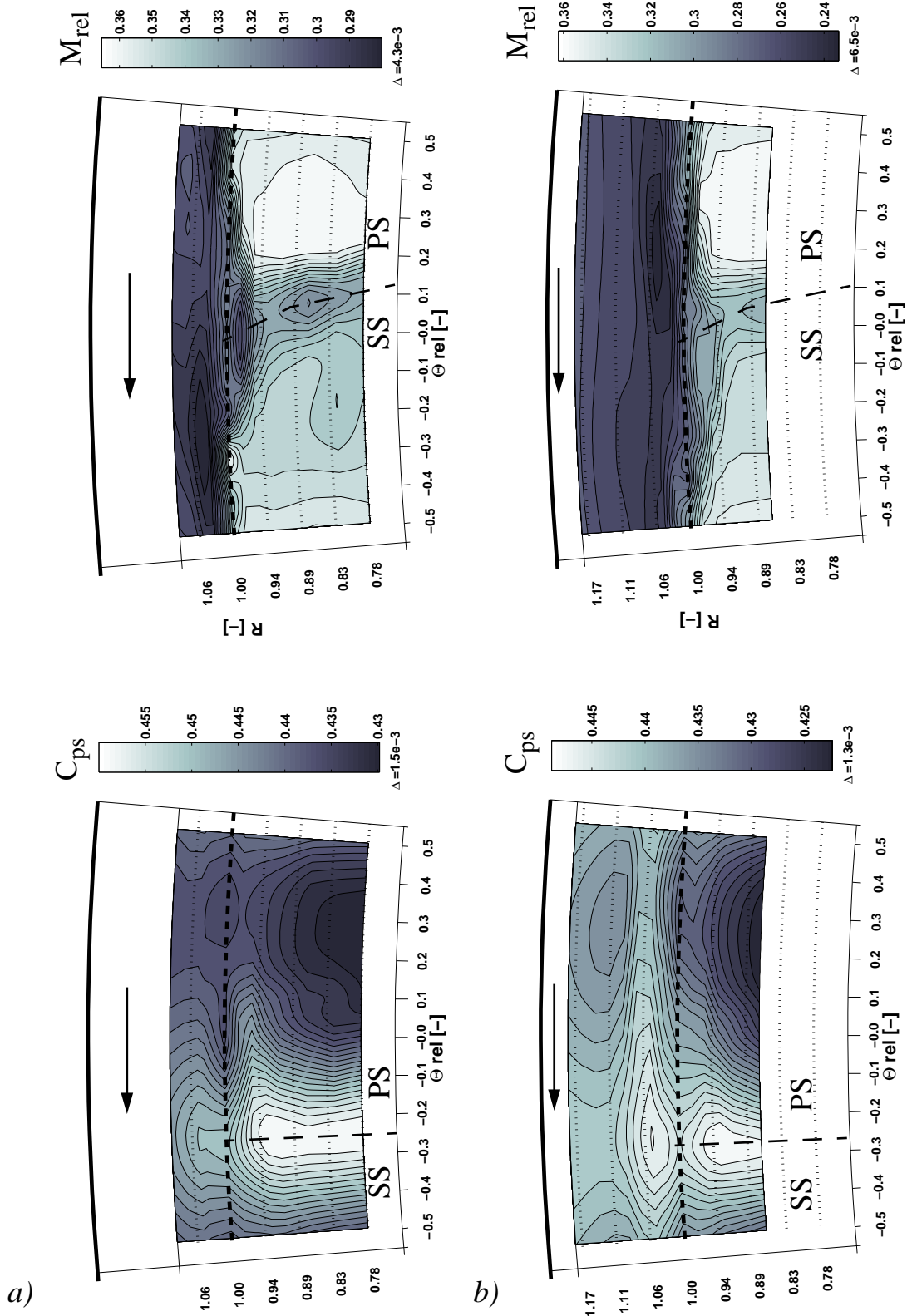
Fig. 7.1.3-1   Time averaged, rotor relative static pressure C_p and M_{rel}, at first rotor exit: a) 0.3% gap, b) 1% gap

stays the same as it is imposed by the blade to blade pressure field. However, the relative total pressure seems to be increased and redistributed such that the local minimum in velocity is shifted by half a blade pitch. The exit cavity flow field in the 0.3% gap case is dominated by the static pressure field of the rotor trailing edge. High static pressure causes low M_{rel}. In the 1% gap case the jet is redistributing the flow field due to its momentum and kinetic energy. The relative streamlines of the leakage sheet are deflected such that the total pressure wake is filled up with additional leakage fluid. This effect is further highlighted in the following section.

Second Rotor Exit

The static pressure field and the M-number at the exit of the second rotor are presented in Fig. 7.1.3-3. First the static pressure results are discussed. The pressure distribution is comparable in shape and position of features to the first rotor exit and the description of the previous section applies. Therefore, some quantitative differences are discussed. For this purpose the pressure difference between the main flow (R=0.92) and the leakage jet region is taken at each circumferential position and then circumferentially averaged. Thus, a quantification of the static pressure gradient across the interaction zone is given. The results of this approach is presented in Tab. 7.1.3-2.

ΔC_p	Rotor 1 exit	Rotor 2 exit
0.3% gap	0.003	0.003
1% gap	-0.007	0.002

Tab. 7.1.3-2   Static pressure differences $\Delta C_p = C_{p(R=0.92)} - C_{p(R=1.05)}$ across the interaction zone

In three cases the main flow static pressure is slightly higher than the cavity jet region. For the 1% gap case at the exit of the first rotor, a significantly lower value is found, i.e. the jet region encounters a higher static pressure. This increase in static pressure is only detected if a strong jet and a subsequent stator blade row is present. The potential field of the stator redistributes the flow three-dimensionally and acts as an obstruction to the flow due to its blockage. This fact additionally decelerates the leakage jet leading to a higher static pressure. The jet has to overcome a higher static pressure gradient in order to be able to leave the cavity.

The M_{rel}-number distributions in Fig. 7.1.3-3 in general show the same structures as in Fig. 7.1.3-1. Therefore, only the differences between first and second rotor exit flow field are discussed. These differences are mainly found within
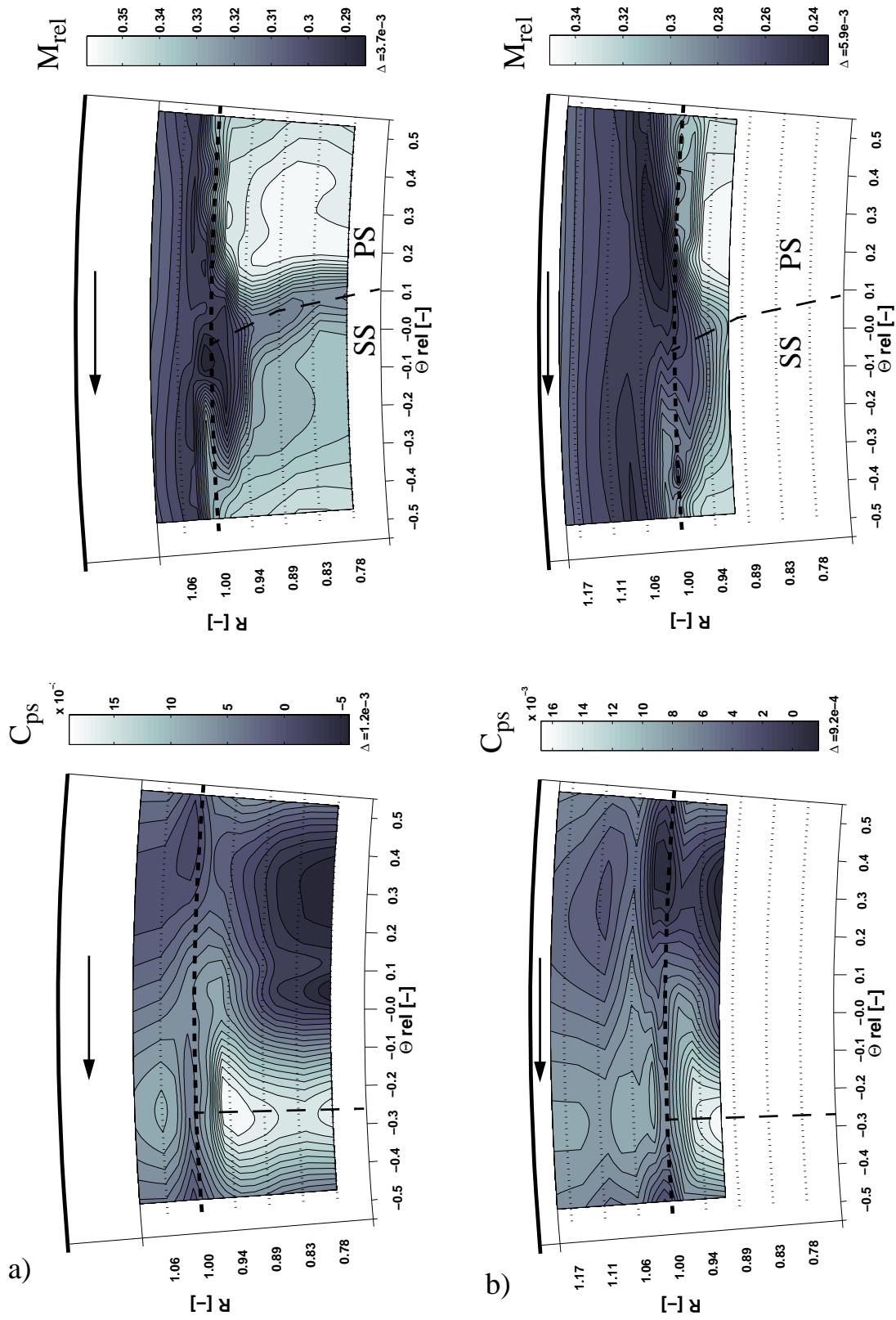
Fig. 7.1.3-3   Time averaged, rotor relative M_{rel}, φ_{rel} at second rotor exit:
a) 0.3% gap, b) 1% gap

the interaction zone. A local minimum of M_{rel} is not present at R=1.05 and Θ_{rel}=-0.35 in the 0.3% gap case. However, the region of broadening of the wake close to the tip radius is enlarged on the suction side.Around R=1 and Θ_{rel}=-0.08 a region of low M_{rel}=0.28 is present, which is in prolongation of the wake centre line. The region of wake broadening in the 0.3% gap case also extents further into the main flow until R=0.94, in comparison to R=0.96 at first rotor exit. At Θ_{rel}=-0.25 an alternating pattern from high to low is found two times while moving into positive radial direction. In the 1% gap case (Fig. 7.1.3-3b), a similar alternating pattern is found at the same circumferential position Θ_{rel}=-0.25. Comparing Fig. 7.1.3-3 against the first rotor exit flow field (Fig. 7.1.3-1) several differences may be named: The circumferential band, within which the leakage jet is found, has a more pronounced s-shape. The region of local minimum M_{rel}=0.24 is also found at Θ_{rel}=0.2 and R=1.05 as in Fig. 7.1.3-1, but it covers a larger area and its centre-line is inclined counter-clockwise by 10° against the horizontal. The measurement grid does not completely cover the broadening region in radial direction. A distinct wake structure is not resolved at the last radial position R=0.92. Therefore, the thickness of the region of wake broadening cannot be deduced. Note that the alternating pattern is only found downstream of the second rotor for both gap cases.

Radial velocity distribution in the relative frame

In order to fully understand and describe the three-dimensional flow effects, the radial velocity component has to be considered (see Fig. 7.1.3-4 and Fig. 7.1.3-5 for the first and second rotor exit flow field). The radial velocity component exhibits an offset from case to case, which is caused by slight differences in the settings between both probes of the virtual four sensor probe. Therefore, the diagrams are deduced by first taking the difference between the pitch-wise average of the data at R=0.92 and the pitch-wise, mass-averaged five hole probe results at this point (Fig. 7.1.1-3). Then the rotor-relative data is shifted by the difference, thus the same value appears at R=0.92 as in Fig. 7.1.1-3. The pitch wise-averaged velocity profiles for both measurement technologies are incorporated into Fig. 7.1.3-4 and Fig. 7.1.3-5. Good agreement in the radial velocity profile is achieved at all other radial positions. Therefore, it is assumed that the contours within each diagram are not influenced by the different settings within the pair of probes. Due to local, large pitch angle variations in combination with a low absolute M-number, some points within R=1±0.02 and across the pitch are at certain times of the blade passing period out of the pitch angle calibration.

In Fig. 7.1.3-4 the radial velocity component in the first rotor exit is presented. Within the wake, which is marked with a dashed line, negative radial velocity is found. The fluid within the wake is moving toward the hub. On the pressure

side of the wake the sign changes and the fluid is moving toward the tip. The up and down movement is inducing an axial vorticity component, which can be interpreted as the trailing shed vorticity of a leaned blade, as the rotor blades are.

At the location, where the leakage jet is found for the 0.3% gap case (Fig. 7.1.3-1, R=1.05 and Θ_{rel}=-0.25), the radial velocity shows a local maximum of v_r=0.044. This location coincides with the low relative Mach number in Fig. 7.1.3-1 and the trailing edge position of the rotor. The local minimum on the same radius R=1.05 is v_r=0.014, which shows that at this location no stream-lines are moving into the cavity. In the case of the strong jet, the radial velocity is negative within the region of the leakage jet having a minimum radial veloc-ity of v_r=-0.09 at the circumferential position of the wake. This value is of the same order of magnitude as the radial velocity within the wake itself.
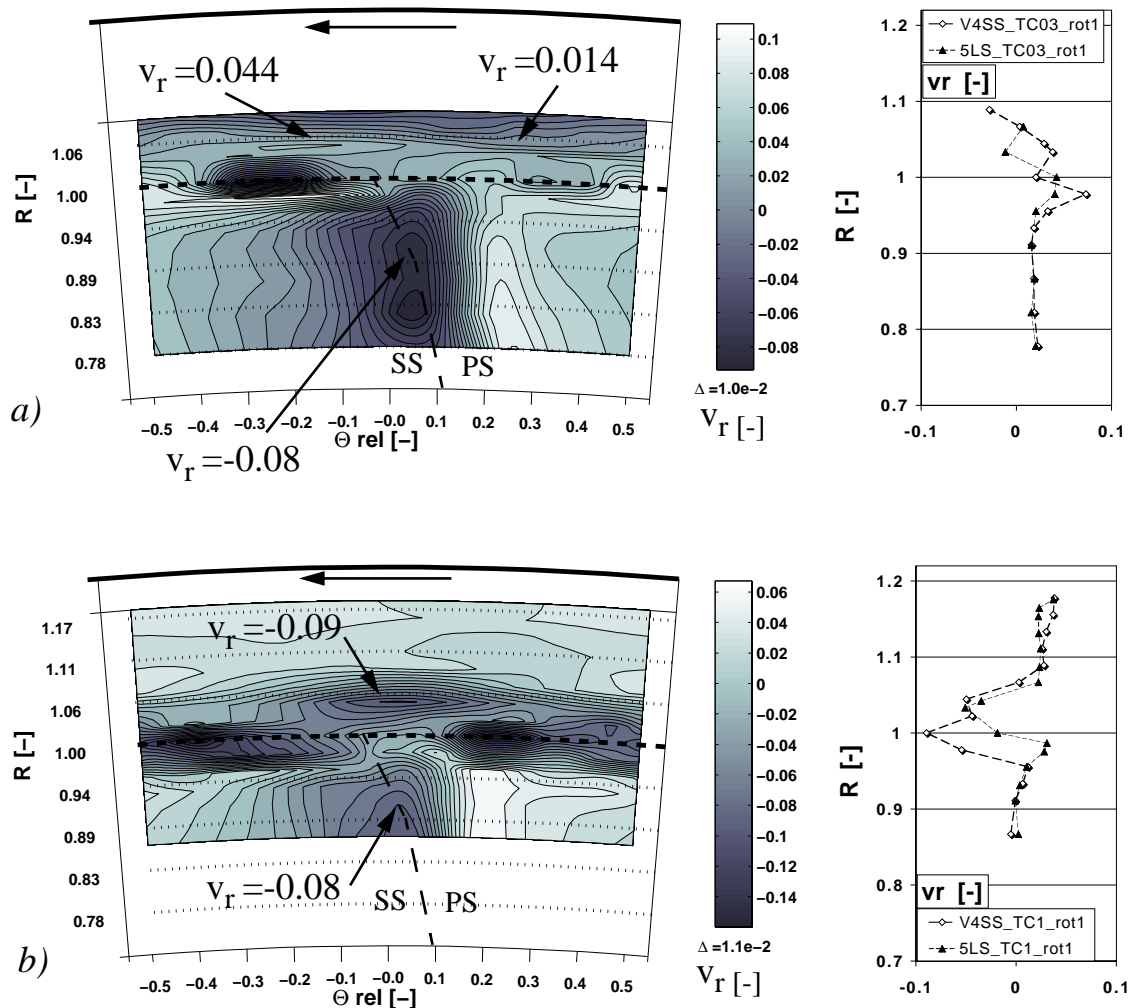
Fig. 7.1.3-4   Radial velocity component, first rotor exit flow field, relative frame, Z=0.5: a) 0.3% gap, b) 1% gap

Comparing first and second rotor exit flow fields some differences are found. For the 0.3% gap case the wake structure of radial migrating flow is extended into the cavity region. On the suction side of the wake, the fluid is moving out of the cavity, on the pressure side it is moving into the cavity. The alternating pattern, found in Fig. 7.1.3-3, is also present in the radial velocity distribution. At the radial location of the leakage jet a minimum radial velocity of $v_r=-0.015$ is found. On the pressure side of the wake a maximum radial velocity of $v_r=0.06$ is observed.

The 1% gap case shows a large region of minimum radial velocity ($v_r=-0.018$) just above the wake. This region is partially covering the region of low M_{rel} found in Fig. 7.1.3-3, but the centre of both are $\Delta\Theta_{rel}=0.2$ apart from each other.
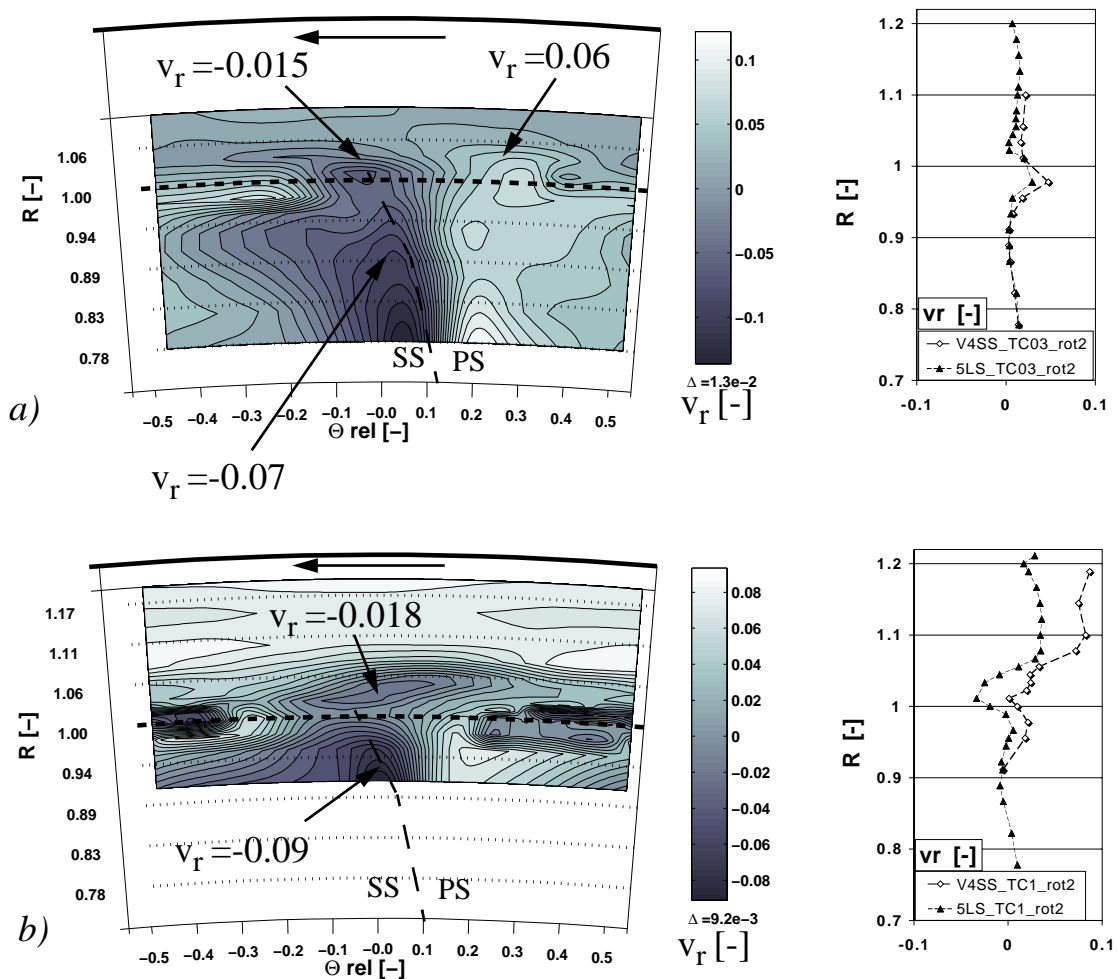
Fig. 7.1.3-5   Radial velocity component, second rotor exit flow field, relative frame, Z=0.5: a) 0.3% gap, b) 1% gap

7.2 SUMMARY OF EXPERIMENTAL OBSERVATIONS

The leakage jet interaction with the main flow was found to follow different schemes. These schemes depend on the strength of the leakage jet and on the fact, whether there is a potential field interaction due to a downstream blade row or not. Both gap cases show that the cavity flow for R>1.06 is driven by the strength of the jet in terms of tangential velocity.

The 0.3% gap case represents the pure cavity to main flow interaction, since the leakage jet is weak. Here, the observations are:

1) The radial migration within the wake attracts low kinetic energy fluid (see Fig. 7.2-1). This effect is acting also within the cavity if no stator follows downstream of the exit cavity. Then the pressure side movement of the passage vortex also penetrates into the interaction zone.

2) The potential field interaction of rotor trailing edge and stator leading edge affects the flow field. The maximum positive radial velocity within the cavity is found at the circumferential position of the rotor trailing edge. Fluid is pushed into the cavity at this point.

Exit Rotor 1   **Exit Rotor 2**

vr >0

SS   TE   wake   PS   SS   TE   wake   PS
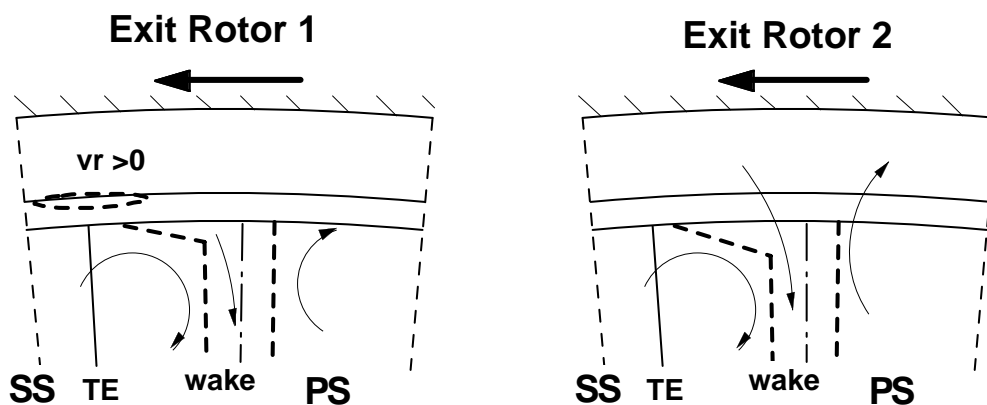
Fig. 7.2-1   Cavity interaction with the main flow, relative frame of reference, 0.3% gap: Z=0.5

The basic components of the leakage jet to main flow interaction found in the 1% gap case are:

1) The potential field of the stator leading edge three-dimensionally redistributes the flow field (7.1.2). This effect is visualised in Fig. 7.2-2, which presents the circumferential distribution of the absolute velocity triangles in the stator frame of reference for the 1% gap case. In the upper part of the diagram the leakage jet and in the lower part the main flow velocity triangles are depicted. Note that the base of the velocity vector is representing the location of the circumferential coordinate. The velocity arrow represents 20% of the shroud ro-

tational speed. The leading edge position of the stator is obvious in the downstream flow field of the first rotor, where it causes a deviation of streamlines. Downstream of the second rotor this effect is not present. Additionally to this effect of redistributing streamlines, the potential field acts as a obstruction to the leakage flow. As a consequence, the leakage flow needs to transform a higher portion of the dynamic head into static pressure in order to be able to overcome the additional resistance and leave the cavity. Therefore, the flow out of the cavity happens at a Z-plane further downstream in the case of a strong jet.
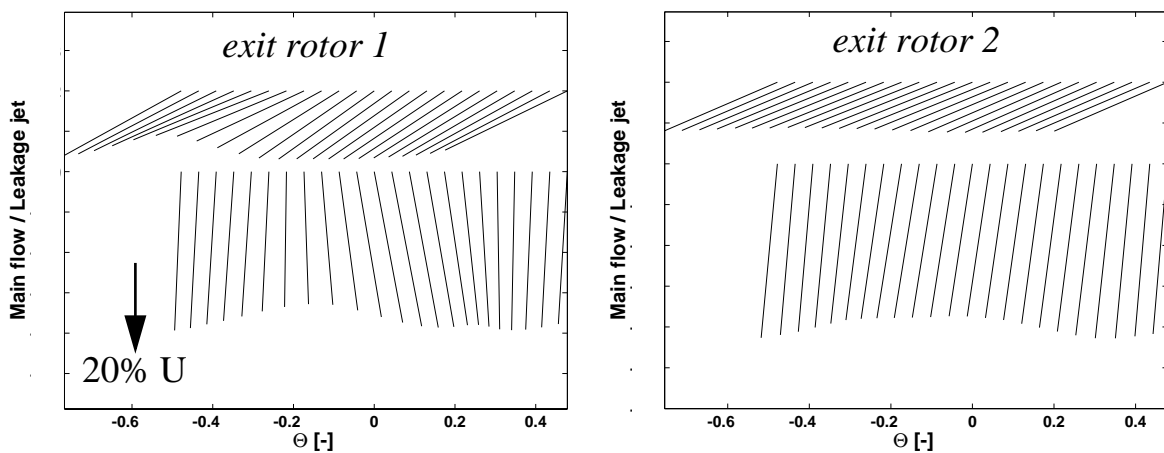
Fig. 7.2-2   Absolute velocity triangles, stator relative: 1% gap

2) The potential field of the rotor trailing edge divides the leakage sheet into distinct jets. Fig. 7.2-3 shows the time averaged velocity triangles within the relative frame of reference for the first and second rotor exit flow field. Again, the upper vectors represent the leakage jet and the lower one the main flow. The arrow represents 100% of the shroud rim speed. The circles point out the base of velocity vectors, which are just facing the trailing edge position of the rotor Θ_{rel}=-0.25. The leakage mass flow is redistributed. A maximum of mass flow is found in the mid position between the trailing edges where it forms a distinct jet. The main flow is much less affected by the trailing edge pressure field than the leakage jet. Within the main flow vectors the wake of the rotor blade is apparent.

3) Leakage fluid migrates into the rotor wake causing the leakage streamlines to contract into the wake area. The radial migration of the leakage fluid leads to a broadening of the wake in the vicinity of the blade tip. The wake seems to attract low energy fluid.
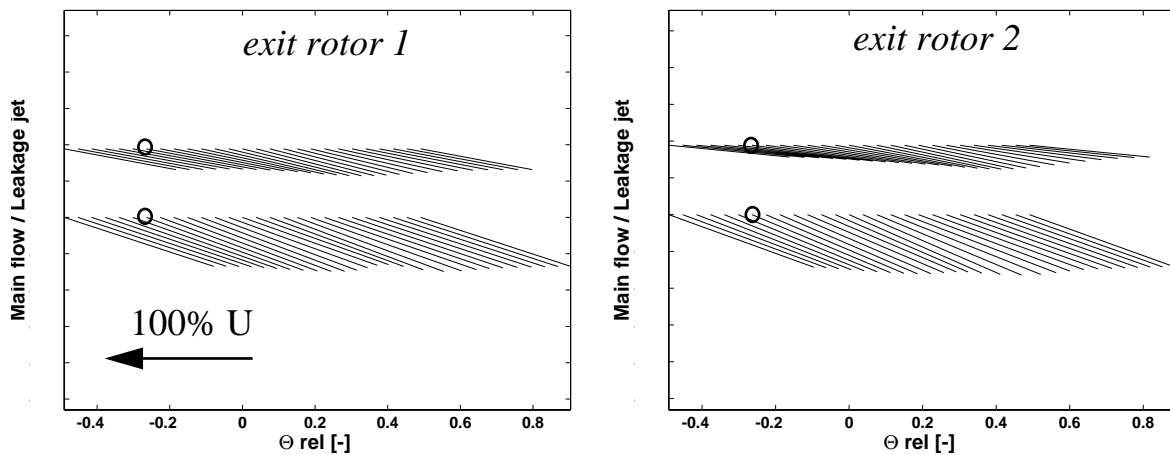
Fig. 7.2-3   Time averaged velocity triangles, rotor relative frame: 1% gap

All components of the leakage jet main flow interaction listed above are present in the entire interaction volume. In Fig. 7.2-4 the development of these flow drivers is depicted as a descriptive flow model. The flow field is discussed within the rotor relative frame of reference. The depicted rotor passage is moving to the left as the bold arrows indicate. Note that the middle axial plane (Z=0.5) is based on experimental data. The leakage flow starts as a veritable leakage sheet and is not yet in contact with the main flow. The mass redistribution due to the potential field of the trailing edge is expected to start at this location. With increasing Z the potential field of the trailing edge decays. Therefore, the redistribution of the leakage mass flow becomes weaker further downstream. The radial migration of low kinetic energy fluid into the wake starts also at Z=0.15, where the wake is in contact with the shroud recirculation zone. As the wake convects downstream it passes the low pressure region between the trailing edges and broadens due to the wake diffusion. The rotor passage vortex is indicated as circular arrows to the left and right of the rotor wake. At Z=0.5 a region of positive radial velocity forms, which has physical contact with the wake flow. The small arrows left and right of the region of high axial velocity components indicate the mass redistribution due to the trailing edge pressure field.

Approaching the forward facing step of the cavity exit the leakage jet streamline is bend radially inward. This movement is expected to happen rather on the suction side of the wake than on the pressure side. The reason for this is that the rotor passage vortex counter acts on the pressure side and supports on the suction side of the wake.
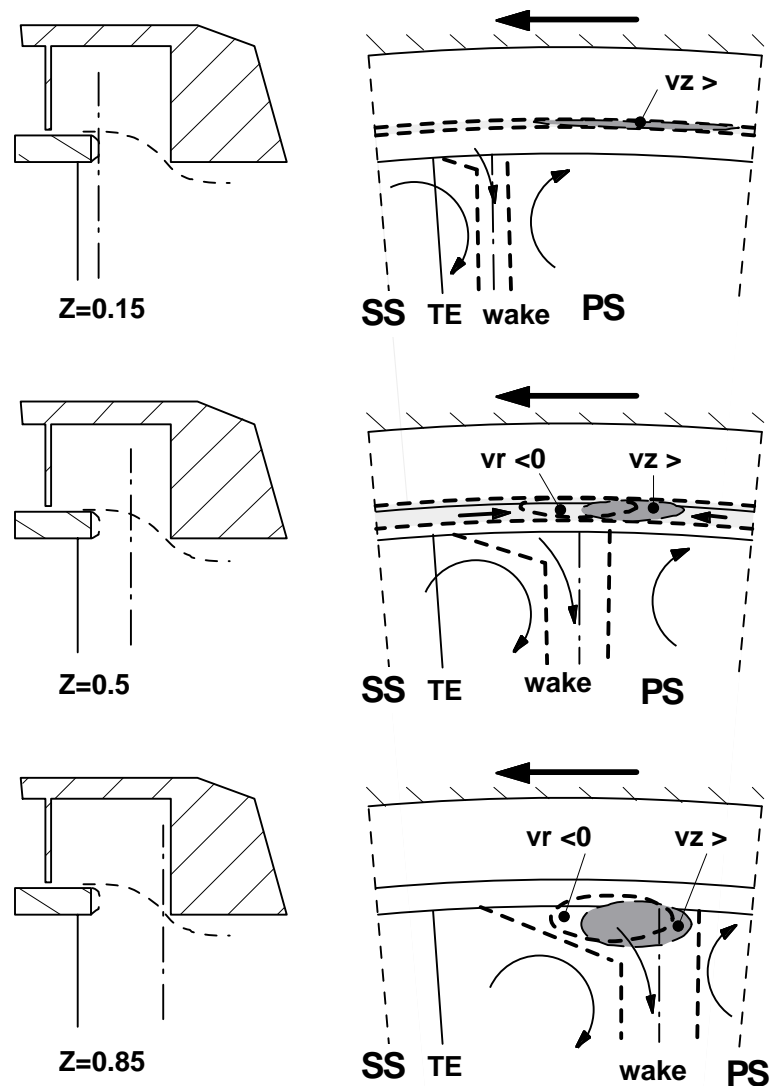
Fig. 7.2-4   Leakage jet formation and interaction with the main flow, relative frame of reference, 1% gap

7.3 MIXING LOSSES

7.3.1   Mixing of jet and cavity flow

The mixing loss of the jet within the exit cavity is quantified using the entropy relation (4.2). The maximum total pressure at Z=0.1 is taken as the reference pressure (see Fig. 5.1.2-1). The local maximum of the total pressure at Z=0.5, identified as the centre of the leakage jet (see Fig. 7.1.1-3), is taken into the nominator of (4.2). It is assumed that the total temperature of the jet core stays constant from Z=0.1 to Z=0.5. Therefore, the term containing the temperature

ratio does not contribute. The specific generated entropy as well as the entropy generation rate are given in Tab. 7.3.1-1. The generated specific entropy for the 0.3% gap case is factor 3 to 6 smaller than in the 1% gap case. The much weaker jet has mixed out comparably more when it reaches the first plane of measurement at Z=0.1. Therefore, the further decay until Z=0.5 is much less than in the 1% gap case. The entropy generation rate S' differs by a factor larger than 10 between 0.3% and 1% gap case. The reason can be found in the associated leakage mass flows, taken from Tab. 5.2.1-2. The entropy generation downstream of the first rotor is higher than downstream of the second rotor.

	0.3% gap		1% gap	
	Δs [J/kg/K]	S' [W/K]	Δs [J/kg/K]	S' [W/K]
Rotor 1	1.41	0.04	4.01	0.54
Rotor 2	0.54	0.02	2.96	0.33

Tab. 7.3.1-1   Mixing loss of leakage jet: First and second rotor exit cavity, 0.3% and 1% gap

A better quantification of the mixing losses is achieved, if the entropy generation rate S' of the jet is compared to the entropy generation rate of the entire stage as found in Tab. 4.1.2-2. The ratio of both entropy generation rates is presented in Tab. 7.3.1-2. In the closed gap case virtually no loss can be associated to the leakage jet. Partially, because the leakage mass flow is so low and partially because the leakage jet already diffused most of its energy. In the 1% gap case the leakage jet causes around 1% of the stage losses. The leakage jet in the exit cavity of the first rotor dissipates 45% more energy than the second leakage jet. This is an experimental evidence that the presence of a stator leading edge downstream of the cavity severely enhances the mixing process within the cavity.

[%]	0.3% gap	1% gap
Rotor 1	0.11	1.28
Rotor 2	0.06	0.87

Tab. 7.3.1-2   Entropy generation rate of the jet expressed as percentage of stage entropy generation

7.3.2   Mixing of jet and main flow

2-step mixing approach

Starting from the descriptive flow model derived in 7.2 the downstream mixing

of the leakage fluid with the main flow fluid is modelled in this section. As reported in Tab. 7.3.1-2 the weak jet in the 0.3% gap case mixes out rapidly and affects the downstream flow field in a negligible way. Therefore, the mixing model is derived with the help of 1% gap case results.

The mixing calculation is performed in the relative frame of reference as depicted in Fig. 7.3.2-1. First the experimental results at Z=0.5 are taken and idealised as indicated with the grey shaded regions. Station 1 denotes the leakage jet, where the mass redistribution of the jet is accounted for. The area covered by station 1 reaches from the shroud radius R=1 to an outer radius R_o. The outer radius is adjusted such that the ratio of leakage to main mass flow matches to the experimental results. Station 2, which denotes the main flow, contains three blocks representing the wake, the pressure side flow with higher relative Mach numbers and the suction side region with lower relative Mach number. The outer diameter of this area is the blade tip diameter. The inner radius R_i is taken taken to be R=0.72, such that section 2 covers the rotor passage loss core.

Since it is a three-dimensional mixing problem, the flow field is separated into 20 circumferential bands. The first mixing step consists of individually mixing these bands at constant area to reach station 3. For this step the entire volume is considered to be pitch periodic, thus no net forces are acting in tangential direction. The equation solved for this mixing step are:

Continuity:

$$v_{z3j} = \frac{1}{A_j}(v_{z1j}A_{1j} + v_{z2j}A_{2j}) \text{ , for j=1 to 20} \tag{7.1}$$

Circumferential momentum (torque):

$$v_{\Theta 3j} = \frac{1}{A_j R_3 v_{z3j}}(A_{1j}R_1 v_{z1j}v_{\Theta 1j} + A_{2j}R_2 v_{z2j}v_{\Theta 2j}) \tag{7.2}$$

Axial momentum:

$$p_{3j} = p_1 - \rho v_{z3j}^2 + \frac{A_{1j}}{A_j}\rho v_{z1j}^2 + \frac{A_{2j}}{A_j}\rho v_{z2j}^2 \tag{7.3}$$

Energy:

$$T_{rel3j}^o = \frac{1}{\dot{m}_3}(\dot{m}_1 T_{rel1j}^o + \dot{m}_2 T_{rel2j}^o) \tag{7.4}$$

The relative total pressure is calculated using p_{3j} and the relative dynamic head. The density is assumed to be constant. The radii for the torque calculation are

taken as the average radius of the corresponding area, e.g. $R_3 = (R_o + R_i)/2$. The inlet boundary conditions for the mixing calculation are discussed later in this chapter.

In a next step the equations (7.1) to (7.4) are approximated in a Taylor series of differential area changes, neglecting the higher order derivatives. Then the values at station 3a are expressed as functions of small cross sectional changes:

$$v_{z3a} = v_{z3}\left(1 - \frac{dA}{A}\right) \tag{7.5}$$

$$v_{\Theta 3a} = v_{\Theta 3}\left(1 - \frac{dR_3}{R_3}\right) \tag{7.6}$$

$$p_{3a} = p_3 + 2\rho v_{z3}^2\frac{dA}{A} - \left(\frac{A_1}{A}\rho v_{z1}^2 + \frac{A_2}{A}\rho v_{z2}^2\right)\frac{dA}{A} \tag{7.7}$$

Note that the index j for each of the radial bands is omitted in the above equations. The total relative temperature stays constant from station 3 to 3a. The advantage of this approach is that no detailed information of how the leakage fluid actually enters the main flow region is needed. In the last step of the mixing calculation from 3a to 4 the radial bands are mixed out at constant area. For this step equations (7.1) through (7.4) are applied again.
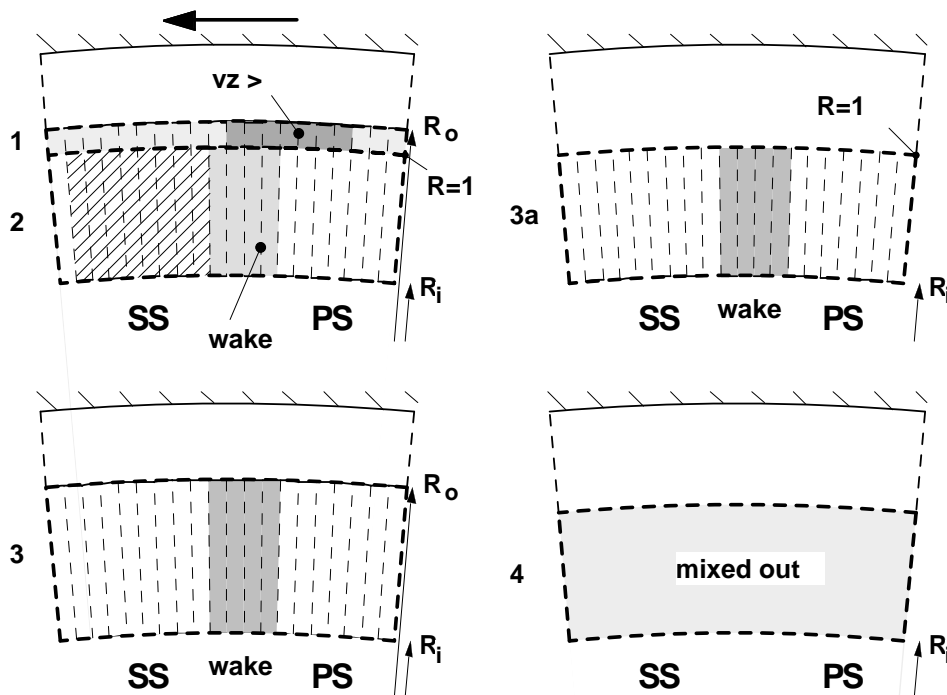
Fig. 7.3.2-1   *Stations of the mixing calculation: 3) radial mixing, 3a) change of area, 4) fully mixed out*

Entropy generation

The quantification of the mixing loss is based on the entropy equation (4.2). The ratios of relative total temperature and relative total pressure are build from circumferentially mass averaged values of station 2 and the results found in station 4. A mixing power follows from (4.4) using the over all mass flow and the static temperature at station 2.

The steady contribution of the relative total temperature ratio to the specific entropy increase Δs can be estimated using the total temperature profiles measured with the 2D FRAP probe (Fig. 4.4.4-1). These measurements indicate that the absolute total temperature at the jet location is about 4.5°K higher than in the main flow. Since this measurement technology delivers the time averaged temperature, the unsteady temperature field is not resolved. Consequently, the entropy increase due to temperature change Δs_T can only be given in a time averaged manner. With the relationship

$$T^o = T_{static} + \frac{v^2}{2c_p}, \tag{7.8}$$

the total temperatures in the relative and absolute frame are related to the static temperature. Using the measured velocity distribution, the relative total temperature difference can be given to 2.1°K downstream of the first rotor and 1.7°K downstream of the second rotor.

The boundary conditions in terms of velocity triangles are depicted in Fig. 7.3.2-2. Note that the shape of velocity triangle distribution reflect Fig. 7.2-3 in an approximate way. The thermodynamic and geometric boundary conditions are summarised in Tab. 7.3.2-3.
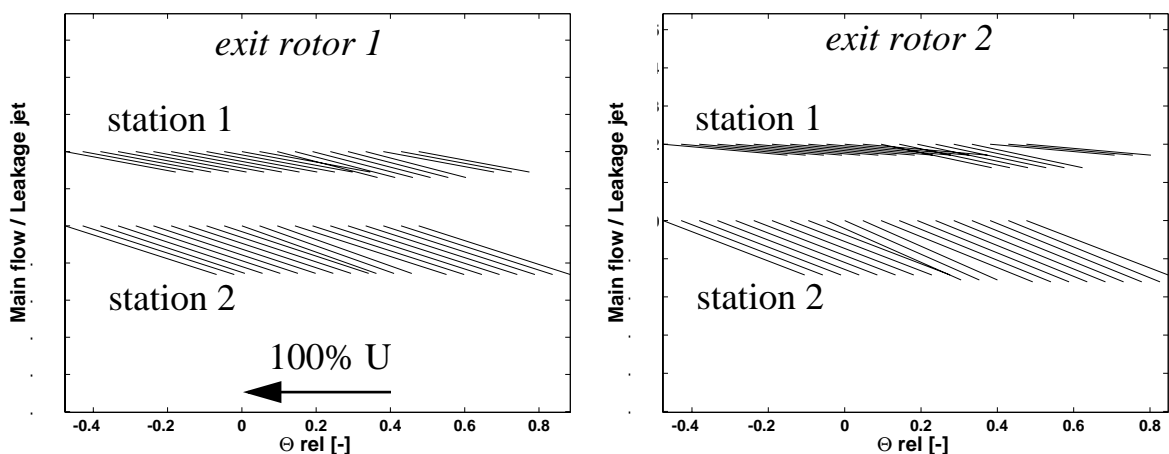
Fig. 7.3.2-2   Boundary conditions at station 1 and 2

	$R_0 - R$ [mm]	T_{static} [°C]	T_{rel}^o [°C]	p_s [kPa]	$\dot{m}_L / \dot{m}$ [%]
Rotor 1: Jet	2.5	31.3	34.7	11.0	1.39
Rotor 1: Main		26.4	33.3		
Rotor 2: jet	3.8	21.2	24.9	9.6	1.18
Rotor 2: Main		16.2	22.4		

Tab. 7.3.2-3   Thermodynamic and geometric boundary conditions

The results of the mixing calculation are discussed with the help of Tab. 7.3.2-4, which also includes a comparison to the results gained with Denton's equation of mixing losses in a shrouded turbine (1.8). The velocity components in (1.8) are taken as the average of the values at station 1 and 2 of the inlet boundary condition to the mixing calculation. Since one assumption in (1.8) is that relative total temperature is constant, this equation represents the entropy generation due to pressure Δs_p, only. Additionally, the results of the loss coefficient defined in (1.7) are given.

The mixing losses downstream of the first rotor are around 50% higher than downstream of the second one. This is found with both approaches, the mixing model and equation (1.8). The level of mixing losses in Denton's approach is much lower, since no wake mixing and no temperature differences between the leakage jet and the main flow are included. The contribution of the temperature term in equation (4.2) to the entropy generation is around 20% of the over all mixing losses. The lost power P_{mix} set in relation to the stage losses given in Tab. 4.1.2-2 shows a 6.7% and 10.7% contribution of the mixing to the stage losses of the first respectively the second stage.

	Mixing model		Denton (1.8)	
	Rotor 1	Rotor 2	Rotor 1	Rotor 2
Δs [J/(kgK)]	0.97	1.4	0.11	0.17
P_{mix} [W]	870	1230	100	150
$\Delta s_T/\Delta s$ [%]	22	23	-	-
ζ [%]	4.2	6.4	0.5	0.8

Tab. 7.3.2-4   Mixing losses of the leakage jet with the main flow: g=1%

The same procedure of deducing the inlet boundary conditions was applied to the experimental data of the 0.3% gap case (see Fig. 7.1.3-3a). All other assumptions are the same as for the 1% gap case. The resulting mixing losses are presented in Tab. 7.3.2-5. The results are consistently lower than in the 1% gap

case, as expected. Again the difference in mixing between both exit rotor flow field is apparent. The loss of power relative to the stage losses is equivalent to 3.3% downstream of the first rotor and 7.3% downstream of the second rotor

	Mixing model		Denton (1.8)	
	Rotor 1	Rotor 2	Rotor 1	Rotor 2
Δs [J/(kgK)]	0.42	0.87	0.04	0.07
P_{mix} [W]	382	768	36	59
$\Delta s_T/\Delta s$ [%]	22	17	-	-
ζ [%]	1.8	3.8	0.02	0.03

Tab. 7.3.2-5   Mixing losses of the leakage jet with the main flow: g=0.3%

7.4 LEAKAGE JET MODIFICATION

In this section the potential of controlling the mixing process between the leakage jet and the main flow is discussed. Keeping in mind that the mixing process is a three-dimensional interaction, it is a question of what happens if the leakage jet is entering into the main flow with a different mass distribution or with different velocity triangles. And if there is a beneficial effect, how could it be achieved with a design change of the labyrinth.

One way to answer this question is to change the inlet conditions of the leakage jet (station 1) and to apply the mixing model described in the previous section.

Case 1: The leakage jet has a constant mass distribution around the circumference. According to Dawes comment in [9] this could be a design goal, since downstream blade rows receive a more homogenous inflow.

Case 2: Invert the leakage jet velocity triangles such that the region of high mass flow is moved on the other side of the wake.

Case 3: Put most of the leakage mass flow into the wake, thus overdoing the mechanism of radial migration described in Fig. 7.2-4.

The boundary conditions of each case including the distribution gained from the experiment is shown in Fig. 7.4-1. The results of this variation is presented in Fig. 7.4-2. The temperature term in the entropy generation equation is omitted. The differences within the cases range between 20W (rotor1) to 70W (rotor2). The relative variation of the mixing loss on the basis of the mixing model becomes a maximum 10%. However, comparing the differences with the results found with Denton's equation in Tab. 7.3.1-2 the leakage jet variation

reaches the same order of magnitude.

The results indicate an optimum in terms of mixing if the jet is homogenous (case 1). A physical reason could be that the flow becomes more uniform for each of the single bands in the first mixing step. Case 3 seems to be beneficial, too, since feeding the leakage flow into the wake reduces non-uniformity in the main flow and therefore reduces the mixing contribution in step 2 of the mixing model. The mixing downstream of rotor 1 is less sensitive to the leakage jet variation than downstream of rotor 2. The reason for this might be the presence of the stator leading edge, which causes a horizontal stratification of the flow field in the time averaged picture. A result of the stratification is a more uniform flow and therefore mixing losses are lower.
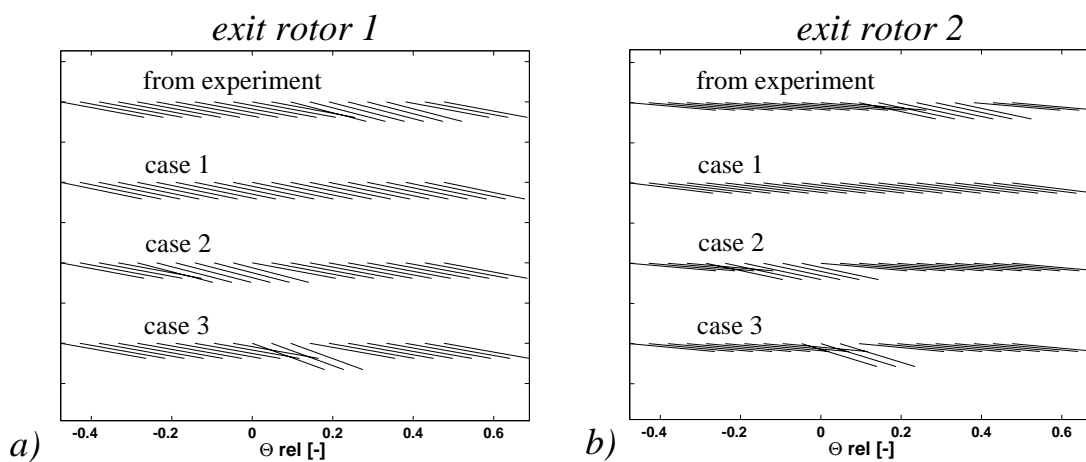
Fig. 7.4-1   Boundary conditions of investigated jet variations:
                  a) rotor 1, b) rotor 2

P_{mix} [W]	Rotor 1	Rotor 2
from experiment	683	944
Case 1	667	883
Case 2	683	953
Case 3	661	943

Fig. 7.4-2   Mixing losses of leakage jet variations: pressure term only

Despite the rough assumptions applied to the mixing model, the results do indicate possible improvements. The level of improvements seems to be around 0.1% efficiency as the mixing model and Denton's approach suggest.

In order to control the leakage jet distribution several design changes may be considered. From jet engines a shroud design comprising fins and fences is known. The fins cause the sealing effect and the fences are positioned down-

stream of the last sealing fin such that the leakage jet is aligned to the relative main flow direction (e.g. [57]). The goal of this approach is to minimize the miss match of leakage jet and main flow velocity triangles.

Another approach, which is probably more suitable to steam turbine configurations, is proposed in this section: The design of a non-axisymmetric last gap. From the jet distributions of cases 1 through 3, case 3 seems to be the most feasible one. Case 1 is difficult to achieve, since the static pressure field of the rotor trailing edge will always act on the leakage flow in a dividing manner. The leakage jet is a driven feature, thus it is too weak to counteract the pressure field. Case 2 would not be beneficial as discussed in Fig. 7.4-2.

The idea is to reconfigure the leakage jet from the last seal gap to the shroud trailing edge such that a high mass of leakage fluid passes through a region called wake window, as depicted in Fig. 7.4.2-1. The view in Fig. 7.4.2-1 is into negative radial direction. The rotor wake is indicated with a thick dashed line. The semi-circles indicate high and low pressure regions set up by the rotor trailing edges. The cavity flow is deviated due to the pitch-wise distribution of both, negative and positive tangential pressure gradients. To predict the process of streamline deviation at this level of modelling is not possible. Therefore, the principal is explained in the next paragraph using pitch-wise and time-averaged velocity triangles.

The wake window describes that region in the cavity, where the leakage out flow coincides with the circumferential position of the wake. The wake window is drawn in Fig. 7.4.2-1 downstream of the mid gap position, since the out flow can be expected from Fig. 7.2-4 to happen mainly at this axial position.

Following a stream line (thick line) from the centre of the wake window to the last gap, a circumferential position relative to the rotor trailing edge can be derived. At this location a gap opening would allow to let pass more leakage mass flow. Note that the location coincides with the circumferential trailing edge position. Keeping the gap area constant, requires a closing of the gap half pitch further in tangential direction. The resulting gap shape is depicted in Fig. 7.4.2-2. The indication of a completely closed gap at mid pitch position is achievable if the sealing fin is run into the rotor shroud.
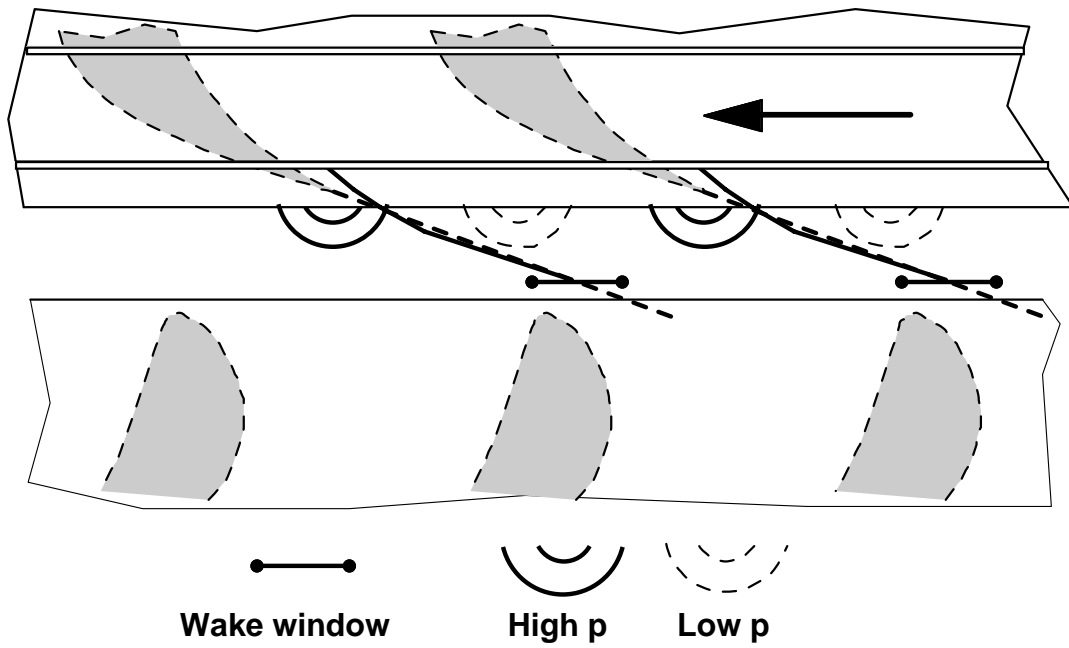
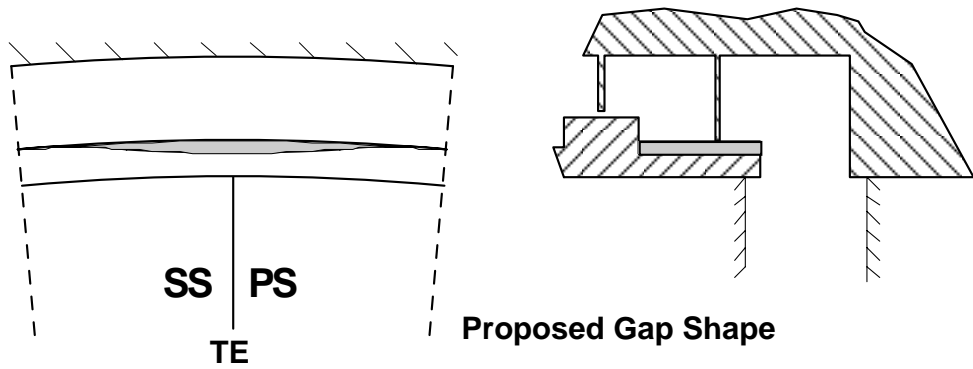*Fig. 7.4.2-1   Leakage jet trajectory through the wake window*

Fig. 7.4.2-2   Non-axisymmetric shaping of last seal gap

8   CONCLUSION

The literature review given in 1.1.3 showed that the leakage and cavity flow interactions with the main flow considerably alters the flow field in the endwall regions of a high pressure turbine. Most of the publications care about the shroud leakage effects on the development of the main flow. Only few publications were found dealing with the mechanisms of those interactions themselves. In fact, knowing the interaction mechanisms is the key to be able to improve the turbine design in this particular area, as it was stated in [65]. Hence, the objectives of the current investigation were:

1) Clarify the steady and unsteady flow interactions associated to open cavities.

2) Describe and quantify loss production mechanisms caused by labyrinth seals in shrouded turbines.

3) Develop theoretical models to describe the flow effects in an analytical way.

4) Translate the knowledge into design recommendations and modifications accounting for the changed end wall inlet conditions to the blade rows. Assess the potential of loss reduction by applying these means.

These objectives were met with an extensive measurement campaign performed in a two-stage, shrouded axial turbine. A specialized probe measurement technology had to be developed in order to be capable of measuring unsteady flow within a small-scale environment. The measurement campaign concentrated on the casing rotor labyrinth, mainly because of accessibility.

This chapter summarises the findings concerning the loss mechanisms and quantifications (8.1). Furthermore, it concludes the present investigation (8.2) and gives an outlook (8.3).

8.1   LOSSES IN LABYRINTH SEALS

The loss generation in the specific flow regions was subject of the chapters 4 through 7. At this point a summary is given. In Fig. 8.1-1, the stations of loss quantification are depicted: 1 refers to the loss generated in the inlet cavity. From station 2 to 3 the contribution of windage and labyrinth dissipation is evaluated. The mixing of the jet with the cavity flow happens from station 3 to 4. Finally, the leakage jet re-enters into the main flow and mixes out until station 5. The results are summarised as percentage of stage losses in Tab. 8.1-2. The results show a loss generation attributable to the labyrinth seal of around 16% in the 0.3% gap case and 28% of the stage losses in the 1% gap case.
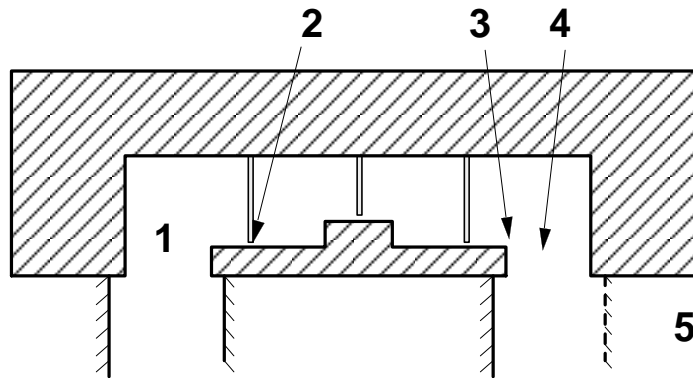
Fig. 8.1-1   Stations of losses within the labyrinth seal

Station	0.3% gap		1% gap	
	rotor 1	rotor 2	rotor 1	rotor 2
1	-	2.7	-	(2.7)
2->3 (aerodynamic)	-	0.8	-	6.6
2->3 (windage)	-	5.3	-	6.7
3->4	0.11	0.06	1.28	0.87
4->5 (mixing model)	3.3	7.3	6.7	10.7
sum	-	16.2	-	27.6

Tab. 8.1-2   Quantified loss mechanisms: in % of stage loss

The inlet cavity in itself is a low loss contributor. It is believed that this cavity should be rather counted to the main flow region than to the labyrinth seal in terms of design: Sealing effects due to dissipation are low and the fluid which does not enter the first gap passes through the rotor. Therefore, a circumferentially more uniform velocity distribution would prevent strong unsteady flow effects at the rotor endwall and the mixing within the cavity.

The windage losses within the closed cavities contribute 33% (0.3% gap) and 23% (1% gap) to the labyrinth losses. This effect not only affects the angular momentum but also induces a temperature increase, which was experimentally verified for this test rig.

The mixing of the jet with the cavity flow strongly depends on the gap width. For very small gaps the jet is already diffused at the shroud trailing edge. For larger gaps the jet induces an increased tangential velocity of the cavity flow and contributes around 1% of stage losses. The presence of a downstream blade

changes the mixing behaviour toward lower mixing losses.

A mixing model was developed on the basis of a two-step mixing approach. The mixing model predicts a portion of labyrinth loss of about 42%. As expected, the model results in higher values of mixing losses than Denton's approach, which does not incorporate the wake mixing. The level of mixing seems to be relatively high. Therefore, Chaluvadi et al. [7] is used to set the mixing losses found with the model in relation to a similar test case in literature. The test case of this publication is a single stage shrouded turbine with a seal gap clearance of around 0.7% blade height. The authors discuss the loss distribution of the stage found with steady CFD. They divided the flow path into loss regions, (named upstream, hub, suction side, core, pressure side, casing, downstream) and assigned percentages of blade losses to them. From this a percentage of downstream losses to stage losses can be given: Downstream of their rotor, this evaluation gives around 17% of stage losses, which includes the wake mixing as well as the vortex mixing. The maximum mixing loss resulting from the model is around 10% of stage loss including the wake and the leakage mixing. From this rough comparison it can be concluded that the mixing model is giving reasonable results on the absolute level. Differences due to changed inlet conditions can be treated as a tendency and a quantification of the potential improvements.

The mixing model is capable of showing changes of losses due to changes of labyrinth jet distribution. One result is that it seems to be favourable to fill the wake with leakage fluid, from which observation a non-axisymmetric last gap shape was deduced. A potential improvement of about 1% stage loss, which is equivalent to 0.1% of efficiency, is attributable to this approach.

8.2 CONTRIBUTION

This chapter summarises the contributions described in detail throughout the dissertation.

From experimental data a detailed picture of the fluid flow within open cavities was gained. Several descriptive flow models of the inlet and exit cavity flow were derived from these data. The inlet cavity is dominated by a system of toroidal vortices, which are driven by a distinct inflow jet originating from the pressure side corner of the stator blade. The tangential velocity of the cavity flow is reflecting the balance of angular momentum between the input originating from the stator and the extraction due to the rotor interactions.

The interaction of the leakage jet with the main flow is coined by the static pressure field of the trailing edge. The jet mass flow is redistributed such that a

higher mass flow is found between the trailing edge positions.

Mixing processes and losses were described and quantified. The mass and momentum exchange within the inlet cavity was quantified using an unsteady control volume integration tool. The mass flows associated to the interaction are around three to four times the leakage mass flow in the 0.3% gap case. The fluctuation amplitudes may involve 70% of the leakage mass flow. A theoretical model was derived predicting the rotor tip incidence angle as a function of gap widths.

Novel design ideas were proposed based on the experimental findings, including non-axisymmetric blowing of the leakage jet, non-axisymmetric shaping of the shroud leading edge, as well as a round inlet cavity design. Further optimization steps on all mentioned design modifications could contribute to an efficiency increase of 0.1% up to 0.5%. In addition, this investigation supplies a test case for CFD calculations on unsteady flow interaction phenomena.

An unexpected experimental result was found in the closed cavity: Between the open and closed cavities unsteady fluctuations are carried over. Although, this effect quickly decays due to damping effects, it might be relevant for flow-induced eigen-frequencies and pressure fluctuations within those cavities.

For this experimental work a new turbine test rig was designed, built, commissioned and set into operation. The test rig combines highest mechanical precision with short change over time from one configuration to the other and fast data acquisition and probe traversing. In addition, the standards in terms of measurement accuracy and reliability of efficiency measurements is high. A new measurement technology was developed and brought into operation: the virtual four-sensor probe (FRAP). The achievements for this probe are firstly a new approach of gaining pitch-angle information with single-sensor fast response probes. Secondly, the probe head is the smallest in the world being capable of measuring 3D flow.

8.3 FUTURE WORK

The mixing model derived for the exit flow of the rotor certainly merits further development, since it may help to optimize the leakage interaction. An important step would be to apply the idea of optimizing the mixing losses to the hub leakage jet. New design ideas and potential in efficiency increase may result from this.

Future work on the shroud leakage interaction should take advantage of the deeper insight gained with CFD. Questions about flow details and loss generation could be answered in much greater detail at lower cost than with an exper-

iment. Another advantage would be the possibility to do geometric variations, starting from a converged numerical solution. Some unusual design ideas, as discussed in chapters 6 and 7 could be tried out, prior to testing them in an experiment.

The additional losses due to the interaction flow at the rotor tip flow field is an open question at this point. The experimental quantification of these losses would require a more sophisticated measurement technology, since the total temperature and the total pressure distribution up- and downstream of the rotor are required. Applying steady temperature measurement technology would require a traversed rotating temperature probe. Together with FRAP measurements within the absolute frame the loss production across the rotor could be quantified on a steady, rotor relative basis. The full unsteady information requires a new temperature measurement technology, which should be capable of measuring temperature fluctuations up to the third harmonic of blade passing frequency or higher. With this technology, yet to be developed, the unsteady performance of the rotor blade could be investigated. In this question, the calculation of the flow with an unsteady CFD code would also be helpful.

The design ideas for the inlet and exit cavities need the verification of concept and the quantification of the beneficial effect. This could be done by testing new configurations within LISA. Such a measurement campaign would require new cavity casing rings for the inlet cavity. The approach of non-axisymmetric shaped shrouds would require a new set of rotor rings for each planned configuration. The corresponding efficiency effects could be measured prior to increasing the resolution of flow measurements. Further optimization steps from the gained insight could be deduced and tested in order to fully exploit the potential of efficiency increase.

9 REFERENCES

[1] Abhari, R.S. (1996). "Impact of rotor-stator interaction on turbine blade film cooling", Journal of Turbomachinery, Vol. 118, pp123-133

[2] Ainsworth, R. W., Miller, R. J., Moss, R. W., Thorpe, S. J. (2000). "Unsteady pressure measurement", Measurement Science & Technology, 11(7), pp1055-1076

[3] Anker J.E., Mayer J.F. (2002). "Simulation of the interaction of labyrinth seal leakage flow and main flow in an axial turbine", GT2002-30348, ASME Turbo Expo, June 2002, Amsterdam

[4] Binder, A. (1985). "Turbulence Production Due to Secondary Vortex Cutting in a Turbine Rotor", Journal of Engineering for Gas Turbines and Power-Transactions of the ASME, 107(4), pp1039-1046

[5] Binder, A., Schroeder, Th., Hourmouziadis, J. (1989). "Turbulence measurements in a multistage low-pressure turbine", Journal of Turbomachinery, Vol. 111, pp153-161

[6] Brouckaert, J.F. (2000). "Development of single- and multi-hole fast response pressure probes for turbomachinery application", Proc. of the 15th Symp. on measuring techniques in cascades and turbomachines, Florence, Italy

[7] Chaluvadi, V. S. P., Kalfas, A. I., Banieghbal, M. R., Hodson, H. P., Denton, J. D. (2001). "Blade-row interaction in a high-pressure steam turbine", Journal of Propulsion and Power, 17(4), pp892-901

[8] Chaluvadi, V. S. P., Kalfas, A. I., Hodson, H. P., Ohyama, H., Watanabe, E. (2003). "Blade row interaction in a high pressure steam turbine", Journal of Turbomachinery, Vol. 125, pp1-11

[9] Dawes, W.N., VKI Lecture series (1998). "Blade row interference effects in axial turbomachinery stages: Simulation of unsteady blade row interaction with CFD: Background", February 9-12, 1998

[10] Denton, J. D., Johnson, C. G. (1976). "An experimental study of the tip leakage flow around shrouded turbine blades", CEGB-R/M/N-848, Central Electricity Generating Board.

[11] Denton, J. D. (1993). "Loss mechanisms in turbomachines", Journal of Turbomachinery-Transactions of the ASME, 115(4), pp621-656

[12] Denton, J.D., Wallis, A.M., Borthwick, D., Grant, J., Ritchey, I. (1996). "The three-dimensional design of low aspect ratio 50% reaction turbines", S461/008/96

[13] Egli, A. (1935). "The leakage of steam through labyrinth seals", Transactions of the ASME, 57, pp115-122

[14] Epstein, A.L. (1985). "High frequency response measurements in turbomachinery", VKI lecture series 85-03, Brussels

[15] Gizzi, W. (2000). "Dynamische Korrekturen für schnelle Strömungssonden in hochfrequent fluktuierenden Strömungen", ETH dissertation No. 13482, Zürich, Switzerland

[16] Gossweiler, C. (1993). "Sonden und Messsystem für schnelle aerodynamische Strömungsmessung mit piezoresistiven Druckgebern", ETH dissertation No. 10253, Zürich, Switzerland

[17] Gregory-Smith, D. G., VKI Lecture series (1997). "Secondary and tip-clearance flows in axial turbines: Physics of secondary flows", 10-13 February 1997

[18] Gregory-Smith, D. G., Ingram, G., Jayaraman, P., Harvey, N. W., Rose, M. G. (2001). "Non-axisymmetric turbine end wall profiling", Proceedings of the Institution of Mechanical Engineers, Part A- Journal of Power and Energy, 215(A6), pp721-734

[19] Haaser, F., Jack, J., McGreehan, W. (1987). "Windage rise and flowpath ingestion in turbine rim cavities", 87-GT-164, ASME Turbo Expo, May 31-June 4, Anaheim, California

[20] Harrison, S., (1989). "Secondary loss generation in a linear cascade of high-turning turbine blades", ASME paper 89-GT-47

[21] Harvey, N.W., Brennan, G., Newman, D.A., Rose, M.G. (2002). "Improving turbine efficiency using non-axisymmetric end walls: Validation in the multi-row environment and with low aspect ratio blading", GT-2002-30337, ASME Turbo Expo, June 3-6, Amsterdam, Netherlands

[22] Havakechian, S., Greim, R. (1999). "Aerodynamic design of 50 per cent reaction steam turbines", in "Development of Turbomachinery Design", edited by Denton J., IMechE, Professional Engineering Publishing Ltd., London

[23] Hobson, D.E., Johnson, C.G. (1990). "Two stage model turbine performance characteristics", Powergen. report No. RD/M/1888/RR90

[24] Hodson, H.P., Dawes, W.N. (1996). "On the interaction of the measured profile losses in unsteady wake-turbine blade interaction studies", ASME 96-GT-494

[25] Huber, F.W., Johnson, P.D., Sharma, O.P., Staubach, J.B., Gaddis, S.W. (1995). "Performance improvement through indexing of turbine airfoils, part1:

experimental investigation", 95-GT-27, ASME Turbo Expo, June 1995, Houston, Texas

[26] Hunter S.D., Manwaring S.R. (2000). "Endwall cavity flow effects on gaspath aerodynamics in an axial flow turbine: Part 1 - Experimental and numerical investigation", 2000-GT-651, ASME Turbo Expo, May 2000, Munich

[27] Hütte - Grundlagen der Ingenieurwissenschaften, 29th edition, 1989, Springer-Verlag

[28] Kupferschmied, P. (1998). "Zur Methodik zeitaufgelöster Messungen mit Strömungssonden in Verdichtern und Turbinen", ETH dissertation No. 12774, Zürich, Switzerland

[29] Kupferschmied, P., Köppel, P., Gizzi, W., Roduner, C., Gyarmathy, G. (2000). "Time-resolved flow mmeasurements with fast-response aerodynamic probes in turbomachines", Measurement Science Technology, Vol.11, pp1036-1054

[30] Langston, L. S. (2001). "Secondary flows in axial turbines - A review", Heat Transfer in Gas Turbine Systems, pp11-26

[31] McGreehan, W.F., Ko, S.H. (1989). "Power dissipation in smooth and honeycomb labyrinth seals", 89-GT-220, ASME Turbo Expo, June 4-8, Toronto, Canada

[32] Meyer, R.X. (1958). "The effect of wakes on the transient pressure and velocity distributions in turbomachines", ASME Journal of Basic Engineering, October 1958, pp1544-1552

[33] Millward, J.A., Edwards, M.F. (1994). "Windage heating of air passing through labyrinth seals", 94-GT-56, ASME Turbo Expo, June 1994, The Hague, Netherlands

[34] Parker, R., Watson, J.F. (1972). "Interaction effects between blade rows in turbomachines", Proc. of I.Mech.E., Vol. 186, No. 21

[35] Peters, P., Breisig, V., Giboni, A., Lerner, C., Pfost, H. (2000). "The influence of the clearance of shrouded rotor blades on the development of the flow field and losses in the subsequent stator", 2000-GT-478, ASME Turbo Expo, May 2000, Munich

[36] Pfau, A., Treiber, M., Sell, M., Gyarmathy, G. (2001). "Flow interaction from the exit cavity of an axial turbine blade row labyrinth seal", Journal of Turbomachinery-Transactions of the ASME, 123(2), pp342-352

[37] Rhode, D. L., Allen, B.F. (1999). "Measurement and visualisation of leakage effects of rounded teeth tips and rub-grooves on stepped labyrinths", 99-

GT-377, ASME Turbo Expo, June 1999, Indianapolis, Indiana

[38] Robic, B., Morrison,G. (2000). "Experimental Analysis of the Effect of Swirl on the Pressure Field in Whirling 50% Eccentric Annular Seal", 2000-GT-286, ASME Turbo Expo, May 2000, Munich

[39] Rockwell, D., Naudascher, E. (1978). "Review - Self-Sustained Oscillations of Flow Past Cavities", Journal of Fluids Engineering-Transactions of the ASME, 100, pp152-165

[40] Roduner, C.H. (2000). "Strömungsstrukturen in Radialverdichtern, untersucht mit schnellen Sonden", ETH dissertation No. 13428, Zürich, Switzerland

[41] Rusch, D., Pfau, A., Schlienger, J., Kalfas, A.I., Abhari, R.S. (2003). "Deterministic Unsteady Vorticity Field in a Driven Axisymmetric Cavity Flow", accepted at the 12th International Conference on Fluid Flow Technologies, September 3 - 6, 2003, Budapest, Hungary

[42] Sauer, H., Muller, R., Vogeler, K. (2001). "Reduction of secondary flow losses in turbine cascades by leading edge modifications at the endwall." Journal of Turbomachinery-Transactions of the ASME, 123(2), pp207-213

[43] Scherer, T. (1994). "Grundlagen und Voraussetzungen der numerischen Beschreibung von Durchfluss und Wärmeübergang in rotierenden Labyrinthdichtungen", Dissertation,Technical University of Karlsruhe

[44] Schlichting, H., Gersten, K., "Grenzschicht-Theorie", 9th edition, Springer Verlag, Berlin

[45] Schlienger, J., Pfau, A., Kalfas, A.I., Abhari, R.S. (2002). "Single pressure transducer probe for 3D flow measurements", Proc. of the 16th Symp. on measuring techniques in cascades and turbomachines, 2002, Cambridge, UK

[46] Schlienger, J., Pfau, A., Kalfas, A.I., Abhari, R.S. (2003). "Effects of labyrinth seal variation on multistage axial turbine flow", GT2003-38270, ASME Turbo Expo, 16-19 June 2003, Atlanta

[47] Schulte, V., Hodson, H. P. (1998). "Prediction of the becalmed region for LP turbine profile design", Journal of Turbomachinery-Transactions of the ASME, 120(4), pp839-846

[48] Schulte, V., Hodson, H. P. (1998). "Unsteady wake-induced boundary layer transition in high lift LP turbines", Journal of Turbomachinery-Transactions of the ASME, 120(1), pp28-35

[49] Sharma, O.P., Butler, T.L. (1987). "Predictions of endwall losses and secondary flows in axial flow turbine cascades", Journal of Turbomachinery, Vol. 109, pp229-236

[50] Sharma, O.P., Renaud, E., Butler, T.L., Milsaps, K., Dring, R.P., Joslyn, H.D. (1988). "Rotor-stator interactions in multistage axial flow turbines", AIAA paper No. 88-3013, AIAA/ASME/SAE/ASEE 24th Joint Propulsion Conference, Boston, July 1988

[51] Sieverding, C. H. (1985). "Recent Progress in the Understanding of Basic Aspects of Secondary Flows in Turbine Blade Passages", Journal of Engineering for Gas Turbines and Power-Transactions of the ASME, 107(2), pp248-257

[52] Sieverding, C. H., Denos, R., Arts, T., Brouckaert, J. F., Paniagua, G., VKI Lecture series (1998). "Blade row interference effects in axial turbomachinery stages: Experimental investigation of the unsteady rotor aerodynamics and heat transfer of a transsonic turbine stage", 9-12 February 1998

[53] Sieverding, C. H., Arts, T., Denos, R., Brouckaert, J. F. (2000). "Measurement techniques for unsteady flows in turbomachines", Experiments in Fluids, 28(4), pp285-321

[54] Sneck, H.J. (1974). "Labyrinth seal literature review", Journal of Lubrication Technology-Transactions of the ASME, October 1974, pp579-582

[55] Stahlecker, D. (1999). "Untersuchung der instationären Strömung eines beschaufelten Radialverdichterdiffusors mit einem Laser-Doppler-Anemometer", ETH dissertation No. 13228, Zürich, Switzerland

[56] Stocker, H.L. (1978). "Determining and Improving Labyrinth Seal Performance in Current and Advanced High Performance Gas Turbines", AGARD CP-237, 1978

[57] Taylor, M., De Pablos, T., Rose, M. (1998). "Time resolved HWA measurements of the OTL flow field from a shrouded turbine HP rotor blade", ASME 98-GT-564

[58] Traupel, W. (1973). "Thermische Turbomaschinen", Springer Verlag

[59] Treiber, M., Kupferschmied, P., Gyarmathy, G. (1998). "Analysis of the error propagation arising from measurements with a miniature pneumatic 5-hole probe", Proc. of the 13th Symp. on measuring techniques in cascades and turbomachines, 1998, Limerick, Ireland

[60] Trutnovsky, K., Komotori, K. (1981). "Berührungsfreie Dichtungen", VDI-Verlag

[61] VDI-Norm 2040 in DIN Taschenbuch 229, "Durchflussmessungen von Fluiden in geschlossenen Leitungen und Drosselgeräten: Blenden, Düsen, Venturirohre", 2nd edition, Beuth Verlag, Berlin

[62] Venable, B.L., Delaney, R.A., Busby, J.A., Davis, R.L., Dorney, D.J.,

Dunn, M.G., Haldeman, C.W., Abhari, R.S. (1999). "Influence of vane-blade spacing on transonic turbine stage aerodynamics: Part I-Time-averaged data and analysis", J. of Turbom., Vol. 121 No.4, pp660-672

[63] VKI Lecture series (1998). "Introduction to measurement technology"

[64] Wallis, A. M., Denton, J. D. (2002). "Comparison of design intent and experimental measurements in a low aspect ratio axial flow turbine with 3D-blading", Turbo Expo, Amsterdam

[65] Wallis, A. M., Denton, J. D., Demargne, A. A. J. (2001). "The control of shroud leakage flows to reduce aerodynamic losses in a low aspect ratio, shrouded axial flow turbine", Journal of Turbomachinery-Transactions of the ASME, 123(2), pp334-341

[66] Wang, H.P., Olson, S.J., Goldstein, R.J., Eckert, E.R.G. (1997). "Flow Visualization in a Linear Turbine Cascade of High Performance Turbine Blade", Journal of Turbomachinery-Transactions of the ASME, 119, pp1-8

[67] Waschka, W. (1991). "Zum Einfluss der Rotation auf das Durchfluss- und Wärmeübergangsverhalten in Labyrinthdichtungen und Wellendurchführungen", Dissertation, Technical University, Karslruhe

[68] Waschka, W., Wittig, S., Kim, S. (1992). "Influence of High Rotational Speeds on the Heat-Transfer and Discharge Coefficients in Labyrinth Seals", Journal of Turbomachinery-Transactions of the ASME, 114(2), pp462-468

[69] Wilcox, D.C., "Basic Fluid Mechanics", 2nd Edition, DCW Industries, La Canada, California

[70] Willenborg, K., Kim, S., Wittig, S. (2001). "Effects of Reynolds number and pressure ratio on leakage loss and heat transfer in a stepped labyrinth seal", Journal of Turbomachinery-Transactions of the ASME, 123(4), pp815-822

[71] Wisler, D. C. (1985). "Loss Reduction in Axial-Flow Compressors through Low-Speed Model Testing", Journal of Engineering for Gas Turbines and Power-Transactions of the ASME, 107(2), pp354-363

[72] Wittig, S., Dörr, L., Kim, S. (1983). "Scaling effects on leakage losses in labyrinth seals", ASME Journal of Engineering for Power, 105, pp305-309

[73] Wyler, J. S. (1975). "Probe Blockage Effects in Free Jets and Closed Tunnels", Journal of Engineering for Power-Transactions of the ASME, 97(4), pp509-515

[74] Zimmermann, H., Wolff, K. H. (1998). "Air system correlations, Part 1: Labyrinth seals", 98-GT-206, ASME Turbo Expo, June 1998, Stockholm, Sweden

10 NOMENCLATURE

Romans

a	[m/s]	Speed of sound
A	[m^2]	Area
C	[-]	Throughflow coefficient
d, D	[m]	Diameter
g	[m]	Effective seal gap width
f	[Hz]	Frequency, blade passing frequency
F	[N]	Force
h	[m]	Blade height
h	[kJ/kg]	Enthalpy
H	[%]	Relative humidity
K	[-]	Calibration coefficient
$\dot{m}$	[kg/s]	Mass flow
M	[-]	Mach-number
n	[-]	Numbers of seals in the labyrinth
p	[N/m^2]	Static pressure
p^o	[N/m^2]	Total pressure
P	[W]	Power
r	[m]	Radius, radial direction
R	[-]	Non-dimensional blade height
s	[J/kg/K]	Specific entropy
S'	[W/K]	Rate of entropy generation
t	[°]	Blade pitch
t	[s]	Time
T	[°K]	Static temperature
T^o	[°K]	Total temperature
T	[Nm]	Torque
u	[m/s]	Local blade speed

U	[V]	Voltage
v	[m/s]	Velocity, in the absolute frame of reference
V	[m^3]	Volume
V	[-]	Non-dimensional velocity V=v/u
w	[m/s]	Velocity, in the relative frame of reference
x	[m]	Characteristic length
z	[m]	Axial direction
Z	[-]	Non-dimensional axial position

Greek

α	[°]	Absolute flow angle
β	[-]	Relative flow angle, ratio of diameters d/D
δ	[-]	Boundary layer thickness
ε	[-]	Labyrinth throughflow coefficient
η	[-]	Efficiency
Φ	[-]	Flow coefficient
φ	[°]	Yaw angle
γ	[°]	Pitch angle
κ	[-]	Isentropic exponent
λ	[-]	Load coefficient
ρ	[kg/m^3]	Density
θ	[rad]	Circumferential direction
Θ	[-]	Non-dimensional circumferential position
ω	[rad/s]	Rotational speed, vorticity
Ω	[-]	Non-dimensional vorticity
ζ	[-]	Entropy loss coefficient

Indices

BP		Blade passing
cav		Cavity

C	Casing
e	Excitation
i	Inner radius
i,j,k	Indices of the coordinate system
l	leakage
m	main flow
mix	Mixing condition
o	Outer radius
r, θ, z	In the direction of the equivalent coordinate
rel	Blade relative system

Formulas

$$C_p = \frac{p - p_{exit}}{p_{in}^{o} - p_{exit}} \quad \text{Non-dimensional pressure}$$

$$\phi = \frac{v_z}{u} \qquad \text{Flow coefficient}$$

$$\lambda = \frac{\Delta v_\theta}{u} \qquad \text{Loading coefficient}$$

Abbreviations

DP	Design operation point
LE	Leading edge
OP1, OP2	Operation point variation
PS	Pressure side
SS	Suction side
TC03	Small seal clearance case, g=0.3%
TC1	Large seal clearance case, g=1%
TE	Trailing edge
FRAP	Fast response aerodynamic probe

APPENDIX

Blade row	Seal	case TC1 Gap	case TC1 Roundness	case TC03 Gap	case TC03 Roundness
stator 1	in			500	±20
stator 1	mid	850	±120	400	±20
stator 1	out	850	±120	450	±20
rotor 1	in			320	±30
rotor 1	mid	820	±20	350	±20
rotor 1	out	870	±30	250	±50
stator 2	in			400	±20
stator 2	mid	1100	±100	420	±30
stator 2	out	970	±100	500	±20
rotor 2	in			350	±50
rotor 2	mid	870	±30	280	±30
rotor 2	out	850	±50	400	±50

Tab. A: Measured gap width test case A, non-running condition, [µm]

Measured gap widths of case A. The effective gap width under running conditions at 2700rpm is reduced by 0.1mm, due to the growth of the rotor rings. Throughout this dissertation the gap width is made non-dimensional with the blade height.

First author publications

Pfau A., Treiber M., Sell M., Gyarmathy G., 2001, "Flow interaction from the exit cavity of an axial turbine blade row labyrinth seal", Journal of Turbomachinery, Vol. 123

Pfau A., Schlienger J., Kalfas A.I., Abhari R.S., 2002, "Virtual four sensor fast response aerodynamic probe (FRAP)", 16. symposium on measurement technology in turbomachinery, 24./25.9.2002, Cambridge

Pfau A., Schlienger J., Rusch D., Kalfas A.I., Abhari R.S., 2003, "Unsteady flow interactions within the inlet cavity of a turbine rotor tip labyrinth seal", GT2003-38271, ASME Turbo Expo,16.-19. June 2003, Atlanta

Pfau A., Schlienger J., Kalfas A.I., Abhari R.S., 2003, "Unsteady, 3-dimensional flow measurement using a miniature virtual 4 sensor Fast Response Aerodynamic Probe (FRAP)", GT2003-38128, ASME Turbo Expo,16.-19. June 2003, Atlanta

Pfau A., 2003, "Loss mechanisms in labyrinth seals of shrouded axial turbines", ETH dissertation, No. 15226

in preparation: Pfau A., Kalfas A.I., Abhari R.S., 2004, "Making Use of Labyrinth Interaction Flow", GT2004-53797, ASME Turbo Expo,14.-17. June 2004, Vienna, Austria

Publications as co-author

Sell M., Schlienger J., Pfau A., Treiber M., Abhari R.S., 2001, "The 2-stage axial turbine test facility LISA", 2001-GT-492, Proceedings of the ASME Turbo Expo, 4.-7. June, 2001, New Orleans, Louisiana

Schlienger J., Pfau A., Kalfas A.I., Abhari R.S., 2002, "Single pressure transducer probe for 3D flow measurements", 16. symposium on measurement technology in turbomachinery, 24./25.9.2002, Cambridge

Schlienger J., Pfau A., Kalfas A.I., Abhari R.S., 2003, "Effects of labyrinth seal variation on multistage axial turbine flow", GT2003-38270, ASME Turbo Expo,16.-19. June 2003, Atlanta

Schlienger J., Pfau A., Kalfas A.I., Abhari R.S., 2003, "Measuring unsteady 3D flow with a single pressure transducer", 5. European Turbomachinery Conference, 17.-22. March 2003, Prague

Rusch, D., Pfau, A., Schlienger, J., Kalfas, A.I., Abhari, R.S. (2003). "Deterministic Unsteady Vorticity Field in a Driven Axisymmetric Cavity Flow", accepted at the 12th International Conference on Fluid Flow Technologies, September 3 - 6, 2003, Budapest, Hungary

CURRICULUM VITAE

Axel Pfau

born on the 6th of September 1970 in Nürtingen, Germany

Education

1977-81:   Elementary School, Leonberg, Germany

1981-90:   High School, Albert-Schweitzer-Gymnasium, Leonberg, Germany

Studies

1990-96:   Mechanical Engineering: University of Karlsruhe (TH), Germany

1994/95:   Student Exchange Program: University of Karlsruhe (TH), Department of Mechanical Engineering and Ecole Nationale Supérieur d'Arts et Métiers, Paris, France

1996:   Diploma Thesis: Aerospace Engineering Department, University of Colorado at Boulder, USA

9/1996:   Diploma Degree in Mechanical Engineering

Working Experience

3/97-8/03: Research Assistant and Doctoral Student at the Turbomachinery Laboratory of the Swiss Federal Institute of Technology

9/03-11/03 Technical coordinator of the Centre of Energy Conversion at the Swiss Federal Institute of Technology